HYDRODYNAMIC AND SURFACE CHEMISTRY EFFECTS IN COAL-OIL AGGLOMERATE FLOTATION

By

Kenneth Peter Darcovich

A THESIS SUBMITTED TO
THE SCHOOL OF GRADUATE STUDIES AND RESEARCH
IN PARTIAL FULFILLMENT OF THE REQUIREMENTS
FOR THE DEGREE OF
DOCTOR OF PHILOSOPHY
IN THE DEPARTMENT OF CHEMICAL ENGINEERING
UNIVERSITY OF OTTAWA

Ottawa, Ontario,
October 1993

ISBN 0-612-15605-2

Canada

UNIVERSITÉ D'OTTAWA
UNIVERSITY OF OTTAWA

Abstract

Oil agglomeration combined with bubble flotation has proven to be an effective means of upgrading and recovering waste fine coal when low-oil floc-type agglomerates are formed. Low-oil recovery is desirable, since less ash is incorporated into the agglomerates and the expense of using oil is reduced. In this state, the flocs are too small and weak for screen separation but can be successfully recovered by flotation as even a small amount of oil imparts a much improved surface character, and agglomerate strength is less important.

Reduction of the amount of wetting phase used in the oil agglomeration process for advanced coal cleaning and utilization technologies is important to the economics of the process. An analysis was made of the agglomerate surface properties and on the size enlargement characteristics and possible mechanisms of the process taking place when floc-type coal-oil agglomerates are formed at oil levels less than about 2% oil by weight.

Since this product exists not as dense agglomerates but only as small aggregates of a few particles, the adhesion technique was used to determine the surface properties of agglomerates made from a high purity coal. The surface properties closely matched those of the oil at agglomerate oil-levels above 2% by weight. Particle-size measurements by laser diffraction were then correlated to the surface properties as a function of the oil-level and of agglomerate particle packing.

Subsequently, the surface free energies of agglomerates made from coals of several different ranks were measured by the adhesion technique. Oil levels from 0 to 10% by weight were used. As was expected, it was found that higher-rank coals are more easily oil-wetted and that the surface properties of the agglomerates correlate with

agglomeration recovery and ash removal data.

It has been illustrated in pilot studies that oil-agglomeration together with flotation gives an enhanced combustibles recovery and ash separation. To corroborate successful flotation results for such agglomerates, a computational fluid dynamics simulation was formulated to model their recovery. This simulation employed the finite volume method, and featured three-phase flow as well as the collection of particles by bubbles. Additionally, a novel formulation of a boundary element method for unsteady full Navier-Stokes flow was undertaken to model the collisional aspects of micro-flotation. This method was successfully implemented, but problems with numerical instability in the required flow regimes prevented a more detailed micro-flotation study in the present work.

The basis of the numerical methods was a linearization and discretization of the governing continuum transport equations. The equations of momentum, and continuity, together with the shear stress expression, provided the framework for the numerical simulation. The $k-\epsilon$ model for turbulence was applied to the basic transport equations to give a complete system of equations for the liquid phase. This model employs an averaged kinetic energy of turbulence k, and its dissipation rate, ϵ.

The general computational fluid dynamics (CFD) model for macro-flotation comprised 12 field variables. In two dimensions they were the two velocities of the gas (u_i in the i-direction), liquid and solid phases, the pressure, the gas and solids concentrations, the flotation bubble loading and two turbulence parameters from the $k-\epsilon$ model. For the finite volume method, the general transport equation which was solved was:

$$\frac{\partial(\rho\phi)}{\partial t} + (\rho u_i \phi - \Gamma_\phi \phi_{,i})_{,i} = S_\phi$$

where Γ_ϕ and S_ϕ are respectively, the diffusive coefficient and volumetric source rate of the general variable ϕ. The purpose of this generalization is to make each equation a module for a single computational routine which simply inserts the appropriate Γ_ϕ and S_ϕ quantities.

The momentum equation was applied to both the liquid and solid phases, adding the coefficient α_i, representing the respective phase volume fraction to each term.

In a multi-phase environment, additional source terms were required; F_{DL} is for the drag between the dispersed phase D, and the liquid, and $\mathcal{F}_i(\rho_D, u_D, \mu_{D,\text{eff}})$ which arise from the curvature of the coordinate system selected. For the solid phase, the viscous terms were neglected.

The gas phase momentum equations were simplified. That is, the action of the liquid phase was assumed to be primarily responsible for the gas phase transport, so only the pressure, drag and buoyancy terms were retained.

A local flux balance at all nodes in the grid was employed to determine a dispersed phase volume fraction. Mass generation or consumption in a finite-volume cell arose from adhesion of particles to bubbles, and was treated as mass transfer from the solid to gas phase.

A turbulent collision model was employed to determine the contacting rate in a flotation system. The fraction of collisions resulting in adhesion was determined as a function of the coal-oil agglomerate surface properties. The adhesion of the agglomerates to the bubbles was treated as mass transfer from the solid phase to the gas phase. Further, once agglomerates were considered attached to a bubble, a drag coefficient was included to account for this. The presence of bubbles and particles required a local adjustment of the laminar viscosity. A test case in a unidirectional tube was made to converge.

The flotation unit modeled in this work was based on a typical commercial cell with dimensions 1.4 by 1.6 meters. The mass flow rate of particulates was 4.32 tonnes/day. The finite volume grid used was made finer near inlets and outlets as regions where mixing and flow deflection occurred required finer numerical resolution for solution stability. The top face was considered open to the atmosphere, and only the gas phase was allowed to exit there. The model was then implemented in a float cell configured with a slurry inlet on one side near the bottom, an air inlet at the bottom and a top open to the atmosphere with an overflow weir. A flotation recovery data set was obtained for a range of bubble-particle attachment efficiencies and particle sizes. Modeling of an attachment efficiency parameter from fundamental agglomerate properties, provided a means to calculate this attachment efficiency from a reference set of experimental data. The surface property data, together with the

calculated attachment efficiency, were able to accurately predict the recoveries of two other subbituminous coal samples. This attachment efficiency was expressed as $r_a = f(\Delta\gamma, d_P, h)$, incorporating agglomerate size, inherent material hydrophobicity and oil wettability.

Thus, the surface properties of coal-oil agglomerates were incorporated into a model based on the resolved hydrodynamics of the flotation process. The overall result was an integrated model where individual local mechanisms could be summed to determine recovery values which compared very well to a wide range of data.

Acknowledgements

I would like to thank everybody associated with my research during the time spent working on my thesis project. The staff at NRC, the Chemical Engineering faculty at the University of Ottawa, colleagues and friends have all provided invaluable assistance and support. Financial support from NSERC and the NRC is acknowledged. In particular I would like to express gratitude to Dr. F.D.F. Talbot, my project co-supervisor at the early stages of the work who has since retired, and to Dr. K.Y.M. Lai of the Gas Dynamics Laboratory at NRC for providing some basic computer code, and for his many helpful discussions on the numerical work, as well as to Drs. N. Tosaka and K. Kakuda of Nihon University in Narashino, Japan for their gracious hosting of a most constructive work-visit with their research group.

Most specially, I would like to extend my deepest thanks to Dr. C.E. Capes, my principal project supervisor, with whom I have worked closely over the course of the project and who provided continual and essential support, insight, and guidance. I am indebted to him for the research opportunities he has given me. For the balance required between mind and body, I would also like to acknowledge the Ultimate fields and xc-skating trails of this continent. Finally, special gratitude is reserved for my family, parents and fiancée Karen, to all of whom, this thesis is dedicated.

Contents

List of Figures

List of Tables

Chapter 1

Introduction

In the context of mineral flotation, the simple interaction between a bubble and particle is of fundamental importance. There are many factors which determine such an interaction, potentially giving rise to a collision, attachment and successful flotation. Of interest in this study are the hydrodynamics of the interaction. Resolving the hydrodynamic forces would provide a basis for describing the overall kinetics of coal-oil agglomerate flotation in a large scale context.

To date, no complete and general model has been developed for mineral flotation, undoubtedly due to the complexity of the overall process. It has been recognized, however, that a successful interaction does require a collision, a contact period, a liquid film thinning process leading to particle-bubble attachment, and subsequent flotation of the captured particle [1]. These micro-processes manifest themselves under the motions of a multi-phase flow field. In addition to the hydrodynamic interaction, the surface chemical interaction contributes to the resulting overall kinetics of the process [2].

Briefly, a description of coal-oil agglomeration will be given to provide some background to the origin of the agglomerates.

Agglomeration processes bring together fine powders into larger masses in order to improve powder properties. In conventional coal mining procedu.. fine coal (typically -100 mesh) is rejected with tailings as it is impractical to recover. Due to the

heterogeneous nature of coal, particles below 100 mesh are often entirely carbonaceous or entirely ash. This discretization facilitates effective separation. The tailings are handled in liquid slurry form and an immiscible oil phase (usually any liquid hydrocarbon of size C_7 or greater) is added under high-shear mixing conditions to enhance surface wetting. The oil selectively adheres to the carbonaceous surfaces and also acts as a bridging liquid to consolidate several oiled coal particles into an enlarged agglomerate. The ash is excluded and is separated via screening or by bubble flotation, since the hydrophobic oil surface of the agglomerate favours attachment to the bubble.

In recent years, in connection with work that has been done on the beneficiation of coal fines by oil agglomeration, it has been found that improved recovery at lower oil levels in terms of yield and purity may be obtained by separating the agglomerates by flotation rather than conventional screening methods [3, 4, 5].

This method was found to have several advantages which include rejection of coarse impurities which would otherwise be retained on screens and the requirement of less oil, as loose agglomerates which have sufficient mechanical integrity to be floated, may be broken and lost on screens. The cost of the oil which is added to the process to form the agglomerates is the major operating expense. Thus recovery of low-oil agglomerates is much more economically attractive. Since weaker flocs are recovered by flotation, the method may be used to recover lower-rank coals, or coals which are relatively poorly wetted by oil. In fact, some preliminary work on low-oil agglomeration shows that purity is increased as excess oil is simply not available to wet ash containing particles (which are more oleophobic/hydrophilic than the more carbonaceous particles) and incorporate them into the agglomerate matrix. This is especially true for pyrite particles which are responsible for the acid rain phenomenon. In fact, it has been demonstrated by Capes [6] that pyrite rejection is significantly enhanced when very low oil levels are used in coal agglomeration.

The agglomerate flotation technique has been used since the turn of the century [7], but to date, there is a considerable gap in the understanding of the fundamentals involved. There has been little or no research done specifically on the flotation of

agglomerates as opposed to individual particles. However, bubble flotation of oil-agglomerated coal fines has been demonstrated to be an effective recovery method. Yield-ash results are shown for the agglomeration flotation of a Pennsylvania coal in figure 1 [8]. The results compare well with other recovery methods.

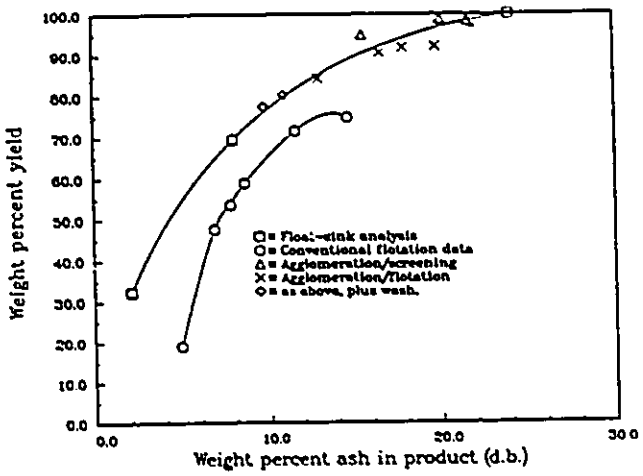

Figure 1.1: Yield-ash results for a minus 28 run of mine coal from Pennsylvania. (Wt.% reagent levels are based on feed solids).

The flotation fundamentals of the coal-oil agglomerate system have yet to be thoroughly studied. Since the coal-oil agglomerates in this context are a product of an upstream formation process, the material properties of the system are more or less fixed. Thus the surface chemical interaction is inherently coupled with the hydrodynamic interaction. A study in the 1950's showed that an oiled coal surface had an improved floatability attributed to its higher contact angle and the diffusional properties of the oil allowing a particle-bubble interface to be more readily formed [9].

An understanding of the underlying flotation mechanisms is intrinsically linked to the equipment used for industrial-scale agglomerate flotation. Particle-bubble contacting is of prime importance and some preliminary studies have illustrated this point [10]. Since the main function of a flotation machine is to provide sufficient mixing or particle-bubble contact, it is evident that equipment design can benefit from further research on the hydrodynamics of the flotation operation, incorporating the

fundamental mechanisms.

1.1 Objectives of the Project

An overview of the research being initiated encompasses the following stages:

1. To study coal-oil agglomerate flotation kinetics requires characterization of the surface properties of coal, coal-oil agglomerates and the aqueous medium as they relate to bubble flotation. Namely, determination of interfacial tensions and contact angles, which are input parameters for various flotation kinetics models. A kinetic model for a batch system is tantamount to a recovery model for a continuous system. Surface properties of liquid-bonded particulate agglomerates have not been previously determined, and it was found that the adhesion technique developed by Absolom et al. [11] was suitable for coal-oil agglomerates.

2. To establish a reliable method of determining the particle-size distribution of coal-oil agglomerates. This is particularly a problem with weak, low-oil agglomerates, as they must be measured in a non-destructive environment. A Malvern Laser Diffraction light-scattering particle-size analyser has proved suitable for this task.

3. To explore the Boundary Element Method as a possible means for a computational fluid dynamics simulation of the microscopic, particle-bubble interaction in flotation.

4. To model the flotation process in a macroscopic fashion via a computational fluid dynamics approach. This simulation will be carried out in two dimensions, and simultaneously treats liquid, gas and solid phases. Aside from agglomerate surface properties, the experimental input variables are bubble size, agglomerate size, which is determined by the oil level, and the slurry flow rate in the cell.

5. To use the flow and turbulence conditions determined for the three phase flow field to incorporate turbulent collision theory into constructing a mechanistically

based model for the recovery of coal-oil agglomerates by flotation. This can be used as a basis for predicting recovery kinetics as a net process result of several input parameters. Hydrodynamic forces thus determined can be used to assess the relative contribution of surface forces and to account for observed collection efficiencies in a mathematical model. Comparison with existing, more empirical models will be made and discussed.

1.2 Background Literature

There has been extensive theoretical work done on the mechanism of bubble flotation of particles. On a fundamental level, the aspects of the process deemed most important are the hydrodynamics and the particle-bubble adhesion criteria which are based on the surface chemistry of the system.

The hydrodynamic theories of flotation are normally based on classical "streamlines around a bubble" models [12]. Often two regimes are treated; the Stokes regime (Reynolds number, $Re \ll 1$) and the potential regime ($Re \gg 1$). Several authors have used this hydrodynamic model to predict the capture efficiency of particles on bubbles [1, 13, 14]. Their findings are usually expressed as an efficiency of collision or capture for particles encountered by a bubble as a function of perpendicular distance from the central axis of the path of the bubble.

1.2.1 Bubble-Particle Collision Modeling

One of the earliest, most complete and relevant models of the flotation process was presented by Sutherland [2]. It is briefly summarized here, as much of the later flotation modeling work used his theories as a starting point. Sutherland began by assuming that the particles' inertia would not be so great as to cause their trajectories to significantly differ from those of the fluid moving past a sphere. The equation for streamlines (assumed potential regime or incompressible, inviscid flow for the case of

flotation) of fluid moving past a sphere of radius R (the bubble) is,

$$\sin^2\theta = \frac{\Psi r}{r^3 - R^3} \tag{1.1}$$

where:
(r, θ) is the polar coordinate
Ψ is a streamline constant.

D is defined as the largest radial distance away from the bubble path axis that a particle originally positioned at $r \gg R$ can collide with the bubble. Hence this streamline must pass through the point $(r = R + a, \theta = \pi/2)$ for a particle of radius a. Thus, at this point,

$$\Psi = \frac{((R+a)^3 - R^3)}{(R+a)} \tag{1.2}$$

Figure 1.2 shows this schematically.

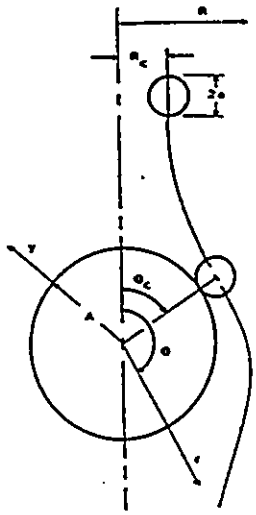

Figure 1.2: Schematic of particle streamline approaching a bubble in flotation context.

When the particle is at an infinite distance above the bubble, then $\theta = 0$, and the value of $r \sin\theta$ or D, is the maximum distance at which the center of the particle can lie from the center of the line of motion of the bubble just to collide with it. Substituting Ψ into 1.1 and taking the limit as $\theta \to 0$ ($r \to \infty$) gives,

$$D = \sqrt{3aR} \quad \text{for } a << R \tag{1.3}$$

This value is then used to define a collision efficiency E, which is a ratio of the area swept out by a rising bubble in which particles will collide with it, to the entire swept area. It is expressed as,

$$E = \frac{D^2}{R^2} \tag{1.4}$$

Hence, the number of collisions per second, n, between a bubble and a suspension of particles of concentration N_0 is,

$$n = E\pi R^2 V N_0 = \pi D^2 V N_0 = 3\pi R a V N_0 \tag{1.5}$$

where V is the velocity of the bubble relative to the particles.

Now consider a particle at a distance d, $(d < D)$ from the center line of motion of the bubble. The polar coordinate where collision occurs is,

$$\left[(r = a + R, \theta = \sin^{-1}[\frac{d\sqrt{R+a}}{(R+a)^3 - R^3}])\right]$$

or neglecting a^3 terms,

$$\theta = \sin^{-1}[-\frac{d}{\sqrt{3aR}}] \tag{1.6}$$

The spatial profile S , (or two-dimensional velocity potential) of the liquid relative to the bubble is,

$$S = v_r \cos\theta + \frac{VR^3 \cos\theta}{2r} \tag{1.7}$$

The tangential velocity is then,

$$v_\theta = \frac{-1}{r}\frac{\partial S}{\partial \theta} = V \sin\theta + \frac{VR^3 \sin\theta}{2r^3} \tag{1.8}$$

Hence, the time for the particle to travel along the streamline from the point $(R + a, \theta)$ to where it would leave the bubble $(R + a, \pi - \theta)$ is given by

$$t_c = \int_\theta^{\pi-\theta} \frac{(R+a)d\theta}{V \sin\theta(1 + \frac{1}{2}\left(\frac{R}{R+a}\right)^3)} = \frac{4(R+a)\ln(\cot\frac{\theta}{2})}{V(2 + \left(\frac{R}{R+a}\right)^3)} \tag{1.9}$$

substituting θ from 1.6,

$$E = \sqrt{3Ra}\,\mathrm{sech}[\frac{Vt_c(2 + \left(\frac{R}{R+a}\right)^3)}{4(R+a)}] \tag{1.10}$$

or, if $a \ll R$,

$$E = \sqrt{3Ra}\,\mathrm{sech}[\frac{3Vt_c}{4R}] \tag{1.11}$$

Sutherland defines an induction period λ, which must be less than t_c for the particle to adhere to the bubble. Thus 1.11 can be written as,

$$E = \sqrt{3Ra}\,\mathrm{sech}[\frac{3V\lambda}{4R}] \tag{1.12}$$

Thus for a given bubble size, E decreases as the induction time increases.

In view of the induction time, equation 1.5 can be modified for the case where N' is the number concentration of bubbles and n_f is the number of fruitful collisions per unit time per unit volume. Thus,

$$n_f = 3\pi RaVN_0N'\mathrm{sech}^2[\frac{3V\lambda}{4R}] \tag{1.13}$$

If ρ_p is the particle density and α is the fraction of fruitful collisions floated, then the rate of flotation R_f, (ie; g/cm^{3}s) is,

$$R_f = 4\pi^2\alpha\,\mathrm{sech}^2[\frac{3V\lambda}{4R}]Ra^4N_0N'\rho_p \tag{1.14}$$

Sutherland also modified his model to account for the presence of gangue, a particle-size distribution, a bubble-size distribution, an induction period distribution as well as for continuous cell operation.

Shortcomings of Sutherland's work are that particle inertial effects are ignored, a two element hydrodynamic interaction is unaccounted for, the elastic nature of the bubble surface is neglected, the scale-up is based on simply adding up the effects predicted for single bubbles, the induction period (ie; adhesion mechanism) is unexplained and simply treated as a phenomenon where some net change occurs.

1.2.1.1 Modifications to the Micro-Collision Model

An alternative expression for contact time was derived by Evans [15] based on an elastic collision model. For a depth of penetration h, the increase in bubble surface area (assuming that $(a \ll R)$) is,

$$2\pi rh - (2\pi rh - \pi h^2) = \pi h^2 \tag{1.15}$$

The work W, done to increase the bubble surface area is,

$$W = \pi\gamma h^2 \tag{1.16}$$

where γ is the bubble-liquid interfacial tension.

The force F, of the distorted surface acting on the particle is,

$$F = \frac{dW}{dh} = 2\pi\gamma h \tag{1.17}$$

Since the force accelerating the particle in the direction normal to the bubble surface is proportional to h, the motion is simple harmonic, with the contact time being half the period of the simple harmonic motion. If m is the particle mass,

$$t_c = \frac{\pi h_{max}}{V} = \frac{\sqrt{\pi m}}{2\gamma} \tag{1.18}$$

Flint and Howarth contributed a major improvement by incorporating particle inertial effects into a collision model [16]. This development was based on observations reported by Herne [13].

The particle velocities are expressed as,

$$v_\theta = \sin\theta\left[(1+G) + \frac{1}{2r^3}\right] \tag{1.19}$$

$$v_r = \cos\theta\left[(1+G) + \frac{1}{r^3}\right] \tag{1.20}$$

where G is a dimensionless inertial parameter.

$$G = \frac{2(\rho_p - \rho_L)a^2 g}{9\mu V} \tag{1.21}$$

This gives Ψ_p, the particle stream function as,

$$\Psi_p = \frac{1}{2}\sin^2\theta r^2\left[(1+G) - \frac{1}{r^3}\right] \tag{1.22}$$

Then calculating Ψ_p at a grazing trajectory gives,

$$E = \frac{G}{1+G} \tag{1.23}$$

which can be applied to both potential and Stokes regimes, since no flow field interaction is assumed.

Reay and Ratcliff [17, 18] carried out a similar analysis, but additionally incorporated a hydrodynamic resistance on the particle to further state that,

$$E = f(a/R, \rho_p/\rho_L) \tag{1.24}$$

and determined the functional form to be

$$E = \beta_1 (a/R)^{\beta_2} \tag{1.25}$$

where β_1 and β_2 are functions of ρ_p/ρ_L.

A collision model was derived by Derjaguin et al. [1, 19], where the hydrodynamic influence of the particle's motion was also taken into account. This interaction becomes increasingly important for smaller, inertialess particles, with about a 10 μm diameter being the upper size limit.

An outline of the mathematics describing this situation is not of great relevance to this discussion. However, briefly, based on Brenner's [20] model of a sphere approaching a flat infinite surface, it is shown that in the region one particle radius away from the bubble surface, the liquid-film thinning process between the particle and the bubble presents a further resistance to particle-bubble contact. The expression for collision efficiency given is,

$$E = \frac{a^2}{R^2} \ln \left(\frac{a}{h_c} \right)^{-2(1+3(\rho_p - \rho_L)/6.46\rho_p)} \tag{1.26}$$

where h_c is the critical film rupture thickness. Figure 1.3 shows the effect of the hydrodynamic interaction on the efficiency of collision compared to when this interaction is unaccounted for.

In a paper by Schulze and Gottschalk, [21] via a stroboscopic photography technique, the dependence of t_c with θ was determined along with the various mechanisms involved. They define a boundary angle, θ_{GR} where all interactions at $\theta < \theta_{GR}$ are collisions, and at $\theta > \theta_{GR}$ they are processes of sliding. Further, they conclude that the kinetic energy of particles flowing near the symmetry axis of the bubble is used

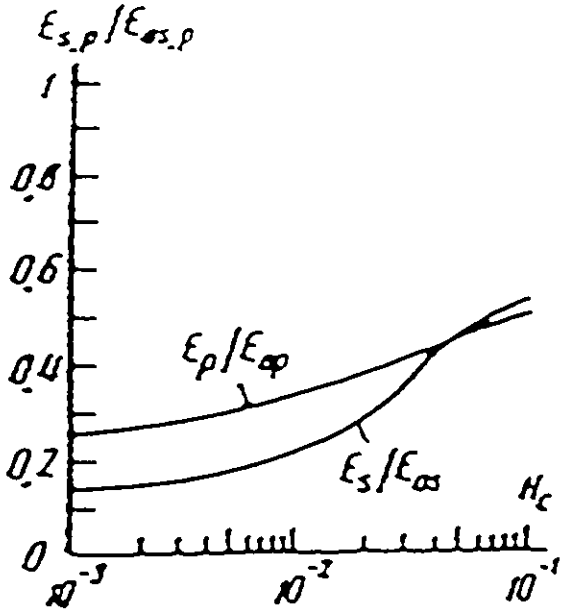

Figure 1.3: The ratio of capture efficiency accounting for hydrodynamic interaction to the capture efficiency without interaction for potential and Stokes conditions. From [1].

for the elastic deformation of the bubble surface. These particles are repelled from the bubble, lose over 70% of their kinetic energy and have a contact time of less than 4 ms.

At $\theta > 30°$, the particle slides over the bubble with a contact time up to 20 times the duration of collision. Contact time is maximum near $\theta = 30°$ and also near this point, attachment seems to be maximum. This is consistent with theoretically calculated particle contact velocities, shown in figure 1.4.

Weber [22] has numerically determined collision efficiencies along the model of Reay and Ratcliff for intermediate (between Stokes and potential regimes) Reynolds numbers which are relevant for most flotation applications.

The stream function Ψ, near the bubble surface is approximated as,

$$\Psi = \frac{V'(r-R)^2 \sin^2\theta}{4}[2 + \frac{R}{r} + \frac{3}{16}\mathrm{Re}[(2 + \frac{R}{r})(1 + \cos\theta) + (\frac{a}{r})^2 \cos\theta]] \qquad (1.27)$$

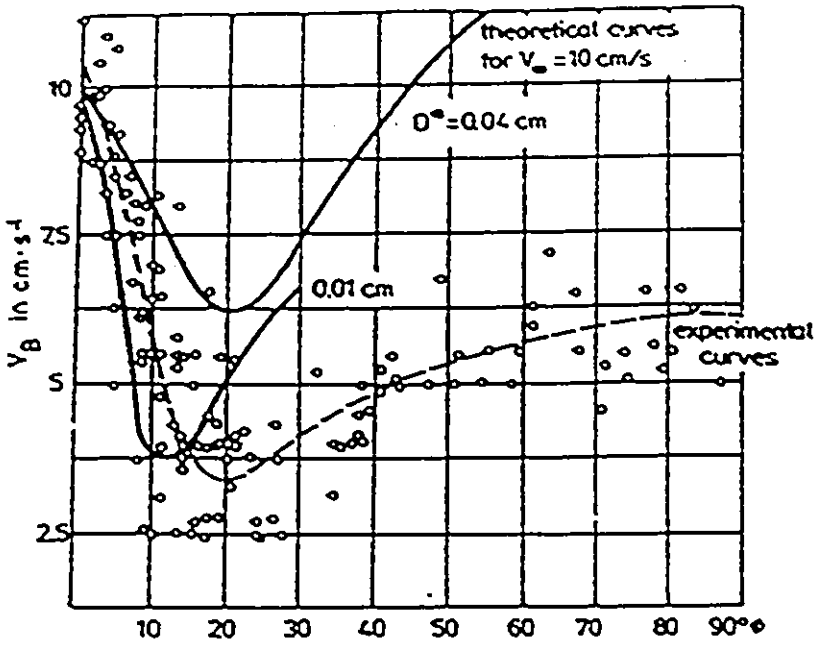

Figure 1.4: Theoretical and experimental particle velocities near the bubble surface as a function of the collision angle. From [21].

Setting $\frac{\partial r}{\partial \theta}|_\psi = 0$, the maximum interception angle, θ_{Cr}, is found to be given by,

$$\frac{\cos\theta_{Cr}}{1-3\cos^2\theta_{Cr}} = \frac{\mathrm{Re}}{8(1+\frac{3}{16}\mathrm{Re})} \tag{1.28}$$

Thus, the grazing streamline moves forward with increasing Re. Also given was a ratio of collision efficiency for intermediate Re (E_I), to the Reay and Ratcliff efficiency for the Stokes' regime (E_S).

$$\frac{E_I}{E_S} = 1 + \frac{\frac{3}{16}\mathrm{Re}}{1+0.249\mathrm{Re}^{0.56}} \qquad \text{for } (0 < \mathrm{Re} \leq 300) \tag{1.29}$$

Figure 1.5 compares theory with data for this relationship.

The sliding time phenomena discussed by Schulze and Gottschalk was quantitatively developed by Dobby and Finch. [23]

Using non-dimensional variables,

$$u^* = v_\theta/U_B \qquad r^* = 1 + a/R$$

$$u^* = 0.7\omega(r^*-1) \qquad \text{for } r < 1.06 \tag{1.30}$$

$$u^* = (0.06)0.7\omega \qquad \text{for } r > 1.06 \tag{1.31}$$

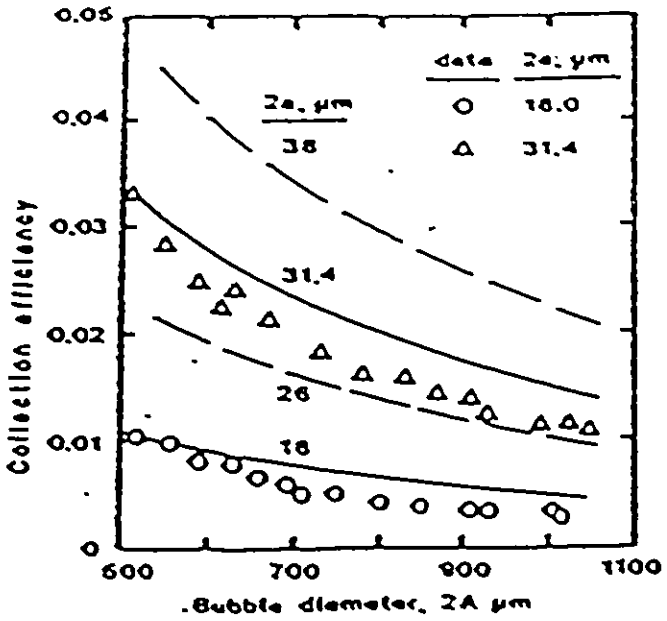

Figure 1.5: Weber's model for collision efficiency. From [22].

which were derived from Woo's numerical data for vorticity ω, on spheres for intermediate Re. [24] For $a/R > 0.03$, the particle velocity is calculated by dividing the particle into two zones, one that sees the velocity gradient given by 1.30, the other by 1.31. The particle tangential velocity $v_{p\theta}$, is given by

$$v_{p\theta} = v_\theta + v_r \sin\theta = 0.7\omega U_B[(\frac{a - 0.03R}{a})0.06 + (\frac{0.03a}{R})0.03] + v_T \sin\theta \qquad (1.32)$$

where v_T is the particle terminal settling velocity and U_B is the bubble rise velocity. The particle sliding time is,

$$t_c = \frac{\pi(a + R)(\theta_m - \theta)}{360\overline{v_{p\theta}}} \qquad (1.33)$$

where $\overline{v_{p\theta}}$ is the average $v_{p\theta}$ from equations 1.30 and 1.31 and θ_m is the angle signifying the end of the particle-bubble contact. This is determined by finding the angle at which the radial component of v_T is exactly opposite the radial component of the liquid velocity, v_r.

Near the surface of a sphere,

$$\Psi = \frac{1}{2} r^{*2} \omega \sin\theta \qquad (1.34)$$

Since ω is a known function of θ, $\frac{\partial \Psi}{\partial \theta}$ can be estimated for any r^* and θ. Thus v_r can be calculated and compared to $v_T \cos\theta$ to find θ_m. θ_m is primarily a function of ρ_p, varying from 67° to 81° as ρ_p goes from 1.3 to 7.0 g/cm^3.

Thus equation 1.33 was evaluated for t_c and compared to the data of Schulze and Gottschalk in figure 1.6. The fit seems fairly good and shows as well that a potential flow model is inadequate, since in reality, the flow is unsteady, viscous flow. Dobby and Finch concluded that since larger particles have higher velocities on the bubble surface, they have a shorter sliding time. Inertial effects and sliding time effects counteract each other and should give a specific ratio of a/R for maximum attachment.

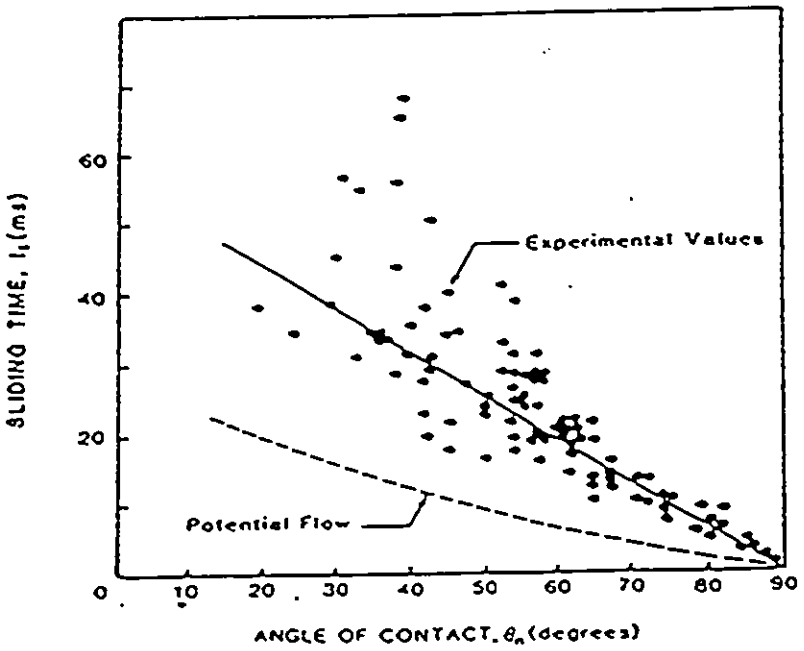

Figure 1.6: Particle sliding time measured by Schulze and Gottschalk and predictions from [23].

Theoretical hydrodynamic modeling of the actual liquid-film thinning process has only been attempted for very simple situations [25] and has yet to be specifically applied to flotation.

1.2.2 Numerical Solutions of Unsteady Flow Fields

The solution of the flow field involved in multibody interactions is often a difficult problem. Simple cases have been modeled, such as a sphere approaching a flat surface [20, 26], but the analytical methods are cumbersome and are restricted to simplified flow regimes; either Stokes or potential flow. However, in most cases, the flow in flotation applications contains significant contributions from both viscous and convective or inertial effects. This is often termed, full Navier-Stokes flow.

The behaviour of the fluid during the particle-bubble interaction influences the results of subsequent possible collisions. The liquid motion is governed by the Navier-Stokes equations, which are given below for incompressible fluids,

$$\frac{\partial u_i}{\partial t} + u_j u_{i,j} = g_i - \frac{1}{\rho} p_{,i} + \frac{\mu}{\rho} u_{i,jj} \tag{1.35}$$

Note that the notation used here is the Einsteinian indicial notation. For readers unfamiliar with this, please refer to appendix B.

Upon inspection, a domain solution of the external flow problem as presented seems quite intractable as the geometry is continuously varying. However, a numerical technique known as the Boundary Integral Equation (BIE) method, can be used [27]. Briefly, by BIE a domain equation is transformed to a boundary equation via Green's theorem and the resulting equations are then discretized and solved. The input required to implement the method is at least an order of magnitude less than for conventional domain methods such as Finite Elements or Finite Differences. The BIE method is also known as the Boundary Element Method (BEM).

Differential equations may be expressed in an integral form [28, 29]. The integral representations are exactly equivalent to the differential equations which describe the flow. Only assumptions and/or approximations from the original forms of the equations are carried over to the integral forms. Each integral equation contains a domain integral and a boundary integral. The mathematical foundation of the integral representation approach is the fundamental solution of differential equations. To demonstrate the solution procedure and several unique features of the approach, the problem of the numerical solution of Poisson's equation is considered below.

Consider Poisson's equation in the form,

$$\nabla^2\phi = g, \quad \text{in the region } R \tag{1.36}$$

where ϕ is the function to be determined in the region R and the inhomogeneous term g can be a function of the domain and its variables. The region R is singly- or multiply-connected, and is bounded by B, which consists of a single closed boundary or a closed outer boundary and any number of closed inner boundaries. An integral representation for the function ϕ is,

$$\phi(\vec{r}) = \int_R g_0 P dR_0 + \oint_B (\phi_0 \frac{\partial P}{\partial n_0} - P\frac{\partial \phi_0}{\partial n_0}) dB_0 \tag{1.37}$$

where $\vec{r}$ is the position vector, n is the outward normal direction, the subscript '0' indicates a variable, or operation in the $\vec{r}_0$ space. The function P is the fundamental solution defined by;

$$P(\vec{r},\vec{r}_0) = \begin{cases} \frac{-1}{4\pi r'} & \text{in three dimensions} \\ \frac{-1}{2\pi} \ln \frac{r}{r'} & \text{in two dimensions} \end{cases} \tag{1.38}$$

where r' is the magnitude of $\vec{r}'$ defined by,

$$\vec{r}' = \vec{r}_0 - \vec{r} \tag{1.39}$$

The fundamental solution P satisfies Laplace's equation $\nabla^2 P = 0$. The singularity of P at $\vec{r} = \vec{r}_0$ is such that

$$\int_R \nabla^2 P dR = \begin{cases} 1 & \text{if } R \text{ contains the point } \vec{r} = \vec{r}_0 \\ 0 & \text{if } R \text{ does not contain the point } \vec{r} = \vec{r}_0 \end{cases} \tag{1.40}$$

Consequently, the Laplacian of equation 1.37 gives equation 1.36.

Suppose that both ϕ and $\frac{\partial \phi}{\partial n}$ are known on the boundary B, then a quadrature, (numerical integration) of the right hand side of equation 1.37 determines the function ϕ everywhere in R. As is well known, however, the correct boundary condition for equation 1.36 is either Dirichelet's (a value for ϕ) or Neumann's (a value for $\frac{\partial \phi}{\partial n}$) or a linear combination of the two, over the entire boundary B. The use of equation

1.37 in place of equation 1.36 appears to require a knowledge of both ϕ and $\frac{\partial \varphi}{\partial n}$ on B and therefore presents a difficulty. The accepted procedure to remove this difficulty is to modify the fundamental solution in such a way that the modified solution, called Green's function, satisfies Laplace's equation and possesses a singularity at $\vec{r} = \vec{r}_0$, characterized by equation 1.40. The Green's function, in addition, is required to have the property that either its value or its normal gradient vanishes on the boundary B.

The fundamental solution P, as defined by equation 1.38, may be considered a special case of Green's function which vanishes at infinity. The fact that the fundamental solution is independent of any specific boundary geometry makes it well suited for numerical procedures. Regarding the proper prescription of boundary conditions, a closer examination of equation 1.37 reveals that it is possible to use this equation in establishing the missing information of the boundary B, using properly prescribed information. Consider the case where the value of ϕ is given on B. In order to obtain the normal derivative $\frac{\partial \phi}{\partial n}$ on B, equation 1.37 is applied at the boundary, yielding upon rearrangement, an integral equation with $\frac{\partial \phi}{\partial n}$ as the unknown function

$$\oint_B P_B \frac{\partial \phi_0}{\partial n0} dB_0 = F(\vec{r}_B) \tag{1.41}$$

where $\vec{r}_B$ is a point on the boundary B, and $P_B = P(\vec{r}_B, \vec{r}_0)$, and

$$F(\vec{r}_B) = \int_R g_0 P_B dR_0 + \oint_B \phi_0 \frac{\partial P_B}{\partial n_0} dB_0 - \phi(\vec{r}_B) \tag{1.42}$$

The integrands of equation 1.42 are known and $\phi(\vec{r}_B)$ is prescribed. Thus $F(\vec{r}_B)$ is determinate.

Quite often in flow problems, the prescribed condition on B is $\frac{\partial \phi}{\partial n}$. In order to establish the missing information, ϕ on the boundary B, equation 1.37 is applied on the boundary. The resulting integral equation contains ϕ_B as the unknown function. The solution of this integral equation gives ϕ_B and enables the computation of ϕ in R, away from B, using equation 1.37.

1.2.3 BIE Applications to Unsteady Viscous Flows

The previously stated Navier-Stokes equation 1.35 and the continuity equation for incompressible flow,

$$u_{i,i} = 0 \tag{1.43}$$

are sufficient for the determination of the flow field, when boundary conditions are provided for the time interval in question. It is convenient to write the Navier-Stokes equations as vorticity transport equations to obtain the required form (Poisson's equation) for BIE implementation.

The vorticity tensor at a point in the fluid is defined as the curl of the velocity, or,

$$w_i = \epsilon_{ijk} u_{k,j} \tag{1.44}$$

where ϵ_{ijk} is the permutation symbol or tensor cross-product operator.

From equation 1.35, the term $u_j u_{i,j}$ can be expressed as,

$$(\frac{u_k u_k}{2})_{,i} - \epsilon_{ijk} u_j w_k \tag{1.45}$$

The term $u_{i,jj}$ can be expressed as,

$$u_{j,ji} - \epsilon_{ijk} w_{k,j} \tag{1.46}$$

The first term can be written as $(u_{j,j})_{,i}$ where $u_{j,j} = 0$ is the continuity equation.

Thus equation 1.35 can be written as,

$$\rho \frac{\partial u_i}{\partial t} + p_{,i} + \frac{1}{2}\rho(u_k u_k)_{,i} + \rho g_i = \rho \epsilon_{ijk} u_j w_k - \mu \epsilon_{ijk} w_{k,j} \tag{1.47}$$

Operating on equation 1.47 with ϵ_{lmn} gives,

$$\frac{\partial w_i}{\partial t} = \epsilon_{ijk}(\epsilon_{klm} u_l w_m)_{,j} + \mu w_{i,jj} \tag{1.48}$$

Equation 1.48 is known as the vorticity transport equation.

Via Green's Theorem, and the method of fundamental solutions, equation 1.44 can be expressed in an integral form [30, 31] as,

$$\int_V e_i(\epsilon_{ijk} w_j G_k)\, dV = \int_S [(e_k G_k) u_i n_i - e_i(\epsilon_{ijk}(\epsilon_{jlm} u_l n_m) G_k)]\, dS \tag{1.49}$$

where G_i is the fundamental solution, e_i is a unit vector, and where V and S respectively imply volume and surface for applications in three dimensions and correspond to the region R and boundary B from previous developments in this section.

Note that 1.49 contains a singularity in G_i for the case where the source point ξ_i and the field point x_i coincide. Via a process outlined by Sokolnikoff and Redheffer [32], the solution to Poisson's equation is represented as $u_{,ii} = -\delta(\xi, x)$ where $\delta(\xi, x)$ is the Dirac delta function, or a localized singularity. Taking the limit as this region is shrunk to zero gives,

$$\beta u_i(\xi_i) = \int_V \epsilon_{ijk} w_j G_k \, dV - \int_S [u_k n_k G_i - \epsilon_{ijk}\epsilon_{jlm} u_l n_m G_k] \, dS \qquad (1.50)$$

$$\beta = \begin{cases} 1 & \text{if } \xi_i \text{ is in the flow field} \\ 0.5 & \text{if } \xi_i \text{ is on the boundary} \end{cases}$$

Equation 1.50 can be used to determine a velocity distribution at any given time. The situation is schematically illustrated by Figure 1.7.

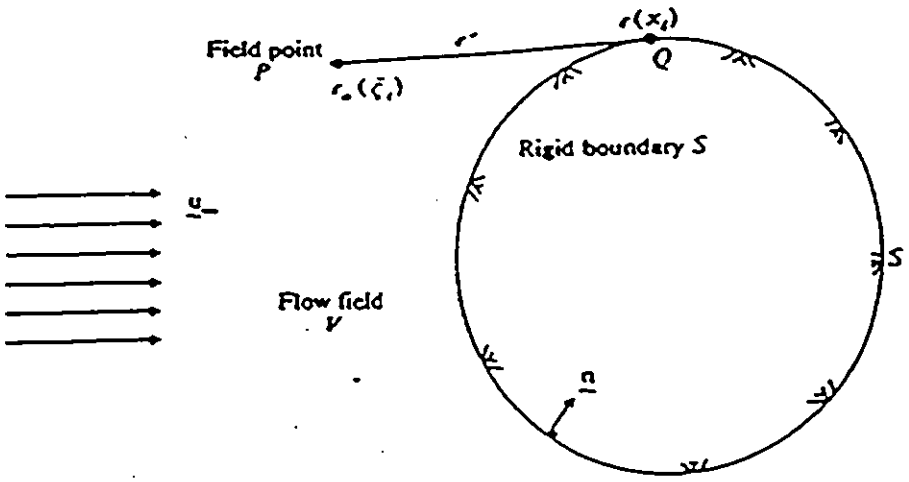

Figure 1.7: Representation of flow field for BEM method. From [27].

Note that the term,

$$\int_V \epsilon_{ijk} w_j G_k \, dV$$

must remain as a domain integral. Transforming it to a boundary integral requires a functional form of $\epsilon_{ijk}w_jG_k$. That is,

$$\int_V \epsilon_{ijk}w_jG_k\,dV = \int_V \epsilon_{ijk}B_{k,j}\,dV = \int_S \epsilon_{ijk}n_jB_k\,dS \tag{1.51}$$

where,

$$B_k = \int_S w_jG_k\,dx_j + \mathcal{F}(x_i)\;\; i \neq j \tag{1.52}$$

Thus, a boundary solution of w_j is required even for a numerical estimate of B_k.

By an analogous procedure the vorticity transport equation is put into an integral form for the vorticity vector [33].

$$w_i(r,t) = \int_V (w_iQ)_{t=0}\,dV + \frac{\mu}{\rho}\int_0^t dt\int_S (w_iQ_{,j} - Qw_{i,j})n_j\,dS + \int_0^t dt\int_V \epsilon_{ijk}\epsilon_{jml}w_lQ_{,k}\,dV \tag{1.53}$$

Q is the fundamental solution of the vorticity transport equation defined by,

$$Q = \frac{1}{4\pi\nu(t-t_0)^{\frac{d}{2}}}\exp\{\frac{(\xi_i - x_i)(\xi_i - x_i)}{4\nu(t-t_0)}\} \tag{1.54}$$

The magnitude of r, or r^2 is $(\xi_i - x_i)(\xi_i - x_i)$ and d is the dimensionality.

The above equations 1.43,1.44,1.53 are discretized and solved via a time-marching sequence. From a known velocity and vorticity distribution, equation 1.53 determines a new vorticity distribution and boundary vorticity values. The velocity distribution is updated by equation 1.44 and thus the time level may be advanced.

An alternative BIE procedure for full Navier-Stokes flow has been developed using velocity and pressure as the unknowns [34, 35]. The gradient of the Navier-Stokes equation 1.35 leads to an expression for the pressure,

$$p_{,ii} + u_{j,i}u_{i,j} = 0 \tag{1.55}$$

The time derivative in the Navier-Stokes equation is replaced by a backwards finite difference to give,

$$\mathrm{Re}(\frac{u_i^m - u_i^{m-1}}{\Delta t} + u_j^m u_{i,j}^m) = \tau_{ij,j}^m \tag{1.56}$$

where m is the time level and,

$$\tau_{ij,j}^m = -\mathrm{Re}\rho^m\delta_{ij} + u_{i,j}^m + u_{j,i}^m \tag{1.57}$$

Integral forms for the velocity and pressure are given along with accompanying fundamental solutions in [34].

Thus, by using an exact method to determine the flow field, input boundary conditions can be used to determine the bubble-particle hydrodynamic interaction in the elementary act of flotation. Flotation sized bubbles are satisfactorily treated as rigid spheres. [36]

1.3 Finite-Volume CFD Model

The finite volume method is a generalized form of the finite difference method, which is a numerical procedure designed to treat partial differential equations. The numerical scheme is designed to implement the conservation of mass, momentum and energy laws by imposing flux balances over a domain which has been partitioned into a number of cells via a grid scheme. The underlying principle is that for any quantity x, its transport through any cell will behave according to:

$$x_{\text{OUT}} = x_{\text{IN}} + x_{\text{GENERATED}} - x_{\text{CONSUMED}}$$

Figure 1.8 schematically illustrates a cell as it relates to finite difference implementation. Consider a partial derivative, $\frac{\partial u}{\partial x}$. For the cell shown in Figure 1.8, a

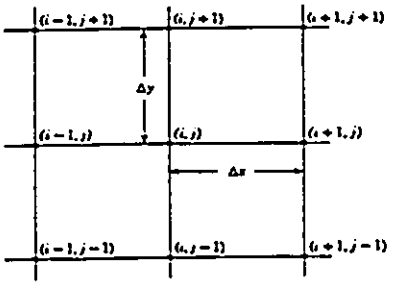

Figure 1.8: Arrangement of grid points for finite differences. From [37].

Taylor series expansion is used to relate $u_{i+1,j}$ to $u_{i,j}$. [37] The partial derivative is discretized by neglecting higher order terms. We begin with,

$$u_{i+1,j} = u_{i,j} + \Delta x \frac{\partial u}{\partial x} + \frac{(\Delta x)^2}{2!}\frac{\partial^2 u}{\partial x^2} + \frac{(\Delta x)^3}{3!}\frac{\partial^3 u}{\partial x^3} + \frac{(\Delta x)^4}{4!}\frac{\partial^4 u}{\partial x^4} \cdots$$

This gives,

$$\frac{\partial u}{\partial x} = \frac{u_{i+1,j} - u_{i,j}}{\Delta x} \tag{1.58}$$

Using the result from equation 1.58, we can also obtain,

$$\frac{\partial^2 u}{\partial x^2} = \frac{u_{i+1,j} - 2u_{i,j} + u_{i-1,j}}{(\Delta x)^2} \tag{1.59}$$

A coding of the fundamental equations of physics governing the hydrodynamics associated with a flotation unit was used to simulate such a process. For this work, a finite-volume approach was taken, building on existing theory and code from previous, TEACH-2E [38], TEMA [39] and TURCOM [40] models. This particular model is unique in that it describes the transport of several distinct dispersed phases, as well as accounting for a "conversion" of initially independent bubble and coal agglomerate phases into a bubble-solid "union" phase. The TURCOM code (designed for turbulent combustion), contains routines which are able to trace the transport of species as they chemically react in a flow situation. That is, some material is consumed while other species are created. The attachment of bubbles and coal-oil agglomerates to form "unions" was treated in an analogous manner as a chemical reaction, substituting flotation kinetics (and its accompanying functionality) for the original gas chemistry kinetic models. The modifications to this finite-volume code and its implementation shall be known as MD-PHASE, referring to its ability to treat multiple, dispersed phases.

1.4 Macro-Flotation Hydrodynamics

Successful mineral flotation depends on having suitable hydrodynamic conditions, or mixing to bring the bubbles and particles into contact with one another, as well as the necessary particulate surface properties to create a lasting adhesion between these particles and bubbles.

With a statistical approach to the collection of particles by bubbles, the micro-kinetics of a flotation system may be expressed. This must be done in view of the prevailing hydrodynamics of the system [41], which can be either laminar or turbulent.

Based on Abrahamson's model [42] for particle-particle collisions in a turbulent fluid, Bischofberger and Schubert [43] derived the following expression for the number of collisions per unit volume per unit time z_{PB}, in a turbulent flotation system.

$$z_{PB} = r_a n_P n_B d_{PB}^2 \left(v_P^2 + v_B^2\right)^{0.5} \tag{1.60}$$

Above, n_P and n_B are respectively the number concentration of particles and bubbles. The term d_{PB} is defined as,

$$d_{PB} = r_P + r_B$$

The terms v_P and v_B are given by,

$$v_i = 0.4 \left(\frac{\epsilon^{\frac{4}{9}} \cdot d_i^{\frac{7}{9}}}{\nu_L^{\frac{1}{3}}}\right) \left(\frac{\Delta\rho}{\rho_L}\right)^{\frac{2}{3}}$$

Above, $\Delta\rho = |\rho_i - \rho_L|$, and ν_L is the kinematic viscosity of the liquid phase.

The term r_a represents the adhesional probability part of the collision expression. It is divided into some additional factors, P_a and P_d, which will be discussed in section 1.5.

1.5 Macro-Flotation Model Parameters

Many parameters are known to exert an influence on the results of a flotation operation. These include the bubble and particle diameters, the surface properties of the materials involved, the relative concentrations and hold-up in the flotation unit, as well as the turbulence, feed fluxes and cell geometry imposed or selected for the system.

As previously outlined, this topic is of interest in that flotation has proven to be an effective recovery method for low-oil coal-oil agglomerates. From this perspective, the parameters of most relevance are the improved surface properties of the solid material to be floated. In addition it is known that the agglomerate diameter and oil-level are necessarily coupled. Typical kinetic studies of flotation often treat only a few parameters. In fact, many fundamental studies deal with the interaction between

one particle and one bubble, and then extrapolate these conclusions to some sort of recovery rate expression.

A number of such studies are cited below, where properties influencing the hydrodynamics in the collision process are examined. Works dealing with the effects of bubble diameter [44, 45] predict increased recovery with smaller bubbles, but the underlying models and mechanisms presented are case-dependent.

Papers by Jiang and Holtham [46] and Reay and Ratcliffe [17, 18] also examined the effect of the ratio of particle diameter to bubble diameter. The general form of the relationship was expressed as,

$$E_c \propto k \left(\frac{d_P}{d_B} \right)^n$$

where n had values ranging from 1.2 to 2.1. The above expression was for E_c, the probability of collection, but it is reasonable to expect this trend to apply to the net recovery of a flotation process when the attachment efficiency is high.

To facilitate this discussion, we can refer to work by Al Taweel et al. [47] where the overall probability of flotation P_f, is broken down into various subprocesses.

$$P_f \propto P_c P_a (1 - P_d) \tag{1.61}$$

Above, the subscripts c, a and d refer respectively to collision, attachment and detachment. The collision part was dealt with previously which leaves the terms P_a and P_d for consideration.

There are some hydrodynamic considerations for P_a. This mainly involves the sliding time of particles over bubbles and is discussed by several authors [21, 23, 48]. The sliding time must be greater than the induction time, which is a time required for the adhesion to take place. It is well known that the induction time decreases markedly with surface hydrophobicity. This is commonly expressed in terms of work of adhesion or work of wetting [49, 50, 51]. The same considerations are used to show a parallel result for detachment forces required to separate bubbles from pyrite particles for a series of apolar and polar liquids [52]. Inclusion of apolar liquid on the particle covering enhances detachment for pyrite and is related to the need for more complex

oils for the successful recovery of lower-rank coals [53]. Mechanical or moment forces at the particle-bubble interface are higher for larger particles, and facilitate their detachment [54]. Finally, flotation recovery has been correlated to the surface tension of the suspending liquid. Lowering the suspending liquid surface tension has the same general effect as increasing the particulate surface tension (ie, using a more hydrophilic solid), which results in decreased attachment or flotability [55, 56]. Other factors, such as viscous and elastic properties of the agglomerating oil have been shown to reduce the P_d term [57]. The influence of what is defined as a *Capillary* number, which is a ratio of viscous to surface forces, is that the dynamic bond strength in an agglomerate is improved with a more viscous binder. This corroborates work by Janczuk et al. which shows that as the chain length of n-alkanes is increased, there is a maximum in bond stability around $n = 7$, since the balance between wettability and viscous retention is optimal here [58].

In this project, there is no real means of decoupling P_a and P_d, but their functionality can be formulated, based on the above considerations, as,

$$P_a(1 - P_d) \propto \frac{f_1(\text{surface properties})}{f_2(\text{particle diameter})} \tag{1.62}$$

Flotation kinetic models are often applied to batch systems in a fashion analogous to chemical kinetics to model the rate of removal of the reactant (or in this case, flotable material) from the system. Such modelling is dependent on what kind of flow configuration is chosen, and can be constructed out of the parameters P_c, P_a and P_d along with data on the fluxes of the input streams. A good general review of the topic, as these criteria relate to flotation practice is given by Ek [59].

1.6 Pilot Testing of Coal-Oil Agglomerate Flotation

The combination of surface treatment of coal fines with oils and subsequent flotation is a technology which has been known since the turn of the century [7]. More recently, the ability of flotation to recover very low oil coal-oil agglomerates has been

demonstrated. This is important since oil consumption is a major process operating expense. Figure 1.9 illustrates recovery of coal-oil agglomerates via floc flotation for a high volatile *A* subbituminous Obed Mountain coal from Alberta (dry basis, 40% volatiles, 48% fixed carbon, 12% ash) , agglomerated with a No. 4 fuel oil [60]. The recovery results are substantially improved compared to 100 mesh screening of the agglomerates, and most notably at the low oil-levels.

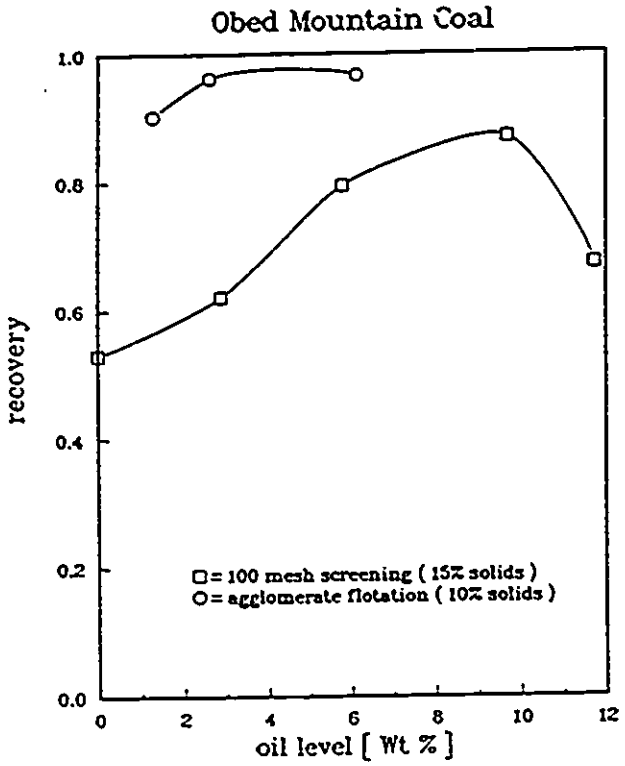

Figure 1.9: Recovery vs. oil-level for Obed coal.

Other papers by Wen and Sun [61], Hirajima et al. [5] and Wojick and Al Taweel [4] all show results indicating that oil conditioning of the surface of coals substantially improves their recovery by flotation. Further, the recovery rises dramatically upon small oil additions, and plateaus at a high value.

Beyond the research stage, reports are appearing of this technology coming into industrial practice. A 250 kg/hr pilot-plant has been successfully operated by the Alberta Research Council, with recoveries upwards of 90% and good desulfurization at oil-levels of 1% by weight [62]. Two larger plants in Pennsylvania, including one

operating at 40 tonnes/hr, using NRC technology were commercially operated [63]. Pilot work with column flotation of coal-oil agglomerates is also being conducted [64]. Related processes like the *Otisca* process have even recently received attention in the mainstream news magazine *Time* [65].

Hence, the general suggestion is that the addition of oil to coal fines will produce an agglomerated state. This synergistic coupled effect of simultaneous surface property enhancement and size enlargement makes flotation of coal-oil agglomerates a very attractive recovery method.

Chapter 2

Experimental and Computational Procedure

2.1 Coal Properties

The materials used in this study had to be properly characterized to permit correlation of their properties with the observed and calculated results.

2.1.1 Sample Preparation

Five different coals were used in this study. Some of the samples arrived in very large pieces. To approximate the state of particulates in waste fines treatment, the following procedure was used to prepare the samples. The coal chunks were reduced to millimeter size by successively passing it through a roll mill, then a Wiley Mill with a 1 mm screen. The samples were then wet ground (to avoid heat and oxidation) in an attrition mill for approximately 30 minutes. The particle size-distributions were then measured with a Malvern 2600 laser-diffraction instrument, and the volume-mean sizes are given in Table 2.1. Also, the "as received" properties of the coals are summarized in Table 2.1. Analysis of the coals' composition was done on a Leco Mac 400 instrument.

Sample	% volatile	% fixed carbon	% moisture*	% ash
Devco	40.57	57.34	3.23	2.09
Highvale	34.85	44.61	10.74	20.54
Montgomery	44.17	47.26	13.30	8.57
Bien Fait	46.69	38.59	30.57	14.72
Costello	51.08	39.79	36.32	9.13

% sulphur	volume-mean diameter [μm]	B.T.U./lb.	classification
0.101	33.0	10102	bituminous
0.332	9.4	8171	subbituminous
0.624	20.3	9731	subbituminous
0.584	6.0	9726	lignite
0.823	7.4	10299	lignite

Table 2.1: Analysis of coal samples. [as received, % by weight] (* dry basis, air dried at 110°C.)

Each coal was agglomerated at oil-levels of 0, 1, 5 and 10 weight% using hexadecane. (n-$C_{16}H_{34}$, ρ = 0.773 g/mL) Agglomerates were prepared at a 10% pulp density. The coal was mixed with distilled water and stirred under vacuum for about 90 minutes to remove any air from the system. After deairing, the required volume of hexadecane was introduced, and the coal-oil-water system was further stirred with a magnetic bar under vacuum in a baffled flask for at least 30 minutes, to achieve air-free agglomeration. Having only two-phase agglomerates (coal and oil) allows for a less complex material for the study of the surface properties. Normally, agglomerations carried out in high-shear mixing vessels (such as blenders), will introduce substantial amounts of air into the system from the vortices created by the stirring as well as by cavitation in the water from the mixing blades moving at extremely high speeds. At the present, very little research has addressed the topic of agglomerates

formed as a three-phase (coal-oil-air) material. A paper by Dryzmala et al. [66] discussed the presence of air in agglomerated systems.

2.2 Surface Tension Measurements

The adhesion technique developed by Absolom et al. [11, 67] was used to characterize the surface properties of the coal-oil agglomerates. This technique has been successfully employed to measure surface tensions of coal particles [11], as well as by Darcovich et al. [68] for coal-oil agglomerates. It was originally developed to measure surface properties of solid materials that occur only in particulate form, such as erythrocytes in blood, as shown by Absolom et al. [67]. The adhesion method involves measuring the extent of particulate adhesion on various substrates as a function of the composition (surface tension) of the suspending liquid.

2.2.1 Thermodynamic Considerations

The free energy of adhesion, ΔF^{adh}, is expressed as,

$$\Delta F^{adh} = \gamma_{PS} - \gamma_{PL} - \gamma_{SL} \tag{2.1}$$

where, γ_{PS}, γ_{PL} and γ_{SL} are respectively the particle-substrate, particle-liquid and substrate-liquid interfacial tensions. The terms "surface tension" and "interfacial tension" (mN/m) and "surface free energy" (mJ/m^2) can be used to represent the same quantity. The latter is of use to associate thermodynamic properties with interfacial systems.

Equation 2.1 is simply a free energy balance for the adhesion process. To determine a particulate surface free energy, Youngs'equation (equation 2.2) together with Neumann's surface tension equation of state [69] (equation 2.3) can be employed to treat the measured data.

$$\gamma_{SV} - \gamma_{SL} = \gamma_{LV} \cos\theta \tag{2.2}$$

$$\gamma_{SL} = \frac{(\sqrt{\gamma_{SV}} - \sqrt{\gamma_{LV}})^2}{1 - 0.015\sqrt{\gamma_{SV}\gamma_{LV}}} \tag{2.3}$$

Of course, both of these equations apply to any solid surface, so that the subscript 'S' referring to a solid surface, in equations 2.2 and 2.3 can be replaced by the subscript 'P' from equation 2.1 (when referring to a particle) or by the subscript 'S' from equation 2.1 (when referring to the substrate). If equation 2.3 is substituted into equation 2.2 and $\cos\theta$ and γ_{LV} are known, an implicit expression for γ_{SV} may be obtained,

$$\gamma_{SV} - \frac{(\sqrt{\gamma_{SV}} - \sqrt{\gamma_{LV}})^2}{1 - 0.015\sqrt{\gamma_{SV}\gamma_{LV}}} = \gamma_{LV}\cos\theta \tag{2.4}$$

Thus obtained, the value of γ_{SV} can be used together with γ_{LV} in equation 2.3 to determine γ_{SL}.

For a range of γ_{SV} and γ_{LV} values, and using equations 2.2 and 2.3, the functional behaviour of ΔF^{adh} can be demonstrated. Assuming a given value of γ_{PV}, then with equations 2.2 and 2.3 (substituting the subscript 'P' for 'S'), values of γ_{PL} can be determined. For a set of subtrates of known γ_{SV}, the γ_{SL} values can be determined. Finally, the γ_{PL} and γ_{SL} values can be put into equation 2.3 to give a value for γ_{PS}. That is, equation 2.3 would take the form of,

$$\gamma_{PS} = \frac{(\sqrt{\gamma_{PL}} - \sqrt{\gamma_{SL}})^2}{1 - 0.015\sqrt{\gamma_{PL}\gamma_{SL}}}$$

where the liquid phase L, assumes the role of the vapour phase V for immersion in a liquid. Thus ΔF^{adh} can be summed from its three constituents. Figure 2.1 shows ΔF^{adh} plotted against γ_{SV} for cases of $\gamma_{PV} > \gamma_{LV}$, $\gamma_{PV} = \gamma_{LV}$, and $\gamma_{PV} < \gamma_{LV}$. For this example, $\gamma_{LV_{HIGH}} = 72.8$ mJ/m^2, $\gamma_{LV_{LOW}} = 59.8$ mJ/m^2 and $\gamma_{PV} = 64.6$ mJ/m^2.

If the surface tension of the suspending liquid is greater than the particle surface tension ($\gamma_{LV} > \gamma_{PV}$), Figure 2.1 shows that the extent of adhesion (ΔF^{adh} larger) should decrease with increasing substrate surface tension (γ_{SV}). The opposite trend is expected when $\gamma_{LV} < \gamma_{PV}$. When $\gamma_{LV} \simeq \gamma_{PV}$, neither the particle nor the liquid will be energetically favoured to form an interface with the substrate and the extent of adhesion should be independent of γ_{SV}. For the treatment of the experimental

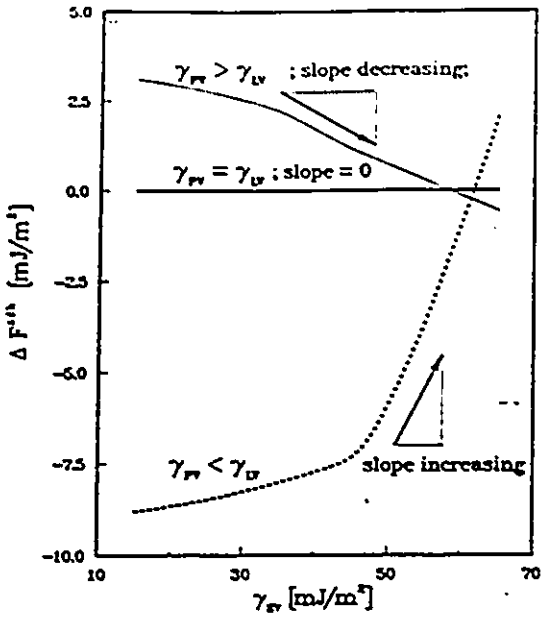

Figure 2.1: ΔF^{adh} versus γ_{SV} for the cases of γ_{LV} being greater than, equal to and less than γ_{PV}.

data, this procedure is more concretely explained in section 2.2.2. As noted already, the experimental adhesion method, involves measuring the extent of particulate adhesion on various substrates as a function of the composition (surface tension) of the suspending liquid. The underlying assumption of the experimental method is that for very small particles, ΔF^{adh} is proportional to the percent area adhesion measured on the substrate surface. Further, it has been demonstrated by Smith et al. [70] that the adhesion technique can be employed to determine γ_{PV} independently of any form of the surface tension equation of state used. The implication of this result is that the graphical procedure outlined above for determining γ_{PV} becomes mathematically identical to the method involving the equation of state calculations.

2.2.2 Experimental Procedure

Virgin teflon blocks one half inch thick with 1 cm diameter holes were used to contain the particulate slurry. The low surface energy of this material minimized interaction of the particulates and suspending liquid with the cell walls. The polymer

film substrates were cut to the size of the teflon blocks, cleaned and affixed to the blocks with an inert medical grade silastic (*Dow Corning MDX4-4210*) leaving the substrate surface exposed to the opening in the teflon block.

Four different polymer film substrates were used to span the possible surface tensions of the coal-oil system. These polymers are detailed in table 2.2. θ_c is the contact angle formed with water in air. These values were measured with an optical goniometer. They closely match values reported by Absolom et al. [11], calculated by Neumann's surface tension equation of state. Solid surfaces tensions in table 2.2 are for the solid-air interface.

Substrate Material	θ_c with water	γ_{SV} [mJ/m^2]
Polystyrene	93.7°	26.5
Dow Chemical (T-1000)		
Sulfonated Polystyrene	25.6°	66.1
Dow Chemical (T-1101)		
Polyethylene	83.0°	33.2
Fischer		
Polyethyleneterephthalate	69.1°	41.8
Hoechst (Hostaphane 2000)		

Table 2.2: Polymer film substrate properties

After the attritor grinding, the moisture in the coal-water mixture was determined by an extraction with toluene. The coal-water mixtures were kept well sealed to prevent evaporation of water.

Particulate slurries were prepared in each of five water-methanol compositions. These coal slurries contained a solids weight fraction of 0.01. Equal aliquots were put in each cell which was then sealed on top with a silastic bonded plastic film to prevent evaporation of the liquid. Two cells were prepared for each case. The water-methanol suspending liquid compositions are summarized in table 2.3. The water-methanol system was selected, since as shown by Stephen and Stephen [71],

hexadecane is essentially immiscible with this system across the entire binary composition range. Thus the agglomerate structure was not interfered with. These data for water-methanol solution surface tensions against air at 20°C were given in [72].

The particles were allowed to settle and adhere to the substrates for three days. It has been shown by Absolom et al. [11], that by this time, the extent of adhesion stabilizes to a plateau value.

Volume % CH_3OH	γ_{LV} [mJ/m^2]
0.0	72.5
9.0	59.8
24.0	47.0
51.0	35.0
95.0	24.2

Table 2.3: Suspending liquid composition and surface tension

The polymer substrate films were carefully peeled from the blocks and gently rinsed to remove settled but non-adhering particles. The samples were dried before viewing. The films were then mounted and centered on a microscope stage (Olympus SZH) and a video image of each sample was taken.

The image of adhering particles from each cell was input to an image analysis program (*Kontron* Image Analyzer) where a grey-level cut-off was determined to discriminate adhering particles from the background. Pixel regions designated as particles were integrated to give a percent area adhesion.

For each sample, a linear fit was determined for the percent area adhesion as a function of substrate surface tension for each different suspending liquid composition. Figure 4.1 shows such a plot, these data being from the Devco coal at 0.25 weight% n-$C_{16}H_{34}$. The slopes of these regressions were then plotted as a function of the suspending liquid surface tension, with an interpolated curve put to the data. (ie; figure 4.2, for Devco coal at 0 to 10 weight% oil) The point where this curve crossed the x-axis was considered to be the particulate surface tension. A more detailed

description of this procedure is given by Darcovich et al. [73].

2.2.3 Three-Phase Contact Angle Measurements

An estimate of the three-phase contact angle of oil on coal in an aqueous medium was required for the analysis of the agglomerate structures. Since the coal used in this work was available only as fines, the contact angle of n-$C_{16}H_{34}$ on coal in water was estimated by measuring the contact angle of n-$C_{16}H_{34}$ in distilled water on a series of polymer substrates and interpolated at the measured surface free energies of the agglomerates. Even if large smooth pieces of each coal sample were available for contact angle measurements, the dry grinding procedures altered the surface character. Further a range of substrate surface tensions were needed to study the wetting behaviour in agglomerates across a range of oil levels. The three-phase contact angle data across a range of of substrate surface tensions were assumed to simulate the three-phase contact angles forming the interparticle bonds in the coal-oil agglomerates made at each different oil level. The same polymers used for the adhesion experiments (Table 2.2) were used in these experiments.

These measurements were done with an optical goniometer. In a special viewing cell, the polymer surfaces were immersed in distilled water, then a drop of hexadecane was introduced to contact their underside.

2.3 Agglomerate particle-size distribution

The mean particle-sizes for the agglomerates were obtained using a Malvern model 2600 laser diffraction particle-size analyser. Several measurements were made at each oil level. Laser diffraction was used for these measurements since it is an accurate and much less time consuming method than image analysis. With mean particle diameters greater than of 5.0 μm, the resolution and reproducibility of result was more than adequate with the Malvern instrument.

Additionally, the particle-size distributions of agglomerates were determined suspended in a mixture of 95% CH_3OH and 5% H_2O, at several oil levels to see if the

methanol in the suspending liquid influenced the particle-size distributions. It was necessary to re-zero the light scattering signal for this methanol-water mixture. (figure 4.5)

2.4 Laboratory Flotation Tests

Agglomerations were run on each of the coals at 1, 5 and 10 weight% oil using hexadecane. Each batch was made with 50 g of coal mixed with 500 mL of distilled water in a Waring Blendor with the appropriate amount of oil added. The coal was thus agglomerated at 10% pulp density, undergoing high shear mixing for 30 seconds and low shear for 1 minute. For the flotation tests, a Denver laboratory flotation cell was used. The 10% pulp density sample was floated in 1500 mL of water. The skimmed product was washed in 500 mL of water for 2 minutes, and then re-floated in the same cell. This product along with the tailings from the first and second floating were dried in an oven at $300°C$ overnight. The masses of the products and the tailings were recorded and then these samples were analyzed for ash content. The same procedure as above was also carried out with No. 4 fuel oil.

2.5 BEM formulation

This section details the development of the explicit forms of the fundamental solutions for the two-dimensional incompressible unsteady time-difference primitive-variable Navier-Stokes boundary element formulation. That is, a primitive-variable formulation has velocity and pressure as the unknown field variables. Time-differencing is an approach where the time derivative in the Navier-Stokes equation is treated as a discrete step rather than a continuous function. Also, explicit forms of singular integrals are derived and presented. In this regard, series expansions of the fundamental solutions, which contain modified Bessel functions, are performed to enable integration of the singular cases. Practical comments are offered in order to allow this method to be more readily used.

2.5.1 Introduction

Using Hörmander's weight-function procedure for fundamental solutions[74], Tosaka developed a primitive-variable (pressure and velocity are the unknowns) global matrix form for incompressible unsteady Navier-Stokes flow [75]. In the course of current work on the simulation of a particle-bubble interaction in the context of mineral flotation [76, 77], the formulations of Tosaka have been adopted for the two-dimensional case. Further, the discrete time-step version was necessary, as the problem at hand involves a two-body interaction producing geometrical changes at each time-level.

The objective is to now present concrete forms of the fundamental solution tensor for the incompressible two-dimensional Navier-Stokes primitive-variable discrete time-step Boundary Element formulation. That is, to make available in the literature, directly usable formulae, as well as to detail the development of solutions for singular-case integrals as they apply to this problem. The presentation of these results should facilitate adoption of this method for use by members of the technical community. Partial results were obtained, but as a practical application for micro-flotation modeling, BEM was an uncertain means to meet the objectives of this project within a reasonable time frame.

2.5.2 Formulation

2.5.2.1 Fundamental Equations

Given below are the non-dimensional equations which define a one-phase continuum flow field under general conditions. Here, Re is the Reynolds number, u_i is the velocity vector, p is the pressure, t is the time and τ_{ij} is the stress tensor.

Equations of momentum:

$$\mathrm{Re}\left(\frac{u_i - u_i(t-\Delta t)}{\Delta t} + u_j u_{i,j}\right) = \tau_{ij,j} + f_i \qquad \text{in } \Omega \tag{2.5}$$

Incompressibility condition:

$$u_{i,i} = 0 \qquad \text{in } \Omega \tag{2.6}$$

Constitutive equations:

$$\tau_{ij} = -\mathrm{Re}p\delta_{ij} + u_{i,j} + u_{j,i} \qquad \text{in } \Omega \tag{2.7}$$

Boundary Conditions:

$$\begin{aligned} u_i &= \hat{u}_i && \text{on } \Gamma_u \\ \tau_i \equiv \tau_{ij}n_j &= \hat{\tau}_i && \text{on } \Gamma_\tau \\ u_i(t=0) &= u_i^0 && \text{in } \Omega \end{aligned} \tag{2.8}$$

In equation 2.8, the vector n_j is the unit normal in the j-direction at the given boundary location.

2.5.2.2 Integral Equation

Let us define, $\lambda \equiv \frac{\mathrm{Re}}{\Delta t}$. Further,$D_i \equiv \partial/\partial x_i$ and Δ is the Laplacian operator equal to D_iD_i (not to be confused with the time step, Δt).

Composing the Navier-Stokes equations from equations 2.5, 2.6 and 2.7, they can be summarized in matrix form. Hence,

$$[\hat{L}_{\alpha\beta}]\{U_\beta\} = \{B_\alpha\} - \lambda\{\tilde{U}_\alpha(t-\Delta t)\} \tag{2.9}$$

where the subscripts $\alpha, \beta = 1,2,3$ and the unknown $U_3 \equiv p$. In particular the elements $\hat{L}_{\alpha\beta}$ can be expressed as:

$$\begin{aligned} \hat{L}_{ij} &= -\frac{\mathrm{Re}}{\Delta t}\delta_{ij} + \Delta\delta_{ij} + D_iD_j \qquad i,j = 1,2 \\ \hat{L}_{i3} &= -\mathrm{Re}D_i \\ \hat{L}_{3j} &= D_j \\ \hat{L}_{33} &= 0 \end{aligned}$$

Thus the matrix $[\hat{L}_{\alpha\beta}]$ may be assembled. In a complete form, the components of equation 2.9 can be written for the two-dimensional case.

$$[\hat{L}_{\alpha\beta}] = \begin{bmatrix} -\frac{\mathrm{Re}}{\Delta t} + \Delta + D_1^2 & D_1 D_2 & -\mathrm{Re} D_1 \\ D_2 D_1 & -\frac{\mathrm{Re}}{\Delta t} + \Delta + D_2^2 & -\mathrm{Re} D_2 \\ D_1 & D_2 & 0 \end{bmatrix}$$

$$\{U_\beta\} = [\ u_1\ u_2\ p\ ]^T$$

$$\{B_\alpha\} = \begin{Bmatrix} \mathrm{Re} u_j u_{1,j} - f_1 \\ \mathrm{Re} u_j u_{2,j} - f_2 \\ 0 \end{Bmatrix}$$

$$\{\tilde{U}_\alpha(t-\Delta t)\} = [\ u_1(t-\Delta t)\ u_2(t-\Delta t)\ 0\ ]^T$$

Now we can rearrange equation 2.9 to the form,

$$[\hat{L}_{\alpha\beta}]\{U_\beta\} - \{B_\alpha\} + \lambda\{\tilde{U}_\alpha(t-\Delta t)\} = 0$$

Let us now introduce a weighting function, $W_{\alpha\gamma}$. Similarly, the subscript $\gamma = 1, 2, 3$. We can write,

$$\int_\Omega (\hat{L}_{\alpha\beta} U_\beta - B_\alpha + \lambda \tilde{U}_\alpha(t-\Delta t)) W_{\alpha\gamma}\, d\Omega = 0 \qquad (2.10)$$

After some manipulation, a boundary integral equation was derived [75]. The coordinate y_i refers to the source point, and x_i denotes the field points. This equation is:

$$c(y)U_\gamma(y) = \int_\Gamma u_i(x)\Sigma_{i\gamma}(x,y)\, d\Gamma(x) - \int_\Gamma \tau_i(x) W_{i\gamma}(x,y)\, d\Gamma(x)$$
$$+ \int_\Omega B_\alpha(x) W_{\alpha\gamma}(x,y)\, d\Omega(x) - \int_\Omega \lambda \tilde{U}_\alpha(t-\Delta t)(x) W_{\alpha\gamma}(x,y)\, d\Omega(x) \qquad (2.11)$$

Here, the tensor $\Sigma_{i\gamma} = (-W_{3\gamma}\delta_{ij} + W_{i\gamma,j} + W_{j\gamma,i})n_j$. From the method of weighted

residuals, the fundamental solution tensor was given as:

$$\begin{aligned} W_{ij} &= (\Delta\delta_{ij} - D_i D_j)\phi \\ W_{i3} &= \frac{1}{\mathrm{Re}} D_i(-\lambda + \Delta)\phi \\ W_{3j} &= -D_j(-\lambda + \Delta)\phi \\ W_{33} &= \frac{1}{\mathrm{Re}}(-\lambda + 2\Delta)(-\lambda + \Delta)\phi \end{aligned} \tag{2.12}$$

Here ϕ is a scalar function. From the differential operator derived for the global matrix system [34], this Green's Function is:

$$\phi = \frac{-1}{2\pi\lambda}\left(\ln r + K_0(\sqrt{\lambda}r)\right) \tag{2.13}$$

where K_0 is the modified Bessel function of the third kind of order zero. In equation 2.13, the variable r represents the distance between a source point and a field point.

2.5.3 Explicit forms of the fundamental solution tensor

To numerically implement equation 2.10, several of the fundamental tensors must be used. Using the values of 1 and 2 for the subscript l is sufficient to produce a velocity field solution. To achieve this, the tensors $W_{i\gamma}$ and $\Sigma_{i\gamma}$ are required. Recall that $\Sigma_{i\gamma} = (-W_{3\gamma}\delta_{ij} + W_{i\gamma,j} + W_{j\gamma,i})n_j$. Hence, with $\gamma = j$, the tensors W_{3j} and $W_{ik,j}$ $(k = 1, 2)$ are also needed.

2.5.3.1 Explicit form of the Fundamental Solution Tensor, W_{ij}

Recall that,

$$W_{ij} = \delta_{ij}\Delta\phi - \phi_{,ij} \qquad \text{and,} \quad \Delta\phi = \phi_{,kk}$$

thus,

$$W_{ij} = \delta_{ij}\phi_{,kk} - \phi_{,ij}$$

Recall also,

$$\phi = \frac{-1}{2\pi}[\ln r + K_0(\sqrt{\lambda}r)]$$

By definition, $r^2 = (y_i - x_i)(y_i - x_i)$. Let $s_i = (y_i - x_i)$, so $r^2 = s_i s_i$. It will be convenient to have an explicit expression for the derivative of r, and it can be easily shown that $dr/dx_i = -s_i/r$.

Beginning with equation 2.13, we can write an expression for $\phi_{,ij}$.

$$\phi_{,ij} = \frac{-1}{2\pi\lambda}[(\ln r)_{,i} + K_0(\sqrt{\lambda}r)_{,i}]_{,j}$$

It will be convenient to combine $\sqrt{\lambda}r$ into one variable, z. From the discussion given in Lebedev [78], the derivatives of the Bessel functions conform to the following recurrence relations:

$$\frac{d}{dz}[z^\nu K_\nu(z)] = -z^\nu K_{\nu-1}(z) \quad \text{and,} \quad \frac{d}{dz}[z^{-\nu} K_\nu(z)] = -z^{-\nu} K_{\nu+1}(z) \tag{2.14}$$

Thus for example,

$$\frac{d(K_0(\sqrt{\lambda}r))}{dx_i} = \frac{d(z^{-0}K_0(z))}{dx_i} = \frac{d(z^{-0}K_0(z))}{dz}\frac{dz}{dr}\frac{dr}{dx_i}$$

Now,

$$\frac{d(K_0(\sqrt{\lambda}r))}{dx_i} = -z^{-0}K_1(z)(\sqrt{\lambda})(-s_i/r) = \lambda z^{-1}K_1(z)s_i$$

Returning to $\phi_{,ij}$, we have,

$$\begin{aligned}
\phi_{,ij} &= \frac{-1}{2\pi\lambda}\left(\frac{-s_i}{r^2} + \lambda z^{-1}K_1(z)s_i\right)_{,j} \\
&= \frac{-1}{2\pi\lambda}\left(\frac{\delta_{ij}}{r^2} + (-s_i)\frac{-2}{r^3}\frac{(-s_j)}{r} + \lambda s_i z^{-1}K_2(z)\sqrt{\lambda}\frac{s_j}{r} + \lambda z^{-1}K_1(z)(-\delta_{ij})\right) \\
&= \frac{-1}{2\pi\lambda}\left(\frac{\delta_{ij}}{r^2} - \frac{2}{r^4}s_i s_j + \lambda^2 z^{-2}K_2(z)s_i s_j - \lambda z^{-1}K_1(z)\delta_{ij}\right)
\end{aligned}$$

Arranging terms gives,

$$\phi_{,ij} = \frac{-1}{2\pi\lambda}\left(\delta_{ij}\left(\frac{1}{r^2} - \frac{\sqrt{\lambda}}{r}K_1(\sqrt{\lambda}r)\right) + s_i s_j\left(\frac{\lambda}{r^2}K_2(\sqrt{\lambda}r) - \frac{2}{r^4}\right)\right) \tag{2.15}$$

Now, recall $W_{ij} = \delta_{ij}\phi_{,kk} - \phi_{,ij}$. Thus,

$$\begin{aligned}
W_{ij} &= \frac{-1}{2\pi\lambda}\left[\delta_{ij}\left(\frac{2}{r^2} - 2\frac{\sqrt{\lambda}}{r}K_1(\sqrt{\lambda}r) + \lambda K_2(\sqrt{\lambda}r) - \frac{2}{r^2}\right) - \delta_{ij}\left(\frac{1}{r^2} - \frac{\sqrt{\lambda}}{r}K_1(\sqrt{\lambda}r)\right)\right. \\
&\quad \left. - s_i s_j\left(\frac{\lambda}{r^2}K_2(\sqrt{\lambda}r) - \frac{2}{r^4}\right)\right]
\end{aligned}$$

Simplifying gives,

$$W_{ij} = \frac{-1}{2\pi\lambda}[\delta_{ij}(\lambda K_2(\sqrt{\lambda}r) - \frac{\sqrt{\lambda}}{r}K_1(\sqrt{\lambda}r) - \frac{1}{r^2}) - s_i s_j(\frac{\lambda}{r^2}K_2(\sqrt{\lambda}r) - \frac{2}{r^4})] \quad (2.16)$$

2.5.3.2 Calculation of $W_{ik,j}$

We can begin by writing $W_{ik,j}$ in a general form.

$$\begin{aligned} W_{ik,j} &= \frac{-1}{2\pi\lambda}[\delta_{ik}(\lambda K_2(z) - \lambda z^{-1}K_1(z) - \frac{1}{r^2})_{,j} - (s_i s_k)_{,j}(\lambda^2 z^{-2}K_2(z) - \frac{2}{r^4}) \\ &\quad -s_i s_k(\lambda^2 z^{-2}K_2(z) - \frac{2}{r^4})_{,j}] \\ &= \frac{-1}{2\pi\lambda}[\delta_{ik}((\lambda K_2(z))_{,j} - \lambda^2 z^{-2}K_2(z)s_j - \frac{2s_j}{r^4}) + (\delta_{ij}s_k + \delta_{kj}s_i)(\lambda^2 z^{-2}K_2(z) - \frac{2}{r^4}) \\ &\quad -s_i s_k(\lambda^3 z^{-3}K_3(z)s_j - \frac{8s_j}{r^6})] \\ &= \frac{-1}{2\pi\lambda}[\delta_{ik}(z^2(\lambda z^{-2}K_2(z))_{,j} + z^2_{,j}(\lambda z^{-2}K_2(z)) - \lambda^2 z^{-2}K_2(z)s_j - \frac{2s_j}{r^4}) \\ &\quad +(\delta_{ij}s_k + \delta_{kj}s_i)(\lambda^2 z^{-2}K_2(z) - \frac{2}{r^4}) - s_i s_k(\lambda^3 z^{-3}K_3(z)s_j - \frac{8s_j}{r^6})] \end{aligned}$$

Collecting like terms and rearranging gives,

$$\begin{aligned} W_{ik,j} &= \frac{-1}{2\pi\lambda}[\delta_{ik}(\lambda^2 z^{-1}K_3(z)s_j - 3\lambda^2 z^{-2}K_2(z)s_j - \frac{2s_j}{r^4}) \\ &\quad +(\delta_{ij}s_k + \delta_{kj}s_i)(\lambda^2 z^{-2}K_2(z) - \frac{2}{r^4}) - s_i s_k(\lambda^3 z^{-3}K_3(z)s_j - \frac{8s_j}{r^6})] \end{aligned} \quad (2.17)$$

2.5.3.3 Calculation of W_{3j}

In equation 2.12, W_{3j} was given in general form.

$$W_{3j} = -D_j(-\lambda + \Delta)\phi$$

As given in Appendix A, the scalar $(-\lambda + \Delta)\phi$ can be expressed as,

$$(-\lambda + \Delta)\phi = \frac{1}{2\pi}\ln r$$

Hence,

$$\begin{aligned} W_{3j} &= -D_j\left(\frac{1}{2\pi}\ln r\right) \\ &= \frac{1}{2\pi}\left(\frac{s_j}{r^2}\right) \end{aligned} \tag{2.18}$$

2.6 Finite Volume formulation

The Finite Volume Method (FVM) used in this work is detailed below. The FVM makes use of the governing partial differential equations (the Navier-Stokes equations) considered over a flow domain. These equations dictate fluid flow through momentum transfer, mass and energy balances and thermodynamic relations describing physical properties of the fluids involved. The $k-\epsilon$ model is employed to incorporate turbulent behaviour into the domain. For this particular hydrodynamics problem, the variables considered are velocity (composed of directional components), pressure, the turbulent parameters, the volume fractions of bubbles and solids, the non-Newtonian local viscosities arising from the multi-phase system, the extent of mass transfer between the dispersed phases, as well as the local velocities of the dispersed phases. The solution of the discretized differential equations is done via a hybrid of central and upwind differencing over the solution domain. The type of differencing depends on the local Peclet number to ensure numerical stability which enhances accurate computation over an extended range of Reynolds and Peclet numbers. Each finite volume equation is solved sequentially, in an iterative manner.

The computer code which implements this FVM formulation is quite modular in structure, allowing simple specifications to dictate steady or unsteady, laminar or turbulent, compressible or incompressible, reacting or stable states as well as heat and mass transfer conditions. Grids defining the flow domain may be prescribed in either Cartesian or cylindrical coordinates.

2.6.1 Mathematical Model

The FVM formulation used in this work employs the basic mass and momentum transport equations with the turbulence features worked into it expressed as statistical averages of the random fluctuations. The turbulence in the flows is accounted for by the statistical means of the turbulent variables, k and ϵ from the two-equation model developed by Launder and Spalding [79]. The problem is fully defined with the specification of boundary conditions, and in the case of unsteady flow, an initial condition is also required. Given below, is a formulation for a general one-phase flow system in the turbulent regime.

2.6.1.1 Transport Equations

The instantaneous properties of a flow are given by the mass and momentum conservation equations [80].

$$\text{Mass:} \quad \frac{\partial \rho}{\partial t} + (\rho u)_{j,j} = 0 \tag{2.19}$$

$$\text{Momentum:} \quad \frac{\partial (\rho u)_i}{\partial t} + ((\rho u)_j u_i)_{,j} = -P_{,i} + \tau_{ij,j} \tag{2.20}$$

Above, τ_{ij} is the shear stress tensor given by:

$$\tau_{ij} = \mu(u_{i,j} + u_{j,i}) - \frac{2}{3}\mu u_{k,k}\delta_{ij} \tag{2.21}$$

Here, μ is the laminar viscosity of the fluid.

2.6.1.2 Averaging Method for Turbulence

In a turbulent flow, any local variable will have a mean time-averaged value, but will also fluctuate to an extent prescribed by the level of turbulence. We can consider an arbitrary variable, a. Instantaneously, a can be decomposed into an averaged component $< a >$, and its fluctuating component, a', as,

$$a =< a > +a' \tag{2.22}$$

The density-weighted ensemble-average (DWEA) approach to making use of equation 2.22 [81, 82] defines the average of our variable a as,

$$\bar{a} = \frac{< \rho a >}{< \rho >} = \frac{1}{\rho} \lim_{m \to \infty} \frac{1}{2m+1} \sum_{n=-m}^{m} \rho(\mathbf{x}, t + nT_0) a(\mathbf{x}, t + nT_0) \qquad (2.23)$$

Here, T_0 is the period of oscillation and x is the point in space being considered. This average procedure redefines a as,

$$a = \bar{a} + a'' \qquad (2.24)$$

where a'' is the fluctuating component calculated by the DWEA procedure.

The relation between the weighted and unweighted averages is,

$$\bar{a} = < a > + < \rho' a' > \qquad (2.25)$$

Above, $< \rho' a' >$ is known as the "correlation" of the fluctuations in a and ρ.

2.6.1.3 Averaged Transport Equations

The transport equations presented as equations 2.19 and 2.20 are rewritten with the all variables (except density and pressure) expressed as DWEA averages and fluctuating terms. The equations now become,

$$\text{Mass:} \qquad \frac{\partial < \rho >}{\partial t} + (< \rho > \bar{u}_j)_{,j} = 0 \qquad (2.26)$$

$$\text{Momentum:} \qquad \frac{\partial (< \rho > u)_i}{\partial t} + (< \rho > \bar{u}_j \bar{u}_i + < \rho > < \overline{u''_j u''_i} >)_{,j} = - < P >_{,i} + \bar{\tau}_{ij,j} \qquad (2.27)$$

2.6.1.4 Treatment of Turbulent Terms

Terms such as $< \rho > < \overline{u''_j u''_i} >$ from equation 2.27, which have a non-zero time-average, are successfully integrated into a turbulent model by expressing them as functions of the *mean* flow variables, and parameters that can be introduced to characterize the turbulence. The above turbulent terms are known as the *Reynolds stresses.*

Explicit solution for $\bar{u''_i}$ and $\bar{u''_j}$ is a method known as Reynolds stress closure. This method introduces higher-order correlation terms, and is not considered to be computationally economic [40].

A more common method, known as as "mean flow closure" is adopted in the MD-PHASE formulation. The assumption is made that the Reynolds stresses behave as a diffusional flux of momentum arising from the turbulence. The Reynolds stresses are thus modeled in a fashion analogous to the stress-strain tensor in a laminar flow. This relation [83], given below, introduces two parameters, the density-weighted turbulent kinetic energy, k, and the turbulent viscosity, μ_t. We have,

$$- < \rho > < \overline{u''_j u''_i} > = \mu_t(\bar{u}_{i,j} + \bar{u}_{j,i}) - \frac{2}{3}(\mu_t \bar{u}_{l,l} + < \rho > k)\delta_{ij} \qquad (2.28)$$

where,

$$k = \frac{1}{2} < \overline{u''_i u''_i} >$$

Via dimensional analysis, two parameters are required to evaluate μ_t. The $k - \epsilon$ model [89] has proven to be a suitable method to model turbulent flows. The parameters have a physical significance, and transport equations may be obtained for them in a straightforward manner. For high Reynolds number flows, the parameter ϵ is defined as,

$$\epsilon = \frac{\mu}{\rho} < u'_{i,j} u'_{i,j} >$$

ϵ defines the dissipation rate of the DWEA turbulent kinetic energy. From dimensional analysis, the relation between μ_t and the two turbulence parameters is,

$$\mu_t = \frac{C_\mu < \rho > k^2}{\epsilon} \qquad (2.29)$$

Above, C_μ is found empirically, and for high Reynolds numbers, has a value of about 0.09.

Finally, we are in a position to write the set of "closed" equations for a turbulent flow field. The equations 2.30 and 2.31 given below are then coupled with transport equations for the turbulence parameters to produce a fully defined system of equations. We now have,

Mass:

$$\frac{\partial < \rho >}{\partial t} + (< \rho > \tilde{u}_j)_{,j} = 0 \tag{2.30}$$

Momentum:

$$\begin{aligned}\frac{\partial(< \rho > u)_i}{\partial t} &+ (< \rho > \tilde{u}_j\tilde{u}_i - (\mu + \mu_t)\tilde{u}_{i,j})_{,j} \\ &= - < P >_{,i} + \frac{2}{3}\left[(\mu + \mu_t)\tilde{u}_{l,l} + < \rho > k\right]_{,i} + \left[(\mu + \mu_t)\tilde{u}_{i,j}\right]_{,j}\end{aligned} \tag{2.31}$$

2.6.1.5 Turbulent Kinetic Energy Transport Equation

The variable k is solved for in the flow domain with its behaviour defined by a transport equation. The DWEA turbulence energy transport equation was derived by Watkins [84] by manipulating the momentum equation and making use of the relations between the fluctuating and mean flow variables. The form of the equation that is used in this work is,

$$\begin{aligned}\frac{\partial(< \rho > k)}{\partial t} &+ \left(< \rho > \tilde{u}_j k - \frac{1}{\sigma_k}(\mu + \mu_t)k_{,j}\right)_{,j} = \mu_t\left(\tilde{u}_i(\tilde{u}_{i,j} + \tilde{u}_{j,i})\right)_{,j} \\ &-\frac{2}{3}\left(\tilde{u}_l\left[\mu_t\tilde{u}_{k,k} + < \rho > k\right]\right)_{,l} - < \rho > \epsilon\end{aligned} \tag{2.32}$$

In equation 2.32, σ_k is an empirical constant of value 1.0.

2.6.1.6 Turbulence Energy Dissipation Rate Equation

The ensemble-averaged energy dissipation equation is given below, in terms of DWEA variables, as this form [82, 84] is considered the most correct, of the available relevant formulations. It is written as,

$$\begin{aligned}\frac{\partial(< \rho > \epsilon)}{\partial t} &+ \left(< \rho > \tilde{u}_j\epsilon - \frac{1}{\sigma_\epsilon}(\mu + \mu_t)\epsilon_{,j}\right)_{,j} = \frac{\epsilon}{k}\left\{C_1\left[\mu_t\left(\tilde{u}_i(\tilde{u}_{i,j} + \tilde{u}_{j,i})\right)_{,j}\right.\right. \\ &\left.\left.-\frac{2}{3}\left(\tilde{u}_l\left[\mu_t\tilde{u}_{k,k} + < \rho > k\right]\right)_{,l} - C_2 < \rho > \epsilon\right\} + C_3 < \rho > c\tilde{u}_{l,l}\end{aligned} \tag{2.33}$$

The model constants, σ_ϵ, C_1, C_2 and C_3 are given in table 2.4.

constant	C_μ	C_1	C_2	κ	E	σ_k	σ_ϵ	C_3
value	0.09	1.44	1.92	0.4187	9.793	1.0	$\frac{\kappa^2}{(C_2 - C_1)\, C_\mu^{0.5}}$	1.0

Table 2.4: Turbulence model constants.

2.6.2 Generalized Transport Equation

All of the previous equations which have been expressed as transport equations have assumed a similar format. In fact, any of the transport variables may be represented by a generalized transport variable, ϕ. ϕ can be interpreted as either a time-average or a density-weighted average. In any case, the form of the equations are all identical. The different averages will no longer be indicated, as turbulence parameters along with the mean flow variables account for the entire flow field description.

In our general form, we have,

$$\frac{\partial(\rho\phi)}{\partial t} + (\rho u_i \phi - \Gamma_\phi \phi_{,i})_{,i} = S_\phi \tag{2.34}$$

where Γ_ϕ and S_ϕ are respectively, the "effective exchange coefficient" and volumetric source rate of the variable ϕ. Table 2.5 explicitly details ϕ, Γ_ϕ and S_ϕ for cylindrical coordinates. The velocity vector is composed of (u, v, w) for the z, r and θ-directions. The variables P_{eff} and G, as shown in table 2.5, are explicitly expanded below.

$$P_{\text{eff}} = P + \frac{2}{3}(\rho k + \mu_t u_{i,i})$$

$$G = \mu_t \left[2\left\{ \left(\frac{\partial u}{\partial z}\right)^2 + \left(\frac{\partial v}{\partial r}\right)^2 + \left(\frac{1}{r}\frac{\partial w}{\partial \theta} + \frac{v}{r}\right)^2 \right\} + \left(\frac{\partial u}{\partial r} + \frac{\partial v}{\partial z}\right)^2 \right.$$
$$\left. \left(\frac{1}{r}\frac{\partial u}{\partial \theta} + \frac{\partial w}{\partial z}\right)^2 + \left\{ r\frac{\left(\frac{w}{r}\right)}{r} + \frac{1}{r}\frac{\partial v}{\partial \theta} \right\}^2 - \frac{2}{3}(u_{i,i})^2 \right] - \frac{2}{3}\rho k u_{i,i}$$

The general transport equation (equation 2.34) can be extended to model other quantities, such as temperatures or concentrations, which are involved in a flow problem.

2.6.3 Boundary Conditions

To successfully resolve any physical flow problem, a complete set of boundary conditions must be specified. This involves applying appropriate conditions for sections of the boundary designated as walls, inlets, outlets, axes of symmetry and free

ϕ	Γ_ϕ	S_ϕ
1	0	0
u	$\mu_t + \mu$	$\frac{-\partial P_{\text{eff}}}{\partial z} + \left[(\mu_t + \mu)\frac{\partial u_i}{\partial z}\right]_{,i}$
v	$\mu_t + \mu$	$\frac{-\partial P_{\text{eff}}}{\partial r} + \left[(\mu_t + \mu)\frac{\partial u_i}{\partial r}\right]_{,i} - \frac{(\mu_t + \mu)}{r^2}\left[2v + 3\frac{\partial w}{\partial \theta}\right]$ $-\frac{w}{r^2}\frac{\partial(\mu_t + \mu)}{\partial \theta} + \rho\frac{w^2}{r}$
w	$\mu_t + \mu$	$\frac{-1}{r}\frac{-\partial P_{\text{eff}}}{\partial \theta} + \left[(\mu_t + \mu)\frac{1}{r}\frac{\partial u_i}{\partial \theta}\right]_{,i} - \frac{w}{r^2}\frac{\partial r(\mu_t + \mu)}{\partial r}$ $+ \frac{1}{r^2}\left[3(\mu_t + \mu)\frac{\partial v}{\partial \theta} + 2v\frac{\partial(\mu_t + \mu)}{\partial \theta}\right] - \rho\frac{vw}{r}$
k	$\frac{(\mu_t + \mu)}{\sigma_k}$	$G - \rho\epsilon$
ϵ	$\frac{(\mu_t + \mu)}{\sigma_\epsilon}$	$C_1\frac{\epsilon}{k}G - C_2\rho\frac{\epsilon^2}{k} + C_3\rho\epsilon u_{i,i}$

Table 2.5: Explicit equation terms in cylindrical coordinates.

surfaces.

2.6.3.1 Axes of Symmetry

The boundary conditions which are specified for an axis of symmetry are:

$$u_{i,n} = 0$$
$$u_n = 0$$

Above, the subscript n refers to a direction normal to to the i-direction, which is the direction of the axis.

2.6.3.2 Outlet Plane

At outlets, normal gradient conditions are imposed. That is, $u_{n,n} = 0$, where n is a direction normal to the plane of the outlet. This condition is also integrated into an overall mass balance to determine the flux at the outlet.

2.6.3.3 Inlet Plane

At all inlets, the profiles of u_i, ϵ and k must be specified. When values of these parameters are not readily available, the convention is to determine ϵ and k by using the turbulence intensity, I and the turbulence length scale ℓ. I is defined as,

$$I = \sqrt{\left\langle \left(\frac{\bar{u}_i'}{\bar{u}} \right)^2 \right\rangle}$$

and is typically given a value of between 0.02 and 0.05, while ℓ is set to be a small fraction of the physical dimension of the inlet.

For such cases, ϵ and k can be evaluated with the following expressions.

$$\epsilon = \frac{C_\mu^{0.75} k^{1.5}}{\ell} \tag{2.35}$$

$$k = \frac{3}{2} \bar{u}^2 I^2 \tag{2.36}$$

2.6.3.4 Solid Walls

Solid walls are considered to be impermeable and subject to a no-slip constraint. For such a case, all the variables may be set to zero. The wall shear stresses and values of the turbulence variables, k and ϵ, are determined using the "wall function" method of Launder and Spalding [79]. The pressure along solid boundaries can be calculated, if the velocity field is specified there.

2.6.3.5 Wall Function Method

The turbulence parameters as modeled in this development assume sufficiently high Reynolds numbers, so that the turbulence structure does not depend on viscosity. Viscous effects are far more pronounced near a solid boundary [85, 86], and thus a modification to the model must be made in these regions.

The approach of Reynolds is adopted [85] where a *wall layer* is defined, and then the turbulent interior flow region is bridged to the solid boundary by special *wall-functions*. The local Reynolds number [79], Y^+, which is given below, describes the flow conditions across the wall-layer.

$$Y^+ = \frac{\rho u_\tau Y}{\mu}$$

Here, Y is the normal distance from the wall and u_τ is the friction velocity related to the wall shear stress, τ_w by,

$$u_\tau = \sqrt{\frac{\tau_w}{\rho}}$$

Observation of turbulent flows have revealed three regions extending from a solid boundary. They are a viscous sublayer, a viscous-turbulent transition zone and an inertial sublayer [87]. The inertial sublayer is assumed to be fully turbulent, but with the shear stress still constant at τ_w. For computational purposes [38], the transition zone is partitioned at $Y^+ = 11.63$. At lower local Reynolds numbers, the flow is assumed totally viscous with a linear profile, and at higher values of Y^+, a fully turbulent character is prescribed, having a logarithmic profile [88]. The velocity

profiles in the wall regions are given by,

$$\frac{U}{u_\tau} = \begin{cases} Y^+ & \text{for } Y^+ \leq 11.63 \\ \frac{\ln(EY^+)}{\kappa} & \text{for } Y^+ > 11.63 \end{cases} \tag{2.37}$$

where E and κ are constants that are given in table 2.4. These values are valid for smooth, impermeable walls. The variable U refers to the one-dimensional velocity along the wall.

2.6.3.6 Turbulent Sublayer

In the turbulent part of the wall layer, fluid shear stress is calculated in a way analogous to that for standard laminar flows. The turbulence dissipation rate ϵ follows from this development

We state the shear stress as,

$$\tau_w \simeq \tau = \mu_t \frac{\partial U}{\partial Y} \tag{2.38}$$

From its definition, μ_t can be calculated in the turbulent part of the wall region, and is typically found to be substantially greater than μ, so that the latter may be considered negligible [40]. Launder and Spalding [89] express the transport equation for the turbulence parameter k near a wall as a balance between the localized production and dissipation of k. This result is,

$$\mu_t \left(\frac{\partial U}{\partial Y}\right)^2 = \rho\epsilon \tag{2.39}$$

Combining equations 2.29 and 2.38, we can state,

$$\tau_w = C_\mu^{0.5} \rho k = \rho u_\tau^2 \tag{2.40}$$

Substituting from equation 2.37, gives,

$$\tau_w = \frac{\rho C_\mu^{0.25} k^{0.5} U \kappa}{\ln(EY^+)} \tag{2.41}$$

Above, the local Reynolds number, Y^+, is determined by,

$$Y^+ = \frac{\rho C_\mu^{0.25} k^{0.5} Y}{\mu} \tag{2.42}$$

For the near wall region, within the viscous sublayer, ($Y^+ \leq 11.63$), the wall shear stress is simply given as,

$$\tau_w = \frac{\mu U}{Y} \tag{2.43}$$

Here, zero turbulent viscosity is assumed. Note that for a three dimensional flow (over a surface), the velocity resultant U, is composed of the two vector components which are parallel to the plane in question. This leads to modifications in the derivations for other variables and is given more completely by Lai and Salcudean [39].

Chapter 3

Computational Implementation

The computational implementation of both the boundary element formulation as well as the finite volume method, was done in the FORTRAN programming language, on a Silicon Graphics Power Series 4D/380S mainframe. The machine has eight processors; two at 33 MHZ, and 6 at 25 MHZ. The machine RAM is 64 megabytes, allowing quite large simulations to be run without resorting to swap space. The compilation was controlled via a Unix-based `makefile` executable.

3.1 BEM implementation

The following section details the discretization and numerical implementation procedure for the two-dimensional unsteady Navier-Stokes primitive-variable discrete time-step formulation.

3.1.1 Discretization Scheme

To allow a pseudo-linear system of equations to be formed for the unknowns (velocity u_i and traction τ_i) at each node, these variables are computed using interpolation functions. It should be noted that the formulations presented here, are done with a *linear* interpolation scheme in two dimensions. For example, on the boundary, the

tractions would be expressed as:

$$\tau_i(\mathbf{x}) = \varphi_n \tau_i(\mathbf{x}_n) \tag{3.1}$$

Similarly, in the domain, the velocities would be expressed as:

$$u_i(\mathbf{x}) = \psi_q u_i(\mathbf{x}_q) \tag{3.2}$$

$\mathbf{x}_q$ and $\mathbf{x}_n$ refer to coordinates at the qth or nth node in the respective domain element or boundary element. The boundary elements employed are the set of partitioned line segments which bound the region, while the domain elements are the set of two dimensional triangular regions of the partitioned interior.

In equations 3.1 and 3.2, the interpolation functions φ_n and ψ_q are given as:

$$\begin{aligned} \varphi_1 &= \frac{1}{2}(1-\xi) \\ \varphi_2 &= \frac{1}{2}(1+\xi) \end{aligned} \tag{3.3}$$

The local parameter ξ is determined as follows. (see figure 3.1)

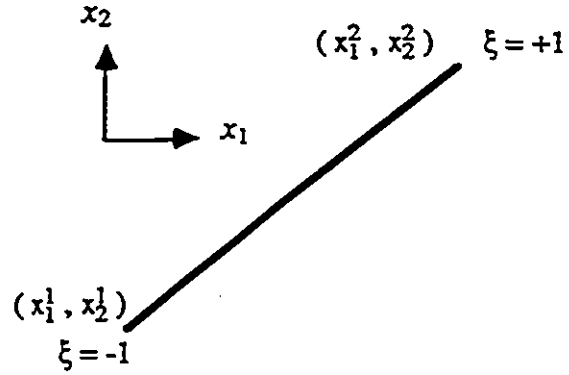

Figure 3.1: Interpolating functions for a boundary element.

$$\xi = \left(\frac{2\sqrt{(x_1 - x_1^1)^2 + (x_2 - x_2^1)^2}}{\sqrt{(x_1^2 - x_1^1)^2 + (x_2^2 - x_2^1)^2}} \right) - 1 \tag{3.4}$$

For domain elements [90], we use a localized triangular coordinate system :

$$\psi_i = \frac{1}{2A}\left(2A_i^0 + b_i x_1 + a_i x_2\right) \tag{3.5}$$

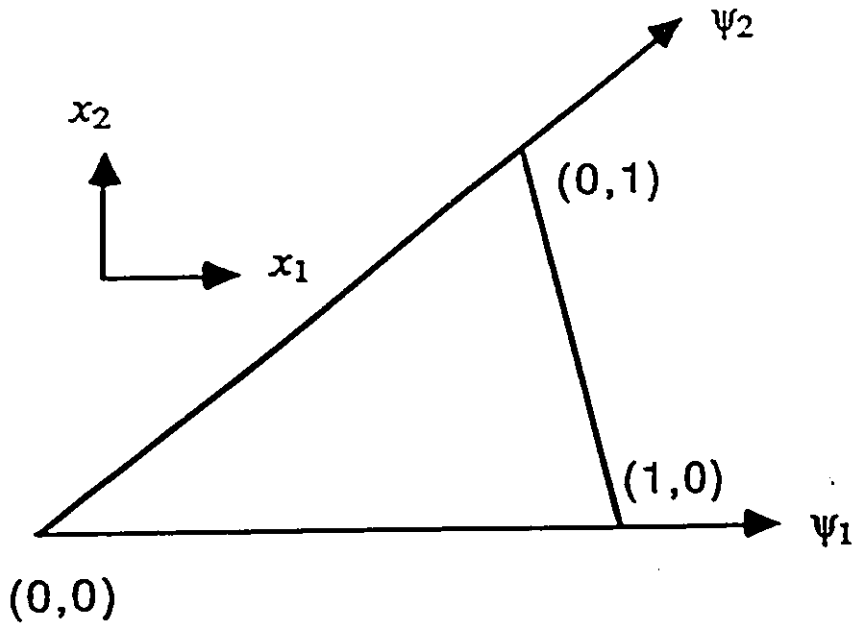

Figure 3.2: Interpolating functions for a domain element.

Here (see Figure 3.2),

$$\begin{aligned} a_i &= \mathrm{x}_1^K - \mathrm{x}_1^J \\ b_i &= \mathrm{x}_2^J - \mathrm{x}_2^K \\ 2A_i^0 &= \mathrm{x}_1^J \mathrm{x}_2^K - \mathrm{x}_1^K \mathrm{x}_2^J \\ A &= \frac{1}{2}(b_1 a_2 - b_2 a_1) \end{aligned}$$

Above, when $i = 1,2,3$ (referring to shape function index), then $J = 2,3,1$ and $K = 3,1,2$. Above, x_i^J is the the value of x_i at the Jth end point or corner of the respective domain element or boundary element. Equation 2.11 can be rewritten in a discretized form when the boundary and domain are divided up into separate elements. In addition, since the unknowns, (velocity u_i and traction τ_i) are expressed as linear combinations of shape functions involving only nodal values, we obtain the following algebraic form:

$$\Lambda_{\gamma l} u_l + G_{\gamma in}\tau_{in} = H_{\gamma in} u_{in} - C_{\gamma iq} u(t - \Delta t)_{iq} + Z_{\gamma iqpa} u_{iq} u_{pa} \qquad (3.6)$$

In the above equation, the coefficients $\Lambda_{\gamma k}$, are given by:

$$\Lambda_{\gamma l} = \begin{cases} (\frac{\theta}{2\pi})\delta_{\gamma l}(\mathrm{y}) & \text{for } y \in \Gamma \\ \delta_{\gamma l}(\mathrm{y}) & \text{for } y \in \Omega \end{cases} \tag{3.7}$$

In equation 3.7, the factor $(\frac{\theta}{2\pi})$ is the angle (in radians) formed between two boundary elements, when the node is at their junction. If the surface is smooth, this factor reduces to a value of $\frac{1}{2}$.

The other coefficients (for integration over the Jth element) from equation 3.6 are given as follows:

$$G_{\gamma in} = \int_{\Gamma_J} W_{i\gamma}(\mathrm{x},\mathrm{y})\varphi_n(\mathrm{x})\, d\Gamma(\mathrm{x}) \tag{3.8}$$

$$H_{\gamma in} = \int_{\Gamma_J} \Sigma_{i\gamma}(\mathrm{x},\mathrm{y})\varphi_n(\mathrm{x})\, d\Gamma(\mathrm{x}) \tag{3.9}$$

$$C_{\gamma iq} = \int_{\Omega_J} \mathrm{Re}W_{i\gamma}(\mathrm{x},\mathrm{y})\psi_q(\mathrm{x})\, d\Omega(\mathrm{x}) \tag{3.10}$$

$$Z_{\gamma iqpa} = \int_{\Omega_J} \mathrm{Re}\psi_{a,p}(\mathrm{x})W_{i\gamma}(\mathrm{x},\mathrm{y})\psi_q(\mathrm{x})\, d\Omega(\mathrm{x}) \tag{3.11}$$

3.1.2 Singular integrals

Solution of the system of equations 3.6 requires integration over all boundary elements and domain elements from each node. When the node in question is contained in the same element (ie; source and field point coincide, $r = 0$), singularities arise.

The integrals in equations 3.8 to 3.11 must be evaluated analytically to avoid substantial error in the flow field solution. Note that with linear shape functions, the term $\psi_{a,p}$ in equation 3.11 will be constant over a domain element. So in total, we must make singular formulations for three cases, namely equations 3.8, 3.9 and 3.10.

3.1.2.1 Singular Case for $\int_\Omega W_{ij}\psi_\alpha\, d\Omega$

Let us define a modified domain element, illustrated in figure 3.3. Using the method of Brebbia et al. [90], we transform the system to polar coordinates, (r,φ). In the triangular element,

$$r(\varphi) = \frac{-2A}{b_\epsilon \cos\varphi + a_\epsilon \sin\varphi}$$

Above, ς is the triangular domain element corner index at the singular point. A, b_ς and a_ς are as defined in equation 3.5.

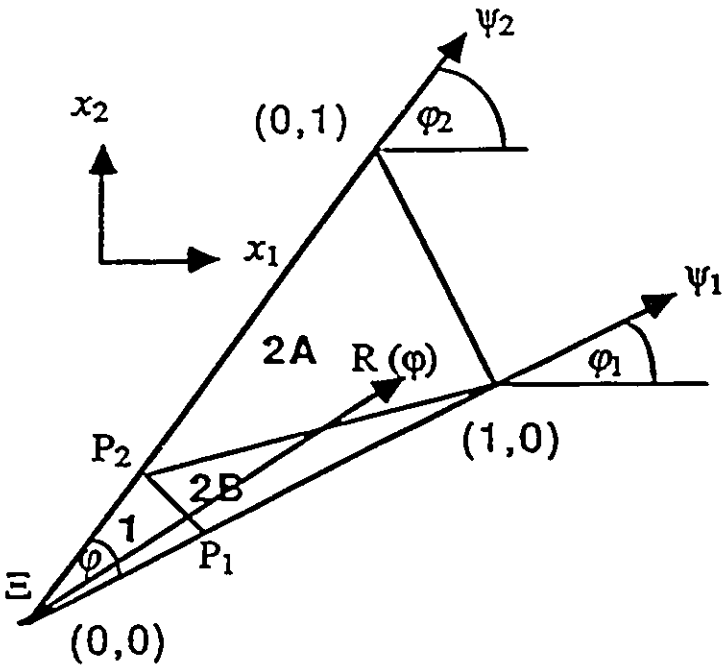

Figure 3.3: Schematic of domain element used in the treatment of a singularity.

Further, the element of area, $d\Omega = r\, dr\, d\varphi$. Using the subscript α as the shape function index, and transforming the linear triangular shape functions to (r, φ) coordinates, we produce,

$$\bar{\psi}_\alpha = \psi_\alpha^\varsigma + \frac{r}{2A}\left(b_\alpha \cos\varphi + a_\alpha \sin\varphi\right) \tag{3.12}$$

where,

$$\psi_\alpha^\varsigma = \begin{cases} 0 & \text{when } \alpha \neq \varsigma \\ 1 & \text{when } \alpha = \varsigma \end{cases}$$

In order to successfully evaluate this singular integral, a limiting case must be considered. Along the radius $r(\varphi)$ away from the singular point, a maximum value of $r(\varphi) = R(\varphi)$ must be selected since the fundamental solution must be transformed to an infinite series format, which involves a convergence criterion on this variable. To

exclude the singularity, the lower limit of integration is taken as ϵ, an infinitesimal number. Recall the following transforms:

$$\begin{aligned} z &= \sqrt{\lambda} r \qquad \text{when } r = \epsilon \Rightarrow z = \sqrt{\lambda}\epsilon = a_1 \\ dz &= \sqrt{\lambda} dr \quad \text{when } r = R(\varphi) \Rightarrow z = \sqrt{\lambda} R(\varphi) = a_2 \\ r &= \frac{1}{\sqrt{\lambda}} z \qquad r\, dr\, dz = \frac{z}{\lambda}\, dz\, d\varphi \end{aligned}$$

In view of these transforms, the shape function becomes,

$$\tilde{\psi}_\alpha = \psi_\alpha^s + \frac{z}{2A\sqrt{\lambda}} (b_\alpha \cos\varphi + a_\alpha \sin\varphi)$$

So, now we begin the evaluation of singular integral.

$$I_\Omega = \int_\Omega W_{ij} \psi_\alpha \, d\Omega = \lim_{\epsilon \to 0} \int_{\varphi_1}^{\varphi_2} \int_\epsilon^{R(\varphi)} W_{ij} \tilde{\psi}_\alpha r \, dr \, d\varphi$$

Inserting the explicit form of the fundamental solution gives,

$$I_\Omega = \lim_{\epsilon \to 0} \int_{\varphi_1}^{\varphi_2} \int_\epsilon^{R(\varphi)} \left[\frac{-\delta_{ij}}{2\pi\lambda} \left(K_2(z) - z^{-1} K_1(z) - \frac{1}{z^2} \right) + \frac{s_i s_j}{2\pi\lambda r^2} \left(K_2(z) - \frac{2}{z^2} \right) \right] \tilde{\psi}_\alpha z \, dz \, d\varphi$$

Note that for the singular case, the ratio s_i/r will be constant in the domain element, equal to $\cos\varphi$ for $i = 1$ and $\sin\varphi$ for $i = 2$. Now, inserting the transformed shape function into the integral gives,

$$\begin{aligned} I_\Omega = \frac{-1}{2\pi} \lim_{\epsilon \to 0} \int_{\varphi_1}^{\varphi_2} \Bigg[& \delta_{ij} \left\{ \int_{a_1}^{a_2} z K_2(z) \tilde{\psi}_\alpha \, dz - \int_{a_1}^{a_2} K_1(z) \tilde{\psi}_\alpha \, dz - \int_{a_1}^{a_2} \frac{1}{z} \tilde{\psi}_\alpha \, dz \right\} \\ & - \frac{s_i s_j}{r^2} \left\{ \int_{a_1}^{a_2} z K_2(z) \tilde{\psi}_\alpha \, dz - 2 \int_{a_1}^{a_2} \frac{1}{z} \tilde{\psi}_\alpha \, dz \right\} \Bigg] \, d\varphi \end{aligned}$$

Let us express,

$$\tilde{\psi}_\alpha = \psi_\alpha^s + \Theta_\alpha(\varphi) z$$

where,

$$\Theta_\alpha(\varphi) z = \frac{1}{2A\sqrt{\gamma}} (b_\alpha \cos\varphi + a_\alpha \sin\varphi)$$

We now insert $\psi_\alpha^s + \Theta_\alpha(\varphi) z$ for $\tilde{\psi}_\alpha$ into the expression for I_Ω.

$$I_\Omega = \frac{-1}{2\pi} \lim_{\epsilon \to 0} \int_{\varphi_1}^{\varphi_2} \Bigg[\delta_{ij} \left\{ \psi_\alpha^s \int_{a_1}^{a_2} z K_2(z) \, dz + \Theta_\alpha(\varphi) \int_{a_1}^{a_2} z^2 K_2(z) \, dz \right.$$

$$
\begin{aligned}
&-\psi_\alpha^\varsigma \int_{a_1}^{a_2} K_1(z)\,dz - \Theta_\alpha(\varphi)\int_{a_1}^{a_2} zK_1(z)\,dz \\
&- \psi_\alpha^\varsigma \int_{a_1}^{a_2} \frac{1}{z}\,dz - \Theta_\alpha(\varphi)\int_{a_1}^{a_2} dz\Big\} \\
&-\frac{s_i s_j}{r^2}\Big\{\psi_\alpha^\varsigma \int_{a_1}^{a_2} zK_2(z)\,dz + \Theta_\alpha(\varphi)\int_{a_1}^{a_2} z^2K_2(z)\,dz \\
&-2\psi_\alpha^\varsigma \int_{a_1}^{a_2} \frac{1}{z}\,dz - 2\Theta_\alpha(\varphi)\int_{a_1}^{a_2} dz\Big\}\Big]\,d\varphi
\end{aligned}
$$

At this point we see that we have integrals of the form,

$$\lim_{\epsilon\to 0}\int_{a_1}^{a_2} z^m K_n(z)\,dz$$

which must be evaluated. This procedure and a table of results for all such integrals required in this thesis are detailed in Appendix B. Using these results for the integrations over z, we have,

$$
\begin{aligned}
I_\Omega = \frac{-1}{2\pi}\int_{\varphi_1}^{\varphi_2} \lim_{\epsilon\to 0}\Big[&\delta_{ij}\Big\{\psi_\alpha^\varsigma \mathcal{S}(zK_2(z)) + 2\psi_\alpha^\varsigma \int_{a_1}^{a_2}\frac{1}{z}\,dz \\
&+\Theta_\alpha(\varphi)\mathcal{S}(z^2K_2(z)) - \psi_\alpha^\varsigma \mathcal{S}(K_1(z)) \\
&-\psi_\alpha^\varsigma \int_{a_1}^{a_2}\frac{1}{z}\,dz - \Theta_\alpha(\varphi)\mathcal{S}(zK_1(z)) \\
&-\psi_\alpha^\varsigma \int_{a_1}^{a_2}\frac{1}{z}\,dz - \Theta_\alpha(\varphi)a_2\Big\} \\
&-\frac{s_i s_j}{r^2}\Big\{\psi_\alpha^\varsigma \mathcal{S}(zK_2(z)) + 2\psi_\alpha^\varsigma \int_{a_1}^{a_2}\frac{1}{z}\,dz \\
&+\Theta_\alpha(\varphi)\mathcal{S}(z^2K_2(z)) - 2\psi_\alpha^\varsigma \int_{a_1}^{a_2}\frac{1}{z}\,dz \\
&-2\Theta_\alpha(\varphi)a_2\}\Big]\,d\varphi
\end{aligned}
$$

It can be seen from the above equation that all the integrals of the form,

$$\int_{a_1}^{a_2}\frac{1}{z^m}\,dz$$

sum to zero.

Now, let $\varphi = \frac{\xi}{2}(\varphi_1 - \varphi_2) + \frac{1}{2}(\varphi_1 + \varphi_2)$. Thus, when $\varphi = \varphi_1$, $\xi = -1$, and when $\varphi = \varphi_2$, $\xi = +1$. Further, $d\varphi = ((\varphi_1 - \varphi_2)/2)\,d\xi$. Since I_Ω is a complicated function of φ, a transform to variable limits of -1 and +1 is employed to facilitate numerical integration over this variable by Gaussian quadrature. The singularity in I_Ω arises in

the variable r, and the integration over r was done analytically in the interior integral of the double integral over the domain. Hence, the net integral procedure for I_Ω is considered semi-analytical.

Finally, we can write,

$$\begin{aligned} I_\Omega = \frac{-1}{2\pi}\int_{-1}^{+1} \Big[& \delta_{ij}\left\{\left[S(K_1(z)) - S(zK_2(z))\right]\psi_\alpha^\varsigma \right. \\ & + \left.\left[S(z^2K_2(z)) - S(zK_1(z)) - a_2\right]\Theta_\alpha(\xi)\right\} \\ & - \frac{s_i s_j}{r^2}\left\{\psi_\alpha^\varsigma S(zK_2(z)) \right. \\ & + \left.\left[S(z^2K_2(z)) - 2a_2\right]\Theta_\alpha(\xi)\right\}\Big] \frac{\varphi_2 - \varphi_1}{2}\, d\xi \end{aligned} \tag{3.13}$$

Thus, equation 3.13 can be implemented numerically and solved by Gaussian quadrature in the interval -1 to +1 in ξ.

3.1.2.2 Singular Case for $\int_\Gamma \Sigma_{ij}\varphi_\alpha\, d\Gamma$

Again, let us define a modified boundary element, shown in Figure 3.4. In this element, a number of transforms are effected. Let $r = (R/2)(1+\xi)$. Thus, $\xi = (2r/R) - 1$. Here, R is a maximum value of r, selected for the convergence criteria of the series forms of the integrals of the modified Bessel functions. The singularity is avoided by choosing the lower limit of the integration to be $\xi = -1 + \epsilon$. Recall the boundary element shape functions,

$$\varphi_\alpha = \frac{1}{2}(1 + (-1)^\alpha\xi) = \frac{1}{2}(1 + C_\alpha\xi)$$

Here we set $C_\alpha = (-1)^\alpha$ and define $\tilde{C}_\alpha = 1 - C_\alpha$. Thus,

$$\begin{aligned} \varphi_\alpha &= \frac{1}{2}\left(1 + C_\alpha\left(\frac{2r}{R} - 1\right)\right) \\ &= \frac{1}{2}\left(\frac{2C_\alpha r}{R} + \tilde{C}_\alpha\right) \end{aligned}$$

We make use of the following transforms:

$$\begin{aligned} & z = \sqrt{\lambda}r \qquad \text{when } \xi = +1 \Rightarrow z = \sqrt{\lambda}R = a_2 \\ & dz = \sqrt{\lambda}dr \quad \text{when } \xi = -1 + \epsilon \Rightarrow z = \frac{\sqrt{\lambda}R\epsilon}{2} = a_1 \\ & r = \frac{1}{\sqrt{\lambda}}z \qquad r\,dr\,dz = \frac{z}{\lambda}\,dz\,d\varphi \end{aligned}$$

In view of these transforms, the shape function becomes,

$$\varphi_\alpha = \frac{1}{2}\left(\frac{2C_\alpha z}{\sqrt{\lambda}R} + \bar{C}_\alpha\right)$$

Thus our singular integral can be stated as,

$$I_{r\Sigma} = \lim_{\epsilon \to 0} \int_{a_1}^{a_2} \Sigma_{ij}\varphi_\alpha \, d\Gamma$$

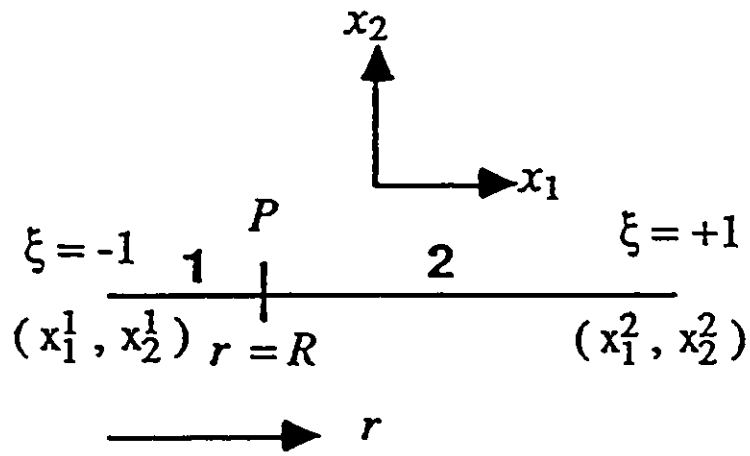

Figure 3.4: Schematic of boundary element used in the treatment of a singularity.

At this point, before inserting the explicit form of the fundamental solution Σ_{ij} into the above equation, the following result is observed. For the singular case, (refer to Figure 3.4) the terms s_i are the components of $\vec{r}$. $\vec{r}$ itself, simply extends along the boundary element in question. By definition, $\vec{n}$ is the normal to the boundary element and hence, its components must form a zero dot-product with s_i. Thus, the terms $s_i n_i = 0$ and can be excluded from the calculations. Further, for the singular case, $s_1/r = \sin\theta$, and $s_2/r = \cos\theta$, which are constants.

So we proceed,

$$I_{r\Sigma} = \frac{-1}{2\pi\lambda} \lim_{\epsilon \to 0} \int_{a_1}^{a_2} \left[\frac{s_j n_i \lambda^{\frac{3}{2}}}{r}\right] \left(\frac{1}{z}\right)$$

$$
\begin{aligned}
&+\left(\frac{s_i n_j}{r}\right)\left(\lambda^{\frac{3}{2}}K_3(z)-3\lambda^{\frac{3}{2}}z^{-1}K_2(z)-2\lambda^{\frac{3}{2}}\left(\frac{1}{z^3}\right)\right)\\
&+\left(\frac{2s_j n_\cdot+s_i n_j}{r}\right)\left(\lambda^{\frac{3}{2}}z^{-1}K_2(z)-2\lambda^{\frac{3}{2}}\left(\frac{1}{z^3}\right)\right)\Bigg]\\
&\frac{1}{2}\left(\frac{2C_\alpha z}{\sqrt{\lambda}R}+\tilde{C}_\alpha\right)\frac{1}{\sqrt{\lambda}}\,dz
\end{aligned}
$$

$$
\begin{aligned}
&=\frac{-1}{4\pi\lambda^{\frac{3}{2}}}\lim_{c\to 0}\int_{a_1}^{a_2}\Bigg[\frac{2s_j n_i\lambda C_\alpha}{rR}+\frac{s_j n_i\lambda^{\frac{3}{2}}\tilde{C}_\alpha}{r}\left(\frac{1}{z}\right)\\
&+\left(\frac{s_i n_j}{r}\right)\left(\frac{2\lambda C_\alpha}{R}zK_3(z)\lambda^{\frac{3}{2}}\tilde{C}_\alpha K_3(z)\right.\\
&-\frac{6\lambda C_\alpha}{R}K_2(z)-3\lambda^{\frac{3}{2}}\tilde{C}_\alpha z^{-1}K_2(z)\\
&\left.-\frac{4\lambda C_\alpha}{R}\left(\frac{1}{z^2}\right)-2\lambda^{\frac{3}{2}}\tilde{C}_\alpha\left(\frac{1}{z^3}\right)\right)\\
&+\left(\frac{2s_j n_i+s_i n_j}{r}\right)\left(\frac{2\lambda C_\alpha}{R}K_2(z)+\lambda^{\frac{3}{2}}\tilde{C}_\alpha z^{-1}K_2(z)\right.\\
&\left.-\frac{4\lambda C_\alpha}{R}\left(\frac{1}{z^2}\right)-2\lambda^{\frac{3}{2}}\tilde{C}_\alpha\left(\frac{1}{z^3}\right)\right)\Bigg]\,dz
\end{aligned}
$$

Now we can insert the results from Table C.1 of the form:

$$\lim_{c\to 0}\int_{a_1}^{a_2} z^m K_n(z)\,dz \quad \text{expressed as:} \quad \mathcal{S}(z^m K_n(z))$$

Upon the above substitution, all the integrals of the form,

$$\int_{a_1}^{a_2}\frac{1}{z^m}\,dz$$

will sum to zero as in the previous singular case. These integrals and their coefficients are not written for the sake of brevity. Finally, for $I_{\Gamma\Sigma}$ we have,

$$
\begin{aligned}
I_{\Gamma\Sigma}=\frac{-1}{4\pi\lambda}\Bigg[&\frac{s_j n_i\lambda C_\alpha a_2}{rR}\\
&+\mathcal{S}(zK_3(z))\left(\frac{s_i n_j}{r}\frac{2\lambda C_\alpha}{R}\right)+\mathcal{S}(K_3(z))\left(\frac{s_i n_j\lambda^{\frac{3}{2}}\tilde{C}_\alpha}{r}\right)\\
&+\mathcal{S}(K_2(z))\left\{\frac{8\lambda C_\alpha}{R}\left(\frac{s_j n_i+s_i n_j}{r}\right)\right\}+\mathcal{S}(z^{-1}K_2(z))\left\{2\lambda^{\frac{3}{2}}\tilde{C}_\alpha\left(\frac{s_j n_i+s_i n_j}{r}\right)\right\}\Bigg]
\end{aligned}
\tag{3.14}
$$

Equation 3.14 can be implemented to give analytical results for integrations of $I_{\Gamma\Sigma}$ over singular boundary elements.

3.1.2.3 Singular Case for $\int_\Gamma W_{ij}\varphi_n \, d\Gamma$

Proceeding in an entirely parallel fashion as for $I_{\Gamma\Sigma}$, we can define the singular integral,

$$I_{\Gamma W} = \lim_{\epsilon \to 0} \int_{a_1}^{a_2} W_{ij}\varphi_\alpha \, d\Gamma$$

Employing the same transforms and operations as in subsection 3.1.2.2 we find that,

$$\begin{aligned} I_{\Gamma W} = \frac{-1}{2\pi\lambda} \Bigg[& \frac{C_\alpha}{R}\left(\delta_{ij} - \frac{s_i s_j}{r^2}\right) \mathcal{S}(zK_2(z)) \\ & + \frac{\tilde{C}_\alpha}{2}\left(\delta_{ij} - \frac{s_i s_j}{r^2}\right) \mathcal{S}(K_2(z)) - \frac{C_\alpha}{R}\delta_{ij}\mathcal{S}(K_1(z)) \\ & - \frac{\tilde{C}_\alpha}{2}\delta_{ij}\mathcal{S}(z^{-1}K_1(z)) \Bigg] \end{aligned} \tag{3.15}$$

Equation 3.15 can be implemented to give analytical results for integrations of $I_{\Gamma W}$ over singular boundary elements.

3.1.3 Numerical Quadrature

3.1.3.1 Domain Elements

The flow field was divided up into triangular domains defined by the node locations. A linear variation of the velocities and pressure was assumed within the domains. This was to enable better interpolated estimates of flow field variables at internal points for increased accuracy of numerical integration. Use of interpolation functions (as opposed to using domains with constant averaged function values) allowed such functions to be better-behaved.

A typical triangular element is shown in Figure 3.1. The flow field coordinates x_i are transformed to local coordinates η_i. We define x_i^m to be the value of x_i at the domain's mth corner. In order to normalize this transform, the following mappings must be effected.

$$(x_1, x_2) \implies (\eta_1, \eta_2)$$

$$\begin{aligned} (x_1^1, x_2^1) &\longrightarrow (1,0) \\ (x_1^2, x_2^2) &\longrightarrow (0,1) \\ (x_1^3, x_2^3) &\longrightarrow (0,0) \end{aligned}$$

This is accomplished with the following relations:

$$\begin{aligned} x_1 &= \eta_1 x_1^1 + \eta_2 x_1^2 + (1 - \eta_1 - \eta_2) x_1^3 \\ x_2 &= \eta_1 x_2^1 + \eta_2 x_2^2 + (1 - \eta_1 - \eta_2) x_2^3 \end{aligned} \tag{3.16}$$

(3.17)

The differential of area $d\Gamma(x)$ must be expressed in terms of the new coordinates of transformation. Thus,

$$d\Gamma(x) = \frac{\partial(x_1, x_2)}{\partial(\eta_1, \eta_2)} d\eta_1 d\eta_2 = \left\| \begin{array}{cc} \frac{\partial x_1}{\partial \eta_1} & \frac{\partial x_1}{\partial \eta_2} \\ \frac{\partial x_2}{\partial \eta_1} & \frac{\partial x_2}{\partial \eta_2} \end{array} \right\| d\eta_1 d\eta_2 \tag{3.18}$$

Solving this Jacobian, we obtain:

$$d\Gamma(x) = \| (x_1^1 - x_1^3)(x_2^2 - x_2^3) - (x_2^1 - x_2^3)(x_1^2 - x_1^3) \| \, d\eta_1 d\eta_2 = \| \mathbf{J} \| \, d\eta_1 d\eta_2 \tag{3.19}$$

Note that for these triangular domains, the factor $d\eta_1 d\eta_2$ is equal to $\frac{1}{2}$. Since the functional variation over the domains is linear, the value of $\| \mathbf{J} \|$ depends only on the respective domain, and not on a particular location of a field point.

We can define $\eta_3 = 1 - \eta_1 - \eta_2$, where η_3 is a new but not independent coordinate. For Gaussian quadrature, the interpolation functions ψ_i can thus be defined as:

$$\psi_i = \eta_i \tag{3.20}$$

Numerical integration over a triangle can be performed in terms of the triangular coordinates η_i, defined previously. The integral I, is determined as follows:

$$\begin{aligned} I &= \int_{x_2^{min}}^{x_2^{max}} \left(\int_{\mathcal{F}_1(x_2)}^{\mathcal{F}_2(x_2)} \mathcal{G}(x_1, x_2) dx_1 \right) dx_2 \\ &= \int_0^1 \left(\int_0^{1-\eta_2} \mathcal{G}(\eta_1, \eta_2, \eta_3) \| \mathbf{J} \| \, d\eta_1 \right) d\eta_2 \\ &\cong \mathcal{G}_i(\eta_1, \eta_2, \eta_3) w_i \| \mathbf{J} \| \, d\eta_1 d\eta_2 \qquad \text{where,} \quad i = 1, Q \end{aligned} \tag{3.21}$$

The subscript i in equation 3.21 refers to the index of the Gaussian quadrature, and Q is its order. That is, the function is evaluated at each of the i quadrature points and multiplied by the corresponding weighting factor w_i and the sum of these Q products is the value of the integral over the domain. In this case, where the functional variation is assumed to be linear over the domains, a cubic quadrature $Q = 4$ is of sufficient accuracy. In general, if the quadrature is one order higher than the actual functional variation, the numerical result will be exact [91]. Table 3.1 shows the quadrature points and weight factors for a cubic integration.

i	η_1^i	η_2^i	η_3^i	w_i
1	$\frac{1}{3}$	$\frac{1}{3}$	$\frac{1}{3}$	$\frac{-9}{16}$
2	$\frac{3}{5}$	$\frac{1}{5}$	$\frac{1}{5}$	$\frac{25}{48}$
3	$\frac{1}{5}$	$\frac{3}{5}$	$\frac{1}{5}$	$\frac{25}{48}$
4	$\frac{1}{5}$	$\frac{1}{5}$	$\frac{3}{5}$	$\frac{25}{48}$

Table 3.1: Parameters for 4th order Gaussian quadrature

Thus, any function defined over the flow field domains can be numerically treated using the above procedures.

3.1.3.2 Boundary Elements

In a fashion analogous to the division of the flow field into domain elements in Section 3.1.3.1, the edges of the domain were divided up into linear boundary elements. Again, a linear variation of functions was assumed over the boundary elements and appropriate interpolation functions were applied.

The flow field coordinates x_i were transformed to a local linear coordinate ξ which ranged between -1 and $+1$. Such a boundary element is depicted in Figure 3.2. We define x_i^m to be the value of x_i at the element's mth node, where m is either 1 or

2. In this scheme, x_i^2 in element n,is at the same point as x_i^1 in element $n+1$. This transform is made using the following mappings.

(x_1, x_2)	$\Longrightarrow$	ξ
$(x_1^1, x_2^1)_n$	$\longrightarrow$	-1
$(x_1^2, x_2^2)_n$	$\longrightarrow$	+1
$(x_1^1, x_2^1)_{n+1}$	$\longrightarrow$	+1
$(x_1^2, x_2^2)_{n+1}$	$\longrightarrow$	-1
$(x_1^1, x_2^1)_{n+2}$	$\longrightarrow$	-1
		etc.

The local parameter ξ is determined as follows.

$$\xi = \frac{\pm 2\sqrt{(x_1 - x_1^1)^2 + (x_2 - x_2^1)^2}}{\sqrt{(x_1^2 - x_1^1)^2 + (x_2^2 - x_2^1)^2}} \mp 1 \tag{3.22}$$

Above, in equation 3.4 the plus–minus option is necessary to ensure that ξ_n equals ξ_{n+1}.

The line differential $dS(x)$ must be expressed in terms of ξ, the new coordinate of transformation. Thus,

$$dS(x) = \sqrt{(\frac{\partial x_1}{\partial \xi})^2 + (\frac{\partial x_2}{\partial \xi})^2}\, d\xi \tag{3.23}$$

Solving this Jacobian, we obtain:

$$dS(x) = \sqrt{(\frac{x_1^1 - x_1^2}{2})^2 + (\frac{x_2^1 - x_2^2}{2})^2}\, d\xi = \| \mathbf{J} \|\, d\xi \tag{3.24}$$

Note that for these line elements, the factor $d\xi$ is equal to 2. Since the functional variation over the boundary is assumed linear, the value of $\| \mathbf{J} \|$ depends only on the respective boundary element, and not on a particular field point within that boundary element.

Let us consider ξ as ξ_1 and define a second dependent transformed coordinate, ξ_2 where $\xi_2 = -\xi_1$. For Gaussian quadrature, the interpolation functions φ_i can thus be defined as:

$$\varphi_i = \frac{1}{2}(1 + \xi_i) \tag{3.25}$$

Numerical integration over a line element can be performed in terms of the coordinates ξ_i, defined previously. The integral I,is determined as follows:

$$\begin{aligned} I &= \int_{(x_1^1, x_2^1)}^{(x_1^2, x_2^2)} \mathcal{G}(x) dS(x) \\ &= \int_{-1}^{+1} \mathcal{G}(\xi) \parallel \mathbf{J} \parallel d\xi \\ &\cong \mathcal{G}_i(\xi) w_i \parallel \mathbf{J} \parallel d\xi \qquad \text{where,} \quad i = 1, N \end{aligned} \tag{3.26}$$

The subscript i in equation 3.26 refers to the index of the Gaussian quadrature, and N is its order. That is, the function is evaluated at each of the i quadrature points and multiplied by the corresponding weighting factor w_i and the sum of these N products is the value of the integral over the boundary element. In this case, where the functional variation is assumed to be linear over the domains, a cubic quadrature $N = 4$ is of sufficient accuracy. Table 3.2 shows the quadrature points and weight factors for a fourth order integration over a line element.

i	ξ_1^i	w_i
1	-0.861136311594053	0.347854845137454
2	-0.339981043584856	0.652145154862546
3	0.339981043584856	0.652145154862546
4	0.861136311594053	0.347854845137454

Table 3.2: Parameters for 4th order Gaussian quadrature over a line element

Thus, any function defined over the flow field domains can be numerically treated using the above procedures.

3.1.4 BEM code organization

The discretized equations developed in the previous sections were encoded in FORTRAN for resolving the field equations for a given set of boundary conditions. The

flowchart shown in figure 3.5 outlines the basic software structure.

Following usual guidelines, the grid should be constructed with additional fineness near corners, where more non-linear behaviour is expected in the various field variables. For each source point the coefficients $\Lambda_{\gamma l}$ were determined, then successively, the coefficients listed in equation 3.6 were obtained by quadrature over the boundary and domain elements.

A system based on pointer arrays was employed to logically connect boundary elements and domain elements, which could belong to several different elements, to the field or source point in question [92]. For a transient solution, the field variables are updated each time-level, and a set of values was stored for $t = t - \Delta t$, to provide a time derivative if needed.

A flow field with N nodes will produce a $2N \times 2N$ system of equations. The terms $Z_{\gamma iqp\alpha} u_{iq} u_{p\alpha}$ give the set of equations a non-linear character, and thus, a Newton-Rhapson routine is employed to perform the calculations.

In general, the Newton-Rhapson method will seek an N-member vector to simultaneously zero N related funtions [93]. That is,

$$f_i(x_1, x_2, \ldots, x_N) = 0 \qquad i = 1, 2, \ldots, N \tag{3.27}$$

If the components x_i are represented by the vector $\mathbf{X}$, then in the neighbourhood of $\mathbf{X}$, all the functions f_i can be expanded via a Taylor series to,

$$f_i(\mathbf{X} + \delta\mathbf{X}) = f_i(\mathbf{X}) + \sum_{j=1}^{N} \frac{df_i}{dx_j} \delta x_j + O\left(\delta \mathbf{X}^2\right) \tag{3.28}$$

Terms of order $\delta\mathbf{X}^2$ and higher are neglected, and a set of linear equations for the corrections $\delta\mathbf{X}$ which simultaneously direct all functions toward zero. The resulting matrix form is,

$$\sum_{j=1}^{N} \alpha_{ij} \delta x_j = \beta_i \tag{3.29}$$

Above,

$$\alpha_{ij} \equiv \frac{df_i}{dx_j} \qquad \beta_i \equiv -f_i$$

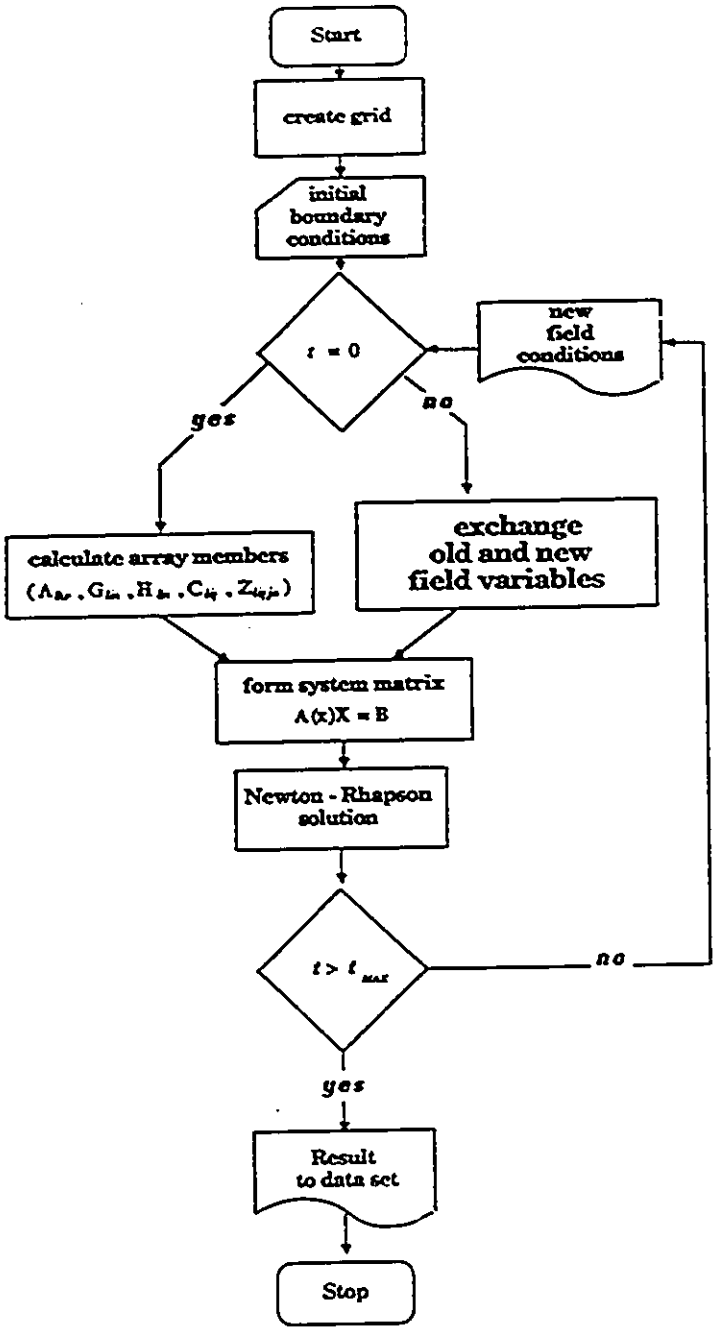

Figure 3.5: Flowchart for BEM code used to resolve 2D primitive-variable Navier-Stokes flow.

The matrix in equation 3.28 was solved by an LU (lower-upper triangular) decomposition routine. The corrections thus determined, are added to the solution vector to give,

$$x_i^{\text{NEW}} = x_i^{\text{OLD}} + \delta x_i \qquad i = 1, \ldots, N \tag{3.30}$$

This process is iterated until convergence is achieved. There are two convergence criteria, one of which is sufficient. The total error criterion is,

$$\sum_{i=1}^{N} f_i < f_{\text{TOL}} \tag{3.31}$$

The zero-correction criterion is,

$$\sum_{i=1}^{N} \delta x_i < x_{\text{TOL}} \tag{3.32}$$

In this work, f_{TOL} was set to 2.5×10^4 and x_{TOL} was set to 5.0×10^5.

The speed of convergence was dependent on how close the initial field provided approximated the final solution. For transient problems, the solution from the previous time level was used as the initial guess.

3.2 Finite-Volume Implementation

3.2.1 Solution Procedure

The solution procedure makes use of the finite volume method [38] which is iterative in approach, solving for the variables at nodes defined by a grid which is superimposed over the flow domain. The vector and scalar grid points are "staggered" for more efficient numerics. For illustration, we consider a cylindrical coordinate system.

3.2.1.1 Flow Domain Grid

The flow domain grid is defined by nodes placed on planes of constant z, r and θ. This configuration is depicted in figures 3.6 and 3.7, which show the control volume shapes and the location of the flow variables.

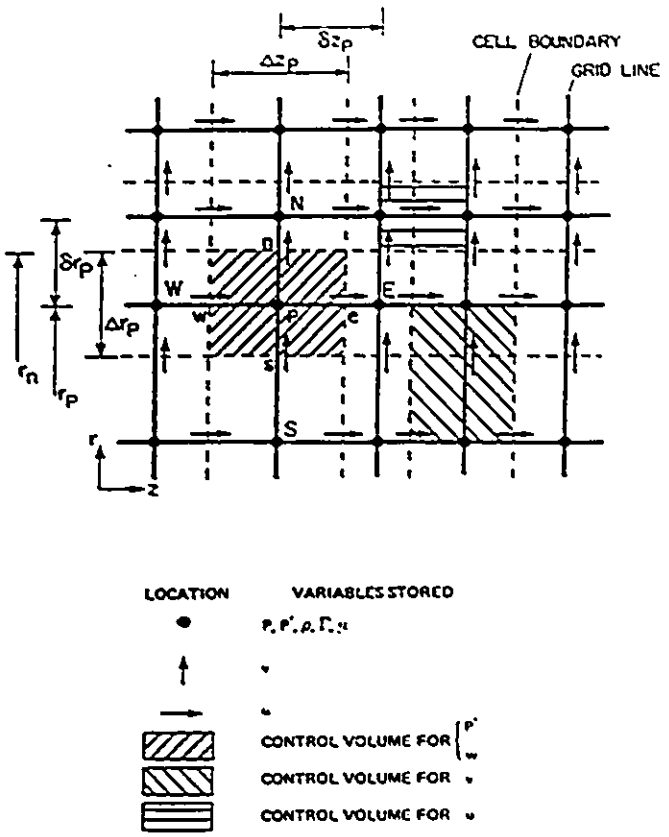

Figure 3.6: Finite volume grid in r-z plane with associated notation. From [40].

Figure 3.8 shows a three-dimensional control volume and accompanying notation. The grid point is located at the geometric center of each cell, with the corresponding grid lines passing through these points.

This grid format includes several advantages. Discontinuities in boundary conditions are handled by making the point of discontinuity part of the cell boundary. Further, the flow domain and grid boundaries can coincide, so that points along the grid boundary can lie outside the flow domain, to assist in ensuring proper conservation of mass and momentum.

Each variable in the problem can have its own grid and finite volume, which may be independent of the other variables. Variable values at cell boundaries are determined via interpolation of adjacent nodal values.

The notation used in this development is illustrated as well in figure 3.8. The node

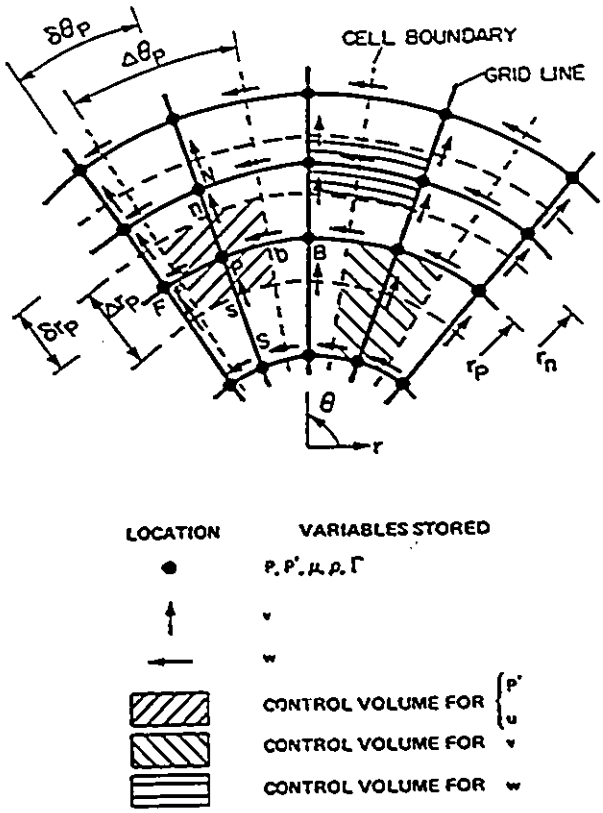

Figure 3.7: Finite volume grid in r-θ plane with associated notation. From [40].

denoted by P is surrounded by adjacent nodes given in upper case symbols, selected to indicate relatively, north, south, east, west, back and front directions. Lower case symbols refer to locations between grid points and at cell boundaries. The grid lines in the z, r and θ directions are respectively indicated by the integers i, j and k.

According to the method of Gosman and Ideriah [38], a staggered grid system is employed. Scalar quantities are determined at the grid point. Momentum quantities, namely velocities (with components u, v and w) are positioned between the grid points where the pressures which drive them are determined. They are displaced respectively in the positive z, r and θ directions. This makes calculation of convection through cell walls more accurate. The scalar control volumes (as shown in figures 3.6-3.8) are centered around the point P, while the vector control volumes are a combination of two half-scalar volumes as shown in figures 3.6 and 3.7, having boundaries normal to

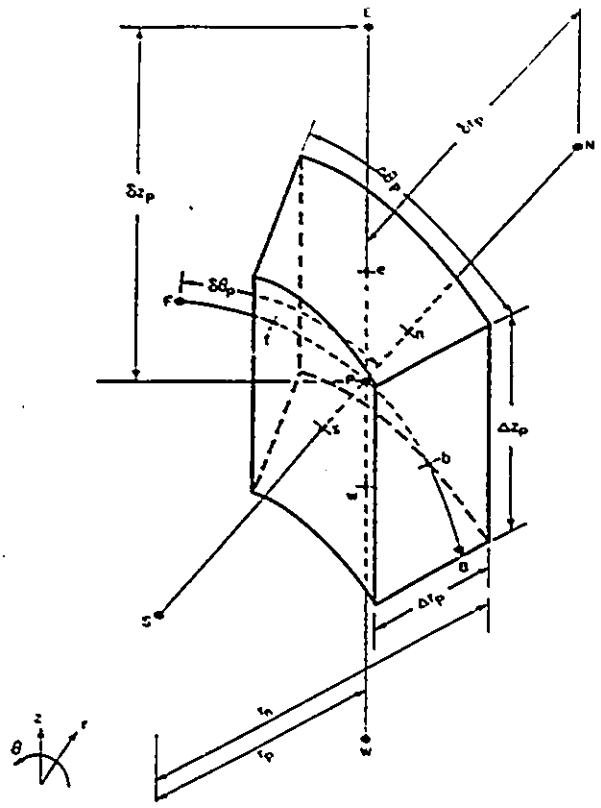

Figure 3.8: Control volume used for finite volume formulation. From [40].

the velocity directions passing through the pressure nodes.

For the z and r boundaries, the grid locations are designed to correspond with normal velocity components. In three dimensional situations, refer to Lai [40] for boundary conditions on θ-boundaries, where "cyclic" boundary conditions are imposed.

3.2.1.2 Grid Generation

The grids used for the solution of problems with the MD-PHASE code were generated with a software package known as ORTHO. ORTHO is an NRC in-house graphics-based package which permits a visual verification of the grid as it is being constructed, and then dumps the numerical data into a file formatted to be read by the MD-PHASE

code.

Features of ORTHO include the inclusion of special indices to denote walls, inlets or outlets at the boundary, and scaling coefficients to convert a generalized domain shape into real linear dimension of any required units.

3.2.2 Finite Volume Equations

3.2.2.1 Discretization Scheme

The differential equations which govern the physics of the flow are integrated over the volume of the flow domain. The entire domain is partitioned into cells delimited by the grid, and the unknown quantities are taken to be "constant" within each cell, with this mean value assigned to the node point.

The general transport equation (equation 2.34), can be written for the generalized variable, ϕ, over one cell volume, V_C, with a time step of δt. We can thus write,

$$\frac{d}{dt}\int_{V_C}(\rho\phi)\,dV + \oint_{A_C}(\rho u_i\phi - \Gamma_\phi\,\phi_{,i})\,n_i\,dA = \int_{V_C} S_\phi\,dV \qquad (3.33)$$

Above, $\vec{n}$ is the unit outward normal from the control surface, A_C. Let us consider the first term from equation 3.33. Recall that point P is the center of the volume cell. We write,

$$\frac{d}{dt}\int_{V_C}(\rho\phi)\,dV \simeq \frac{[(\rho\phi)_P^n V_P^n - (\rho\phi)_P^o V_P^o]}{\delta t}$$

The superscripts o and n in the above relation, refer to the old and new time steps respectively, bounded by the interval, δt. Above, we have the element of volume, V_P, which is defined as,

$$\begin{aligned} V_P &= \int_{z_w}^{z_e}\int_{r_s}^{r_n}\int_{\theta_b}^{\theta_f} r\,dr\,d\theta\,dz \\ &= \frac{1}{2}\left(r_n^2 - r_s^2\right)(\theta_f - \theta_b)(z_e - z_w) = (r\Delta r\Delta\theta\Delta z)_P \end{aligned}$$

In MD-PHASE, the numerical formulation is fully-implicit, whereby, all terms apart from the first one detailed above, use only terms from the "new" time step. Thus, the superscript n is discarded.

The second term from equation 3.33 is the convective term. It accounts for the convective and diffusive flux of ϕ across the cell boundaries. In terms of the finite difference grid scheme, it is expressed as,

$$\begin{aligned}\oint_{A_c} (\rho u_i \phi - \Gamma_\phi \phi_{,i})\, n_i\, dA &= \int_{r_s}^{r_n} \int_{\theta_b}^{\theta_f} \left[\left(\rho u \phi - \Gamma_\phi \frac{\partial \phi}{\partial z} \right) \right]_w^e r\, dr\, d\theta \\ &+ \int_{z_w}^{z_e} \int_{\theta_b}^{\theta_f} \left[\left(\rho v \phi - \Gamma_\phi \frac{\partial \phi}{\partial r} \right) \right]_s^n r\, d\theta\, dz \\ &+ \int_{z_w}^{z_e} \int_{r_s}^{r_n} \left[\left(\rho w \phi - \Gamma_\phi \frac{1}{r} \frac{\partial \phi}{\partial \theta} \right) \right]_b^f dr\, dz \end{aligned} \quad (3.34)$$

To concretely illustrate the discretization scheme, we consider the term in the axial or z-direction. We have,

$$\int_{r_s}^{r_n} \int_{\theta_b}^{\theta_f} \left[\left(\rho u \phi - \Gamma_\phi \frac{\partial \phi}{\partial z} \right) \right]_w^e r\, dr\, d\theta = Q_Z \simeq m_e \left(\phi - \frac{\delta z}{\mathrm{Pe}} \frac{\partial \phi}{\partial z} \right)_e - m_w \left(\phi - \frac{\delta z}{\mathrm{Pe}} \frac{\partial \phi}{\partial z} \right)_w \quad (3.35)$$

Above, the terms m_e and m_w are mass flow rates, given by,

$$m_e = (\rho u)_e (r \Delta r \Delta \theta)_P$$

Nodal velocities are used as the area-average normal velocities at the cell boundaries. A linear variation in velocities from cell to cell is assumed for calculating the cell-boundary densities and exchange coefficients. These are shown below concretely as,

$$\begin{aligned} \rho_e &= f_e \rho_E + (1 - f_e) \rho_P \\ \Gamma_e &= f_e \Gamma_E + (1 - f_e) \Gamma_P \end{aligned}$$

Here, f_e is a spatial weighting factor, relating the cell spacing to the grid spacing. It is defined as,

$$f_e = 0.5 \frac{\Delta z_p}{\delta z_p}$$

Also above was the cell-boundary Peclet number, Pe, defined as,

$$\mathrm{Pe}_e = \left[\frac{(\rho u)\, \delta z}{\Gamma} \right]_e$$

The above definition for Peclet number is inserted into the appropriate terms in equation 3.35 to produce the following approximation,

$$\left(\phi - \frac{\delta z}{\mathrm{Pe}}\frac{\partial \phi}{\partial z}\right)_e = (1-\gamma_e)\phi_E + \gamma_e \phi_P$$

The weighting factor γ_e is defined as,

$$\gamma_e = \left[(1-f) + \frac{\max[-(1-f)\mathrm{Pe}, f\mathrm{Pe}, 1]}{\mathrm{Pe}}\right]_e \tag{3.36}$$

To enhance numerical stability, an "unwind difference" scheme for high Peclet numbers, and a "central difference" scheme for low Peclet numbers, as proposed by Spalding [94] is employed. Briefly, these schemes give a correct limiting behaviour as the Peclet number becomes large or small. Thus, equation 3.35 becomes,

$$Q_Z = m_e\left[(1-\gamma_e)\phi_E + \gamma_e\phi_P\right] - m_w\left[(1-\gamma_w)\phi_P + \gamma_w\phi_W\right] \tag{3.37}$$

Similarly, the second and third terms of equation 3.34 are expressed in an analogous fashion as equation 3.37.

We now introduce our formulation of what are known as source terms in the equations used in MD-PHASE. These terms arise from the last term in equation 3.33, and are written as,

$$\int_{V_C} S_\phi \, dV = \int_{z_w}^{z_e}\int_{r_s}^{r_n}\int_{\theta_b}^{\theta_f} S_\phi \, r \, dr \, d\theta \, dz = S_U^\phi - S_P^\phi \phi_P \tag{3.38}$$

Here, S_ϕ is modeled to vary linearly throughout the the flow domain, and is assumed to be constant within each control volume. The positive definite nature of S_U^ϕ and S_P^ϕ helps to ensure the numerical stability of the procedure [40].

Following the method of Watkins [84], the finite volume mass conservation equation is coupled with the general transport equation (equation 3.33) to yield the discretized version of the general transport equation. We have,

$$\begin{aligned}(\rho V)_P^\circ \frac{(\phi_P - \phi_P^\circ)}{\delta t} &+ m_e\left[(1-\gamma_e)(\phi_E - \phi_P)\right] + m_w\left[\gamma_w(\phi_P - \phi_W)\right] \\ &+ m_n\left[(1-\gamma_n)(\phi_N - \phi_P)\right] + m_s\left[\gamma_s(\phi_P - \phi_S)\right] \\ &+ m_f\left[(1-\gamma_f)(\phi_F - \phi_P)\right] + m_b\left[\gamma_b(\phi_P - \phi_B)\right] + S_P^\phi\phi_P - S_U^\phi = 0\end{aligned} \tag{3.39}$$

We now re-express equation 3.39 in its final condensed form,

$$A_P\phi_P = \sum_c A_c\phi_c + A_P^o\phi_P^o + S_U^\phi \tag{3.40}$$

Above, $\sum_c$ denotes summation over the surrounding nodes which are identified as north, south, east, west, back and front (N, S, E, W, B, F). All A coefficients are non-negative and are explicitly given below.

$$\begin{aligned} A_P &= \textstyle\sum_c A_c + A_P^o + S_P^\phi & A_P^o &= \frac{(\rho V)_P^o}{\delta t} \\ A_E &= m_e(\gamma_e - 1) & A_W &= (m\gamma)_w \\ A_N &= m_n(\gamma_n - 1) & A_S &= (m\gamma)_s \\ A_F &= m_f(\gamma_f - 1) & A_B &= (m\gamma)_b \end{aligned} \tag{3.41}$$

These coefficients produce a diagonally dominant matrix.

3.2.2.2 Finite Volume Momentum Equations

Since the nodes for velocity values are staggered with respect to the nodes for scalar quantities, the finite volume velocity equation will be a similar but modified form of equation 3.40. The control volumes are set up slightly differently (illustrated in figures 3.6 and 3.7), and the definitions of the mass flow rates and associated Reynolds numbers will be modified accordingly.

For example, consider the momentum equation in the z-direction. Figure 3.9 shows the control volume for this case. Mean values are taken for scalar coefficients. We have,

$$m_e = (r\Delta r\Delta\theta)_P(\rho u)_e$$

In this case,

$$(\rho u)_e = \tfrac{1}{2}\left(\left[f_e\rho_E + (1-f_e)\rho_P\right]u_P + \left[f_{ee}\rho_{EE} + (1-f_{ee})\rho_E\right]u_E\right)$$

$$f_e = 0.5\frac{\Delta z_P}{\delta z_P} \qquad \text{and,} \qquad f_{ee} = 0.5\frac{\Delta z_E}{\delta z_E}$$

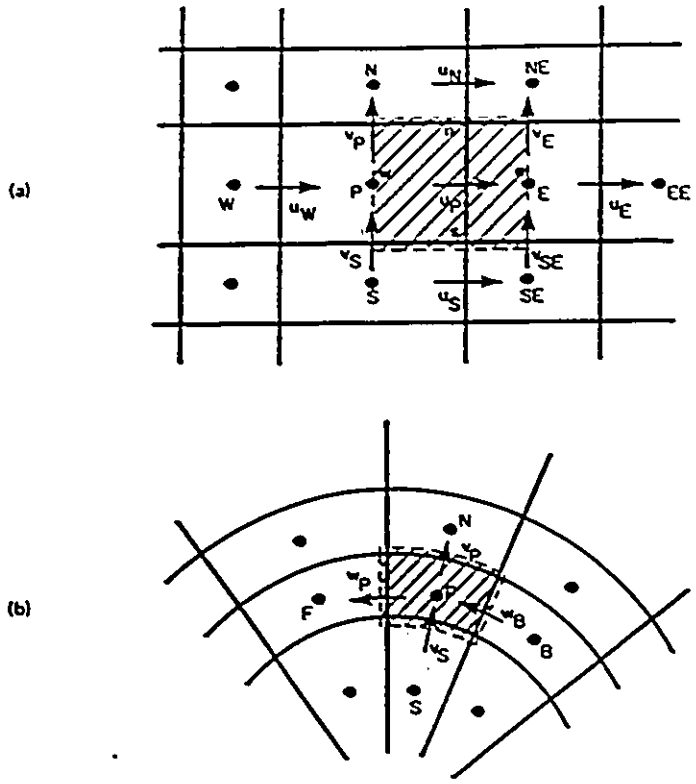

(a) θ = CONSTANT PLANE; (b) z = CONSTANT PLANE

Figure 3.9: Control volume and notation for axial momentum equations. From [40].

Similarly, for the cell-boundary Peclet number,

$$\mathrm{Pe}_e = \frac{(\rho u)_e \Delta z_E}{\mu_{eff,E}} \qquad \text{where, } \mu_{eff} = \mu + \mu_t$$

Similarly, discretized expressions are developed for the r and θ-directions [40].

Finally, from the equations 3.41 we have,

$$A_P^o = \frac{0.5}{\delta t}\left[(\rho V)_E^o + (\rho V)_P^o\right]$$

Parallel derivations are used for momentum equations for the other directions.

3.2.2.3 Discretization of Source Terms

The application of equation 3.38 to the source terms which are listed in table 2.5 is now performed to determine discretized source terms.

Axial Momentum Equation

Integration over the control volume shown in figure 3.9 yields,

$$S_P = 0 \tag{3.42}$$

$$S_U = -\int_{V_c} \frac{\partial P_{\text{eff}}}{\partial z}\, dV + \int_{A_c} \left[\mu_{\text{eff}} \frac{\partial v_i}{\partial z}\right] n_i\, dA \tag{3.43}$$

The first term of equation 3.43 is discretized as follows,

$$-\int_{V_c} \frac{\partial P_{\text{eff}}}{\partial z}\, dV = \left(\left[P + \frac{2}{3}(\mu_t u_{i,i} + \rho k)\right]_P - \left[P + \frac{2}{3}(\mu_t u_{i,i} + \rho k)\right]_E\right)(r\Delta r\Delta\theta)_P$$

The terms arising from the second integral in equation 3.43 are given by,

$$\begin{aligned}
\int_{A_c} \left[\mu_{\text{eff}} \frac{\partial u_i}{\partial z}\right] n_i\, dA &= \left[\left(\mu_{\text{eff}} \frac{\partial u}{\partial z}\right)_e - \left(\mu_{\text{eff}} \frac{\partial u}{\partial z}\right)_w\right](r\Delta r\Delta\theta)_P \\
&+ \left[\left(r\mu_{\text{eff}} \frac{\partial v}{\partial z}\right)_n - \left(r\mu_{\text{eff}} \frac{\partial v}{\partial z}\right)_s\right](\Delta\theta\delta z)_P \\
&+ \left[\left(\mu_{\text{eff}} \frac{\partial w}{\partial z}\right)_f - \left(\mu_{\text{eff}} \frac{\partial w}{\partial z}\right)_b\right](\Delta r\delta z)_P
\end{aligned}$$

Above, the first-order differentials are evaluated via a central-difference approximation. The partial derivative terms are written as,

$$\begin{aligned}
\left(\mu_{\text{eff}} \frac{\partial u}{\partial z}\right)_e &= \mu_{\text{eff},E} \frac{(u_E - u_P)}{\Delta z_E} \\
\left(\mu_{\text{eff}} \frac{\partial v}{\partial z}\right)_n &= (r\mu_{\text{eff}})_n \frac{(v_E - v_P)}{\delta z_P} \\
\left(\mu_{\text{eff}} \frac{\partial w}{\partial z}\right)_f &= \mu_{\text{eff},f} \frac{(w_E - w_P)}{\delta z_P}
\end{aligned}$$

The divergence term is written as,

$$u_{i,i\,P} = \frac{(u_P - u_W)}{\Delta z_P} + \frac{(r_n v_P - r_s v_S)}{(r\Delta r)_P} + \frac{(w_P - w_B)}{(r\Delta\theta)_P}$$

The expression for $\mu_{\text{eff},n}$ is given explicitly below.

$$\mu_{\text{eff},n} = [\mu_{\text{eff},P}(1 - f_n) + \mu_{\text{eff},N} f_n]\, f_e + [\mu_{\text{eff},E}(1 - f_n) + \mu_{\text{eff},NE} f_n](1 - f_e)$$

Radial Momentum Equation

Introducing a weighting factor f_v [38], we integrate over the cell volume depicted in figure 3.10 to produce the following source terms. Typically, the coefficient f_v lies in the range $0.3 \leq f_v \leq 0.7$.

$$\begin{aligned} S_P &= \int_{V_c} \left[\frac{2\mu_{eff}}{r^2} + \frac{f_v(\rho w^2)}{rw} \right] dV \\ &= \left(\frac{2\mu_{eff}}{r} + f_v \rho w \right)_{V_c} (\delta r \Delta\theta \Delta z)_P \end{aligned} \tag{3.44}$$

Above,

$$r_{V_c} = \frac{1}{2}(r_N + r_P)$$

The other quantities μ_{eff}, ρ, and w to be evaluated over V_c are given explicitly by Lai [40].

The second source term S_U is evaluated as follows,

$$\begin{aligned} S_U &= -\int_{V_c} \left[\frac{\partial P_{eff}}{\partial r} + \frac{3\mu_{eff}}{r^2}\frac{\partial w}{\partial \theta} + \frac{w}{r^2}\frac{\partial \mu_{eff}}{\partial \theta} \right] dV \\ &+ \int_{V_c} \left[1 + \frac{f_v v}{w} \right] \frac{\rho w^2}{r}\, dV + \int_{A_c} \left[\mu_{eff} \frac{\partial u_i}{\partial r} \right] n_i\, dA \end{aligned} \tag{3.45}$$

The first term of equation 3.45 is expanded into discretized form as,

$$\begin{aligned} -\int_{V_c} \left[\frac{\partial P_{eff}}{\partial r} + \frac{3\mu_{eff}}{r^2}\frac{\partial w}{\partial \theta} + \frac{w}{r^2}\frac{\partial \mu_{eff}}{\partial \theta} \right] dV &= (P_{eff,P} - P_{eff,N})(\Delta\theta\Delta z)_P r_{V_c} \\ +3\left(\frac{\mu_{eff}}{r}\right)_{V_c} &[(w_B - w_P) f_n + (w_{NB} - w_N)(1 - f_n)](\delta r \Delta z)_P \\ +\left(\frac{w}{r}\right)_{V_c} (\delta r \Delta z)_P \{ f_n [&[f_b \mu_{eff,P} + (1 - f_b)\mu_{eff,B}] - [f_f \mu_{eff,F} + (1 - f_f)\mu_{eff,P}]] \\ +(1 - f_n)[&[f_b \mu_{eff,N} + (1 - f_b)\mu_{eff,NB}] - [f_f \mu_{eff,NF} + (1 - f_f)\mu_{eff,N}]] \} \end{aligned}$$

The second term of equation 3.45 is discretized as,

$$\int_{V_c} \left[1 + \frac{f_v v}{w} \right] \frac{\rho w^2}{r}\, dV = \left[\left(1 + \frac{f_v v}{w} \right) \rho w^2 \right]_{V_c} (\delta r \Delta\theta \Delta z)_P$$

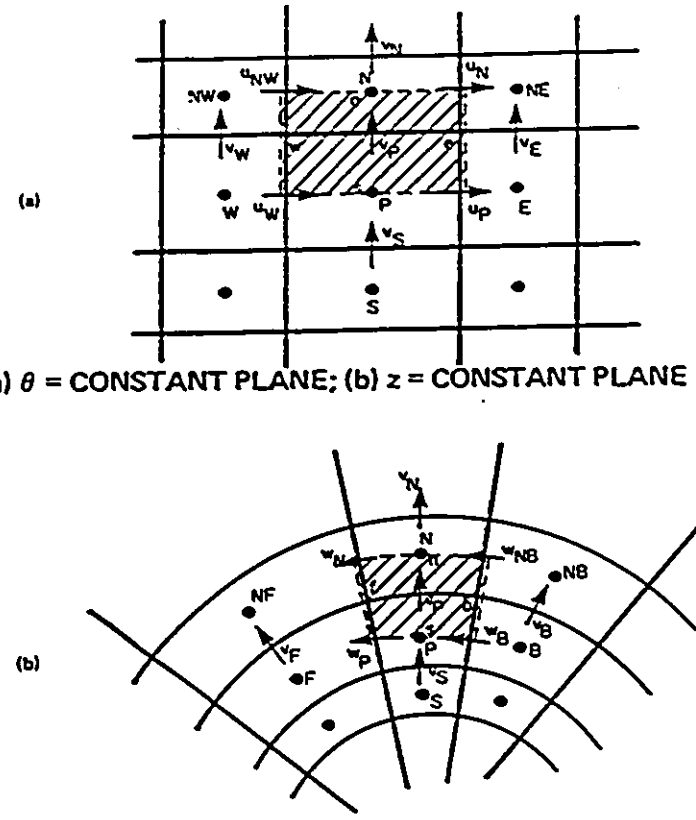

(a) θ = CONSTANT PLANE; (b) z = CONSTANT PLANE

Figure 3.10: Control volume and notation for radial momentum equations. From [40].

The last term of equation 3.45 is discretized as,

$$\begin{aligned}\int_{A_c}\left[\mu_{eff}\frac{\partial u_i}{\partial r}\right]n_i\,dA &= \left[\left(\mu_{eff}\frac{\partial u}{\partial r}\right)_e-\left(\mu_{eff}\frac{\partial u}{\partial r}\right)_w\right]r_{V_c}(\delta r\Delta\theta)_P\\ &+\left[\left(r\mu_{eff}\frac{\partial v}{\partial r}\right)_n-\left(r\mu_{eff}\frac{\partial v}{\partial r}\right)_s\right](\Delta\theta\Delta z)_P\\ &+\left[\left(\mu_{eff}\frac{\partial w}{\partial r}\right)_f-\left(\mu_{eff}\frac{\partial w}{\partial r}\right)_b\right](\Delta r\Delta z)_P\end{aligned}$$

Angular Momentum Equation

Only a two dimensional simulation was employed in this project. Details on implementing the angular momentum equation are given by Lai [40].

Turbulence Kinetic Energy Equation

The source term for the turbulence kinetic energy equation which includes the variable G from table 2.5 is integrated as shown below.

$$\int_{V_c} (G - \rho\epsilon) = (G - \rho\epsilon)_P V_P$$

Substituting for ϵ_P according to equation 2.29 enhances numerical stability and gives,

$$S_P = \left[\frac{C_\mu \rho^2 k V}{\mu_t}\right]_P \tag{3.46}$$

$$S_U = (GV)_P \tag{3.47}$$

The first-order differential terms which are contained in G are evaluated with a central-difference approximation.

Turbulence Dissipation Rate Equation

By the same method employed with the turbulence kinetic energy equation, the discretized source terms for the dissipation rate equation are determined. We have,

$$S_P = C_2 \left[\frac{\rho\epsilon V}{k}\right]_P \tag{3.48}$$

$$S_U = \left[\frac{C_1 G}{k} + C_3 \rho u_{i,i}\right]_P \left(\frac{C_\mu \rho k^2 V}{\mu_t}\right)_P \tag{3.49}$$

3.2.2.4 Continuity Equation and Mass Balance

To ensure mass conservation, a special procedure is adopted for calculating the pressure field. A "pressure correction" scheme is employed, and imparts an iterative character to the solution.

A procedure devised by Patankar and Spalding [95] was adopted for the pressure correction P', which combines the local finite volume continuity and momentum equations. The pressure field cannot be explicitly calculated, so it is determined by an iterative calculation. The momentum equations are solved for an assumed pressure field, correspondingly, the velocities u_i, will satisfy this pressure field, but may

not permit a correct mass balance. For the considerations at hand, the pressure field associated with the velocity field will be denoted by the superscript $*$.

Simultaneously, adjustments are made to both the velocity and pressure fields to eliminate the mass imbalance. The local pressure correction, P', is defined as,

$$P = P^* + P' \tag{3.50}$$

The velocity corrections are made to depend upon the pressure corrections. For example,

$$u_e = u_e^* + u_e' = D_e(P_P' - P_E') \tag{3.51}$$

Above, D_e comes from the u-momentum equation and its associated source terms (equations 3.40 and 3.43) to give,

$$D_e = \frac{\partial u_P}{\partial (P_P - P_E)} \simeq \frac{a_e}{A_P^u}$$

Here, $a_e = (r\Delta r\Delta\theta)_P$ is the area of the east cell boundary of the scalar finite volume cell. A_P^u is the A_P term associated with the velocity equation. Substituting the modified pressure and velocity terms into equation 3.40 yields,

$$A_P P_P' = \sum_c A_c P_c' + S_U^{P'} \tag{3.52}$$

The summation over the neighbours c is as previously described. In this case, the term $S_U^{P'}$ is given by,

$$S_U^{P'} = m_w^* - m_e^* + m_s^* - m_n^* + m_b^* - m_f^*$$

Further, we have, $A_E = (\rho a)_e D_e$, and so on, for each neighbouring location.

The cell boundary values for ρ and the m^* terms are determined by the interpolation rules given in section 3.2.2.1.

3.2.3 Discretization of Boundary Conditions

The boundary conditions which identify each particular problem are put into the numerical calculations by modifying the flux terms for the cell faces next to the boundary. Typically, this means that the flux expressions for such boundaries are set to zero. (ie. $A_N = 0$ for cells adjacent to a north boundary etc.)

3.2.3.1 Boundary Source Terms

The "sources", S_B, due to a neighbouring boundary follow the principle of equation 3.38 as,

$$S_B = -S'_P \phi_P + S'_U \tag{3.53}$$

S'_P and S'_U are determined according to the prescribed conditions at the boundary, and are given more concretely in the following subsubsection.

3.2.3.2 Wall Source Terms

Velocities $\vec{u}$

Our interest for this work focuses primarily on tangential velocities at walls. Typically normal velocities are set to zero, and if needed, normal stresses may be determined by the conventional flux expression and the boundary velocities.

The source term S_N, due to a wall shear stress τ_W arising from a tangential flow next to a "north" wall is,

$$S_N = \tau_W a_W = \mu_W a_W \frac{(U_W - U_P)}{Y_P} \tag{3.54}$$

In relation to equation 3.53, the term S_N above, is the term S_B for a "north" case. The subscript W refers to values of the variable on the wall. U_W and U_P are the *resultants* of the velocity components u and w for a three dimensional problem, and default to the component u for a two dimensional case. Y_P is the normal distance from the cell center to the wall and a_W is the wall area of the north face of the cell. The coefficient μ_W is obtained via equations 2.41 and 2.43 as shown below.

$$\mu_W = \begin{cases} \mu & \text{for } Y_P^+ \leq 11.63 \\ \dfrac{\kappa Y_P^+ \mu}{\ln(E Y_P^+)} & \text{for } Y_P^+ > 11.63 \end{cases} \tag{3.55}$$

Above, we use the relation,

$$Y_P^+ = \frac{C_\mu^{0.25}}{\mu} \left(\rho k^{0.5} Y\right)_P$$

The velocity components may be used in place of the resultants to give directional shear stress components, as shown in [40].

Further, the normal stress at a wall may be calculated from the standard flux expression and the prescribed boundary velocities.

Turbulence Energy

The steep gradients near a wall for the turbulence kinetic energy k, require modification of the source terms in the transport equation. k drops to zero at solid walls. Briefly, the generation rate G_P, as given in equation 3.47, can be expressed in terms of the shear stress at the wall.

Dissipation Rate

Unlike the turbulence energy, the dissipation rate ϵ, reaches its highest value at the wall. Consequently, an equilibrium value for ϵ_P is used, to avoid any ambiguities that might arise for the term A_N. The relation used is,

$$\epsilon_P = \frac{C_\mu^{0.75} k_P^{1.5}}{\kappa Y_P}$$

For numerical control of ϵ, the terms S_U' and S_P' from equation 3.53 are given large values via an inflated coefficient (on the order of 10^{30}). When the Reynolds number is high, ϵ_P may be expressed in the inertial sublayer by equation 2.35, which contains the dissipation length, ℓ. The above expression implies that $\ell = \kappa Y$ in the wall region.

Pressure Correction

At boundaries where the normal velocity is prescribed, equation 3.52 must be modified to account for this condition. For example, cells adjacent to the north wall have A_N set to zero, implying the prescription of a zero normal gradient condition for P'.

3.2.3.3 Axes of Symmetry Source Terms

For cells adjacent to an axis of symmetry, the condition of zero normal gradient is imposed. For example, for such a case along the south boundary, the term A_S is set to zero as well as the boundary source S_B as shown in equation 3.53. This applies to all dependent variables except the normal velocity itself, in which case the term S_B and the boundary velocity are set to zero.

3.2.3.4 Inlet Planes

The profiles of all dependent variables must be prescribed over all inlet planes. One special condition is that for cells adjacent, say, for example, to a west boundary, the term A_W in the pressure correction equation (equation 3.40) is set to zero, thereby implying that $\partial P'/\partial z = 0$, so that velocities at these locations are held constant.

3.2.3.5 Outlet Planes

The mass flow rates across outlet planes are fixed by the overall mass balance, as controlled by the continuity equation. As a consequence of the upwind differencing technique used to solve the equations, the exit values of variables do not enter into the calculations, and may be simply equated to values at the adjacent upwind node.

3.2.4 Numerical Algorithm for Solution

Beginning with the initial values for all the field variables, the governing equations are solved in sequence until the convergence criteria are satisfied. These are referred to as the outer iterations.

Each linear equation, which is formulated over the domain for each variable, is solved by an inner iteration, an efficient scheme for treating a large matrix.

3.2.4.1 Finite Volume Equation Solution Scheme

The matrix which is assembled for each variable's equation set is solved by a block iteration technique. This procedure sweeps across planes defined by a coordinate index. A tri-diagonal matrix form is assembled locally as in the Gauss-Seidel method. This matrix can be solved implicitly. Details are given by Lai [40]. The plane is solved, grid line by grid line, and is repeated in alternating directions towards convergence. Since this is the inner iteration, full convergence is not required, since related variables are being simultaneously modified. The outer iterations ensure full final convergence, so usually no more than 3 inner sweeps are performed for each variable.

The Tri-diagonal matrix algorithm

For the purposes of solving a set of linear equations, equation 3.40 is written as follows,

$$\begin{aligned} A_P\phi_{[i,j,k]} = {} & A_N\phi_{[i,j+1,k]} + A_S\phi_{[i,j-1,k]} + A_E\phi_{[i+1,j,k]} \\ & + A_W\phi_{[i-1,j,k]} + A_F\phi_{[i,j,k+1]} + A_B\phi_{[i,j,k-1]} \\ & + A_P^\circ\phi_{[i,j,k]}^\circ + S_U^\phi \end{aligned} \tag{3.56}$$

Above, the subscripts written as $[i, j, k]$, represent the node on the flow domain grid. One equation in the format of equation 3.56 can be written for each grid point where the variable ϕ will be determined.

For example, let us consider a plane of constant k. For the purposes of iterating, the values of ϕ on neighbouring planes are held constant to their most recent calculated values. Similarly, if we want to solve $\phi_{[I,j,K]}$, where the upper-case subscripts indicate values of ϕ being held constant, equation 3.56 becomes,

$$\phi_{[I,j,K]} = A_{[I,j,K]}\phi_{[I,j+1,K]} + B_{[I,j,K]}\phi_{[I,j-1,K]} + C_{[I,j,K]} \tag{3.57}$$

where,

$$A_{[I,j,K]} = \frac{A_N}{A_P} \qquad \text{and,} \qquad B_{[I,j,K]} = \frac{A_S}{A_P}$$

$$C_{[I,j,K]} = \frac{1}{A_P}\left(A_E\phi_{[i+1,j,k]} + A_W\phi_{[i-1,j,k]} + A_F\phi_{[i,j,k+1]} + A_B\phi_{[i,j,k-1]} + A_P^o\phi_{[i,j,k]}^o + S_U^\phi\right)$$

Now, if the values of ϕ are specified at the boundaries $j = 1$ and $j = M$, we then have,

$$A_{[I,1,K]} = B_{[I,1,K]} = 0 \qquad \text{and,} \quad C_{[I,1,K]} = \phi_{[I,1,K]}$$

Hence, in this case, equation 3.57 represents $M - 2$ equations with a tri-diagonal coefficient matrix. This equation set is solved via the Thomas algorithm [96], an adaptation of the Gaussian elimination procedure.

If $\phi_{[I,j,K]}$ is expressed in terms of $\phi_{[I,j+1,K]}$, we have

$$\phi_{[I,j,K]} = A'_{[I,j,K]}\phi_{[I,j+1,K]} + C'_{[I,j,K]} \tag{3.58}$$

The $(j-1)$st case may be substituted into equation 3.57 to give,

$$\phi_{[I,j,K]} = A_{[I,j,K]}\phi_{[I,j+1,K]} + B_{[I,j,K]}A'_{[I,j-1,K]}\phi_{[I,j,K]} + B_{[I,j,K]}C'_{[I,j-1,K]} + C_{[I,j,K]}$$

After algebraic manipulation we have,

$$\phi_{[I,j,K]} = \frac{A_{[I,j,K]}}{1 - B_{[I,j,K]}A'_{[I,j-1,K]}}\phi_{[I,j+1,K]} + \frac{B_{[I,j,K]}C'_{[I,j-1,K]} + C_{[I,j,K]}}{1 - B_{[I,j,K]}A'_{[I,j-1,K]}} \tag{3.59}$$

Combining the coefficients from equation 3.58 and the result from equation 3.59, we obtain the following recurrence relations,

$$A'_{[I,j,K]} = \frac{A_{[I,j,K]}}{1 - B_{[I,j,K]}A'_{[I,j-1,K]}} \qquad \text{and,} \quad C'_{[I,j,K]} = \frac{B_{[I,j,K]}C'_{[I,j-1,K]} + C_{[I,j,K]}}{1 - B_{[I,j,K]}A'_{[I,j-1,K]}}$$

The values for $A_{[I,1,K]}$, $B_{[I,1,K]}$, and $C_{[I,1,K]}$ given above are then used to start the recurrence process with,

$$A'_{[I,1,K]} = 0 \qquad \text{and,} \quad C'_{[I,1,K]} = \phi_{[I,1,K]} \tag{3.60}$$

The recurrence proceeds from $j = 2$ to $j = M - 1$.

When the coefficients $A'_{[I,j,K]}$ and $C'_{[I,j,K]}$ are known for the jth grid line, the values of $\phi_{[I,j,K]}$ can be determined by equation 3.58.

This process is carried out sequentially for each value of i, starting with a line adjacent to a boundary (say $i = 2$), and marching across to the opposite side ($i = N - 1$).

Similarly, the values of ϕ may be assumed constant on adjacent j lines and the sweeps made over the grid lines of constant j to solve for values of $\phi_{[i,J,K]}$. It is often an effective method to alternate the directions and coordinates of the sweeps to achieve a more rapid convergence.

3.2.4.2 Equation Solution Sequence

As seen, the governing finite difference equations are coupled and non-linear, thereby requiring an iterative method of solution. In each outer iteration, the equations are individually solved with inner iterations in a sequential fashion, adjusting each variable by its own equation, while holding the others constant. The steps comprising the numerical algorithm are itemized below.

1. The fields of all variables are initialized, either by guess or calculation.

2. The discretized coefficients of the momentum equations are assembled. The updated values of u_i are obtained by the block iteration procedure, making use of the current values of pressure. Several sweeps of the grid may be made, but without updating the coefficients.

3. The discretized coefficients of the modified pressure equation are assembled and treated by the block iteration method.

4. Corrections are made to the pressure and velocity fields by means of equations 3.50 and 3.51. Velocity adjustments, for flows normal to outlets are adjusted to satisfy an overall mass flow balance.

5. The discretized coefficients of the non-hydrodynamic equations are assembled (for one equation at a time), and the respective ϕ's are solved for by the block iteration technique.

6. The field of turbulent viscosities is updated.

7. The newly-calculated fields of variables are further updated by steps 2 through 6 until a satisfactory convergence has been achieved.

3.2.4.3 Convergence, Accuracy and Efficiency

Convergence and Stability

Convergence Criteria

The residual sources of each finite volume equation for each variable are compared to a reference tolerance to assess the convergence of each equation. This reference tolerance $R_{\phi,\mathrm{REF}}$, is selected as the inlet flux of the dependent variable, ϕ. This convergence criterion indicates how well the current values of ϕ solve the equation in question, rather than how much the values of ϕ have changed over successive iterations.

Referring to equation 3.40, which is the generalized finite volume equation, the local residual for the ϕ-equation for the ith iteration is defined as,

$$R_\phi = \sum_c A_c \phi_c + A_P^\circ \phi_P^\circ + S_U^\phi - A_P \phi_P \tag{3.61}$$

It can be seen that when the solution is obtained, R_ϕ goes to zero. Convergence is considered satisfactory if the sum of the normalized absolute residuals has fallen below a specified value, λ, usually $\sim 10^{-3}$. That is, for each equation ϕ,

$$\sum_i \sum_j \sum_k \left| R_{\phi,[i,j,k]} \right| < \lambda R_{\phi,\mathrm{REF}} \tag{3.62}$$

For a one-phase system, this iterative procedure should directly seek convergence without any oscillations in the table of residual values. Oscillation of residuals tends to indicate programming errors, typically with the specification of the boundary conditions. If values of ϕ at interior monitoring points remain steady, but the residuals oscillate, this is a stronger indication of incorrect boundary conditions [40].

A spurious source term introduced into an equation will tend to make an equation converge to a non-zero value. Often, this term may arise from an error in boundary

condition specification.

Under-Relaxation

The equations to be solved are strongly non-linear in character. To obtain a numerical solution, under-relaxation in employed to keep step-wise changes under control and thereby enhance convergence and at the same time, prevent divergence. The scheme employed in MD-PHASE is described below. The variables, ϕ are partitioned via a weighting factor f.

$$\phi_P = f\phi_P^i + (1-f)\phi_P^{i-1} \tag{3.63}$$

The superscript i denotes the ith iteration and f is the under-relaxation factor, in the range $0 \leq f \leq 1$. Substituting equation 3.63 into equation 3.40, we have,

$$\frac{A_P}{f}\left[\phi_P - (1-f)\phi_P^{i-1}\right] = \sum_c A_c\phi_c + A_P^o\phi_P^o + S_U^\phi \tag{3.64}$$

This gives modified coefficients for A_P and S_U^ϕ as,

$$A_P \longrightarrow \frac{A_P}{f} \qquad \text{and,} \quad S_U^\phi \longrightarrow S_U^\phi + A_P\phi_P^{i-1}\frac{(1-f)}{f}$$

There are no general rules for selecting the optimum value of f. Practical computational testing provides a suitable working value for f.

Treatment of Mass-Flow Imbalance

If all mass flow exits from a single control volume, then the finite difference equations become singular and a "false" source is introduced to stabilize the equations. The mathematical details of this procedure are given by Lai [40].

Numerical Stability

The more complex the flow, the more likely the opportunity to introduce numerical instabilities into the solution. However, the same applies to simple flows, and three main reasons may be cited to account for this.

1. If the initial field specification is too far removed from the nature of the solution, the algorithm may go astray. Improved initial field guesses or modifying the under-relaxation factors may alleviate this problem.

2. Inappropriate under-relaxation factors may be sufficient to produce unstable results. Testing the solution by varying these values may restore stability.

3. If the number of inner iteration sweeps is insufficient, the solution of the finite volume equations will be inherently incomplete. The pressure correction equation is most sensitive to this aspect, as it is calculated from zero each iteration, and has a bearing on the results for the other variables.

Accuracy

There are several factors which contribute to the accuracy of the calculated solution. The residual source tolerance can be reduced to increase accuracy. The velocities that are calculated are done so to satisfy the momentum equations, as well as the continuity equation, which integrates the flux over the domain by specifying velocities to conserve the mass flow balance. If the grid is too coarse, then the result may appear approximate compared to some expected result. The fineness of the grid can be increased until the resolution in the velocities is satisfactory.

In view of the above considerations on the integration of the flux, boundary inlet profiles (if they must be tied to a given flux) must be specified by an integral to produce appropriate conditions for a good result.

At high Peclet or Reynolds number, the value of ϕ_P is calculated as a function of the surrounding ϕ's. If the grid is constructed parallel to flow streamlines, then spurious numerical fluxes can be minimized.

Finally, the accuracy for any numerical solution can only be as good as the physical model upon which it is based. This is not a computational error, rather a measure of suitability of the physical model itself.

Computational Efficiency

A number of points should be considered for the efficient numerical solution of problems with MD-PHASE.

Testing of simulations can be done on coarse grids with a relatively high convergence tolerance, to first ensure that correct general behaviour in the results is achieved. Accuracy can be enhanced once the solutions appear realistic.

Other factors can enhance efficiency:

- A solution to a similar problem can serve as an initial guess to cut down on the number of iterations needed.
- Fewer grid lines may be used in low-gradient regions.
- The convergence tolerance may be enlarged for highly complex flows.

3.3 3-phase Finite-Volume Model

The previous section described in general how the basic transport equations were discretized for numerical implementation. We now proceed with specific equations for the 3-phase numerical simulation of a flotation operation. Schematically, a flowchart depicting the organization of the numerical model is given in Figure 3.11. The governing transport equations for each phase are input to the simulation along with the boundary conditions and particular input parameters which are then treated in an iterative manner until a flow field solution is obtained for all variables simultaneously, which corresponds to a level of flotation performance for the particular conditions.

Below are given the set of equations and boundary conditions constructed for the simulation at hand.

3.3.1 Gas Phase Equations

Continuity,

$$(\alpha_G \rho_G u_{Gi})_{,i} = 0 \tag{3.65}$$

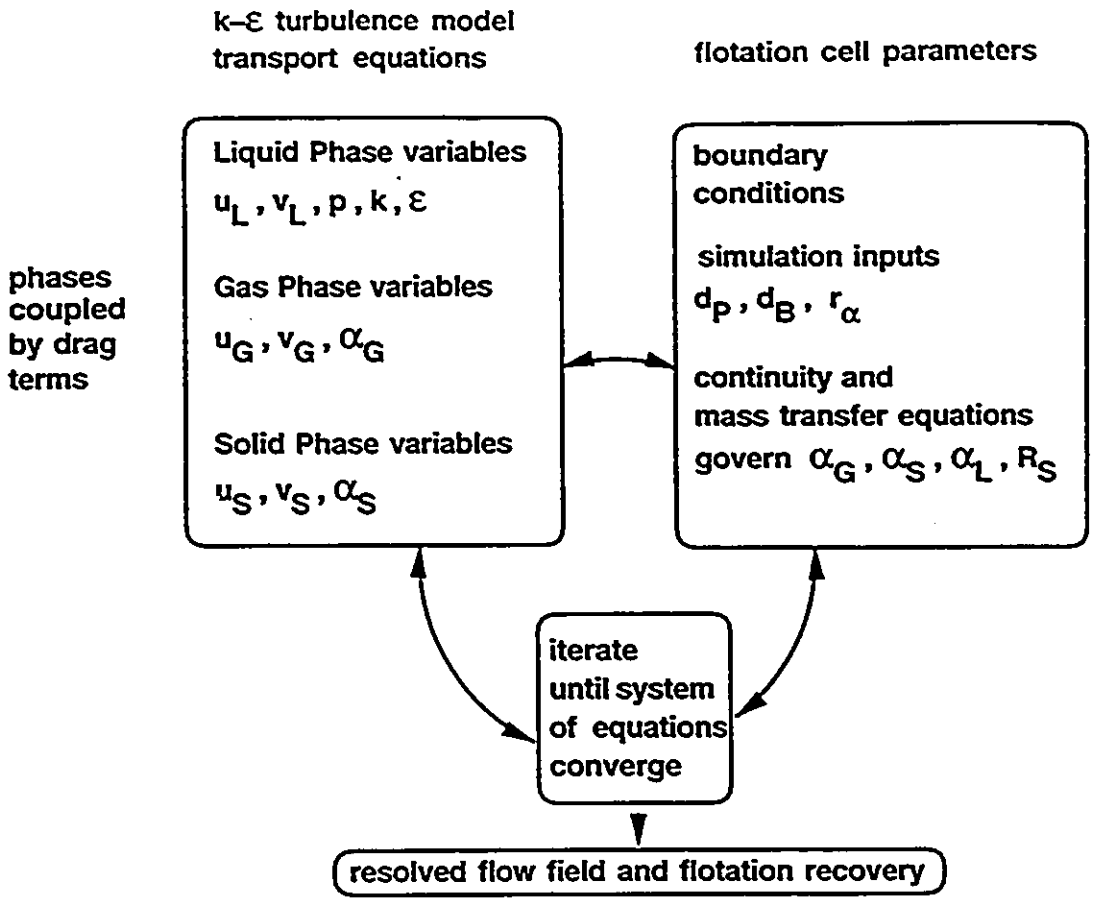

Figure 3.11: Process flowchart for the numerical flotation simulation.

Momentum Equations,

$$(\alpha_G(\rho_G u_{Gj} u_{Gi} - \mu_{G_{eff}} u_{Gi,j})_{,j} = -\alpha_G P_{,i} + \alpha_G \rho_G g_i + F_{GLi} + \alpha_G \mathcal{F}_i(\rho_G, u_G, \mu_{G_{eff}}) \quad (3.66)$$

Above, α_G is the gas-phase volume fraction, and the term F_{GL} is the interphase drag terms for the gas phase in relation to the liquid phase [97, 98]. The terms indicated by $\mathcal{F}_i(\rho_G, u_G, \mu_{G_{eff}})$ arise from the curvature of the coordinate system selected. For this work, cylindrical coordinates were used in the tube model test case, and Cartesian coordinates were used for the float cell simulation. For cylindrical coordinates, these extra terms are given in table 3.3. The interphase drag terms are summarized in table 3.4. The effective viscosity term, $\mu_{G_{eff}}$ is the sum of laminar and turbulent

contributions to the viscosity. In this simulation, μ_{G_t} is not considered as the turbulence is restricted to the main transporting phase, which is the liquid. Further, the terms outlined in tables 3.4 and 3.3 are often referred to as the *source* terms.

The terms in the gas momentum equation arising from the curvature of the cylindrical coordinate system are summarized in table 3.3.

direction	line element	source term, $\mathcal{F}_i$
z	dz	
r	dr	$\left[\rho_G \frac{w_G^2}{r} - \mu_{G_{eff}} \frac{1}{r^2}\left(v_G + 2\frac{\partial w_G}{\partial \theta}\right)\right]$
θ	$r\,d\theta$	$-\left[\frac{1}{r}\rho_G v_G w_G + \mu_{G_{eff}} \frac{1}{r^2}\left(w_G - 2\frac{\partial v_G}{\partial \theta}\right)\right]$

Table 3.3: Source terms arising from curvature of cylindrical coordinate system.

Below, the variables u, v and w, respectively refer to the gas velocities in the z, r and θ directions.

Based on assumptions made by Lai [97], the gas phase momentum equations may be simplified. If the action of the liquid phase is assumed to be primarily responsible for the gas phase transport, then only the pressure, drag and buoyancy terms are retained. In this way, the gas velocities may be explicitly determined from the gas velocity term in the drag expression. The resulting momentum equation becomes,

$$0 = -\alpha_G P_{,i} + \alpha_G \rho_G g_i + F_{GLi} + \alpha_G \mathcal{F}_i(\rho_G, u_G, \mu_{G_{eff}}) \tag{3.67}$$

3.3.2 Liquid Phase Equations

Continuity,

$$(\alpha_L \rho_L u_{Li})_{,i} = 0 \tag{3.68}$$

Momentum Equations,

$$(\alpha_L(\rho_L u_{Lj} u_{Li} - \mu_{L\text{-}\pi} u_{Li,j})_{,j} = -\alpha_L P'_{,i} + F_{LGi} + \sum_M F_{LS_M i} + \alpha_L \mathcal{F}_i(\rho_L, u_L, \mu_{L\text{-}\pi}) \quad (3.69)$$

Above, α_L is the liquid-phase volume fraction. In equation 3.69, the term $\alpha_L \rho_L g_i$ is omitted since the equation makes use of a *corrected* pressure P', where,

$$\frac{\partial P'}{\partial x_i} = \frac{\partial P}{\partial x_i} + \alpha_L \rho_L g_i$$

Hence, it can be seen that using P' instead of P takes care of this term. The interphase friction terms are the same ones as given in table 3.4. The terms $\alpha_L \mathcal{F}_i(\rho_L, u_L, \mu_{L\text{-}\pi})$ are the same as those listed in table 3.4, except that the subscript G should be replaced by an L for equation 3.69. The term $\sum_M F_{LS_M i}$ represents M drag contributions from M different solid phases. It should be noted that in general, when a phase 1 interacts with a phase 2 in a j-direction, it can be said,

$$F_{12j} = -F_{21j}$$

Hence, with respect to equations for other phases, the signs are reversed on the interphase drag terms when inserted into the liquid-momentum equation.

3.3.3 Solid Phase Equations

Continuity,

$$(\alpha_S \rho_S u_{Si})_{,i} = 0 \quad (3.70)$$

Momentum Equations,

$$(\alpha_S(\rho_S u_{Sj} u_{Si})_{,j} = -\alpha_S P_{,i} + \alpha_S \rho_S g_i + F_{SLi} + \alpha_S \mathcal{F}_{Si}(\rho_S, u_S) \quad (3.71)$$

Above, α_S is the solid-phase volume fraction. For the solid phase, the viscous terms will be of a negligible magnitude in comparison with the inertial terms, and are thus dropped from equation 3.71. Similarly, the terms $\alpha_S \mathcal{F}_{Si}(\rho_S, u_S)$ are the same terms as listed in table 3.4, with the subscript G replaced by S, and dropping the viscous contribution.

3.3.4 Interphase Drag Models

Based on results from Soo [99] and Lai [97], the liquid-gas interphase drag term is listed in table 3.3. Also in table 3.4, we have the coefficient B for the liquid-solid interphase drag coefficient. This term is based on derivations by Ergun [100], Wen and Yu [101] and Lyczkowski and Wang [98]. We use ϵ and ϵ_S to refer to normalized (gas phase excluded) liquid and solid void fractions. This approximation is made as it is assumed that the liquid phase is responsible for transporting the dispersed phases, and that gas-solid and solid-solid interactions are neglected.

$$\epsilon = \frac{\alpha_L}{\alpha_L + \alpha_S}$$

Also,

$$\epsilon_S = \frac{\alpha_S}{\alpha_L + \alpha_S}$$

phases	drag term
liquid-gas	$F_{LGi} = \frac{9\alpha_G \mu_L}{r_G^2}(u_{Gi} - u_{Li})$
liquid-solid	$F_{LSi} = B(u_{Li} - u_{Si})$

Table 3.4: Interphase drag terms for the momentum equations.

As shown in [98], two cases are considered for B. We have,

$$B = 150\frac{\epsilon_S^2 \mu_L}{4\epsilon r_S^2} + 1.75\frac{\rho_L \mid u_{Li} - u_{Si} \mid \epsilon_S}{2r_S} \qquad \text{for } \epsilon_S > 0.2 \qquad (3.72)$$

In dense slurries, the flow field disturbances around spheres begin to overlap and hence a separate expression is needed for such a case. For more dilute liquid-solid systems, a different regime exists and is modeled [101, 98] as,

$$B = 0.75 C_D \frac{\epsilon^{-1.65}\epsilon_S \mid u_{Li} - u_{Si} \mid \rho_L}{2r_S} \qquad \text{for } \epsilon_S \leq 0.2 \qquad (3.73)$$

Rowe [102] related the drag coefficient to the Reynolds number by,

$$C_D = \begin{cases} \frac{24}{\mathrm{Re}_s}(1 + 0.15\mathrm{Re}_s^{0.687}) & \text{for } \mathrm{Re}_s < 1000 \\ 0.44 & \text{for } \mathrm{Re}_s \geq 1000 \end{cases}$$

where,

$$\mathrm{Re}_s = \frac{2\epsilon\rho_L(u_L - u_S)r_S}{\mu_L}$$

3.3.5 Volume Fraction Constraint

Throughout the flow domain, a check must be made on the sum of the volume fractions of the various phases. At all locations, the following condition must be satisfied,

$$\sum_M \alpha_M = 1 \tag{3.74}$$

3.3.6 Multi-Phase Mass Balance

3.3.6.1 Continuity of Phases

In this simulation, there are three phases considered; water, bubbles of varying particle loading, and particles. The particles or solid phase, represent the coal-oil agglomerates. In reality, these agglomerates are themselves a two-phase, coal and oil system, but for the purposes of this numerical simulation, are treated as single solid objects with averaged properties. Each phase is subject to a momentum balance which is employed for the calculation of its respective velocities, which in turn must be used to determine local volume fractions to ensure proper continuity for each phase, and taken all together, to conserve an overall, multi-phase mass balance.

3.3.6.2 Liquid Phase

As described by Lai [40], the main transport phase velocities are determined by solution of the momentum equation, and then the conservation of mass is ensured by coupling the velocity determination with a pressure correction, which diminishes with convergence. The volume fraction for the liquid phase is not explicitly calculated,

rather it is simply calculated as the remaining volume fraction, once gas and solid phase volume fractions have been calculated. That is, the liquid volume fraction, α_L is calculated as,

$$\alpha_L = 1 - \alpha_G - \alpha_S \tag{3.75}$$

If at any point in the numerical computation of the phase volume fractions, the local sum of them exceeds unity, then they are all simultaneously normalized following,

$$\alpha_i = \frac{\alpha_i}{\sum_{j=1}^{3} \alpha_j} \tag{3.76}$$

3.3.6.3 Gas Phase

A local flux balance at all nodes in the grid is employed to determine the gas phase volume fraction at all points in the flow domain. This is based on an upwind scheme presented by Spalding [103].

We can express the flux G_i, for the ith phase, as $G = \rho_i A u_i$, where A is the area of the face through which this flux takes place. A local flux balance for any phase can be written as,

$$\sum_{\text{OUT}} \alpha_i G_i = \sum_{\text{IN}} \alpha_i G_i + R_i \tag{3.77}$$

The term R_i refers to a mass generation or consumption in a finite-volume cell. The adhesion of particles to bubbles represents a mass transfer from the solid to gas phase. The derivation of this term is discussed in section 3.3.7. Any outgoing flux from a cell will obviously represent the volume fraction $\alpha_{i[P]}$ in that cell. The incoming fluxes will contain the volume fractions in the respective neighbouring cells. We can rewrite equation 3.77 in view of the upwind differencing scheme as,

$$\alpha_{i[P]} \sum_{\text{OUT}} G_i = \sum_{\text{IN}} \alpha_i G_i + R_i \tag{3.78}$$

Now, we have a finite volume expression for $\alpha_{i[P]}$, which is the unknown volume fraction at the point P, or cell where this flux balance is applied.

$$\alpha_{i[P]} = \frac{\sum_{\text{IN}} \alpha_i G_i + R_i}{\sum_{\text{OUT}} G_i}$$

Substituting the above result into equation 3.74 gives,

$$\frac{\sum_{\text{IN}} \alpha_G G_G + R_G}{\sum_{\text{OUT}} G_G} + \frac{\sum_{\text{IN}} \alpha_L G_L}{\sum_{\text{OUT}} G_L} + \alpha_S = 1 \tag{3.79}$$

Rearranging gives,

$$\sum_{\text{OUT}} G_L \cdot \left(\sum_{\text{IN}} \alpha_G G_G + R_G \right) + \sum_{\text{OUT}} G_G \cdot \sum_{\text{IN}} \alpha_L G_L + \left(\sum_{\text{OUT}} G_L \sum_{\text{OUT}} G_G \right) \cdot \alpha_S = \sum_{\text{OUT}} G_L \cdot \sum_{\text{OUT}} G_G$$

Now, substituting $(\sum_{\text{IN}} \alpha_G G_G + R_G)/\alpha_{G[P]}$ for $\sum_{\text{OUT}} G_G$ on the right hand side of the above expression, then rearranging gives,

$$\alpha_{G[P]} = \frac{\left(\sum_{\text{IN}} \alpha_G G_G + R_G \right) \cdot \sum_{\text{OUT}} G_L}{\left(\sum_{\text{IN}} \alpha_G G_G + R_G \right) \cdot \sum_{\text{OUT}} G_L + \sum_{\text{OUT}} G_G \left(\sum_{\text{IN}} \alpha_L G_L + \alpha_S \cdot \sum_{\text{OUT}} G_L \right)} \tag{3.80}$$

Equation 3.80 may be used in the finite volume scheme for solving the gas phase volume fraction, in an iterative fashion, using current values of α_L and α_S to update $\alpha_{G[P]}$. Upon inspection, it may be seen that equation 3.80 is inherently stable, as it has been constructed to calculate values of $\alpha_{G[P]}$ which are between 0 and 1.

3.3.6.4 Solid Phase

In a fashion analogous to the previous sections, the mass balance for the solid phase is derived.

3.3.7 Interphase mass transfer

The conservation of the mass of a phase is governed by the transport equation 3.81. For this work, it is written in terms of the solid phase, as this is used as the reference phase where material is lost through mass transfer to the gas phase. Below f_{ρ_S} is the density fraction of the species in the particular phase (solids) which is participating in the mass transfer [104]. By definition, $f_{\rho_S} = 1$ at the start of any iteration, as the

entire particulate phase is considered to be coal-oil agglomerates which are involved in the mass transfer.

$$\frac{\partial f_{\rho_S}}{\partial t} + \left(f_{\rho_S} u_j + J_{S_j}\right)_{,j} = R_S \tag{3.81}$$

Above, J_{S_j} is the diffusion flux vector for the solid phase, and R_S is the rate of consumption of the solid phase, in units of kg/s. The term J_{S_j} refers to molecular diffusion, and can be neglected for this system which models large dispersed bodies. Since a steady-state system is being simulated, the time derivative term may also be dropped. Thus equation 3.81 simplifies to,

$$R_S = f_{\rho_S} u_{j,j} \tag{3.82}$$

The rate term R_S is calculated using the rate of collision term z_{PB} from equation 1.60, which gives a value in units of [collisions $\cdot$ s^{-1} $\cdot$ m^{-3}]. Thus,

$$R_S = \tau_\alpha \left(N_{P/B_{MAX}} - N_{P/B}\right) z_{KB} V_{CELL} m_S \tag{3.83}$$

There are a number of additional factors in the above expression for R_S. The variable τ_α represents the attachment and collection probability associated with the collision. With reference to equation 1.61, τ_α can be equated to the product of the terms $P_a(1 - P_d)$. The term,

$$\left(N_{P/B_{MAX}} - N_{P/B}\right)$$

expresses the fraction of the bubble surface which is still available to contact a particle. V_{CELL} is the volume of the local cell where this collision rate is applied, and m_S is the mass of one solid particle.

Solution of equation 3.82 will produce an array of f'_{ρ_S} values between 0 and 1, which represents the fraction of the solid phase remaining after some of it has transferred into the gas phase under the prevailing transport conditions. We set,

$$R_i = f'_{\rho_S}$$

where R_i is the mass generation or consumption term for the ith phase, used in the equations in section 3.3.6.3 which determine the local volume fractions of the dispersed phases accounting for the transport conditions with simultaneous mass transfer.

3.3.7.1 Effective mass transfer

The problem being modeled in this work involves the adhesion of solid particles to gaseous bubbles. Numerically it is treated as a transfer of mass or material from the solid phase to the gas phase. This requires that the effective local bubble diameter must increase as mass is transferred. An average bubble size can be computed for each cell in the flow field. To do this, we employ the method of Spalding known as the *shadow* solution [103].

The shadow volume fraction $\tilde{\alpha_G}$, is the volume fraction the gas phase would have possessed, at each node, if the interphase mass transfer had not taken place. That is, equation 3.77 is employed without the R_i term. However, since these equations represent a continuum where the outgoing fluxes must balance those coming in, equation 3.80 is modified to the form below for determining the shadow volume fraction.

$$\alpha_{\tilde{G}[P]} = \frac{\left(\sum_{\text{IN}} \tilde{\alpha_G} G_G\right) \cdot \sum_{\text{OUT}} G_L}{\left(\sum_{\text{IN}} \alpha_G G_G + R_G\right) \cdot \sum_{\text{OUT}} G_L + \sum_{\text{OUT}} G_G \left(\sum_{\text{IN}} \alpha_L G_L + \alpha_S \cdot \sum_{\text{OUT}} G_L\right)} \tag{3.84}$$

The difference between α_G and $\tilde{\alpha_G}$ can be attributed to diameter growth via mass transfer. Thus,

$$\frac{d_B}{d_{B_0}} = \left(\frac{\alpha_G}{\tilde{\alpha_G}}\right)^{\frac{1}{3}} \tag{3.85}$$

Above, d_{B_0} is the diameter of the bubble in the particular cell at the start of the iteration. Further, it can be deduced that,

$$\Delta N_{P/B} = \frac{V_G - V_{G_0}}{V_S} \tag{3.86}$$

since the gain in gas phase volume is at the expense of the solid phase. The term V_i refers to the volume of one body (bubble or particle) from either the gas or solid phase.

3.3.8 Drag on a Loaded Bubble

3.3.8.1 Bubble Loading

This simulation has incorporated a modified drag on a bubble which has particles adhering to it. Two constraints were implemented to control the level of particles adhering to a single bubble. The maximum bubble loading is calculated by assuming that circular projections of the areas of the particles may occupy the surface of the bubble. The particles are modeled to pack in a two-dimensional hexagonal lattice, thereby covering a maximum of 90.7% of the bubble's geometrical area. The maximum number of particles per bubble, $N_{P/B_{MAX}}$, is thus,

$$N_{P/B_{MAX}} = 0.907 \left(\frac{r_P^2}{4r_B^2} \right) \tag{3.87}$$

A second constraint arises from considering the relative fluxes of the gas and particulate phases in the float cell. Numerical instability could arise if the bubbles became too heavily loaded and gave outlet particulate fluxes greater than their inlet fluxes. Assuming all the inlet gas exits in the product stream (not via the liquid exit) then the maximum number of particles per bubble becomes,

$$N'_{P/B_{MAX}} = \frac{g_S \rho_G V_G}{g_G \rho_S V_S} \tag{3.88}$$

Above g_i refers to the flux of a phase, and V_i refers to the volume of one dispersed body. In practice, if a mass-flux instability arose, $N_{P/B_{MAX}}$ was replaced by $N'_{P/B_{MAX}}$ in the algorithm.

3.3.8.2 Particle Patches

Particles are modeled to form concentric hexagons on the back side of moving bubbles as shown in Figure 3.12. These hexagons are denoted as levels, and the total number of particles at each level, n is,

$$\begin{aligned} N_1 &= 1 \\ N_n &= 1 + \sum_{j=2}^{n} 6(j-1) \end{aligned} \tag{3.89}$$

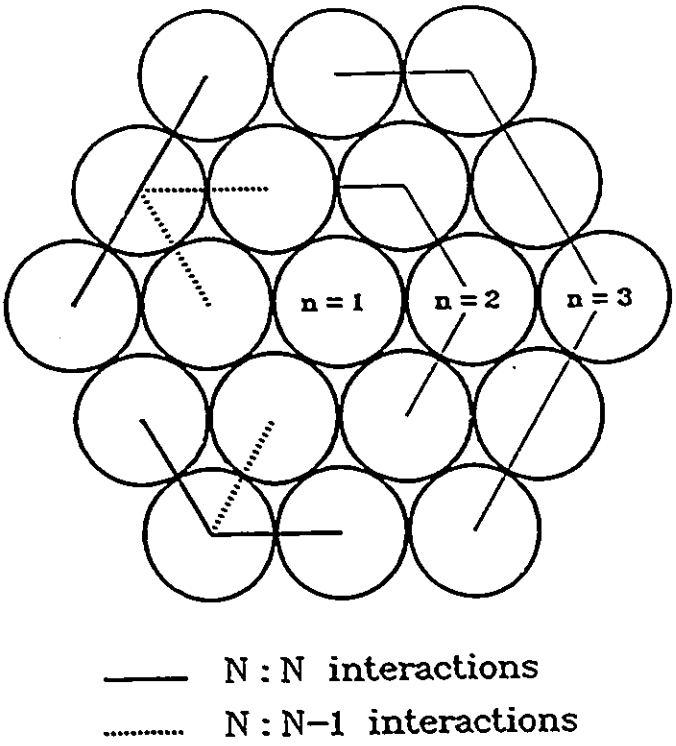

Figure 3.12: Schematic particle patch.

3.3.8.3 Particle Patch Drag Model

The particle patch is then applied to a model developed by Pendse et al. [105], which was for drag force calculations of spherical collectors with deposited particles in various configurations. For cases with several particles attached, the hydrodynamic interaction among the attached particles must be considered.

For our case, we make the assumption that loaded bubbles transported by fast-moving water will orient themselves with the particle patch at the rear of the bubble, in line with the velocity vector of the bubble. The drag effects are a function of the position of the particle relative to the bubble's line of motion, as well as the product of all the interaction terms from all the attached particles.

Pendse et al. [105] give the following expression for a multi-particle interaction which augments the drag force.

$$\Delta F_{D,M_j} = \Delta F_{D,0} \cdot f(P_{M_{1,1}}, P_{M_{2,1}}, P_{M_{2,2}}, \ldots P_{M_{N,j}}) \tag{3.90}$$

Above, $\Delta F_{D,M_j}$ represents the increment of the jth particle from the Mth level on the drag of a bubble carrying such a number of particles. This increment is normalized with respect to the drag of an unloaded bubble. The function $f(P_{M_{1,1}}, P_{M_{2,1}}, P_{M_{2,2}}, \ldots P_{M_{N,j}})$ represents the interaction of all attached particles with each other. Thus, the overall change in drag for a loaded bubble of N levels, with j particles at this level, $\Delta F_D[N:j]$, will be,

$$\Delta F_D[N:j] = F_{D,1_1} + \sum_{M=2}^{N} \sum_{i=1}^{L} \Delta F_{D,M_i} \tag{3.91}$$

$$\text{where, } L = \begin{cases} 6(M-1) & \text{for } M < N \\ j & \text{for } M = N \end{cases}$$

The interaction term for only two particles arises from a derivation by Happel and Brenner [106]. This is given as,

$$f(P_i, P_j) = f\left(\frac{l}{r_P}, \alpha\right) = \left[\left(\frac{1}{1+\frac{3}{2}\left(\frac{l}{r_P}\right)-\left(\frac{l}{r_P}\right)^3}\right)\cdot\cos^2\alpha + \left(\frac{1}{1+\frac{3}{4}\left(\frac{l}{r_P}\right)+\frac{1}{2}\left(\frac{l}{r_P}\right)^3}\right)\cdot\sin^2\alpha\right] \tag{3.92}$$

Above, the variable l is the center-to-center distance between the two attached particles, and α is the angle between the flow line of motion and the line of centers of the particles. r_P is the particle radius. Further [106], only interactions between neighbouring attached particles need to be taken into account. Thus, we have two kinds of pairs in our particle patch model, $M:M$ pairs for two particles in the same level, and $M:M-1$ pairs for a particle in the outer level interacting with those already in place in a lower level.

For the particle patch as modeled here, the distance l will always be equal to $2r_P$. Based on the concentric hexagonal arrangement, the angle α will always be equal to 90^o for $M:M$ pairs. This gives the interaction function for such a pair to be,

$$f(M:M) = 0.695652$$

Consider the diagram in Figure 3.13. According to the definition for angles γ and α,

by resolving the geometry, we can write,

$$\gamma_{[2:1]} = \cos^{-1}\left(\frac{2(a+b)^2 - 4b^2}{2(a+b)^2}\right)$$

Now,

$$\alpha_{[M:M-1]} = M\gamma_{[2:1]} - \frac{\gamma_{[2:1]}}{2}$$

Figure 3.13 illustrates a and b in this context.

particle patch relative to line of flow

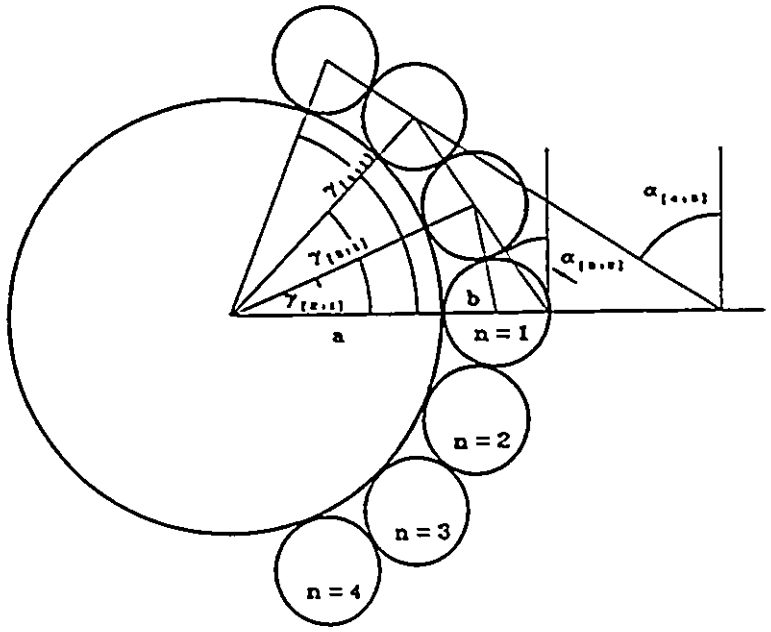

Figure 3.13: Particle patch geometry.

Further,

$$\alpha_{[3:2]} = 2\alpha_{[2:1]} \quad \text{and,} \quad \alpha_{[M:M-1]} = (M-1)\alpha_{[2:1]}$$

Thus we can write,

$$f(M : M-1) = \left[\frac{-\cos^2 \alpha_{[M:M-1]}}{1.65} + \frac{\sin^2 \alpha_{[M:M-1]}}{1.4375}\right]$$

We are now in a position to resolve the function $f(P_{M_{1,1}}, P_{M_{2,1}}, P_{M_{2,2}}, \ldots P_{M_{N,j}})$ from equation 3.90. We can begin by stating,

$$f(P_{M_{1,1}}, P_{M_{2,1}}, P_{M_{2,2}}, \ldots P_{M_{N,j}}) = f^q(M : M-1) \cdot f^v(M : M) \qquad (3.93)$$

This is based on the analysis of Pendse et al. [105], where the drag increment for the addition of the jth particle is given as the product of the interaction terms with its immediate neighbours. Thus equation 3.93 reduces this function to q interactions among $(M : M-1)$ pairs and v interactions between $(M : M)$ pairs. Further, q and v can be employed exponentially, since all $(M : M-1)$ interactions are equivalent, and likewise for $(M : M)$ interactions.

Consider figure 3.12. This shows the Nth level particles added to the patch. Depending on which particle the jth one is, there may be one or two interactions with the $N-1$st level, and also one or two interactions within the Nth level. The general rule is summarized in Table 3.5. The first coefficient in equation 3.90, $\Delta F_{D,0}$

level	condition	interactions
$N : N-1$	$j \bmod (N-1) = 0$	$q = 1$
$N : N-1$	$j \bmod (N-1) \neq 0$	$q = 2$
$N : N$	$j = 1$	$v = 0$
$N : N$	$1 < j < 6N-6$	$v = 1$
$N : N$	$j = 6N-6$	$v = 2$

Table 3.5: Rules for interactions for adding the jth particle to the Nth level on a loaded bubble.

is given in [105] as,

$$\Delta F_{D,0} = \left(\frac{r_P}{r_B}\right)\left(1 - \left(\frac{r_B}{r_M}\right) + \frac{1}{4}\left(\frac{r_B}{r_M}\right)\left(1 - \left(\frac{r_B}{r_M}\right)^2\right)\left(1 - 3\cos^2\gamma\right)\right) \qquad (3.94)$$

Here, $r_M = r_P + r_B$, and γ is the angle indicated in figure 3.13. Thus, with input bubble and particle radii, and given a bubble loading, equation 3.90 can be evaluated, and then used in equation 3.91 to determine a coefficient which augments the drag

on a bubble due to particle loading. The term $F_{D,1_i}$ in equation 3.91 is determined using equation 3.94 with the off-center angle γ set to zero.

As an example, for a bubble of 2.0mm diameter and a particle of 60 μm diameter, the calculated drag coefficients are given in table 3.6. They agree with the results of Pendse et al. for the cases of one particle lined up in parallel [105].

particles	drag coefficient
1	1.000642
2	1.001538
3	1.002162
4	1.002785
5	1.003409
6	1.004033
7	1.004466
8	1.005362
9	1.006318
10	1.006941

Table 3.6: Drag force coefficients for increasing bubble loading.

3.3.9 Multi-phase viscosity model

The presence of up to three phases in variable concentration throughout the flow domain necessitates a means for specifying a basic laminar viscosity in each cell. The viscosity of a slurry is well known to increase with solids concentration. The presence of air tends to give a much reduced viscosity, along the lines of a weighted average of the liquid and air viscosities. Since the viscosity of air is about three orders of

magnitude below that of water, its effect is neglected [107]. That is,

$$\mu_{\text{TOTAL}} = (1 - \alpha_G)\mu_{\text{SLURRY}}$$

A model was incorporated into the simulation to account for variations in the laminar viscosity arising from local conditions. The two effects considered were those of particle size and particle concentration. Data was taken from [108] and fitted with a multivariate linear response surface. The response function was *reduced* (or normalized) viscosity, which is the viscosity of the slurry, divided by the viscosity of the pure suspending liquid. Hence, this provides a local coefficient, k_μ, for the laminar liquid viscosity which is used in the program.

The model was constructed as,

$$k_\mu = \sum_{j=1}^{N} b_j x_j \tag{3.95}$$

Below, table 3.7 summarizes the regression variables and coefficients.

The goodness of fit is demonstrated in figure 3.14. The analysis of the residuals shows an average error of about 8% over the entire range of the model. A model of this nature is quite adequate to convey any trends associated with the rheological properties of the 3-phase system.

3.3.10 Finite-Volume code organization

The computer flow sheet in figure 3.15 schematically depicts the basic code organization. The functions of the various subroutines are thoroughly explained in [40].

3.3.10.1 Input Data and Grid

The input data and grid supplied to a particular problem must fully define the particular problem to ensure that a meaningful solution ensues. As previously mentioned in section 3.2.1.2, the grid-generating software ORTHO is used to make a finite-volume grid which is fully integrated with the MD-PHASE code. There is also a data file to

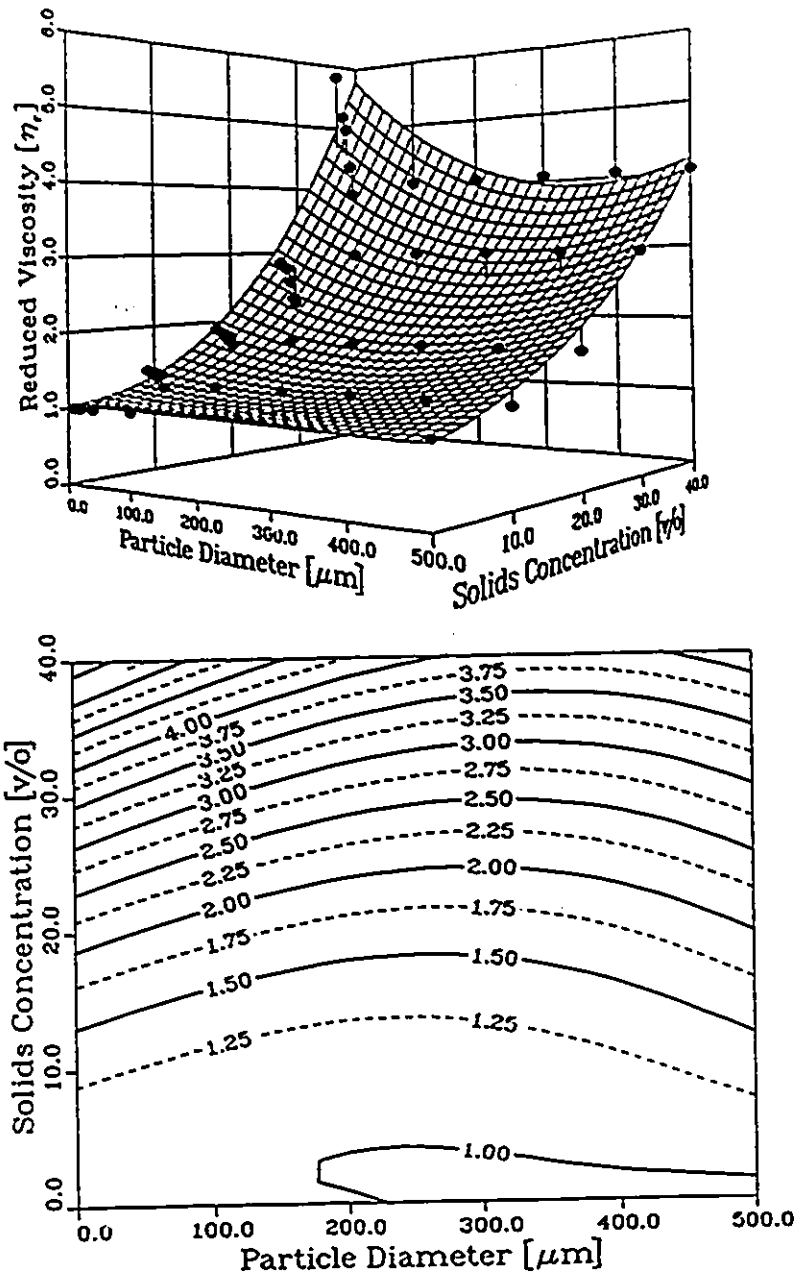

Figure 3.14: Response surface for 3-phase viscosity model based on the parameters in table 3.7.

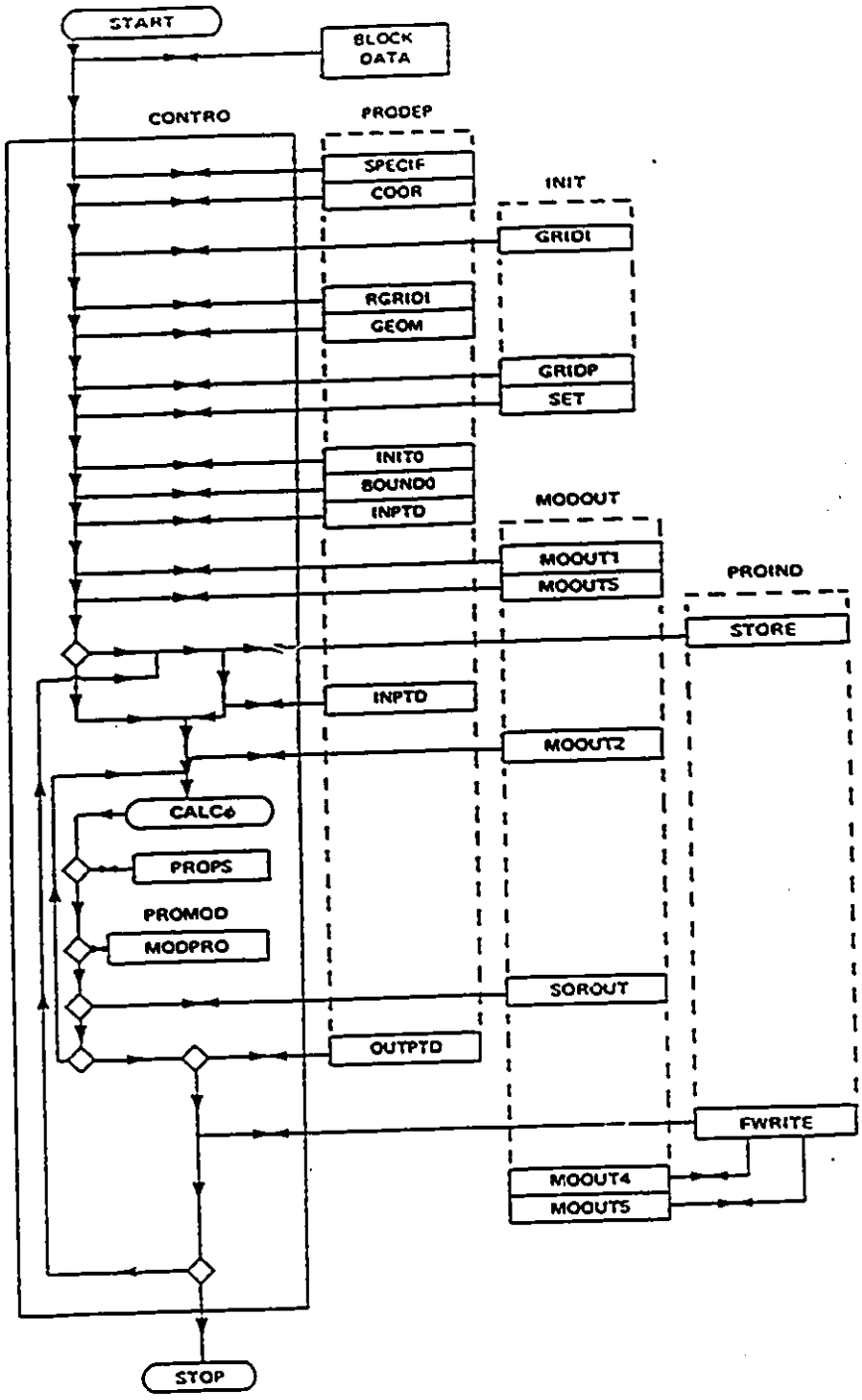

Figure 3.15: Basic finite-volume software flow sheet. From [40].

x_j	coefficient	value
1	b_0	1.045079
d_P	b_1	-1.9809527e-04
α_S	b_2	-6.8113446e-04
$d_P\alpha_S$	b_3	-1.1600669e-04
α_S^2	b_4	2.6053579e-03
$d_P^2\alpha_S$	b_5	3.7090535e-07
$d_P\alpha_S^2$	b_6	-3.5555784e-06
α_S^3	b_7	9.2202827e-06

Table 3.7: Multi-phase viscosity model regression coefficients. (α_S in [v/o] ; d_P in [μm])

supply all parameters for the physical properties of the materials used in a particular simulation, as well as the boundary values and/or initial values for the field variables. The use of the this file structure minimizes undesirable code editing and compile time. Appendix D contains an example input data file.

3.3.10.2 Equation solution algorithm

The subroutine named CALCϕ in figure 3.15 is the basic routine for the solution of any generalized field variable. The detailed software structure of this routine is shown in figure 3.16.

The three routines, HYBRID, CORESI and LISOLV, in figure 3.16, are employed in the construction and solution of the system of linear equations for each field variable. Some of their main features are described below.

HYBRID The discretized coefficients from equation 3.41 are assembled, and the hybrid differencing of equation 3.36 is applied.

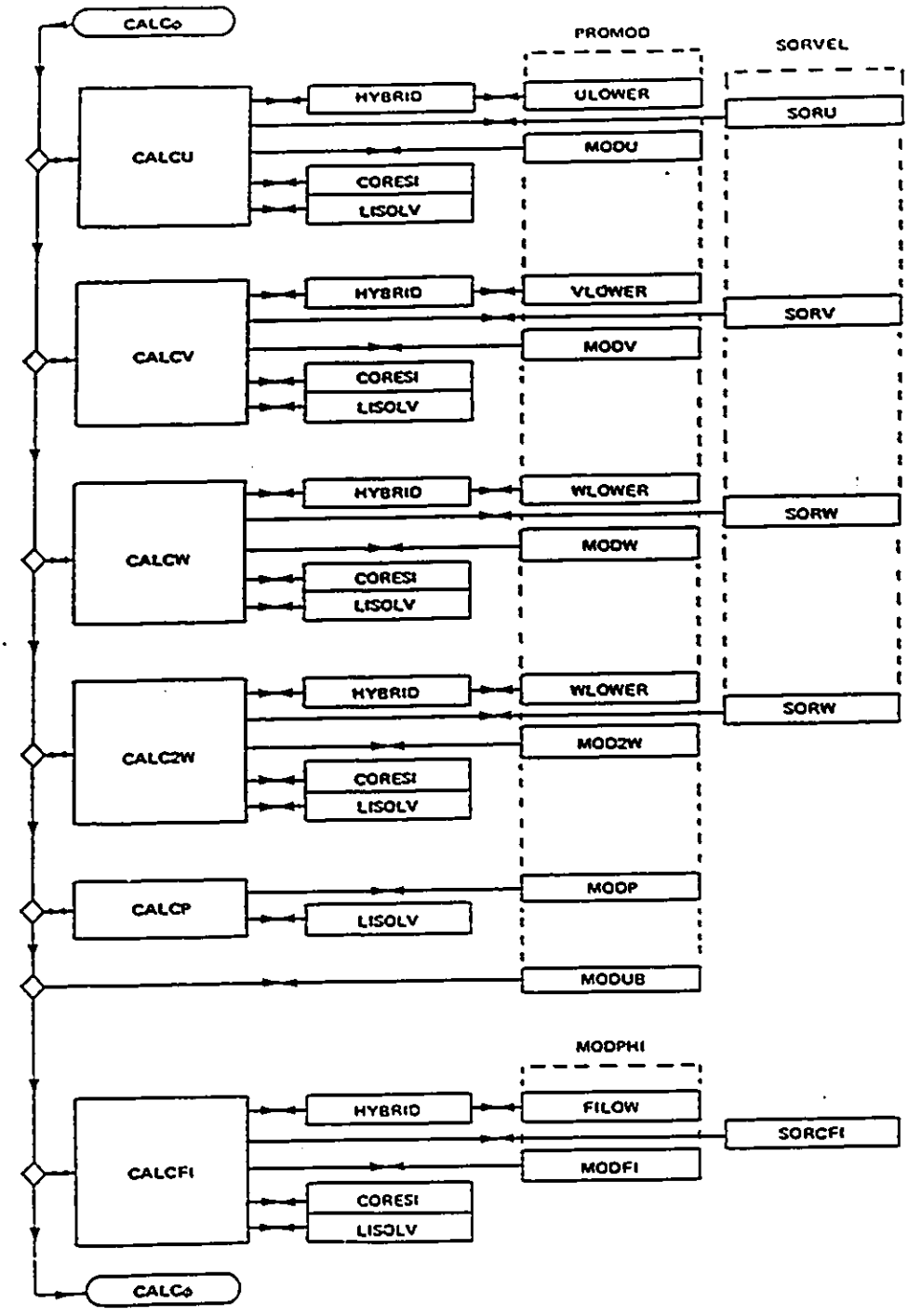

Figure 3.16: MD-PHASE CALCϕ subroutine flow sheet. From [40].

CORESI Under-relaxation is performed explicitly here through modification of the discretized coefficients. Also a residual source is calculated.

LISOLV The block iteration sequence is performed here by sweeping in the i-direction. The coefficients of the recurrence relations (equations 3.58 and 3.60) are assembled on the N-S line, and these relations are then used to calculate the unknown field variables.

3.3.10.3 Post-processing

Upon convergence of the MD-PHASE program, additional routines may be added through the main controlling program to supplement the output, taking advantage of all the field variable arrays being still active in the computer RAM.

Standard MD-PHASE field variable output can be integrated into two formats for either the NRCPLOT or FAST graphics packages. The former is used for standard two-dimensional vector and contour plots, while the latter may be employed for essentially the same purposes, but with much enhanced graphics capabilities in terms of colours, shading and its own post-processing abilities. FAST is also suited for 3-dimensional graphics.

A fluid particle trace program was incorporated into the output options. Using any of the liquid, gas or solid velocity fields, a particle trace routine was constructed via the following algorithm.

Initially, a fluid particle will be positioned at the inlet. That is, $p_0 = (x_0, y_0)$. With a chosen δt, the fluid particle will be displaced.

$$p_1 = (x_0 + u_{p_0}\delta t, y_0 + v_{p_0}\delta t)$$

Now, at position 1, u_{p_1} and v_{p_1} are interpolated from the field solution with a bilinear algorithm. In general,

$$p_i = \left(x_{i-1} + u_{p_{i-1}}\delta t, y_{i-1} + v_{p_{i-1}}\delta t\right) \tag{3.96}$$

The trace routine enables density effects to be observed, and also provides a means of estimating the residence time of the various phases as they pass through the float cell.

The flotation recovery in a simulation can be determined by examining the various phase fluxes as they enter and leave the float cell. The fraction recovery is simply,

$$\text{recovery} = \frac{\text{solids in top face gas flux}}{\text{inlet solids flux}} \tag{3.97}$$

3.3.10.4 Notes on running a 3-phase MD-PHASE simulation

It is not always sufficient to correctly define a problem and then allow the computer to proceed with the simulation. As pointed out in [97], when cross-flow patterns are imposed and several phases are operating simultaneously, the transport equations can appear to be working *in opposition* to each other. That is, convergence for one phase, may destabilize the convergence for other phases. This is because the momentum equations for the three phases considered here are highly interdependent, yet at the same time exhibit differing individual tendencies.

The following strategy was adopted to overcome these stability concerns. Since the gas transport equation solved its velocities explicitly, and this result together with the solid transport equations were used to determine the interphase mass transfer, the dispersed phase transport could only be iterated one time for each iteration on the liquid phase equations. Typically, a problem was initiated with a near-convergence liquid phase flow field and the dispersed phases were introduced and solved every 25 iterations. When 3-phase solution stability increased, the frequency of solving the dispersed phase transport equations was increased to once every 10 iterations, then for final convergence, all equations were solved each iteration. The convergence scheme for a simulation is shown in figure 3.17. Only the u-velocity residual is shown, as these were the limiting residuals for convergence. It can be seen that solving the dispersed phase equation creates a disturbance which dampens out after a sufficient number of iterations. If the freqency of solving the dispersed phase equations is not increased, the convergence pattern simply becomes oscillatory, and would stabilize at some residual value well above the tolerance. The convergence behaviour in figure 3.17 is taken from a simulation where $r_\alpha = 0.20$, $d_P = 20\mu$m and $d_B = 0.5$mm. The required convergence was achieved in 3475 iterations. Several patterns may be observed in this figure. The initial oscillations (under 600 iterations) arise from the

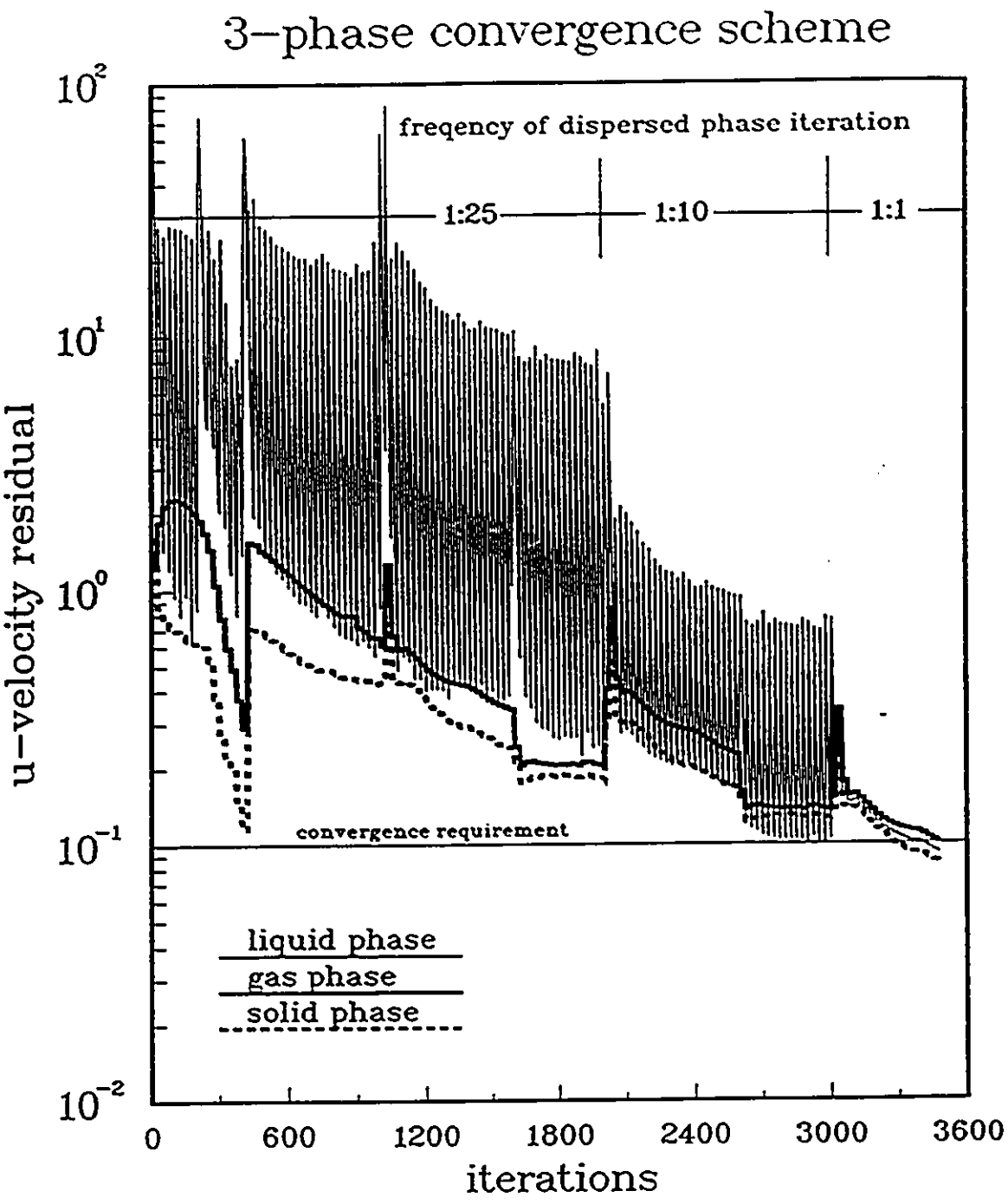

Figure 3.17: 3-phase flotation simulation convergence scheme.

basic 3-phase flow pattern establishing itself. The peak near 1000 iterations occurs because the recovery flux of solids in the gas stream reaches 100% and the mass balance throws the solution back to a realistic separation (it was around 95% in this case) producing a readjustment of the flow field solution with a corresponding jump in residuals. The ratio of 1:25 for dispersed phase iterations to liquid phase iterations produces steady oscillating residuals before 2000 iterations. This ratio is reduced to 1:10 and there is an initial growth of the residual before it falls and levels off again before 3000 iterations. The bandwidth of the oscillations is reduced in proportion to the frequency of the dispersed phase iterations. In a sense, with a more established three-phase flow field, each iteration on the dispersed phases is less of a shock to the stability of the liquid phase. Finally the ratio is made 1:1 and the required convergence is attained. Residual oscillation has become quite small.

Chapter 4

Results

4.1 Surface Property Measurements

Results were obtained for the surface tension of the agglomerate particles and the mean particle-sizes at several oil levels.

4.1.1 Surface Tension Results

The adhesion method was employed to determine the surface tension of hexadecane-coal agglomerates at several oil levels. Figure 4.1 is an example of the raw data obtained at 0.25 weight percent hexadecane for the Devco coal sample. Linear regressions of the adhesion data for each suspending liquid (giving the range of γ_{LV}) were calculated and are shown in the figure as well. It is noticed that the slopes are negative for the case where $\gamma_{LV} > \gamma_{PV}$, as expected from the free energy of adhesion criteria [11].

Briefly, for the particle, solid and liquid system, the free energy of adhesion, ΔF^{adh} is given as,

$$\Delta F^{adh} = \gamma_{PS} - \gamma_{PL} - \gamma_{SL} \tag{4.1}$$

where the subscripts P, S and L respectively refer to the particle, substrate and liquid interfaces.

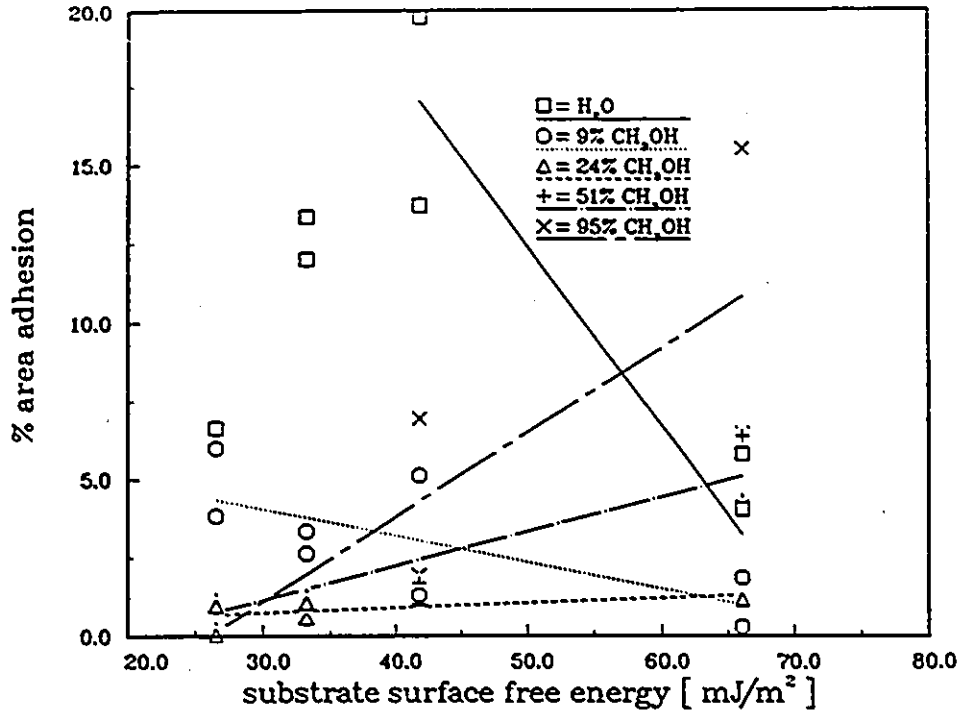

Figure 4.1: Agglomerate adhesion vs. substrate surface tension. (for hexadecane bridging liquid)

Hence, for the case where $\gamma_{LV} > \gamma_{PV}$, ΔF^{adh} increases with increasing γ_{SV} thus predicting a decreasing extent of particle adhesion with increasing substrate surface tension. When $\gamma_{LV} < \gamma_{PV}$, the opposite trend is expected.

Absolom et al. [11] reported a particle-size range of 1-20 μm for his work with the adhesion method. In this work, samples with mean particle-sizes from 6 μm to 65 μm were used. Approximately the same degree of adhesion was found for the samples in both studies, indicating that the change in mean size did not significantly alter the particles' capacity to adhere to the substrates in view of increased mechanical resistance for larger particles.

Figure 4.2 then shows the slopes of the regression fits from Figure 4.1 (as well as the other oil levels) plotted against γ_{LV}. γ_{PV} is determined at the point where the slope is zero. This regression and slope plotting procedure is done at each oil level (including zero oil) to determine γ_{PV}. Figure 4.3 shows the agglomerate surface

tensions versus oil level. The surface tension of the unoiled coal measured by the adhesion technique was 62.0 mN/m, in agreement with other published results for bituminous coal [109, 110, 111]. At 10 weight% oil, the agglomerate surface tension closely approximates that of pure hexadecane.

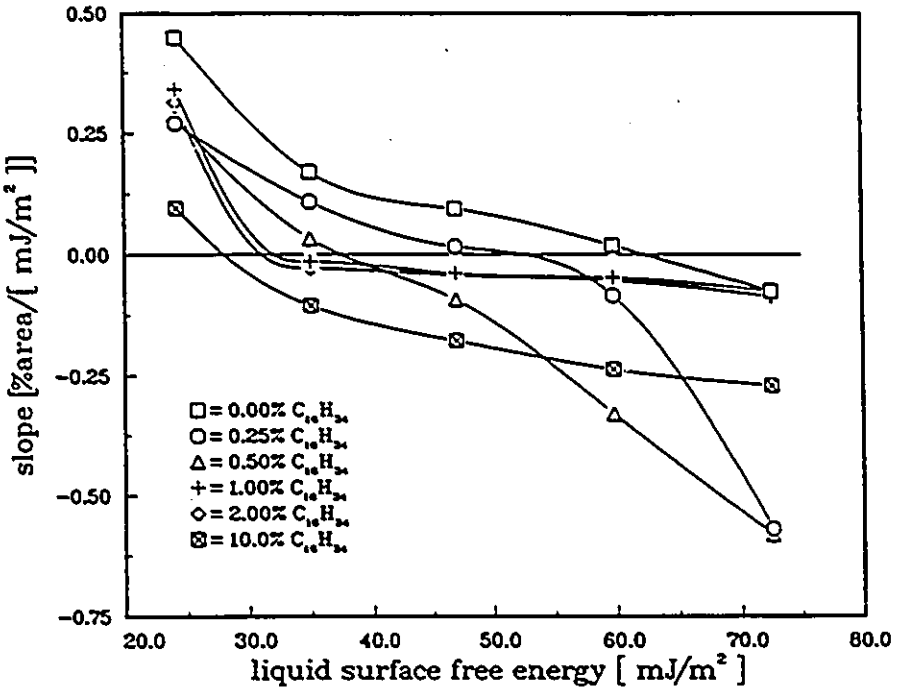

Figure 4.2: Adhesion slope vs. liquid surface tension

4.1.2 Surface Tensions of Agglomerates from Coals of Various Ranks

The same procedure as detailed in section 4.1.1 was carried out for the two subbituminous and lignite coals. Interpreting the data from the area of adhesion measurements, the surface properties of the agglomerates across the range of oil-levels tested are shown in figure 4.4. These data pertain only to agglomerates formed with hexadecane. The surface tensions of the unoiled coals fall in the range of 54.0 to 64.0 mJ/m^2, in agreement with the previous findings of Varga-Butler et al. [110] and

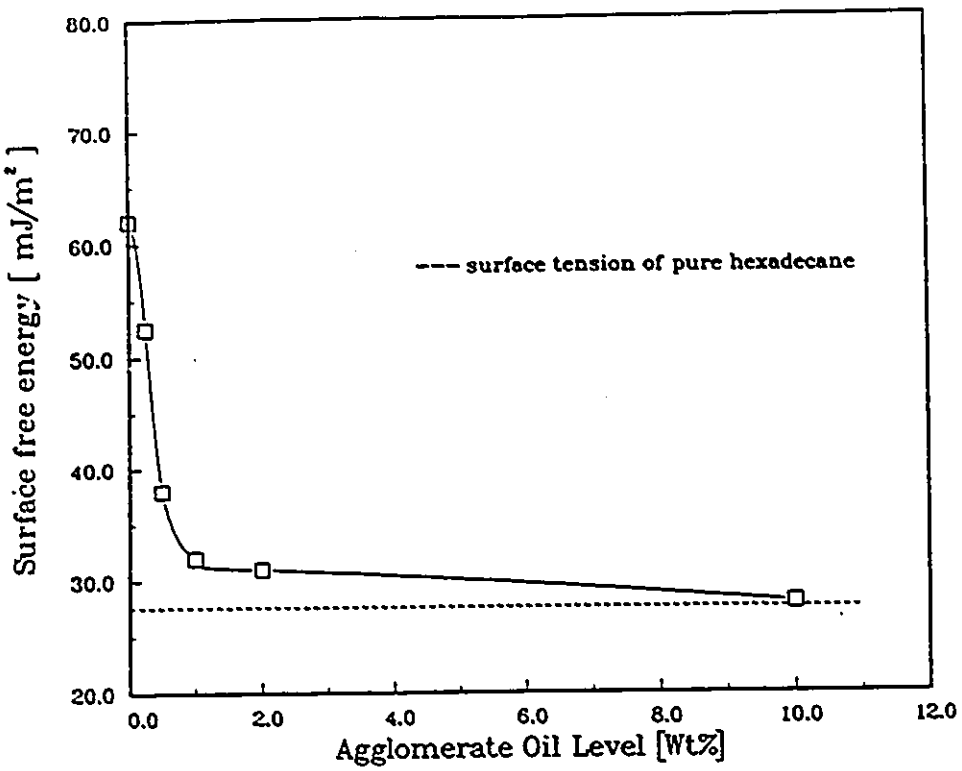

Figure 4.3: Agglomerate surface tension vs. oil level

Sablik [111]. At 10 weight% oil, the surface tensions of the bituminous and subbituminous coals closely approximate that of pure hexadecane. The two lignite samples show a more gradual wetting curve, and a surface which, even at 10 weight% oil, does not exhibit a hexadecane character.

4.1.3 Mean Particle-Size Results

Figure 4.5 shows the cumulative size distribution of the agglomerates at 0.50% and 10.0% oil suspended in both water and a mixture of 95% CH_3OH and 5% H_2O. It is shown here that the methanol does not significantly degrade the agglomerate structure, and as such, the surface tension measurements should be valid.

The mean particle-sizes of the unagglomerated coals are given in figure 4.6. As one would expect, the mean agglomerate size increases as more oil is added to the system.

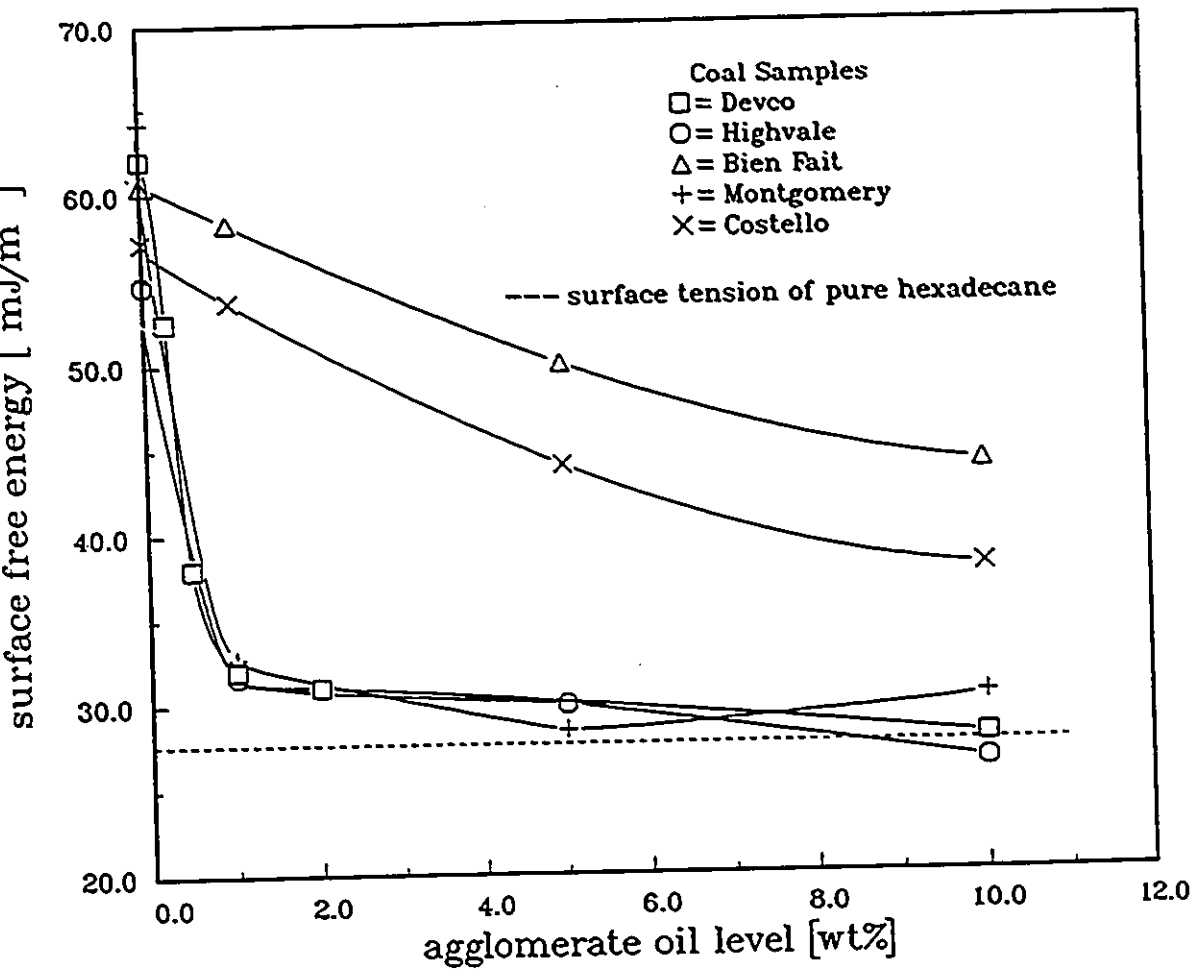

Figure 4.4: Agglomerate surface free energy vs. weight % oil.

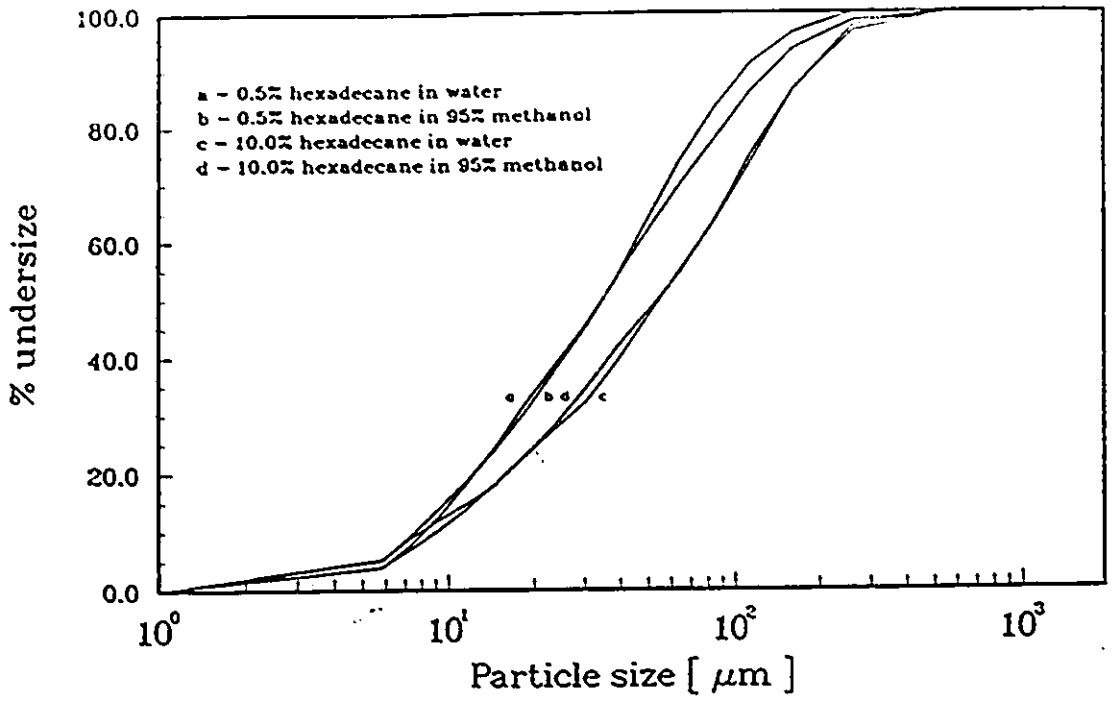

Figure 4.5: Suspending liquid influence on Devco coal agglomerate size distribution.

Figure 4.6 is a plot of an enlargement factor F, (discussed below) vs. agglomerate oil level. The enlargement of the lignite samples was slight compared to the higher rank samples. Several measurements (ie; 10 or more) were made with each agglomerate sample and the standard deviation of measured means was always less than 1 μm.

4.2 Flotation Results

As previously introduced, the combination of oil agglomeration and flotation produces good separation at low oil levels for fine coal recovery. Yield-ash results were shown for the agglomeration flotation of a Pennsylvania coal in figure 1 [8]. The results compare well with other recovery methods.

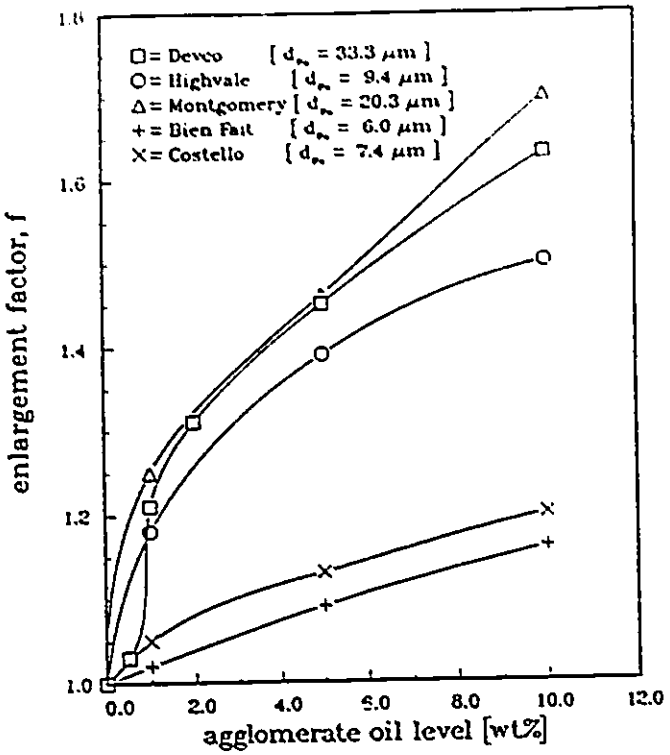

Figure 4.6: Enlargement factor vs. oil level for all samples. (for hexadecane bridging liquid)

4.2.1 Agglomerate recovery and ash removal

The agglomerate flotation recovery and ash rejection data are shown in figures 4.7 and 4.8. The % ash rejection is defined as,

$$\frac{([\%\text{ ash in feed}] - [\%\text{ ash in cleaned product}])}{[\%\text{ ash in feed}]} \times 100$$

Two oils were used in this work, hexadecane and No. 4 fuel oil. The fuel oil was used primarily to show the recovery properties of the lignite samples. They simply did not agglomerate sufficiently to be recovered with hexadecane, but some recovery, illustrative of their wettability, was achieved with the heavier, more viscous, No. 4 fuel oil. As reported by Capes and Germain [112], more complex oils contain some inorganic polar species such as nitrogen, oxygen and sulphur. These functional groups impart a greater oil wettability to a lower rank, more hydrophilic coal surface such as lignite.

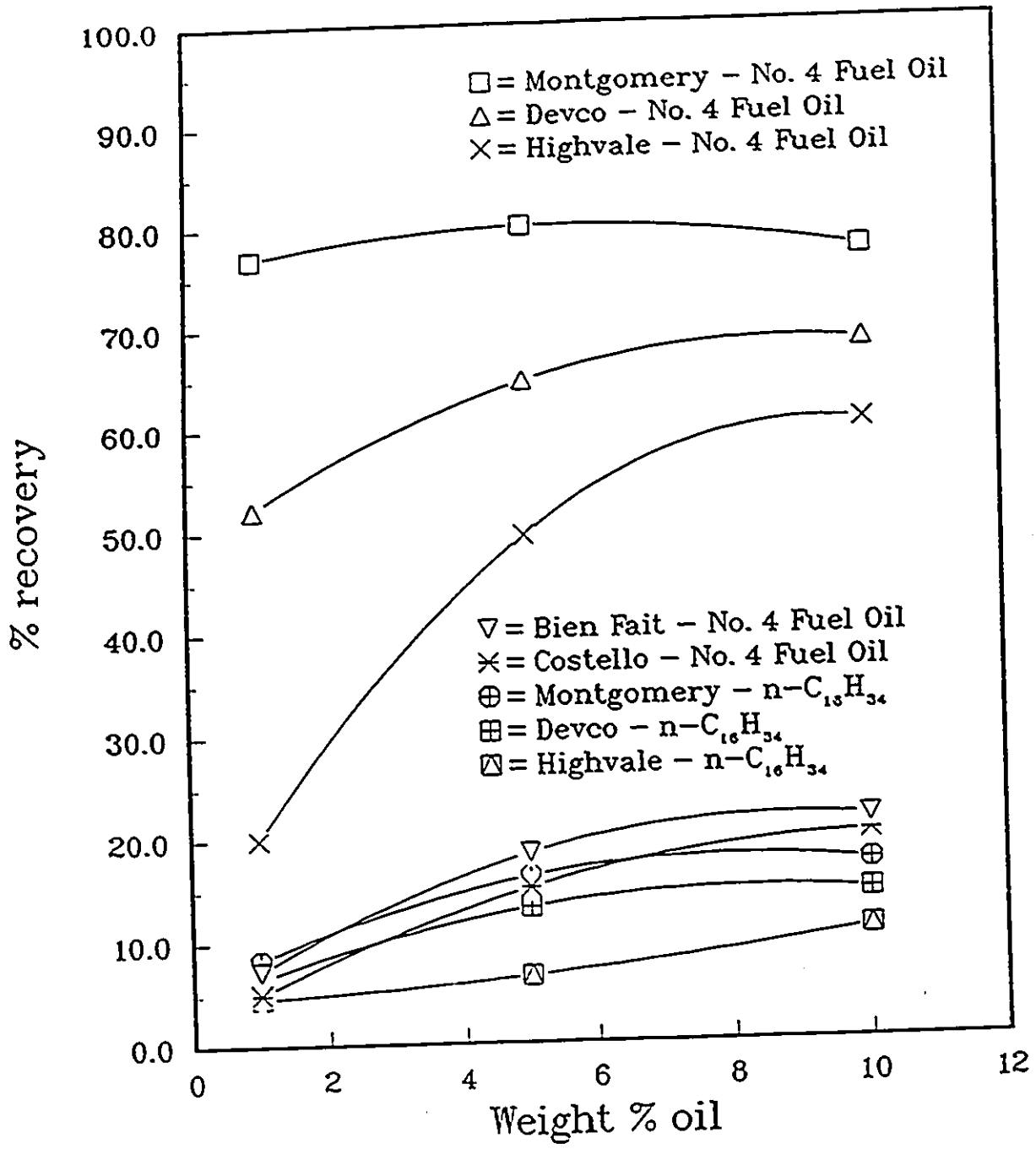

Figure 4.7: % recovery vs. weight% oil.

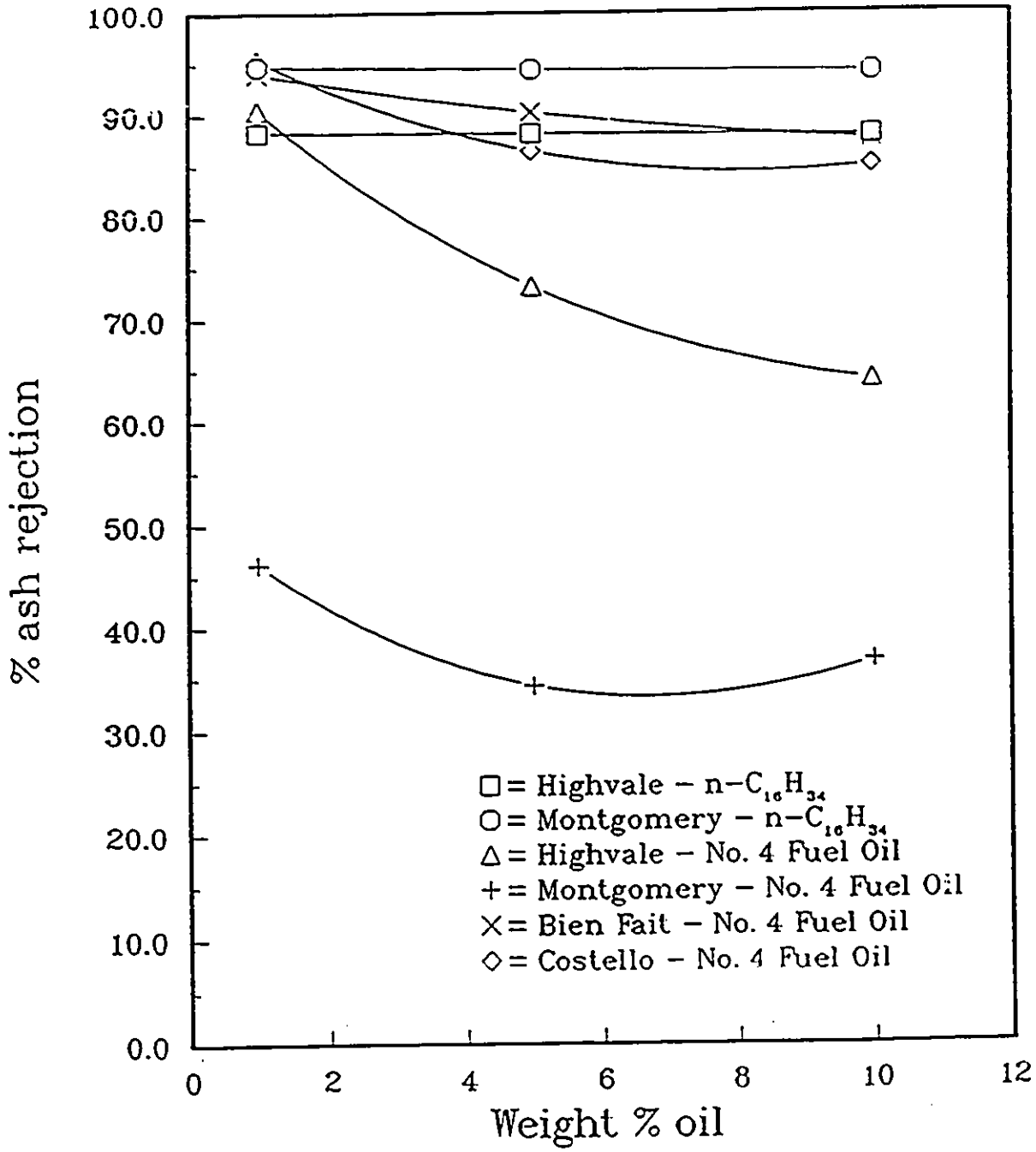

Figure 4.8: % ash rejection vs. weight% oil.

4.2.2 Relation of pilot tests to laboratory work

Some consistency of method was required for the laboratory work, to have it comparable to pilot studies using continuous float cells, and subsequently, the computational simulation of the recovery process. Air is incorporated into this system, but energetically, a coal-oil interface would be formed first. Thus, the sequence of mechanisms for these experimental results, and the computational work which is discussed later, is conserved.

In some work conducted on various coal samples from the Quintette mine in British Columbia, data clearly show that the laboratory float test method has been brought suitably into line with the continuous float cell operation in terms of similarity of result [113]. That is, the conditions in the laboratory cell and the pilot cells were such that the degree of mixing and air-solids contact producing the flotation result were similar. Results for several different coal blends are presented in figure 4.9. Data on or near the $y = x$ line indicate agreement between the continuous pilot cells and the laboratory float cell test. The pilot data were obtained at oil levels ranging from 0.5 to 2.5 weight %, at solids flow rates of up to 2 tonnes/hr. The float cell throughput for the pilot work would thus be of the same order of magnitude as the one modeled in the numerical simulation. The data plotted in figure 4.9 show quite adequate correlation.

4.3 BEM Results

There are two options for implementing the unsteady primitive-variable BEM formulations by Tosaka. They are both outlined in [75]. The first method makes use of a time-dependent fundamental solution. The second method uses a finite difference method for the time derivative. The finite difference time derivative method was chosen as it was far more suitable for variable geometries. Moving boundary aspects are more thoroughly discussed in [76].

The coding of the 2D unsteady primitive-variable full Navier-Stokes BEM was a substantial job in itself. The full working code including grid generator, pointer

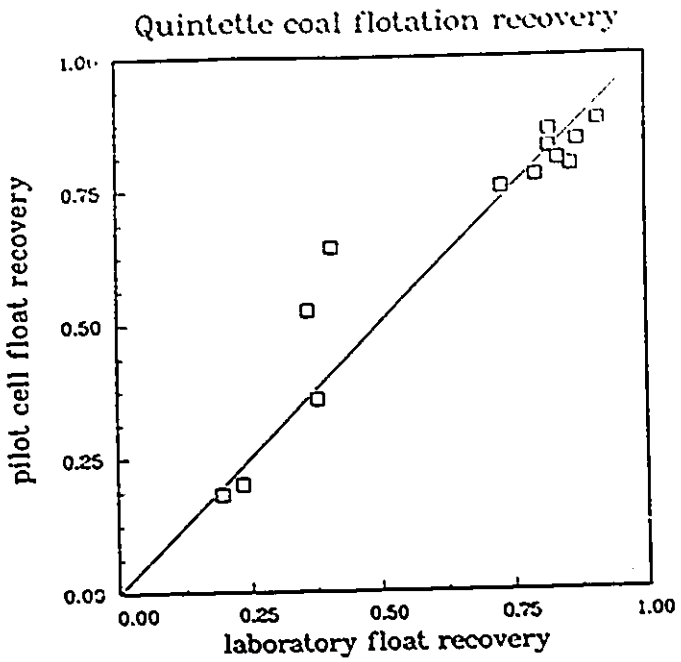

Figure 4.9: Comparison of pilot plant and laboratory flotation recovery data for Quintette coal blends. (Based on pilot plant sampling of feed and tailings.) From [113].

routines, problem specifier, matrix assembler and equation solver comprised over 4000 lines of FORTRAN. To test its correctness, a two dimensional driven cavity flow was selected as the test implementation for the code. The same BEM formulation, but with the time-dependent fundamental solution, had already been applied to this problem, and would thus serve as a benchmark for verification [114]. Hence, the same boundary conditions were adopted. For this simulation, no separate treatment of the pressure equation was made. The momentum equations contain velocity and traction terms which implicitly make use of a relative or reduced pressure which need not be explicitly decoupled. (ie; equation 2.7)

Figure 4.10 illustrates the problem statement. A unit-length square is used, with an impulsively started sliding lid moving at unit velocity to drive the flow in the cavity. The time step chosen was $\Delta t = 0.5$sec and a Reynolds number of 10^4 was used. The Reynolds number is defined as $\mathrm{Re} = Lu\rho/\mu$ for the cavity flow, where L is the unit length, u is the sliding velocity, ρ is the density and μ is the viscosity. The

density and viscosity were set to unity. For comparison purposes, the final time was at $t = 28$ seconds. The grid used for computation is shown in figure 4.11.

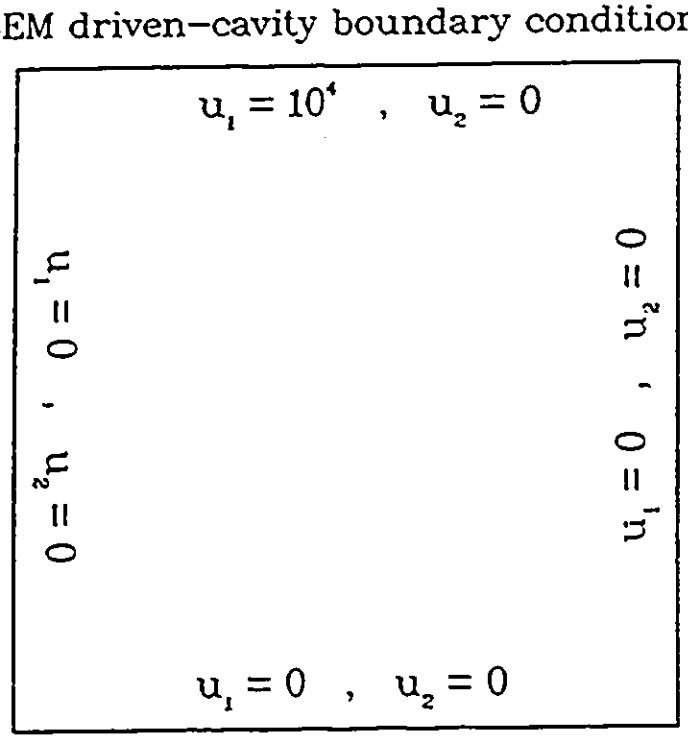

Figure 4.10: Boundary conditions for BEM driven-cavity flow simulation.

Figure 4.12 shows a series of velocity fields for this driven-cavity simulation. It can be seen that the vortex center approaches the geometrical center of the cavity as time progresses.

By interpolation along each horizontal and vertical grid line in the domain, a point can be found where the velocity in the central vortex is zero in respectively the y and x-directions. The intersection of these two loci is taken to represent the center of the vortex at each time level. For example, at $t = 5$, the vortex center is located at $(x, y) = (0.579, 0.511)$. Figure 4.13 illustrates this. Figure 4.14 shows the change of the vortex center position with time, and from $t = 15$ to $t = 28$, there was little change, indicating that the flow is approaching a steady-state.

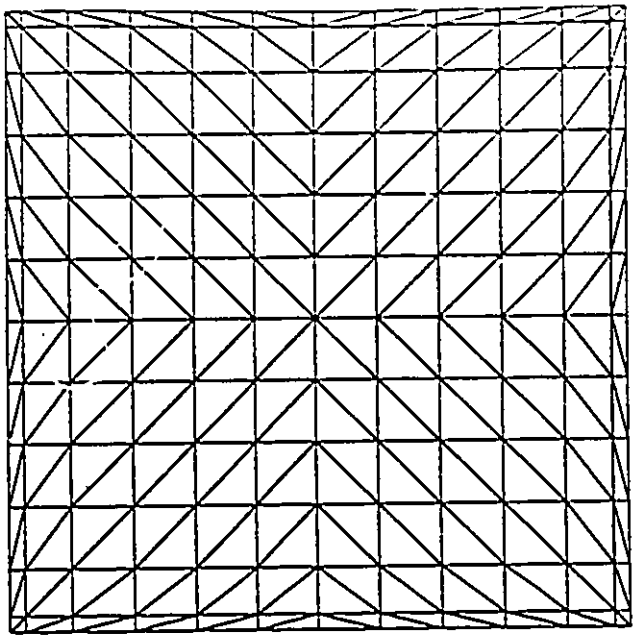

Figure 4.11: Grid for BEM driven-cavity flow simulation.

4.3.1 Comparison of BEM and Finite-Volume Calculations

The finite-volume code was also adapted to solve the same driven-cavity problem as the BEM code. A modification was required for the MD-PHASE code, as its default condition is to treat walls as stationary. The u-velocity source terms required revision. For a boundary, the sources S_B can be expressed as,

$$S_B = -S'_P \phi_P + S'_U$$

Above, S' refers to source terms which may be modified due to proximity to the boundary. For u-velocity,

$$\begin{aligned} S_B &= \frac{\mu A}{Y} (u_w - u_P) \\ &= -\frac{\mu A u_P}{Y} + \frac{\mu A u_w}{Y} \\ &= -S'_P u_P + S'_U \end{aligned} \tag{4.2}$$

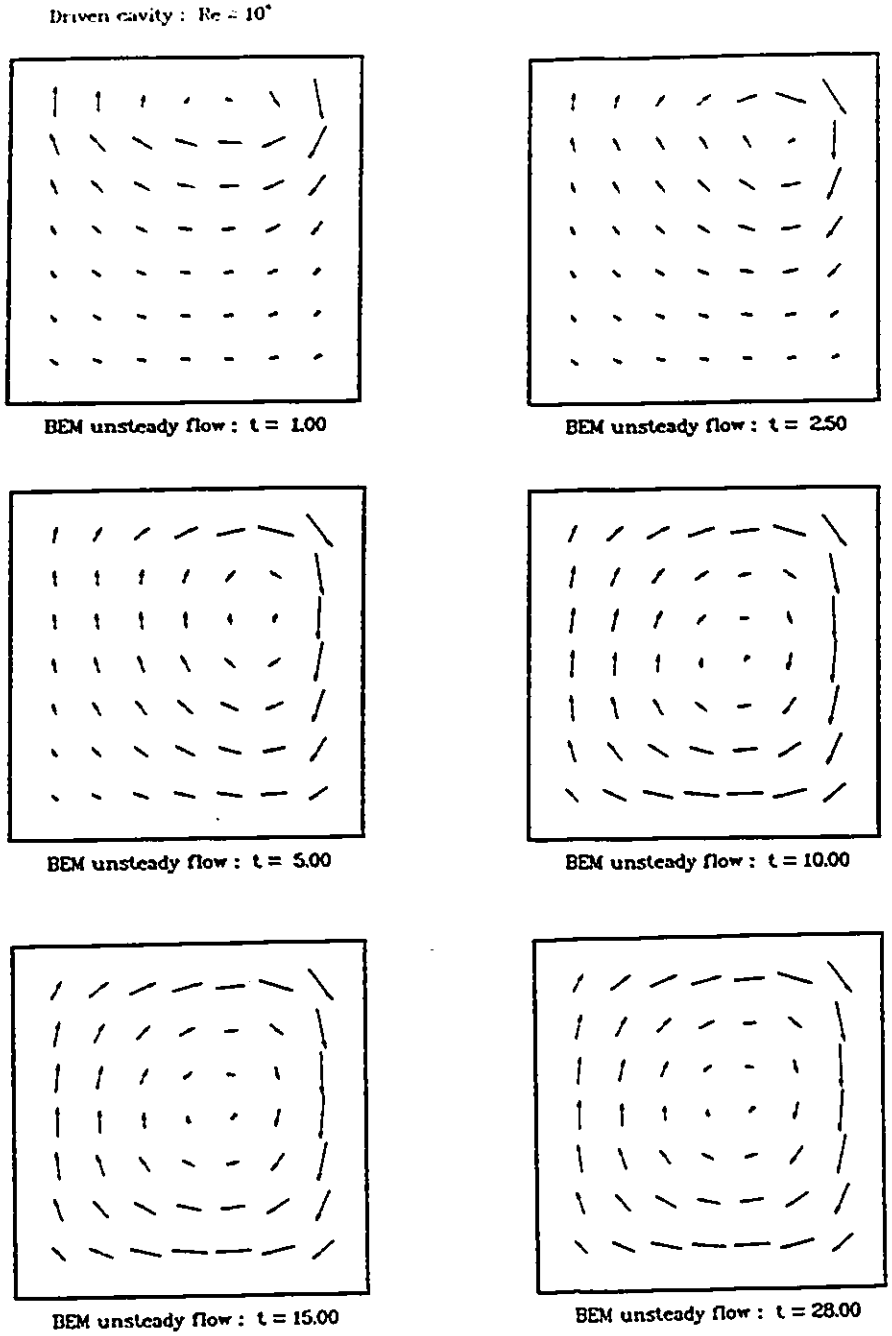

Figure 4.12: Flow field solutions for BEM driven-cavity simulations, at $t = 1.0, 2.5, 5.0, 10.0, 15.0$ and 28.0 seconds. (2D velocity vectors)

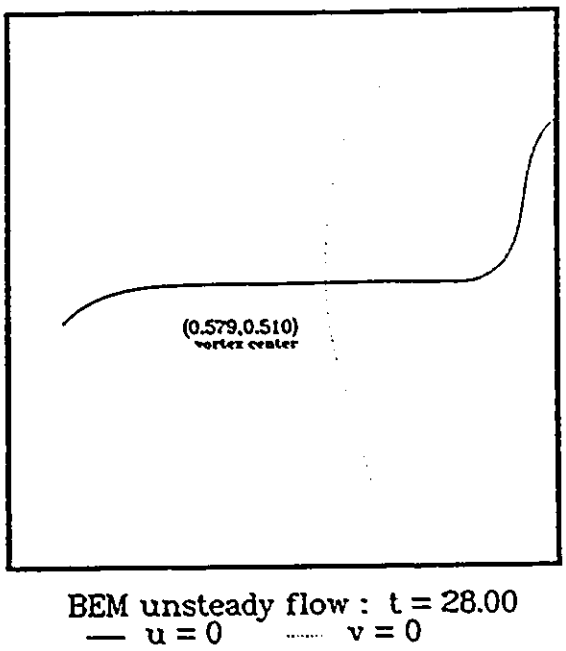

Figure 4.13: BEM vortex center at $t = 28$sec.

Thus, for the moving boundary, an additional non-zero source term is required, namely,

$$S'_U = \frac{\mu A u_w}{Y}$$

Very similar results were obtained for the MD-PHASE simulations in comparison with the BEM results (see figure 4.15).

Simply applying the straightforward BEM program to the same problem was done with successively lower Reynolds numbers, down to about 800. Below this value, the simulation resulted in unstable solutions which no longer converged. Reynolds numbers in the region of 100 to 400 are typical of the bubble-particle interaction for the study of micro-flotation hydrodynamics [22]. Thus, work with the BEM was not pursued since stable convergence could not easily be achieved in the required Reynolds number range.

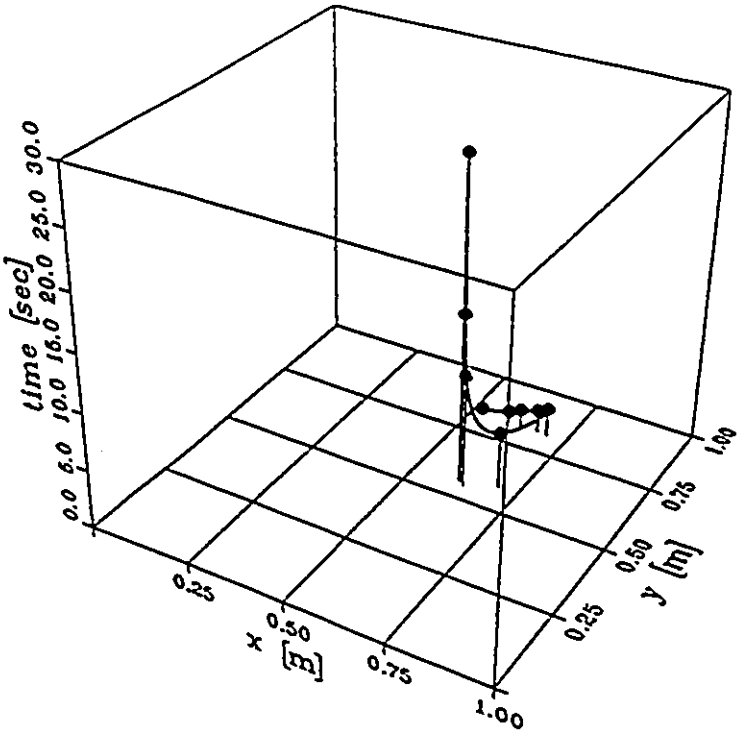

Figure 4.14: BEM predicted vortex migration over time.

4.4 3-phase Finite-Volume Model - Initial Calculations

A test simulation devised by Lai [40] was run to inspect the workings of the 3-phase with mass transfer model. A flow is passed through a cylindrical tube with the inlet profile divided into two regions. Using only gas flow at first, the solution was matched identically to that of Lai to verify general correctness of boundary conditions and inputs.

Figure 4.16 shows the grid that was used for this simulation. A coarse grid was used since what was of interest was the general convergence behaviour of the equations, not specific details from the solution itself.

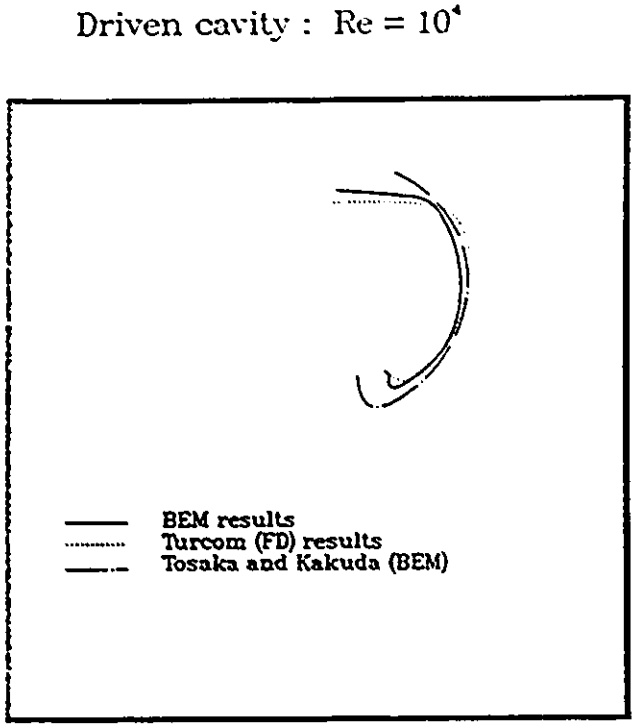

Figure 4.15: Comparison of BEM and finite-volume transient vortex migration. Also shown are solutions from [114].

4.4.1 Tube flow - simulation conditions

The following conditions were applied to the tube flow simulation. The total flow rate was fixed to a Reynolds number of 10^5. The diameter ratio of the inner to outer inlet profiles was 0.707. The outer diameter, D_o, was 0.09553 meters. The axial distance considered was $3.739D_o$. The ratio of the mean velocities between the outer and inner inlets, V_o/V_i, was 0.169. The mean velocity through the tube was 18 m/s. The inlet profile was flat in the outer portion and the inner portion had a power law profile given below. Uniform distributions of k and ϵ were assumed at the inlet plane.

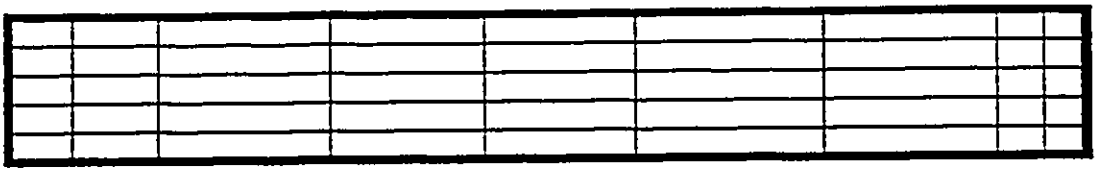

Figure 4.16: Tube flow MD-PHASE grid.

For the inner inlet:

$$v_i = 0$$

$$u_i(r) = u_{MAX}\left[\frac{2\left(\frac{D_i}{2}-r\right)}{D_i}\right]^{\frac{1}{7.1}}$$

where: $u_{MAX} = 1.22V_i$ from [88]

$$k_i = IV_i^2 \qquad I = 0.005$$

$$\epsilon_i = \frac{k^{1.5}}{\ell} \qquad \ell = 0.025D_i$$

Above, I is the turbulence intensity, and ℓ is the turbulence mixing length.

For the outer inlet:

$$v_o = 0$$

$$u_o = V_o$$

$$k_o = IV_o^2$$

$$\epsilon_o = \frac{k^{1.5}}{0.025\left(D_o - D_i\right)}$$

4.4.2 Boundary Conditions for tube flow

The boundary conditions for this problem are listed in table 4.1. Figure 4.17

boundary	u	v	k	ϵ
wall	0	0	Couette flow	Near-wall values from length scale
symmetry axis	$\frac{\partial u}{\partial r} = 0$	0	$\frac{\partial k}{\partial r} = 0$	$\frac{\partial \epsilon}{\partial r} = 0$
outlet plane	mass balance	$\frac{\partial v}{\partial z} = 0$	$\frac{\partial k}{\partial z} = 0$	$\frac{\partial \epsilon}{\partial z} = 0$
outer inlet	V_o	0	k_o	ϵ_o
inner inlet	$u_i(r)$	0	k_i	ϵ_i

Table 4.1: MD-PHASE tube flow boundary conditions. From [40].

shows the solution for the tube simulation with one phase. Velocity vectors and pressure contours are given. The arrows on any of the following plots are pointed in the direction of the local velocity vector and are shown with a length proportional to the magnitude of the velocity. The two inlet profiles can be seen to merge in the sense that the slow profile is accelerated and the fast profile is decelerated as they advance in the z-direction. This homogenization is due to turbulent mixing and momentum

transfer through the action of the viscosity. A more uniform profile is not achieved, since the length of the tube is too short. This result demonstrates expected flow behaviour.

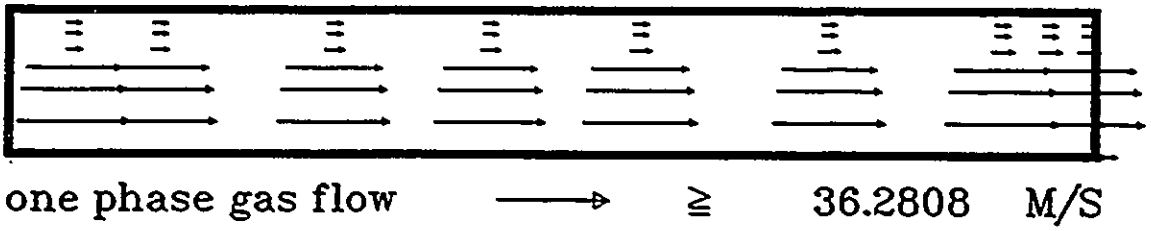

Figure 4.17: Gas flow in tube - test case.

4.4.3 3-phase tube flow

The same basic simulation was run in the tube, but modified by the addition of gas and solid dispersed phases. These dispersed phases were included only in the outer portion of the inlet. Their volume concentrations were 10% each. They were given the same inlet velocity as the liquid phase and were specified with the same velocity boundary conditions as the liquid phase. The outlet condition was not required, since the equation for determining the local volume concentrations of a dispersed phase is essentially a mass balance over each cell, so once converged, a mass-flux correction would be redundant. In fact, a mass-flux correction for the dispersed phases hampered convergence as it interfered with the establishment of the cell to cell mass balance network throughout the flow domain.

The three phases in this simulation were input with the physical properties listed in table 4.2. The units are based in the m-kg-s system.

Since the flow in this case is essentially unidirectional, the oscillatory convergence behaviour did not arise in the tube flow. The program could be run in its entirety without output inspections and restarts. The results of this simulation are shown

phase	density	viscosity	diameter
liquid	997.1	$8.94 \cdot 10^{-4}$	N/A
gas	1.2	$1.42 \cdot 10^{-6}$	2.5 mm
solid	1200.0	N/A	50 μm

Table 4.2: Physical properties of the three phases.

in figures 4.18 to 4.20. Figure 4.18 shows the velocity vectors of the three phases. In the cases of the dispersed phases, the vector was omitted if the volume fraction of the phase was lower than 10^{-10}. Figure 4.19 shows the concentration profiles of the dispersed phases as they pass through the tube. The bubble-loading plot shows contours of the ratio of number of attached particles per bubble throughout the flow domain. The loading grows steadily as the flow advances through the tube. Figure 4.20 shows plots of the two turbulent parameters k and ϵ as well as the pressure contours. Note that these quantities are most variable in the region where the mixing of the two streams occurs.

4.5 Finite-volume model - initial float-cell results

The algorithms which were tested in the tube flow simulation were next one by one implemented in a float cell geometry. The grid used in this simulation is shown in figure 4.21.

This is modeled after a *Minpro* float cell with dimensions given in table 4.3.

4.5.1 Liquid phase results

The flow pattern for a one-phase liquid simulation was determined. The inlet velocity was 0.5 m/s, which is the inlet rate which would transport the eventual solid

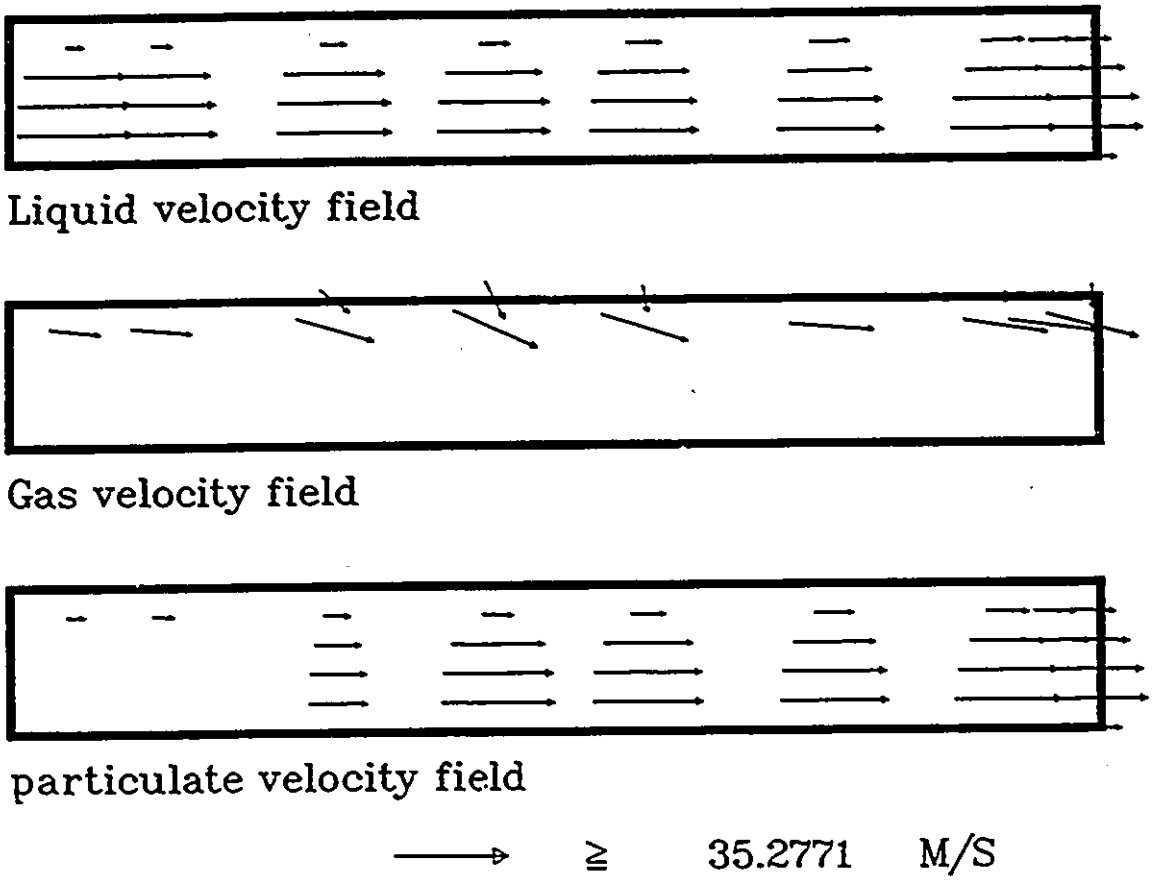

Figure 4.18: 3-phase tube flow - velocities.

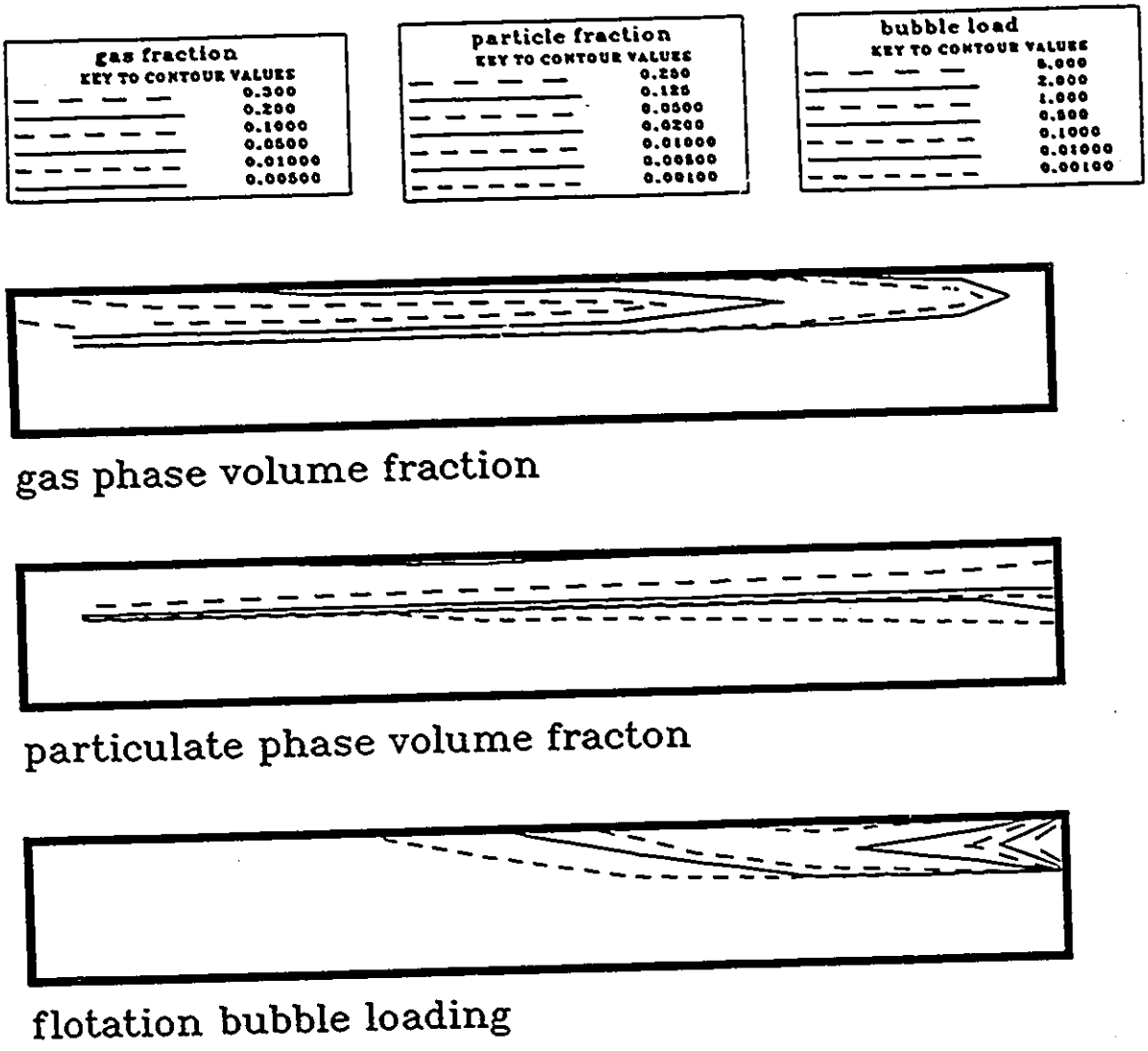

Figure 4.19: 3-phase tube flow - dispersed phases.

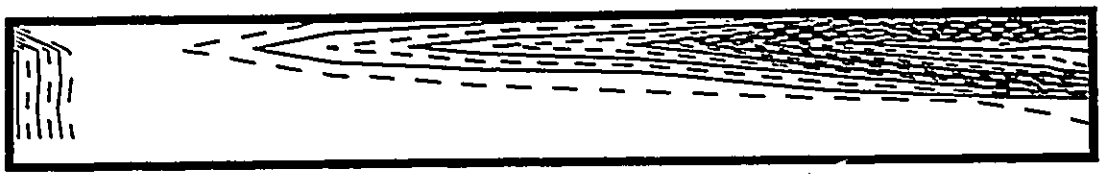

3–phase dissipation energy

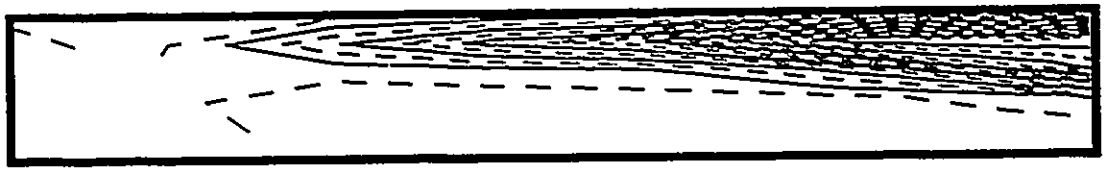

3–phase turbulence intensity

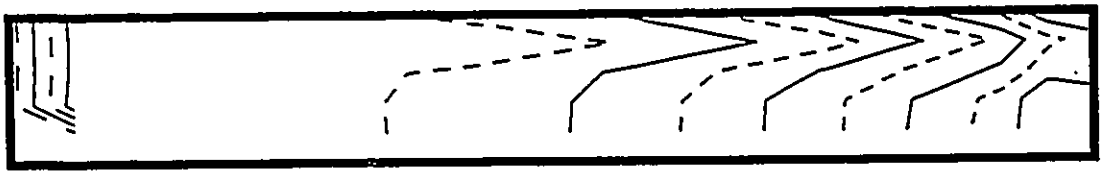

3–phase pressure contours

Figure 4.20: 3-phase tube flow - turbulence and pressure.

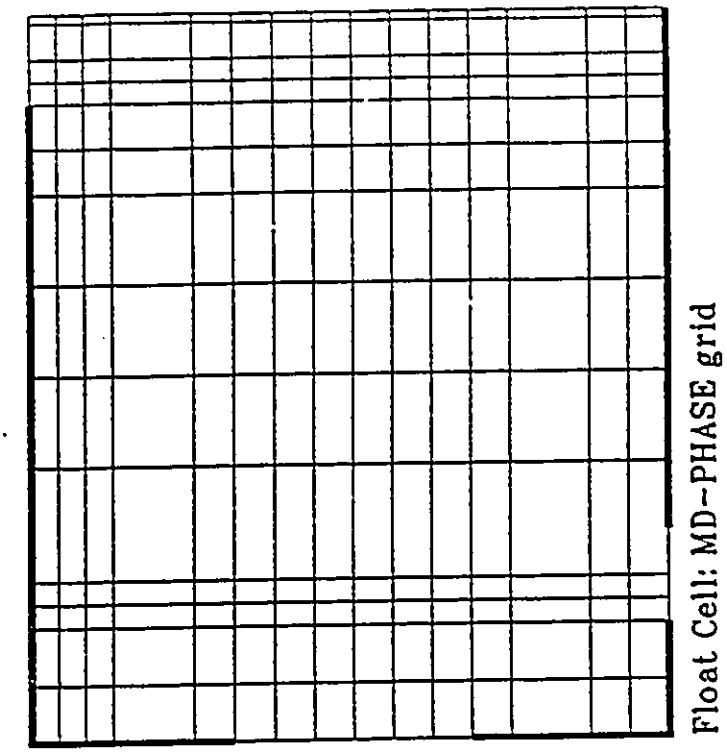

Figure 4.21: Grid used for finite-volume simulations in the float cell.

portion of the slurry at 4.3 t/h. For all inlets considered here, and in all subsequent simulations, the velocity profiles were considered flat. On the top open-to-air surface the condition of $u = 0$ was imposed. A zero-gradient v-velocity was imposed at the overflow weir outlet. The velocity field obtained is shown in figure 4.22.

4.5.2 Liquid and Gas results

The flow pattern for a two-phase liquid and gas system was simulated. At the bottom inlet, the gas was given an inlet velocity of 0.05 m/s in the vertical direction. Its volume fraction, α_G, was 0.5, to give an air consumption of about 1.5 m^3/min., which is typical of flotation machines of this size. The gas phase was allowed to exit through the top surface with a zero-gradient boundary condition, and could also be entrained out the weir with a zero-gradient boundary condition as well. The bubble diameter chosen was 2.5mm, which is in a typical range of bubble sizes for this type of operation [115]. The velocity field for this simulation is shown in figure 4.23.

width	1.42 m
height	1.6 m
sparger width	52.7 cm
slurry inlet diameter	20 cm
weir drop	5 - 15 cm

Table 4.3: Float cell dimensions.

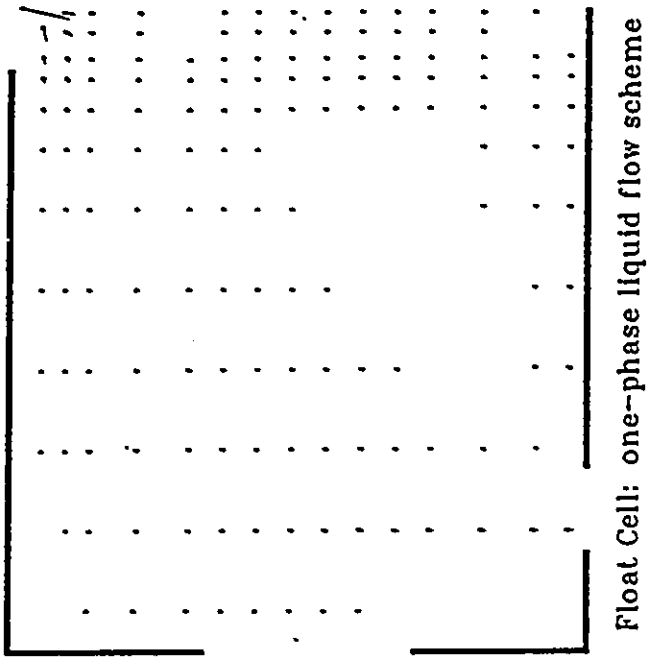

Figure 4.22: One-phase liquid velocity in float cell.

The bubble motion interacts with the liquid motion to produce a net result that is characteristic of the tendencies of both phases. The gas vectors in figure 4.23 can be seen to be exiting the top open surface. Run-time control of the program as discussed in section 3.3.10.4 was required to achieve correct convergence, since the gas phase and the liquid phase exhibit opposing tendencies which would bring a numerical solution

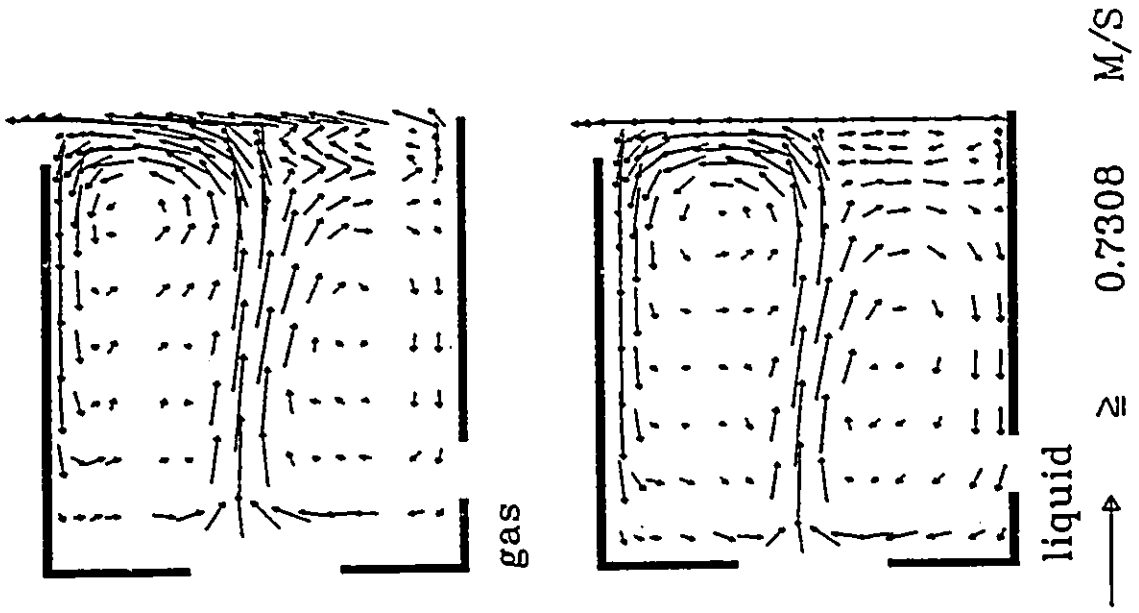

Figure 4.23: 2-phase liquid and air velocity fields in the float cell.

into a state of suspended oscillation.

4.5.3 Slurry flow results

The code was tested with a 2-phase liquid and solid slurry simulation. The solid phase was introduced as particles with a 50 μm diameter at a solids volume fraction, $\alpha_S = 0.10$. The solid phase was subject to the same boundary conditions as the liquid phase. The effect of gravity was marked since the inlet velocity is very low at 0.05 m/s. Two results are shown; -the first with the effects of gravity removed, and the second with a standard vertical gravity force in effect. The relative motion arising from the density differential between the phases accounts for the difference in the two results. The velocity field for these simulations are shown in figures 4.24 and 4.25.

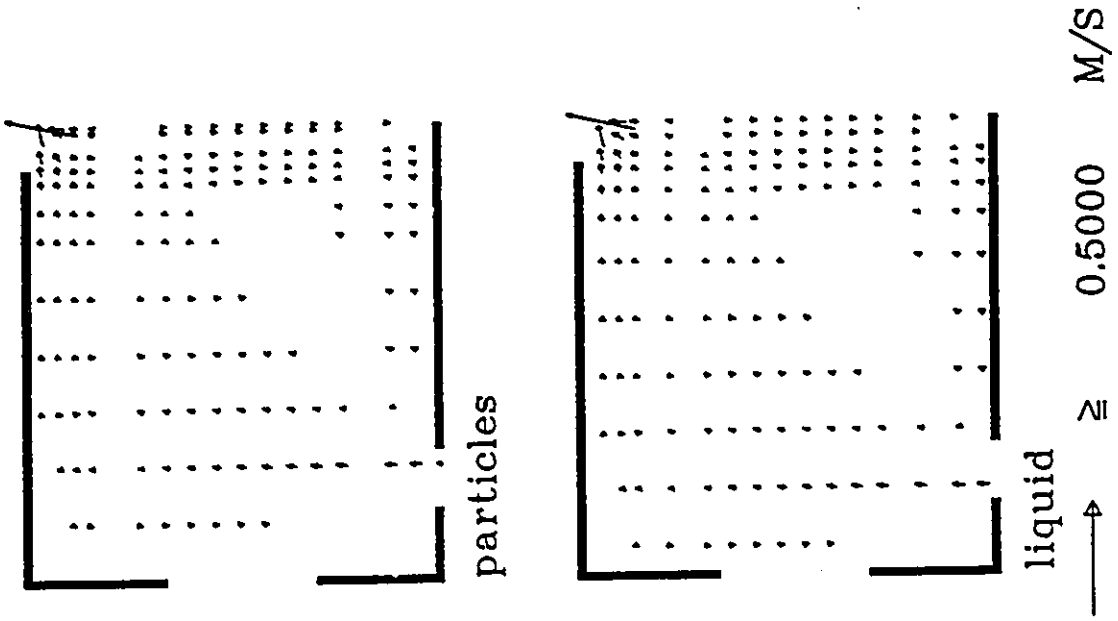

Figure 4.24: 2-phase liquid and solid velocity fields in the float cell with no gravity force.

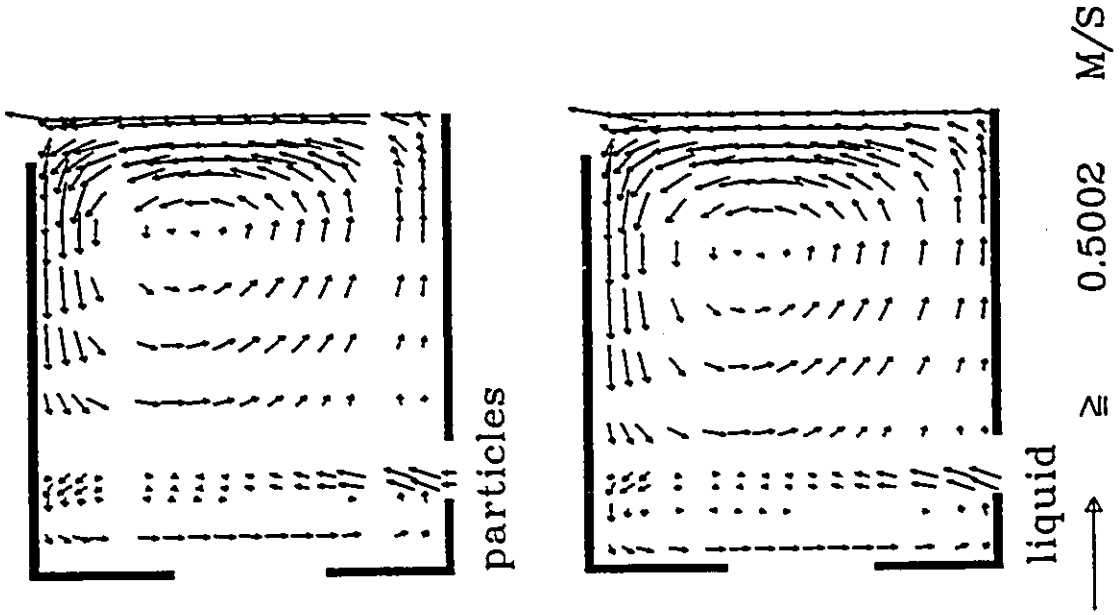

Figure 4.25: 2-phase liquid and solid velocity fields in the float cell with gravity force.

4.6 3-phase Finite-Volume Model - Float-Cell Results

The boundary conditions for the three phases were kept as described previously. Run-time control was achieved by running all three phases at once, but with the frequency of iteration for the dispersed phases reduced until a stable basic flow field pattern based on liquid transport was established. As discussed in section 3.3.10.4, the frequency of iteration for the dispersed phases was gradually increased until a ratio of 1 : 1 was stable, and convergence could be achieved. Figure 4.26 shows the velocity patterns and pressure contours in the float cell for a 3-phase system with no mass transfer between the dispersed phases.

The vector fields shown in figure 4.26 follow expected trends.

When the mass transfer was activated in the simulation, the flow behaviour changed due to the density effects on the bubble motion. The opposing tendencies of the equations for the motion of the three phases made it prohibitively lengthy and tedious to obtain a convergence below a tolerance of 10^{-3}. This requirement was relaxed to 10^{-1} without significant changes in flow field patterns obtained and results pertaining to flotation performance. It should be emphasized as well, that this convergence criterion of 10^{-1} is for the sum of residuals over the whole domain. Thus for a 16×14 grid, the individual residual for each node will be on average at least two orders of magnitude less than the convergence tolerance.

The difference in the results for the two tolerances of 10^{-1} and 10^{-3} typically arose in the third significant digit of any flow field variable. To provide some perspective on run-times, with a tolerance of 10^{-1}, solutions were obtained usually within 4000 iterations at a CPU time of approximately 16-18 minutes. For a tolerance of 10^{-3}, firstly, the oscillation control was less straightforward. Not only was iteration frequency adjustment necessary, but also monitoring and control of the under-relaxation factors, thereby requiring usually over 15,000 iterations with run-times upwards of one hour. The difference in the basic result did not warrant the extra computation. Tables E.1 and E.2 in Appendix D give all nodal values of the bubble particle loading for

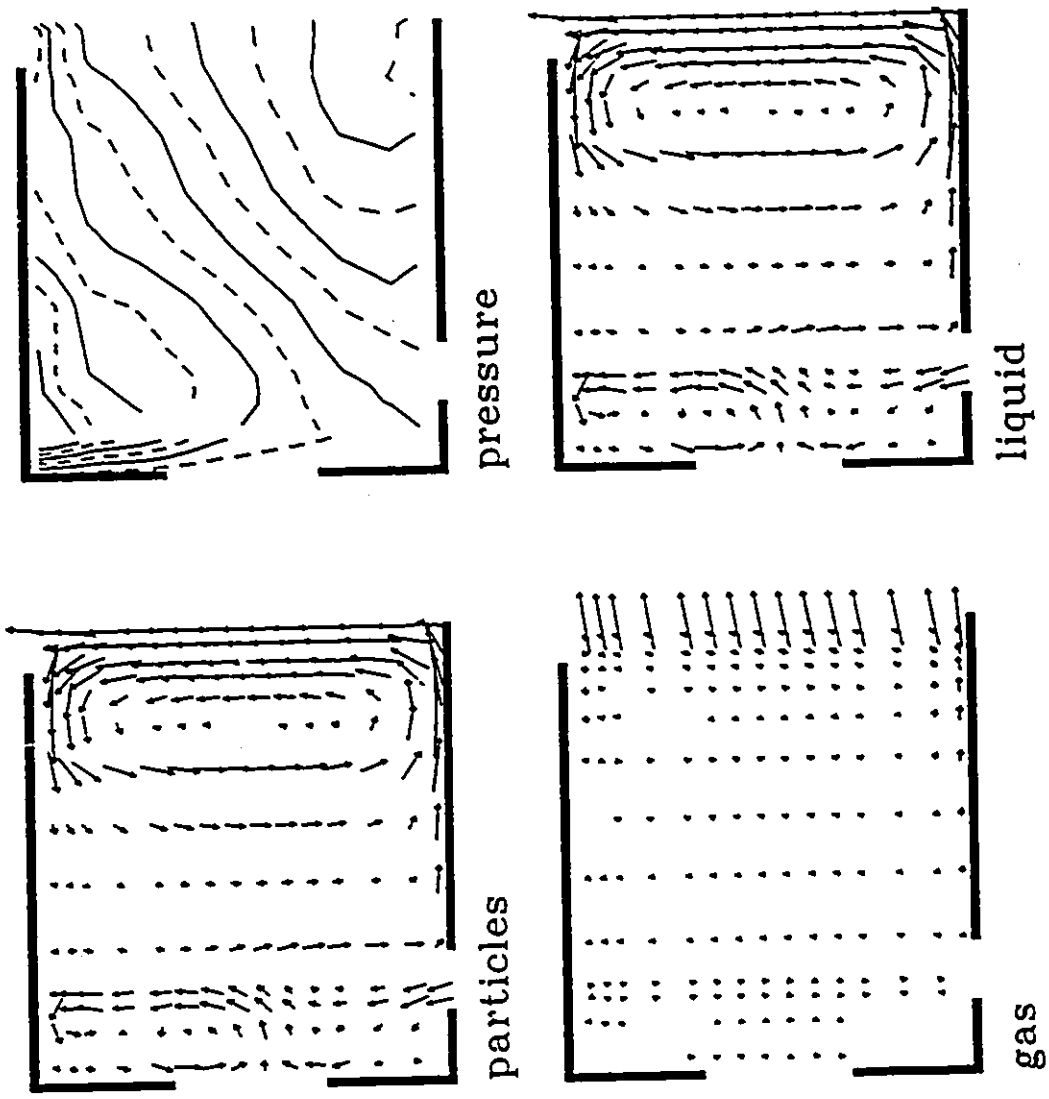

Figure 4.26: 3-phase float cell flow fields.

convergence criteria of 10^{-1} and 10^{-3}.

A data set for the study of the flotation parameters was constructed by running the 3-phase simulation for a combination of particle diameters (corresponding to the agglomerate sizes of the Devco coal-oil agglomerates formed across the range of 0 to 10 wt% oil) and a variable for the attachment efficiency, r_a, which was introduced in equation 3.83. This data set can then be used to deduce a relation between the properties of the floated material and its recovery.

Figures 4.27 to 4.29 show a full 3-phase flotation flow field simulation result. This case had $d_P = 43.6\mu$m corresponding to an coal-oil agglomerate made with 2 wt% oil and the collection efficiency, $r_a = 0.20$.

For the example illustrated in the above figures, the flux of solids accompanying the gas phase out the top exit was 0.447 kg/s, giving a flotation recovery for this case of 37.2%.

For the other cases run, the graphical output is very similar. The same basic trends are followed. What can be noticed is slight streamline differences for heavier particles. Two cases are shown in figures 4.30 and 4.31. Another feature evident in figures 4.30 and 4.31 is that for the 60 μm case, the streamlines travel at the top of the cell in the y-direction as they exit over the weir. Their greater settling tendency does not enable the flux in this case to transport them up over the weir as with the 20 μm particles. A stronger circulation is established in the top half of the cell to create a current of sufficient flux to carry the unfloated solids out over the weir. For the case of slurry flow with no gravity effects, (figure 4.24), the streamlines can be seen to go essentially from the inlet to the outlet, with recirculation zones established in "dead" regions where little of the main flux is transported.

Further, figures 4.32 and 4.33 show streamlines calculated for bubble diameters of 2.5 and 1.0mm respectively. The particle diameter in this case is 60 μm. The density effects here are less straightforward as the bubble loading increases in the x-direction through the cell, but the greater buoyancy force on the larger bubbles renders them less subject to the trajectory deviations brought about by the slurry motion.

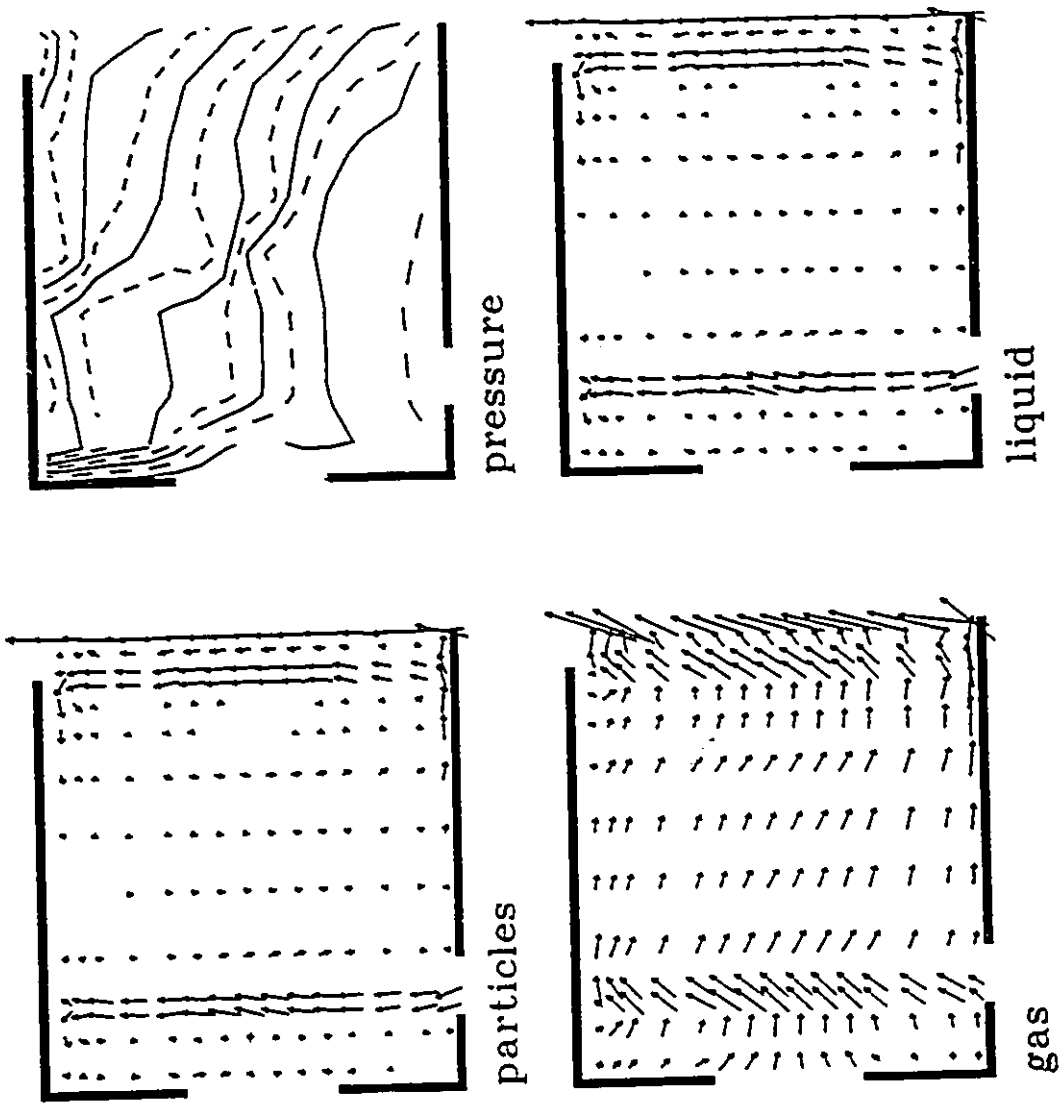

Figure 4.27: 3-phase flotation velocity and pressure fields. ($d_P = 43.6\mu$m and $r_a = 0.20$.)

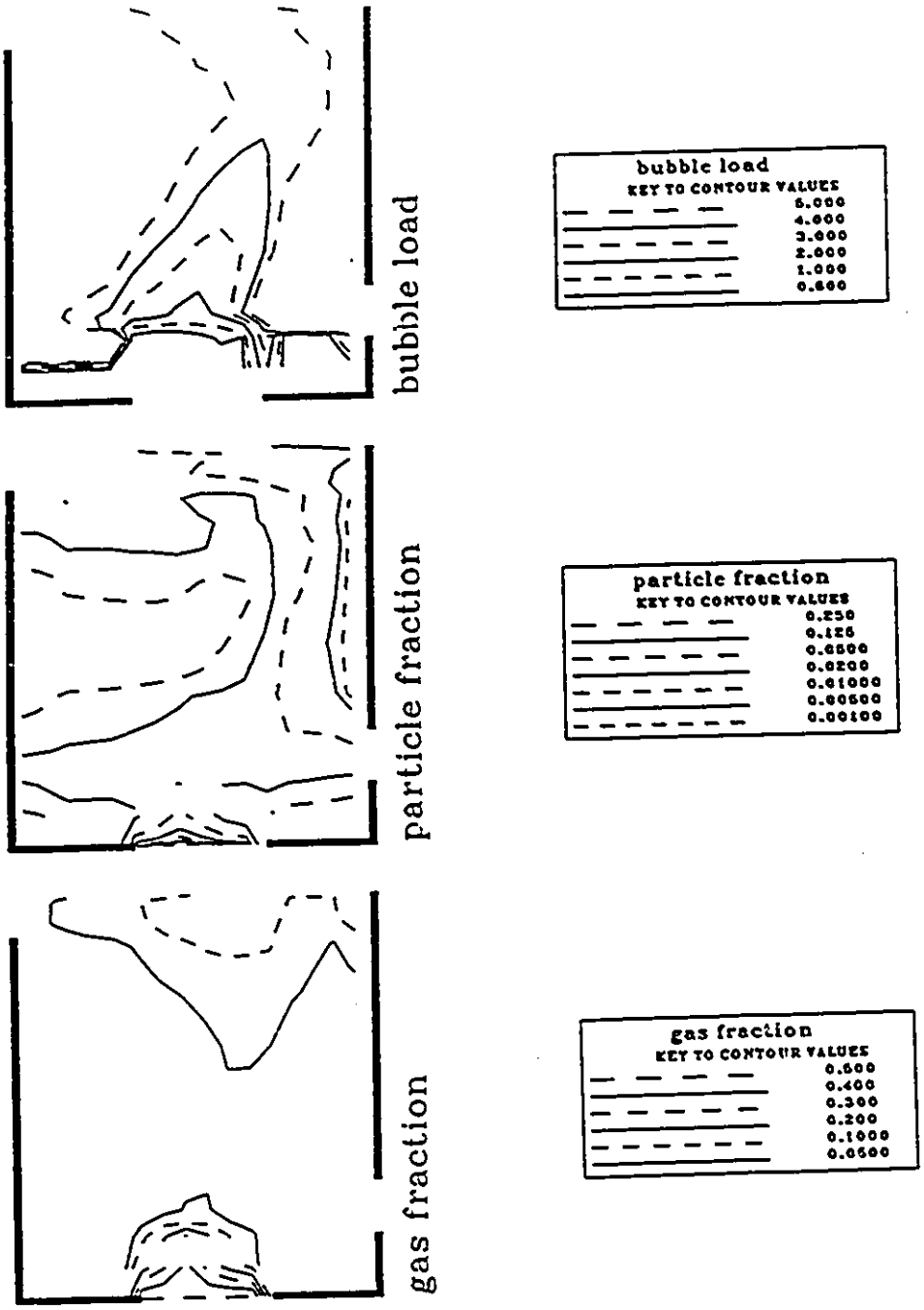

Figure 4.28: 3-phase flotation concentration and mass transfer contours. (d_P = 43.6μm and $\tau_a = 0.20$.)

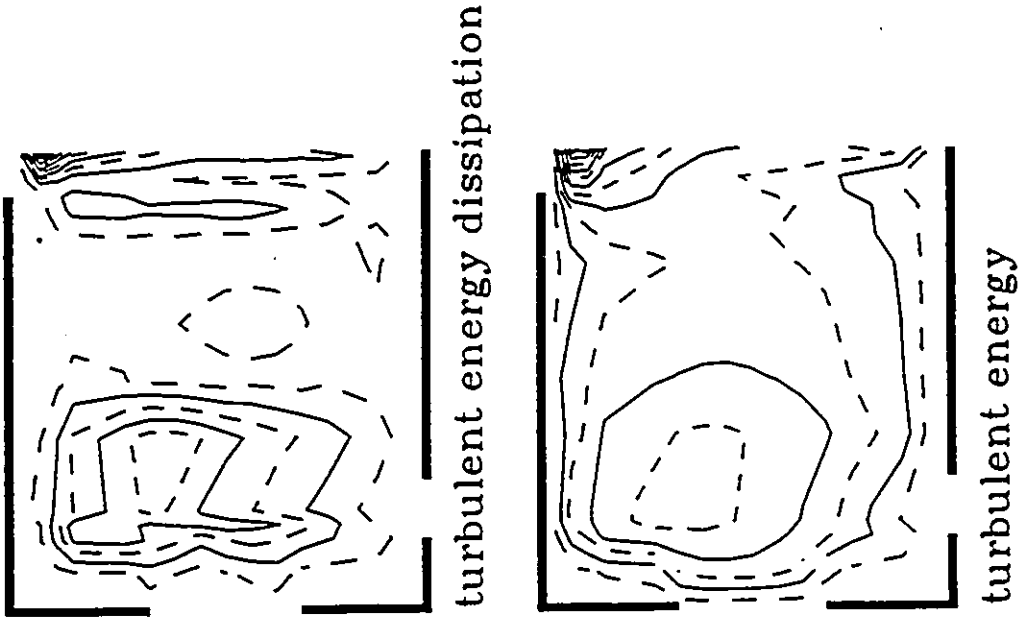

Figure 4.29: 3-phase flotation turbulence contours. ($d_P = 43.6\mu$m and $r_\alpha = 0.20$.)

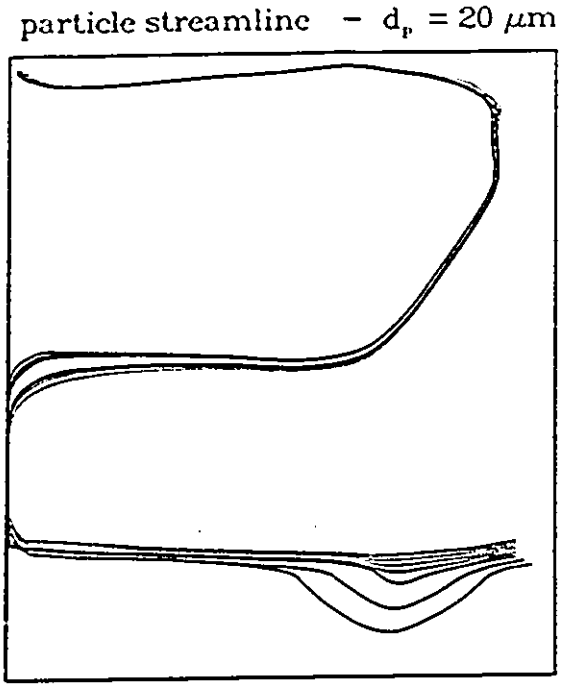

Figure 4.30: Particle streamline - $d_P = 20\mu$m.

4.7 Post-processing of flotation simulation

Pursuant to the results presented in the previous section, the flotation recoveries can be tabulated as a function of the simulation input parameters.

Figure 4.34 shows the recovery of the coal-oil agglomerates as determined by the simulation as a function of r_α, with the agglomerate diameter as a parameter. Figure 4.35 shows the recovery of the coal-oil agglomerates as a function of d_P, with r_α as a parameter.

To further enable these results to be compared with known basic flotation behaviour, the effects of altering the bubble diameter were briefly examined. Figure 4.36 shows the calculated recovery as a function of particle diameter for various bubble sizes at $r_\alpha = 0.20$.

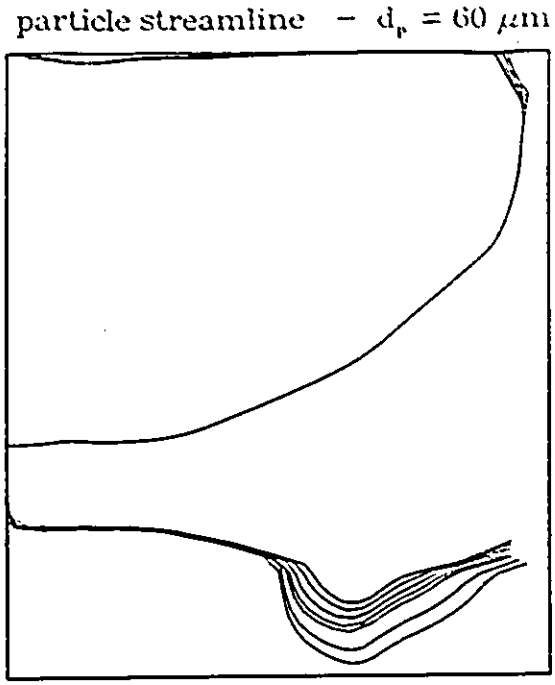

Figure 4.31: Particle streamline - $d_P = 60\mu$m.

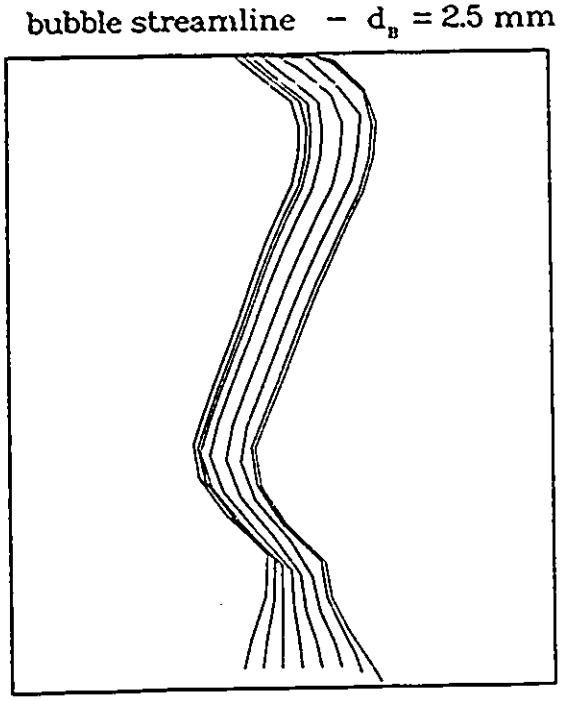

Figure 4.32: Bubble streamline - $d_B = 2.5$ mm.

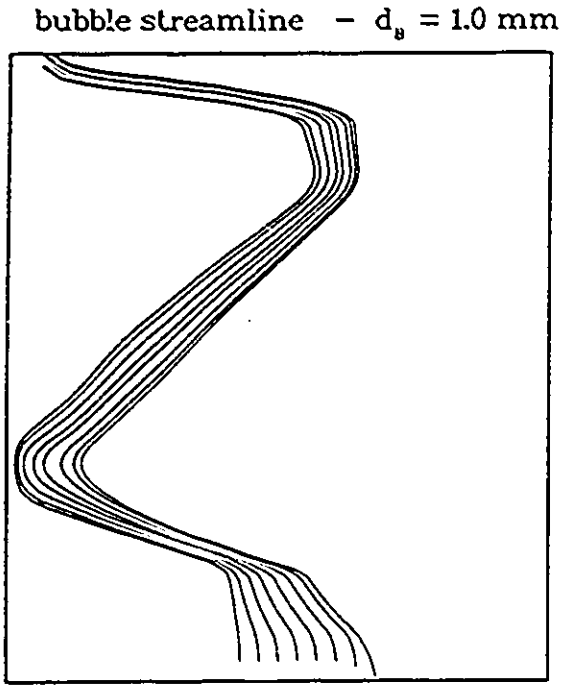

Figure 4.33: Bubble streamline - $d_B = 1.0$ mm.

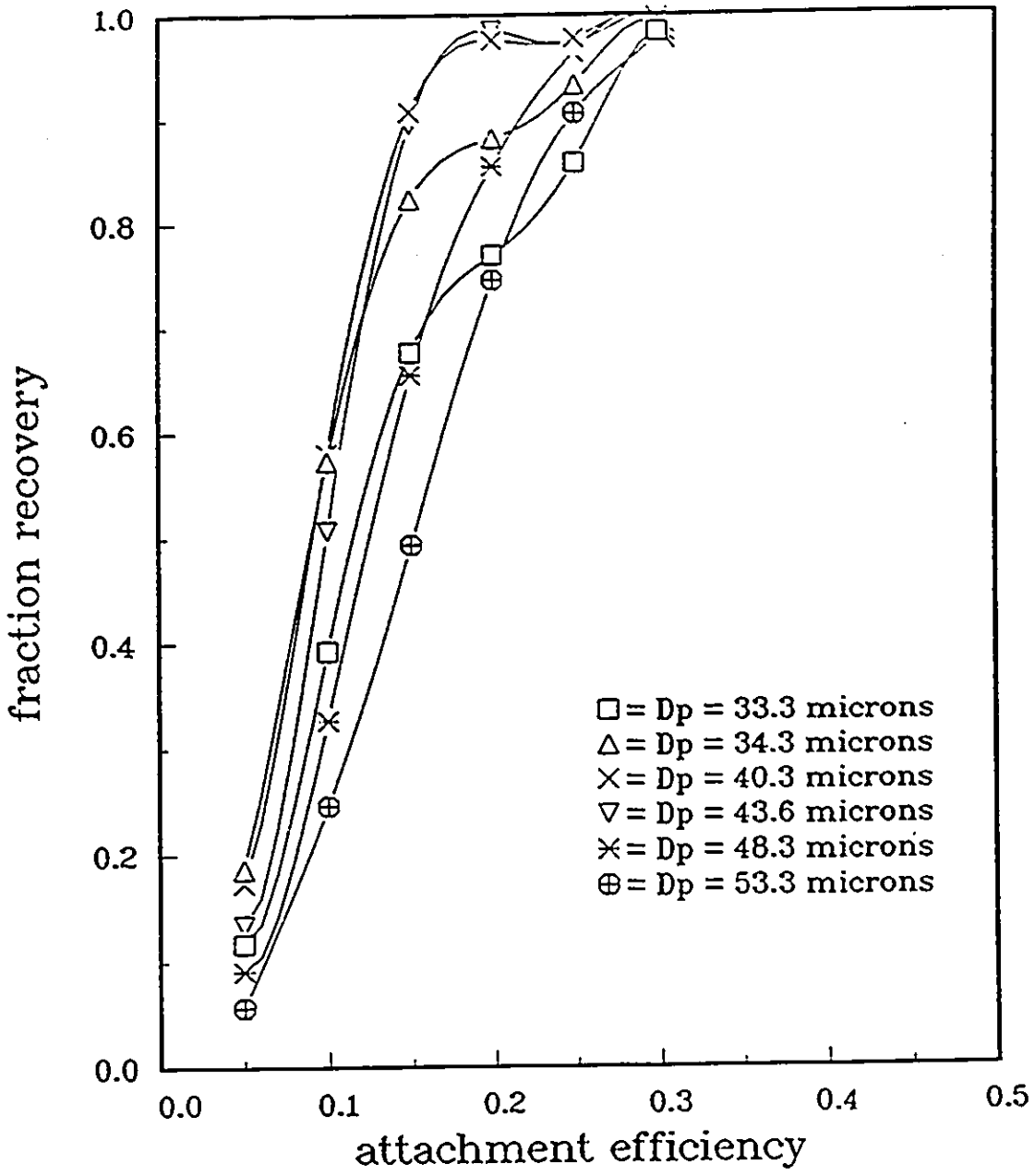

Figure 4.34: Recovery vs. r_a as determined by MD-PHASE simulation.

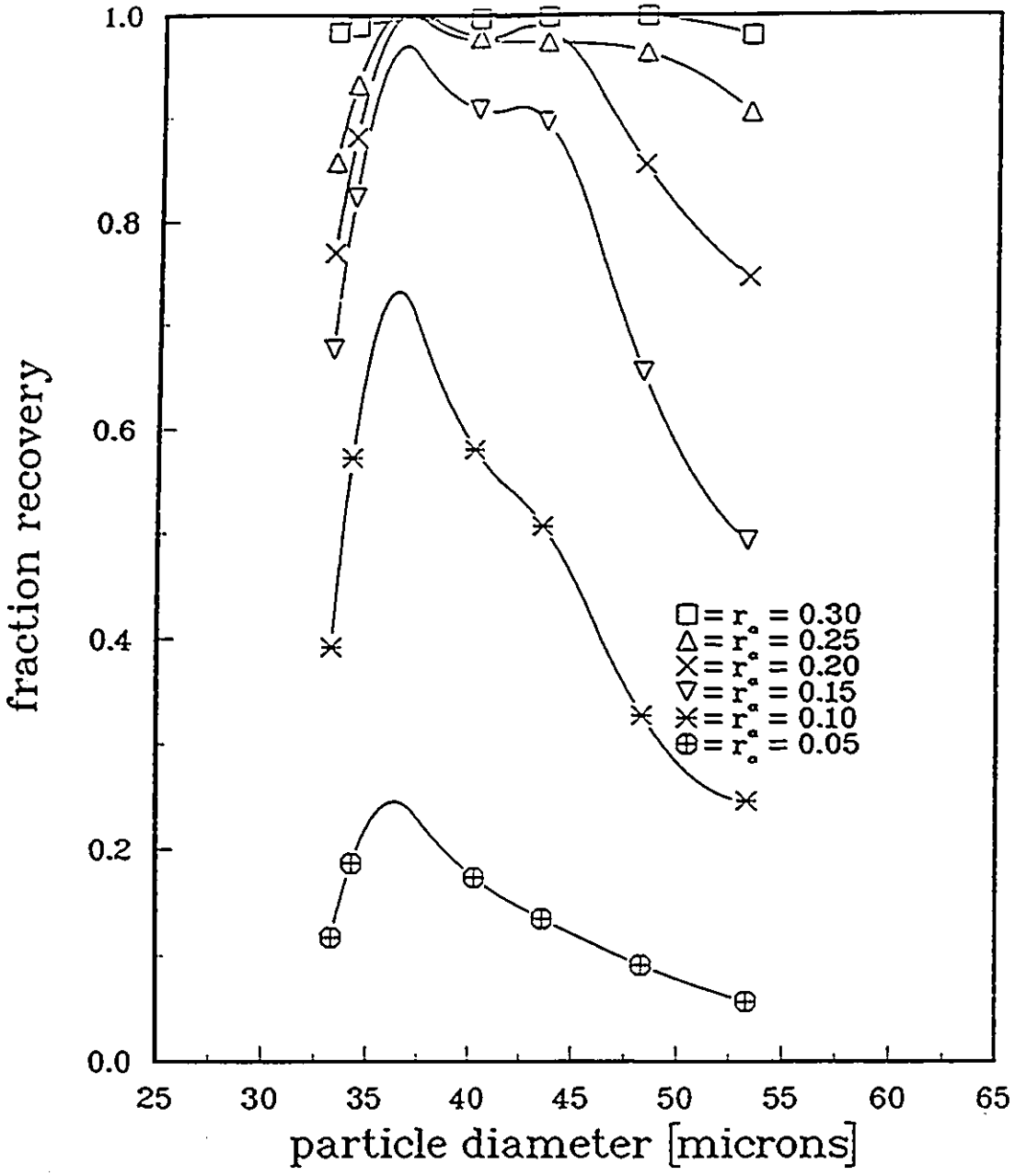

Figure 4.35: Recovery vs. d_P as determined by MD-PHASE simulation.

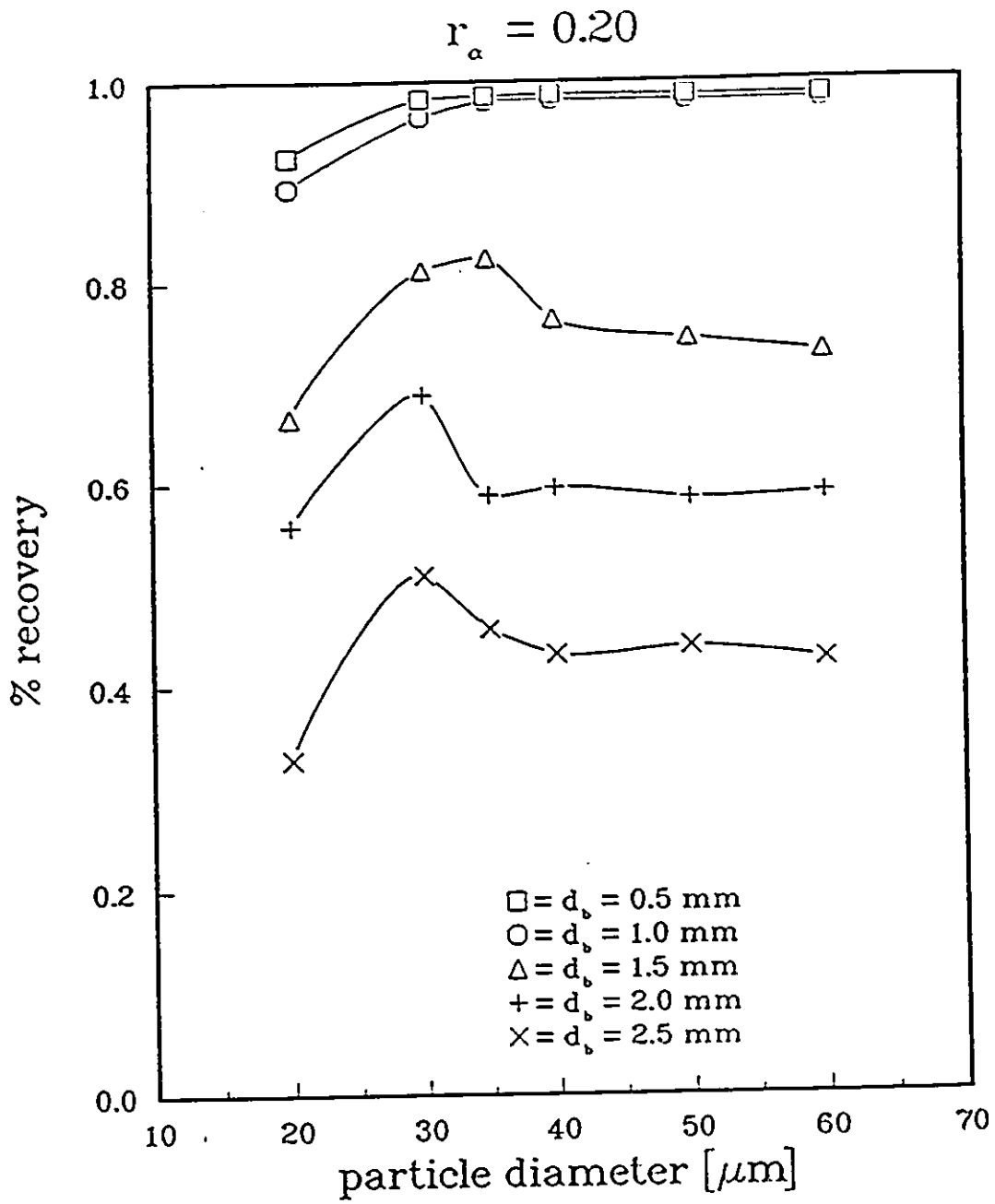

Figure 4.36: Recovery vs. d_P with d_B as a parameter as determined by MD-PHASE simulation.

Chapter 5

Discussion

5.1 Coal-Oil Agglomerate Surface Properties

Intrinsically, the oil added to the coal particles in the process of agglomeration produces an interdependent system of properties for the agglomerate. The size, surface properties and agglomerate structure all stem from the amount and type of oil used as an agglomerating binder.

Coal-oil agglomeration is done at low oil levels, and the following analysis of the agglomerate structure serves to verify that indeed, the process takes place in a small floc regime. As will be illustrated, structural effects are closely linked with the measured agglomerate surface free energies [116].

5.1.1 Agglomerate structure

An informative way of expressing agglomeration data is with an enlargement factor, F. F can be defined as,

$$F = \frac{d_p}{d_{p_o}} \tag{5.1}$$

where d_p is a mean agglomerate diameter at a given oil level and d_{p_o} is the mean diameter of the unagglomerated coal. (recall figure 4.6)

Assume that at low oil levels, only single particles and doublets will contribute to the resulting enlargement factor. Now say that there are n particles plus agglomerates

and one of them is double size (an agglomerate). Thus,

$$F - 1 = \frac{1}{n} \quad \text{or,} \quad n = \frac{1}{F-1} \tag{5.2}$$

One bond will exist for every $n + 1$ particles, so the fraction of the total solid volume that is bonded in doublets, V_{SB}, is,

$$V_{SB} = \frac{2}{n+1} \tag{5.3}$$

Thus the bonding volume of oil, V_{OB}, relative to the volume of two bonded particles is,

$$V_{OB} = \frac{V_O(n+1)}{2} \tag{5.4}$$

where V_O is the total volume of oil expressed as a fraction of the total solids volume. However, for a given volume of solids, the oil will first be consumed in wetting the solid surface, then any excess will then be used up in forming bonds. The total oil volume fraction, V_O, will be composed of two parts, a bonding volume fraction, V_B, and a wetting volume fraction, V_W. Thus,

$$V_B = V_O - V_W \tag{5.5}$$

Thus equation 5.4 should be re-expressed as,

$$V_{OB} = \frac{V_B(n+1)}{2} \tag{5.6}$$

to account for the wetting volume.

5.1.1.1 Three-Phase Contact Angle

n-$C_{16}H_{34}$ contact angles on polymer substrates in water are plotted in figure 5.1. Using a Lagrangian interpolation routine, hexadecane contact angles on the agglomerates at the different oil levels (surface tensions) were estimated. In figure 5.2, the three-phase contact angle is plotted against the agglomerate oil level.

The addition of adsorbing oil was not found to have caused a step change in the agglomerate surface properties at low oil levels. This is because problems such as incomplete wetting and surface roughness [117] of the coal will contribute some coal character to the surface at very low oil levels. This point is further discussed in section 5.1.1.2.

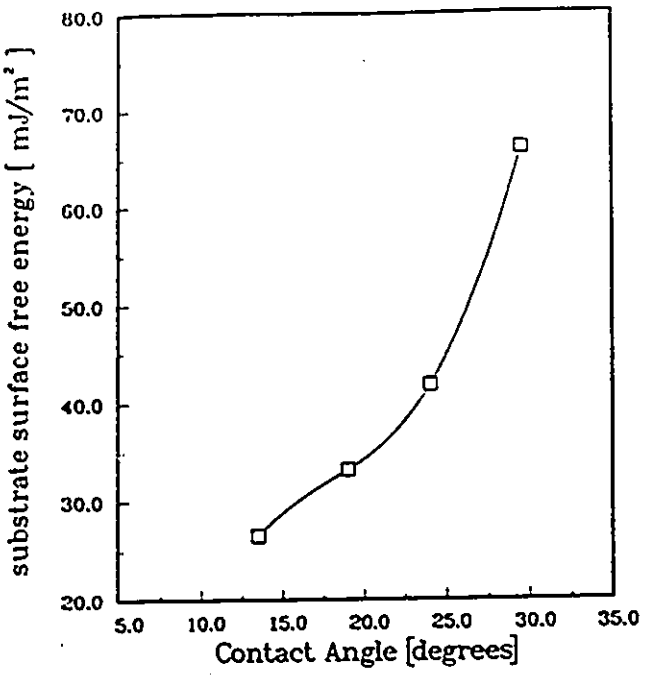

Figure 5.1: Contact angle of hexadecane in water vs. substrate surface tension.

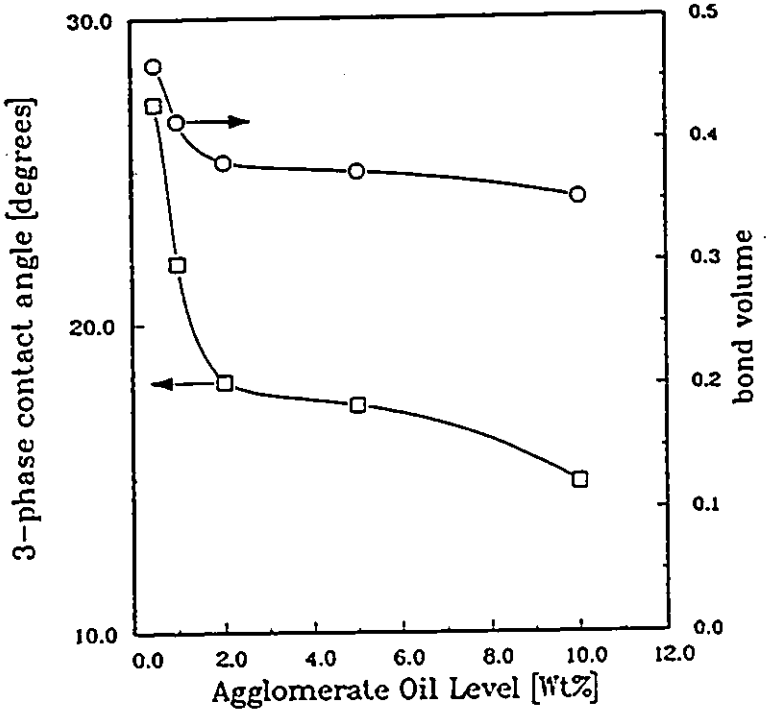

Figure 5.2: θ_C vs. Oil Level (□), and bond volume vs. Oil Level (○).

5.1.1.2 Calculation of Bond Volumes

It has been shown that bonding structure of agglomerates is determined by the volume ratio of binding liquid to solid present in the system. At the binder levels considered in this work, the bonding should be exclusively pendular [118, 119]. Pendular bonds are discrete lens-shaped rings at the point of contact of two particles.

Since the surface tension of the coal-oil agglomerates was found to be a function of the oil level, it is suggested that the contact angle at the three-phase junction of the oil-wetted particle, the bonding oil and the water will also vary with the oil level. The surface tension of the agglomerates as measured represents a macroscopic or gross average of local surface properties. This was proposed by Cassie [120] and verified with many supporting citations by Crawford et al. [121].

On a microscopic scale, surface roughness and surface heterogeneity characterize real solid surfaces. Wetting by an oil would have to exceed the dimensions of these irregularities before an essentially oil surface would be detected. Additionally, coal is a slightly porous material. Oil would be withdrawn from the surface and into the pores. Further, in view of the way the agglomerates are prepared, a perfectly uniform wetting could only be the result of a perfect dispersion of the oil in the aqueous medium. At best, the coal surface is wet in a "pebbled" or "mosaic" fashion. This has been reported elsewhere [122]. Note that at agglomerate oil-levels above 2% by weight, the surface that is observed is essentially an oil surface. It is in the region of 0 to 2 weight percent oil where incomplete wetting occurs and the existence of an intermediate coal-oil surface is postulated. This concept concurs with flotation recovery data as a function of oil level given by Capes et al. [123].

One would expect a constant contact angle only in the case of uniform wetting on smooth homogeneous surfaces. Otherwise, below a plateau oil level, the three-phase contact angle should vary with oil level.

If the effect of gravity is neglected, the binder-liquid interface will assume a profile of near constant curvature [124]. For our purposes, this profile can be represented by an arc of a circle of radius b. Figure 5.3 illustrates this configuration.

The meridian angle, θ_m can have a maximum size of 45° in the pendular regime,

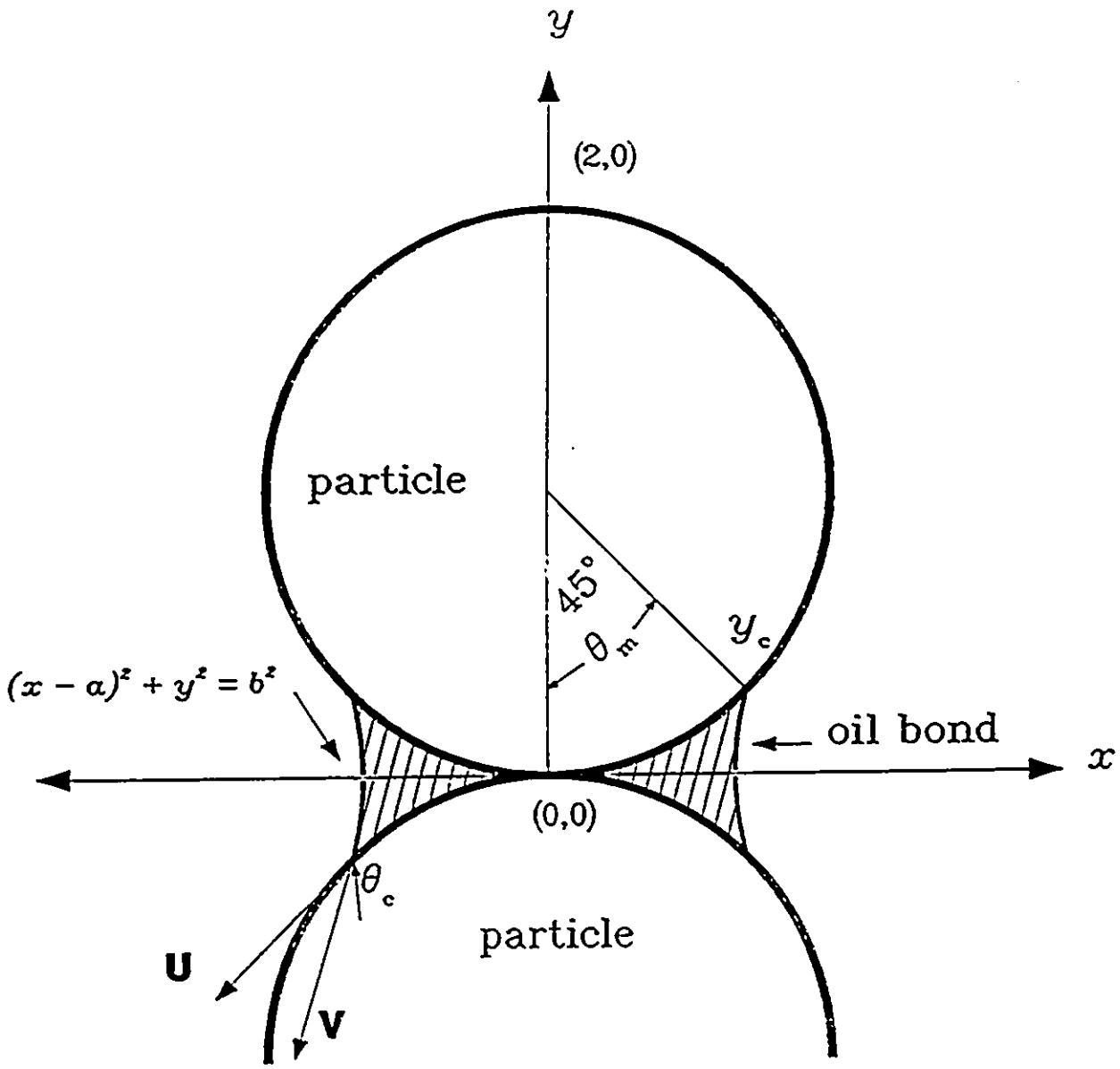

Figure 5.3: Schematic diagram of geometry for the bond volume in view of contact angle.

or else neighbouring bonds will coalesce. Now assume the particle has a unit radius, defined by the equation $x^2 + (y-1)^2 = 1$. With θ_m equal to 45°, the three-phase junction will occur at the point $x = 1/\sqrt{2}, y = 1 - 1/\sqrt{2}$. The slope of the surface at this point is 1. (refer to figure 5.3)

Let (u_1, u_2) and (v_1, v_2) refer respectively to the direction (slope) vectors of the particle surface and the meniscus surface at the three-phase contact point. The meniscus surface can be defined by an arc of a circle defined as,

$$(x-a)^2 + y^2 = b^2 \tag{5.7}$$

The contact angle, θ_C is related to the two direction vectors by,

$$u_1 v_1 + u_2 v_2 = \| \vec{u} \| \, \| \vec{v} \| \cos\theta_C \tag{5.8}$$

With (u_1, u_2) equal to (1,1), and setting $v_1 = 1$, determining v_2 gives the slope of the circle defined by equation 5.7 at the three-phase contact point. Thus,

$$\frac{dy}{dx} = v_2 = \frac{\pm(x-a)}{\sqrt{b^2 - (x-a)^2}} \tag{5.9}$$

Thus equation 5.7 along with equation 5.9 determine the parameters a and b. Thus for a given contact angle, the meniscus profile is defined.

The absolute bond volume, V_{BA}, can be then taken as a volume of revolution of the meniscus area. Let the meniscus surface be $\mathcal{F}_2(y)$ and the particle surface be $\mathcal{F}_1(y)$. y_c is the three-phase contact point y-coordinate.

$$\mathcal{F}_1(y) = 1 - (y-1)^2 \tag{5.10}$$

$$\mathcal{F}_2(y) = a \pm \sqrt{b^2 - y^2} \tag{5.11}$$

$$V_{BA} = 2\pi \int_0^{y_c} [\mathcal{F}_2(y)]^2 \, dy - 2\pi \int_0^{y_c} [\mathcal{F}_1(y)]^2 \, dy \tag{5.12}$$

Equation 5.12 was integrated numerically. This was done with a 15-point Gaussian quadrature routine. The bond volume as a function of oil level is also plotted in figure 5.2. Newitt and Conway-Jones [119] define the bond volume as a function of meridian angle θ_m as,

$$V_{BA} = 2\pi r^3 (\sec\theta_m - 1)^2 [1 - (\frac{\pi}{2} - \theta_m)\tan\theta_m] \tag{5.13}$$

The V_{BA} calculated for $\theta_C = 0°$ is exactly the same result as predicted by equation 5.12.

The absolute bond volume is related to V_{OB} (the volume ratio of one bond to 2 particles) by,

$$V_{OB} = \frac{V_{BA}}{\frac{8\pi}{3}} \quad \text{for,} \quad r_P = 1 \tag{5.14}$$

5.1.1.3 Interdependence of the Surface Tension, Oil Level and Enlargement Factor

It has been demonstrated that the result of low-level oil agglomeration of coal is dictated by the amount of oil added to the system. It is of interest to determine how the oil distributes itself to bring about this result.

Recall equation 5.6. Since $1/n = F - 1$, it may be re-expressed as,

$$V_{OB} = \frac{V_B F}{2(F-1)} \tag{5.15}$$

Assume that at low oil levels only pendular bonds will exist. Using V_{BA} from figure 5.2 and F from figure 4.6 the volume of one bond V_{OB}, is known and can be used to calculate V_B. At 0.5 weight% oil, from equation 5.14, $V_{OB} = 0.0425$. Thus,

$$0.0425 = \frac{V_B F}{2(F-1)} = \frac{V_B(1.03)}{2(0.03)} \quad \text{so,} \quad V_B = 0.0025$$

So from equation 5.5, $V_W = 0.0058$. Assuming V_W is constant for all oil levels, equation 5.15 may be used to determine the bond volume per particle pair. This value should be equal to the value of V_{OB} from equation 5.14 if the system is made up exclusively of singlets and doublets.

Denote V_{OB} from equation 5.15 as real volume V_R, and V_{OB} from equation 5.14 as a theoretical volume V_T. The ratio V_R/V_T will give a mean value of bonds per particle. If $V_R/V_T > 1$, then this implies that agglomerates larger than doublets exist. Figure 4.6 also shows this ratio plotted versus oil level. One may note the correspondence between the two curves in figure 4.6 and figure 4.3. At an oil level of about 1 to 2 weight%, the slopes on these plots significantly change. The underlying reason for this change should be a fundamental change in the agglomerate structure.

Based on the size data and the surface approximating that of hexadecane, it appears that beyond 2 weight% oil, larger, more compact agglomerates are formed.

A number of factors constrain the system. The result must conform to a mass balance of solids, an oil balance, and a weighted sum of various agglomerate sizes that accounts for the observed size. A system of three linear equations may be written which determine the distribution of singlets, doublets and triplets at each oil level based on the above criteria. They may be expressed as follows,

$$\begin{aligned} a_{11}q_1 + a_{12}q_2 + a_{13}q_3 &= F \quad \text{(agglomerate sizes)} \\ a_{21}q_1 + a_{22}q_2 + a_{23}q_3 &= 1 \quad \text{(mass balance)} \\ a_{31}q_1 + a_{32}q_2 + a_{33}q_3 &= V_B \quad \text{(oil balance)} \end{aligned} \tag{5.16}$$

where the q_i's are the fraction of singlets, doublets and triplets, the a_{1i}'s are the mean size of each type of agglomerate, the a_{2i}'s are all equal to 1 by definition of the mass balance and the a_{3i}'s are the bond volumes per agglomerate based on the oil level. The triplets were assumed to form a triangle which is the most stable three-body arrangement. The mean sizes were taken as an average of the maximum dimension that could be orthogonally projected against three normal planes. (ie; for a triplet, $a_{13} = (2 + 2 + 1.866)/3 = 1.95533$)

This system of equations was solved numerically and it gave positive element solution vectors up to 2 weight% oil. At that point, the number of doublets predicted was negative (physically impossible) thereby indicating agglomerates larger than doublets are present which require substantially more oil due to the increased number of bonds per agglomerate.

The system was remodeled including a quadruple that was considered to be in tetrahedral form and having six bonds. This required an additional linear equation, and one was formulated based on the strength of the agglomerates. Consider each agglomerate in terms of the probability that it will break up, P_b. In general P_b should be proportional to the inverse of the number of bonds present. That is,

$$P_b \propto \frac{1}{n_b b_s}$$

where n_i is the number of bonds in the agglomerate and b_s is the bond strength. The probability of break-up of the singlet may be expressed as $k_0 b_s$, where k_0 is some unknown constant. $k_0 b_s$ may be thought of as a hypothetical quantity related to the compressive strength of the solid coal. Thus for singlets to quadruples we have,

$$P_b = k_0 q_1 b_s + \frac{q_2}{b_s} + \frac{q_3}{3b_s} + \frac{q_4}{6b_s} \tag{5.17}$$

The strongest system, or minimum probability of break-up will occur when,

$$\frac{\partial P_b}{\partial b_s} = k_0 q_1 - \frac{q_2}{b_s^2} - \frac{q_3}{3b_s^2} - \frac{q_4}{6b_s^2} = 0 \tag{5.18}$$

Rewriting equation 5.18 we obtain,

$$k_0 b_s^2 q_1 - q_2 - \frac{q_3}{3} - \frac{q_4}{6} = 0 \tag{5.19}$$

In this form, the coefficient a_{41} of the new 4×4 matrix is indeterminate. However, in view of the agglomerate data, it can be assumed that at 1 weight% oil, the solution element q_4 will be zero and a_{41} can be calculated from the 3×3 system results. The 4×4 system was then solved and gave positive solution element vectors from 1 weight% through 10 weight% oil. Interestingly, the 4×4 system predicts essentially the same distribution of sizes at 2 weight% oil as does the 3×3 system, indicating that the omission of quadruples from the model at very low oil levels is justified.

Figure 5.4 is a plot of the frequency of each agglomerate size versus oil level as calculated by the system of linear equations. Figure 5.5 plots the same data as agglomerate size distributions with oil level as a parameter. It is emphasized in this figure that the doublet is an uneconomical bonding arrangement, and from 1 weight% and upwards, the number of doublets drops steadily. It can be seen from figure 5.4 that the frequency of singlets as a function of oil level is a smooth curve, which supports the assumption of there being primarily only singlets, doublets and triplets at very low oil levels. (ie; in figure 5.4, data for 0.5 to 2% oil is from the 3×3 system, 2% to 10% oil from the 4×4 system)

The above development was also calculated with the assumption of a zero contact angle at the three-phase interface, as assumed in previous papers [109, 125]. The

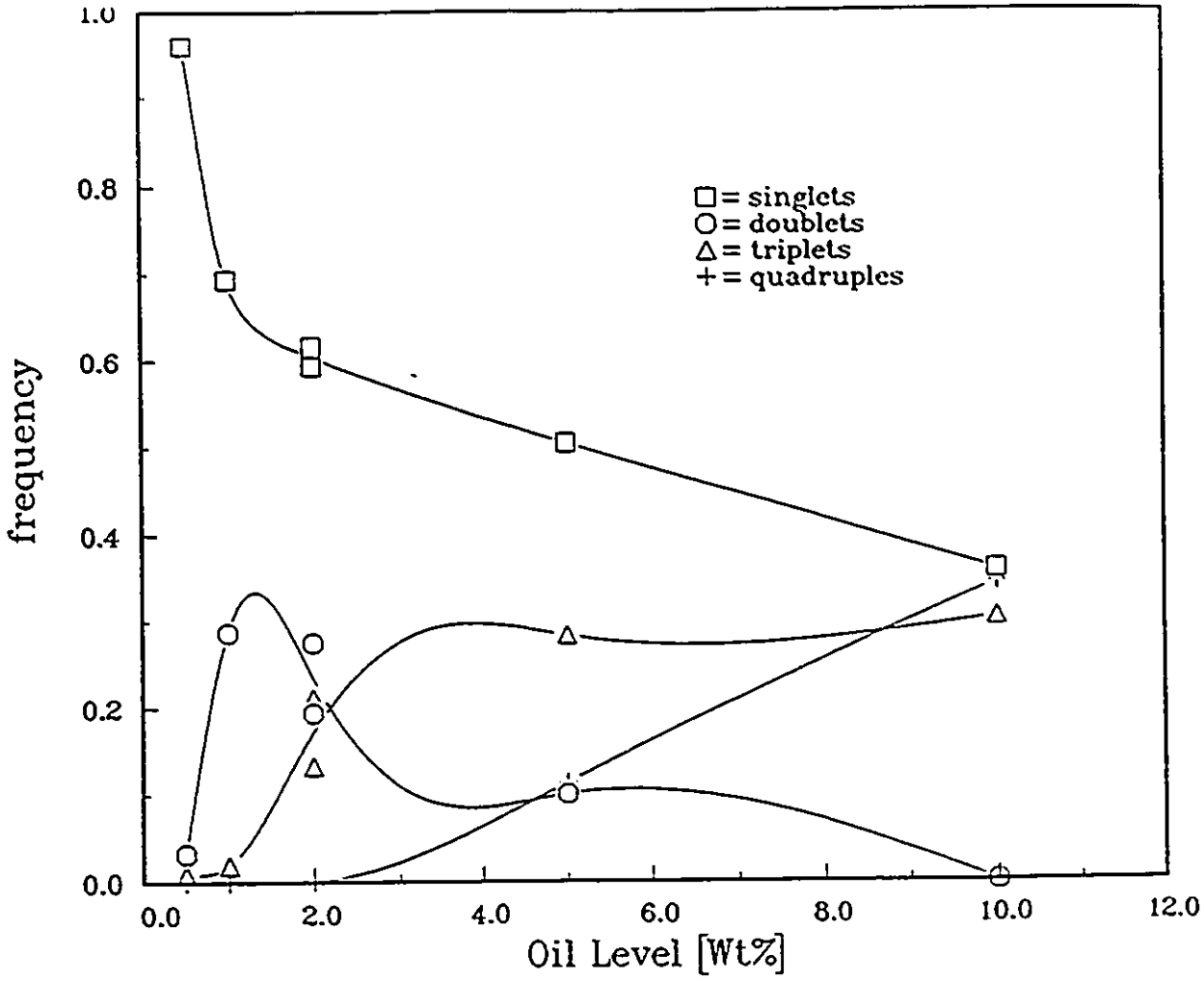

Figure 5.4: Agglomerate size frequency vs. Oil Level

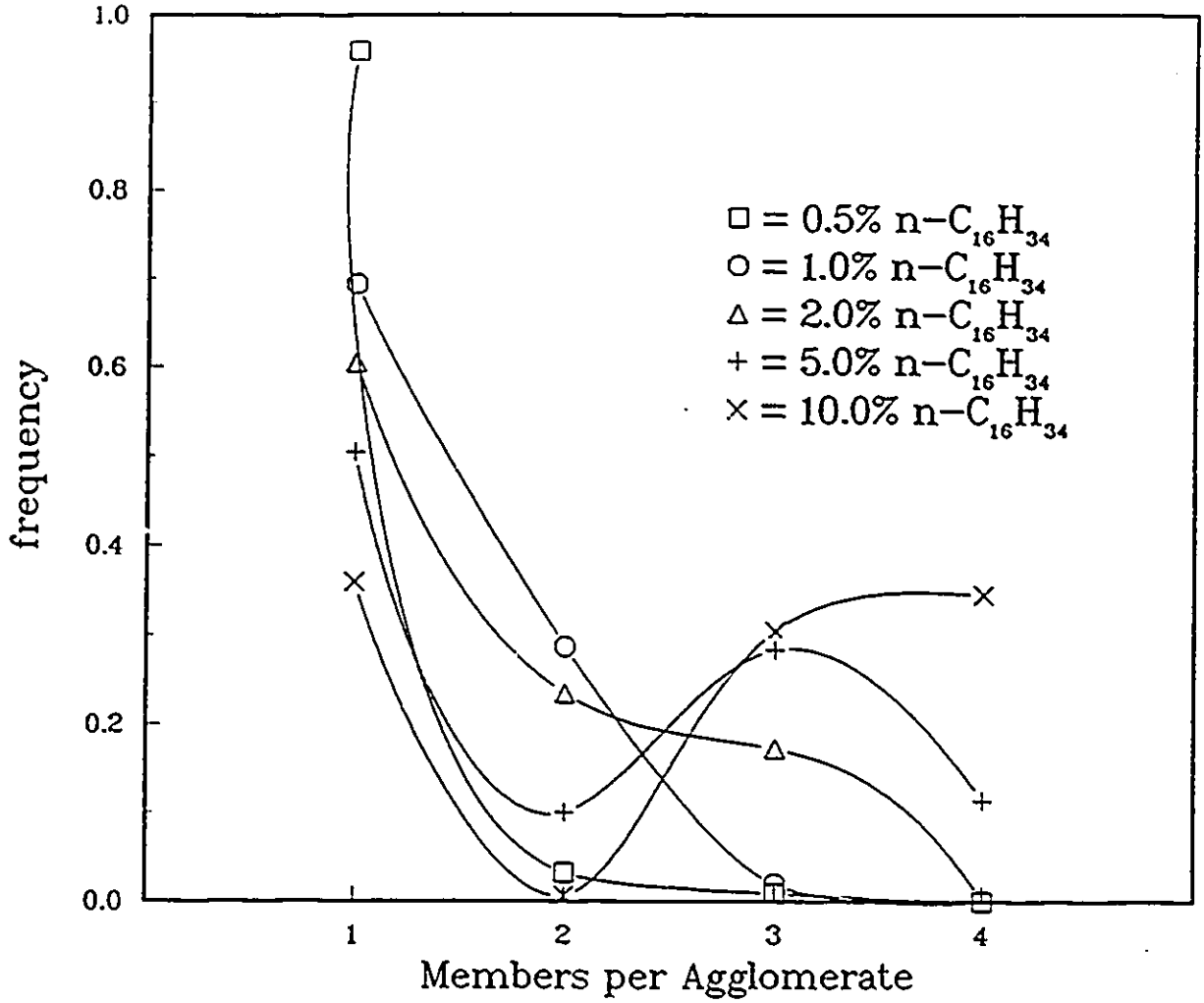

Figure 5.5: Agglomerate size distributions

results predicted overly large agglomerates at low oil levels as the zero contact angle bond is about 65% of the volume of the finite contact angle bond. Correspondingly the wetting volume with a zero contact angle was calculated to be much larger as well.

5.1.2 Coal rank and surface properties

The data in Figure 4.3 show how the amount of oil used to form coal-oil agglomerates produces a net surface free energy for that agglomerate. As was discussed by Darcovich et al. [116], the surface free energies at intermediate oil levels (from 0 to 1 weight% oil), reflect a heterogeneous surface composed of both coal and oil components. These intermediate surface free energy values can be attributed to imperfect wetting of the surface arising from surface heterogeneities, surface roughness and discretized dispersion of the oil through the aqueous medium in which the agglomeration takes place.

Further, the wetting occurs with a non-zero contact angle, so that the wetting and spreading will not be spontaneous and complete, rather the oil will coat the surface in patches and spread as it can locally. A monolayer coverage of oil on the coal would only be achieved if the surface were very smooth and the oil was perfectly dispersed in the aqueous phase. The monolayer coverage is more related to model systems, rather than with impure, irregular real surfaces. It can be seen that for the Devco, Highvale and Montgomery coals (subbituminous and higher in rank), the surface free energy drops very sharply at low oil levels, to a value near the surface free energy of pure hexadecane. Thus the surface of these agglomerates has essentially an oil character at low oil levels.

At 10 weight% oil, the data for the Highvale coal shows a surface free energy less than that of hexadecane. This difference is slight, and should be understood to be within the range of experimental error for this measurement. The adhesion method is subject to several sources of error. The presence of ash in the adhesion cells with the agglomerates may have interfered with the settling and adhesion. It was assumed that because of its inorganic, mineral nature, the ash is of sufficiently high

surface free energy that it was unlikely to adhere to the polymer substrate surfaces. Further, the surface tensions of the water-methanol suspending liquid mixtures were very sensitive to composition. Any amount of evaporation or even small volumetric inaccuracies in their preparation, could make substantial errors. Great care was taken in the experimental work to ensure sound and reasonable data.

In the case of the Bien Fait and Costello lignite samples, the surface free energy does not decrease sharply with oil level, and even at 10 weight%, has a value at least 10 mJ/m^2 greater than that of hexadecane. Typically, lignites have a high moisture content and contain many polar groups that inhibit oil wetting. This has been confirmed by Jin et al. [126] showing poor flotation results and long contact time, as well as by Naka and Nishida [127], who showed lignites to be much more water wettable than other coal ranks. Similarly, Rosenbaum and Fuerstenau [128] note that coal surfaces contain an increasing amount of hydrophilic functional groups as rank is lowered.

A comparison between the two lignites can also reveal mechanistic reasons for the observed results. The Costello sample was found to be more wettable by hexadecane than the Bien Fait sample, as shown by the data in Figure 4.3. The most marked composition difference between the two lignites is that the Bien Fait sample contains relatively 50% more ash, contributing to hydrophilic behaviour suppressing oil wetting.

It has been reported by Wojcik et al. [129], Good et al. [130] among others, that the surface free energies of coal are similar for a wide variety of coals, independent of rank. This is confirmed by the small range of surface free energy values obtained for the five coal samples in this study, shown in Figure 4.3 for the case of zero weight% oil. However, it is well known that recovery processes based on surface wetting are very rank dependent.

Figure 4.7 shows the flotation recovery data and figure 4.8 shows the ash rejection data for the subbituminous and the lignite samples. The oil-wettable subbituminous samples are far more easily recovered than the lignite samples. The flotation tests done with hexadecane as the agglomerating oil show poor recovery results, but they do uphold the trend of increased recovery with increased oil wettability. Hexadecane

has been found by Janczuk et al. [58] to have a weak bonding ability between coal particles and air bubbles in dynamic systems. However, it is not intended to use hexadecane for commercial recovery processes, rather it is simply a well characterized pure hydrocarbon suitable for this wettability study. As a practical point, hexadecane is much less viscous than No. 4 fuel oil, so it is more amenable to wetting the coal in the low shear vacuum flask agglomeration procedure. The agglomeration in the case of the flotation measurements was done in a high-shear blender, capable of more thoroughly dispersing heavier oils.

No. 4 fuel oil was also used to conduct flotation recovery tests. The recovery of the subbituminous coals was markedly improved compared with the hexadecane results, and further, a small amount of recovery was achieved with the lignite samples. Tampy et al. [131] have attributed this to the presence of aromatics in the fuel oil which interact more favourably with the coal surface to form some hydrogen bonds with polar groups. This phenomenon in turn, will hold the oil-bubble interface more securely in a flotation situation. This concept is confirmed by the data showing the lignite samples which have a much higher composition of polar groups, responding favourably to the fuel oil as an agglomeration/flotation agent, while essentially failing to be recovered by the purely dispersive hexadecane oil. If size data were available for the hexadecane-lignite agglomerates, it would likely show little or no enlargement, which would be a process to enhance the probability of successful flotation.

The surface free energy of the unoiled lignites were 60.5 mJ/m^2 for the Bien Fait sample and 57.3 mJ/m^2 for the Costello sample. Across the entire range of oil levels tested, the Costello sample agglomerates maintained a lower surface free energy. If we consider $d\gamma_{PV}/d\text{wt\%}$ oil, there appears to be no substantially different thermodynamic driving force to promote the oil wetting of these coals. In this sense, the recovery data, which show the Bien Fait sample to be slightly superior, can be explained by suggesting that the absolute *extent* of wetting may be the same. The lower (lyophobic) volatile content and the lower (hydrophilic) moisture content of the Bien Fait sample could then account for its slightly greater recovery between the two lignites, in the sense that it would have a more favourable interaction with the No. 4 fuel oil. A macroscopic surface free energy model for heterogeneous surfaces has been

proposed by Cassie [120]. It is stated as $\gamma_H = \sum c_i\gamma_i$, where γ_H is the macroscopic surface free energy of the heterogeneous solid, γ_i is the surface free energy of the ith component which comprises the fraction c_i of the entire surface. In general, ash content will contribute to a higher surface free energy, while volatiles and fixed carbon would tend to reduce it. If the volatile fraction is assumed to have a surface free energy value similar to that of hydrocarbon oils, then the addition of such oils as a wetting agent would be preferentially attracted to the carbonaceous portion of the coal since the ash content is significantly more hydrophilic than the rest of the surface, and the wetting of an oil over an already oil-like (volatiles) surface is not very thermodynamically favourable. Thus with fixed carbon contents of 38.59% and 39.79% respectively for the Bien Fait and Costello samples, the extent of wetting ($d\gamma_{PV}/d$wt% oil) could be considered to be very similar.

It is of interest to compare the differences in agglomeration/flotation recovery shown in Figure 4.7 for the Highvale and Montgomery subbituminous samples, in view of their apparently similar wettability. Consider the surface free energy values for their unoiled surfaces. The Montgomery sample result was 64.2 mJ/m^2, while the Highvale coal value was 54.6 mJ/m^2. While both coals can be considered recoverable by the agglomeration/flotation method, the Montgomery sample showed a markedly superior recovery, (see Figure 4.7) especially with the No. 4 fuel oil, and notably with the No. 4 fuel oil at low oil levels. The Montgomery sample had a higher recovery with hexadecane as well. The lower ash content of the Montgomery sample, coupled with its higher unoiled surface free energy could indicate more of a fixed carbon fraction at the surface which would lend itself to a more complete wetted state. That is, if the surface free energy of a solid is higher, but not as high as say the ash fraction so to be hydrophilic, the thermodynamic driving force for oil wetting will be greater. Further, if a larger fraction of the surface is oil wettable, this will enhance probabilities of both agglomeration and the subsequent flotation. If the quantity ($d\gamma_{PV}/d$wt% oil) is considered, the Montgomery sample exceeds the Highvale sample by about 10 mJ/m^2-wt%-oil. This is another way of saying that for the same amount of oil present, the surface character of the Montgomery sample has been subject to far more modification by wetting that improves its agglomeration/flotation performance.

If it can be supposed that with a smaller area available for wetting, the Highvale sample may have a thicker covering of oil on its wettable regions. It has been shown by Janczuk et al. [58] that the detachment force for air bubbles on oiled coal surfaces is lower when the oil layer is thicker. This finding is thus consistent with the idea of a restricted wetting area and hence a thicker wetting layer. At higher oil levels, when the wetting becomes less selective, this effect is less pronounced both in terms of the quantity ($d\gamma_{PV}/d$wt% oil) as well as the difference in the agglomeration/flotation recovery obtained.

Figure 4.8 shows the ash rejection as a function of agglomerate oil level. The Montgomery coal which is recovered to a greater degree is, at the same time, less efficiently deashed. This was the case with the No. 4 fuel oil. The lower unoiled surface free energy of the Highvale coal would make the wetting more selective, and further, at a particle size much smaller than the Montgomery coal, there is a higher probability to have a clearer discretization between ash and carbonaceous matter.

One point which has not been given too much consideration in this discussion is that of the mean particle size. The Highvale sample had a mean size of 9.4 μm, while the Montgomery coal was larger, with a mean size of 20.3 μm. The data in Figure 4.3 suggest that the oil character given to the agglomerate surface is roughly the same at oil levels from 1 through 10 weight%. Even at 1 weight% oil, there is still more than sufficient oil present to fully wet the entire surface area of both samples of coal. If particle size (or surface area) were to have an effect, it would likely be at an oil level such as 0.50 weight% or below, where the larger coal would be expected to show a comparatively more oil-like surface character. Where this factor does make a difference is with the agglomeration/flotation recovery data. It was shown by Darcovich et al. [116] that excess oil on a coal surface contributes to improved inter-particle bonds for the formation of agglomerates. Well wetted, larger agglomerates would improve flotation recovery, as larger particles offer more inertia to counter hydrodynamic resistance in the bubble-particle collisions necessary for attachment. Thus for a less easily oil wetted coal such as the Highvale sample, the choice of agglomerating oil becomes more crucial for achieving good recovery.

The data in Figure 4.3 show the difference between the subbituminous and bituminous coals that are easily oil wetted and the lignites which do not readily acquire an oil character at their surfaces. The oil wetted coals have the sharp drop in surface free energy at low oil levels and have a surface character essentially of the wetting oil itself at higher oil levels. This characteristic of the curve indicates that it is reasonable to expect successful recovery and upgrading of the coal by the agglomeration/flotation procedure, but it does not really predict what extent of recovery can be expected. The success of recovery depends on the components of the coal matrix itself, and how these components interact with whatever agglomerating oil is selected to bind them.

In view of the above discussion, consider a definition of hydrophobicity index h, for the as received coal, formulated as:

$$h = \frac{\text{wt\% fixed carbon + wt\% volatiles}}{\text{wt\% ash + wt\% moisture}} \tag{5.20}$$

This parameter h, is essentially the ratio of the amount of the components of the coal that will be hydrophobic and oil wettable (carbon and volatiles), to the amount of components (ash and moisture) that are comparatively much more hydrophilic. Figure 5.6 shows a three-dimensional surface where the surface tension of the agglomerate is mapped out as a function of the oil-level used in making the agglomerate, and the value of h determined for the five coal samples used. The surface was generated from the data with a two-variable constrained quadratic interpolation routine. In Figure 5.6, it can be seen that if the coal is not overly hydrophilic ($h > \sim 2$), only a small amount of oil is required to make an agglomerate with a surface that can be considered to be the same as that of the agglomerating oil. The ridges on the surface can be attributed to the scatter in the data.

With a properly chosen oil for flotation, agglomerates can be recovered with high yields at oil levels below 2 weight%. The low oil requirement is an attractive feature of the agglomeration/flotation process.

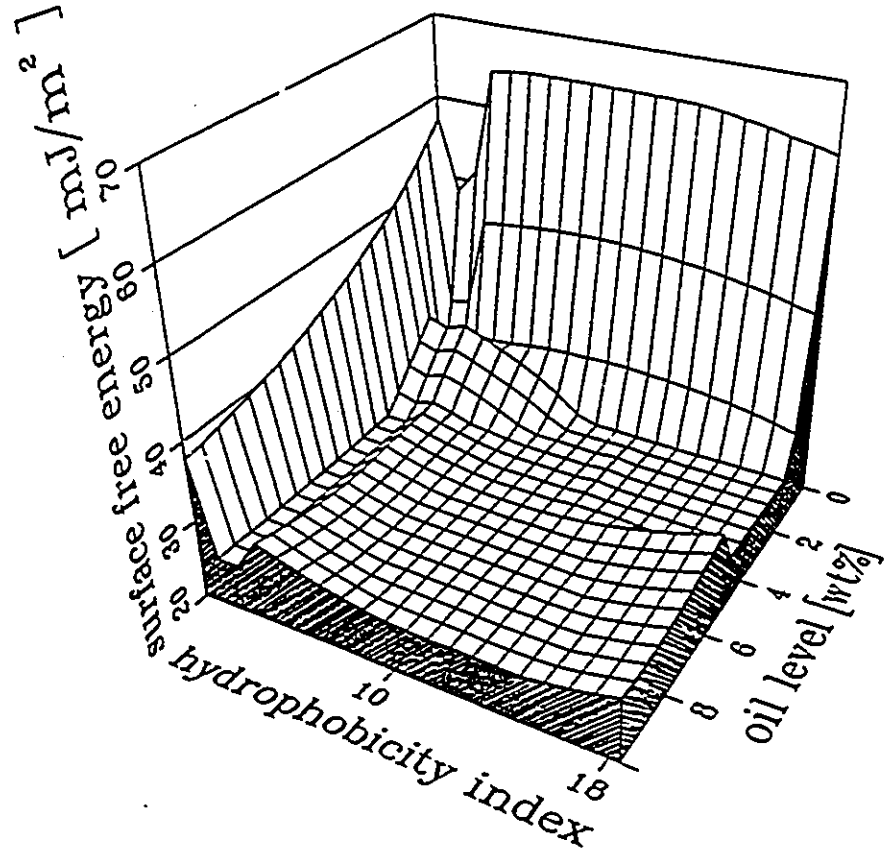

Figure 5.6: Agglomerate Surface Tension vs. h and oil level.

5.2 BEM Results and Limitations

The two dimensional, transient, full Navier-Stokes primitive-variable BEM formulation developed for this project turned out to be of limited usefulness. The method was implemented for trial cases, but was not able to converge at low enough Reynolds numbers to be useful for simulating the transient particle-bubble interaction which is the essence of any flotation study on the micro-scale.

In any event, some test results were obtained. Recall figure 4.14. The plot shows the transient migration of the vortex center. The results obtained with the finite-volume simulation closely approximate those obtained by BEM. The data obtained by Tosaka and Kakuda which are also shown in this figure are also similar. For such a case, the disparity can be accounted for by the fineness of the grid. The finite-volume and BEM solutions were from a 10×10 grid, whereas the Tosaka and Kakuda results were obtained from a 21×21 grid [114]. The general behaviour was consistent with expected and published results. The driven-cavity simulation is a common benchmark test. A paper by Sekar and Nath gives results for steady flow in a driven-cavity by a stream-function BEM simulation [132].

It is not completely clear why the simulation diverges at low Reynolds numbers. Recall the expression for the boundary traction.

$$\tau_i = \tau_{ij} n_j = -\mathrm{Re} p n_i + u_{i,j} n_j + u_{j,i} n_j$$

It was assumed that no boundary condition for the tractions needed to be applied. The unknowns on the boundary were only the tractions, and their solution depended only on the velocity field. The pressure field could be solved independently using the results from the velocity field. It can be postulated that at lower Reynolds numbers, the term $-\mathrm{Re} p n_i$ in the traction expression becomes increasingly significant. This would necessitate a simultaneous solution of the pressure field (and pressure boundary conditions) to be able to treat the boundary tractions in a numerically stable way. A paper by Gresho and Sani [133] underlines the complexities of formulating a pressure boundary condition. The uncertainties associated with implementing the above scheme for a successful micro-scale flotation simulation were considered too

great. The BEM formulation as developed here was thus not further modified for flotation modeling.

5.3 3-phase flotation model

5.3.1 Basic results

The raw results from the MD-PHASE simulation for recovery was plotted in figure 4.34. Recovery was seen to increase with increasing r_α, up to a limit of full recovery. The collection probability monotonically corresponds to a lowering of the unoiled coal surface tension as the oil-level is increased. The data in figure 4.34 do not reveal any straightforward trend in terms of the d_P parameter. However, when the data are replotted in figure 4.35 with r_α as the parameter, the recovery is seen to follow curves containing a maximum recovery at each r_α, and with the maximum becoming less distinct as r_α increases. Figure 5.7 shows a theoretical plot of a parameter E_K, which corresponds to the overall probability of flotation P_f [134]. E_K comes from calculating sliding times for particles over bubbles in terms of a collision position model and assigning the induction time parameter to assess the probability of collection.

The data from figures 4.35 and 5.7 show a similar functional form. The maximum recovery is observed at a particle diameter of about 25-30μm for the model by Dobby and Finch with d_B = 1.0mm. The one case for r_α = 0.2 (figure 4.36) where recovery with a 1.0 mm bubble is predicted with MD-PHASE simulation shows a recovery maximum at $d_P = 30\mu$m, which is in excellent agreement. The induction time parameter of figure 5.7 corresponds inversely to the parameter r_α. With an induction time of 0, it means that any contact at all between a particle and a bubble will result in particle collection. The induction time can be considered to be a measure of the surface property of the particle. With reference to coal-oil agglomerate flotation, the oil level used in making the agglomerates improves the solid phase surface for flotation and has a direct bearing on these parameters.

Consider figures 4.35 and 5.8. The effect of the bubble diameter is investigated. Again, a similar functional form is observed for both results. At smaller bubble sizes

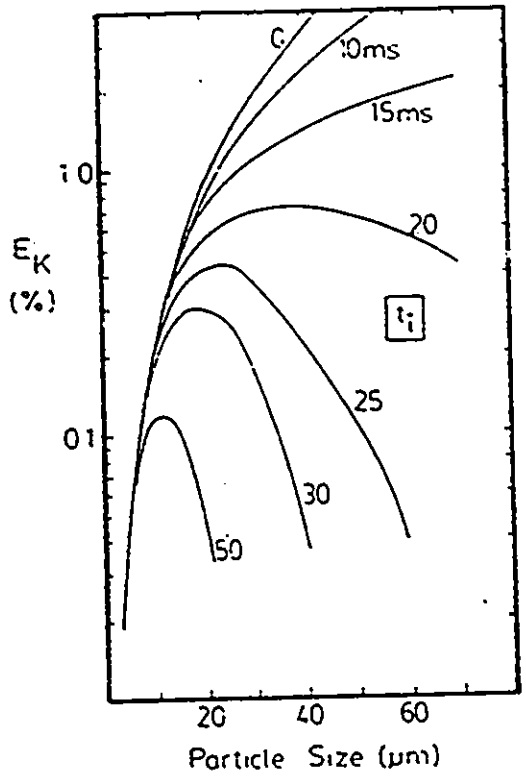

Figure 5.7: Collection efficiency vs. particle size and induction time from Dobby and Finch model. Conditions: $d_B = 1.0$mm, $u_B = 10$ cm/s, $\rho_P = 4.0$ g/cm^3. From [134].

the curves both show a less distinct maximum. Also, results from Dobby and Finch show that the maximum recovery occurs at increasing particle sizes as the bubble diameter is decreased. The MD-PHASE simulation results make the same prediction.

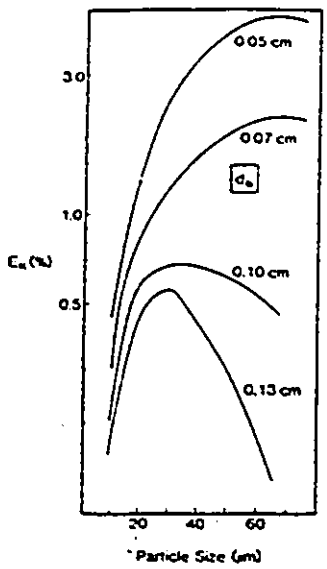

Figure 5.8: Bubble diameter effect on E_K from model by Dobby and Finch. Conditions: $t_i = 20$ms, $\rho_P = 4.0$ g/cm^3. From [134].

From the analysis by Dobby and Finch, the improved E_K with smaller bubbles was explained by saying that despite the smaller surface over which to achieve a particle sliding time, the reduction in gas velocity owing to a lesser bubble diameter still gives an overall increased sliding time. From a macro-hydrodynamic point of view (recall the bubble streamlines shown in figures 4.32 and 4.33), smaller bubbles are more subject to the influence of the liquid and solid phase flow fields since there is a less strong buoyancy force driving them upwards. Hence, their streamlines are less direct between the inlet and the outlet, allowing for a higher residence time and better mixing of the three phases in the turbulence, and hence more frequent collisions. Further, at a constant air flux, smaller bubbles will produce a higher number density, and thus again, more collisions.

It is interesting to note that the approach of Bischofberger and Schubert which is based on collisions arising through turbulent energy dissipation, and which was

incorporated in the the present CFD model, gives quite similar trends in collection and recovery as a function of the particle diameter as does the model of Dobby and Finch. This indicates that the local hydrodynamic forces under the prevailing turbulence in a many-particle float cell produce collisional estimates of a nature similar to those from the laminar two-body approach resistance method, used in the model of Dobby and Finch, when individual particle interactions are scaled up to a unit operation. The parallel results thus suggest that the micro-flotation interactions of an essentially laminar nature may be quite valid within length scales less than the turbulent mixing length.

5.3.2 Agglomerate surface property model

An objective was to correlate the observed flotation recovery with the surface free energy of the agglomerates. The parameter for flotation recovery which directly depends on the surface properties is the attachment efficiency, τ_a. The CFD model is intended to predict a recovery, given the flow conditions, particle and bubble diameters and a value for τ_a which should depend on the measured agglomerate surface tension. Recalling figures 4.4 and 4.7, it can be seen that the Montgomery coal was recovered by flotation to the greatest extent. Further, this sample had an initial unoiled surface tension of 64.2 mJ/m^2, compared with 54.6 mJ/m^2 for the Highvale sample. Small oil additions resulted in similar agglomerate surface tensions for the two samples. The difference in recovery due to surface properties is thus attributed to the extent of the wetting, or the difference between the agglomerate surface free energy and the surface free energy of the unoiled coal. This quantity is referred to as $\Delta\gamma$.

The model in this case can be developed as a monotonic relation between the attachment efficiency, τ_a, and the extent of oil wetting $\Delta\gamma$. The effect of the bubble diameter was not considered in this model and is not necessary for illustrating the surface property influence. The bubble diameter was kept constant at 2.5mm in the numerical simulations, and the recovery data from the laboratory float cells were all obtained under standard testing conditions. For expressing τ_a as a function of $\Delta\gamma$,

the agglomerate diameter was not included as it could not be decoupled from the oil level and as such, inherently had its contribution input.

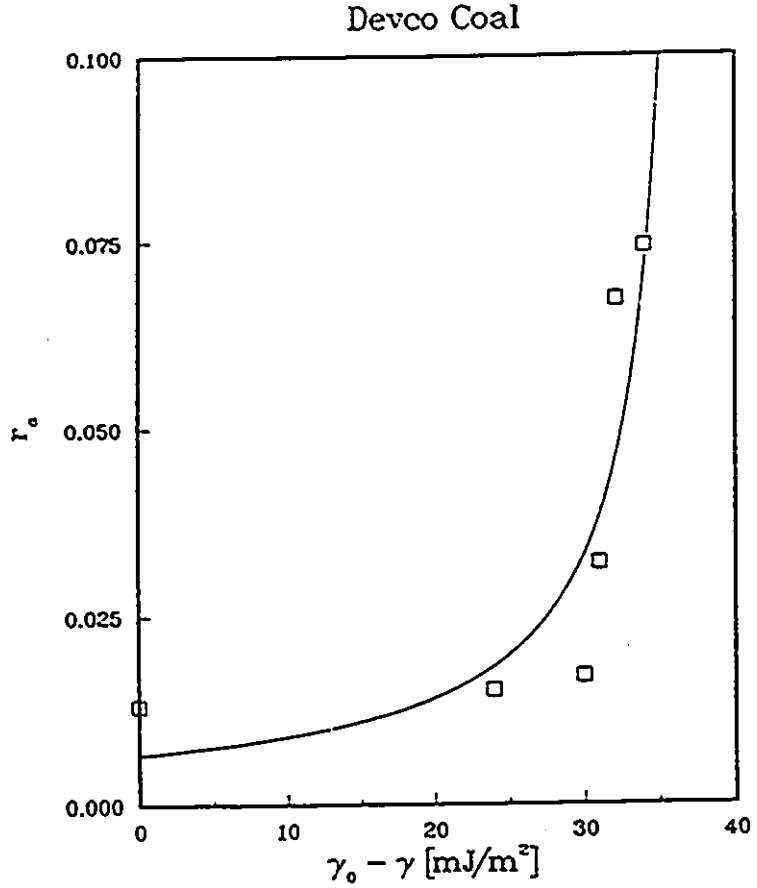

Figure 5.9: Calculated r_α vs. $\Delta\gamma$ for Devco sample.

The Devco sample was used as a calibrating sample simply because there were six data points available for all the required parameters, while there were only three data points for the Montgomery and Highvale coals. The data in figure 4.34 were numerically interpolated to give values of r_α which correspond to the measured flotation recoveries of the Devco sample at each oil level. These values of r_α are plotted versus corresponding $\Delta\gamma$ in figure 5.9 and are indicated by the squares. In general, these data show a direct and monotonically increasing relationship between r_α and $\Delta\gamma$, but with a non-linear shape. To impart some physical meaning to this relationship,

a hyperbolic functionality is adopted [135]. That is,

$$\frac{1}{r_a} = \frac{m}{\Delta\gamma} + b \tag{5.21}$$

This model contains two asymptotes, described below.

asymptote	physical meaning
$r_a = 0$	zero recovery
$\Delta\gamma = \frac{-b}{m}$	full oil surface

The regression analysis was done for the expression of equation 5.21 and the regression curve is also shown in figure 5.9. The model coefficients were determined as $b = 149.79$ and $m = -3.5934$. The abscissa asymptote is calculated as 41.7 mJ/m^2 while the maximum value of $\Delta\gamma$ for the Devco sample is 34.4 mJ/m^2. Again, this is physically meaningful in the sense that for the given float cell system, near 100% recovery would be achieved with finite values of r_a, which anyhow, has a maximum value of unity. Further, applying the maximum value of $\Delta\gamma$ to the model gives an r_a corresponding to the flotation recovery at high oil levels.

5.3.2.1 Energetics of flotation

The surface property dependence of flotation can also be characterized from an energetic point of view. Consider the schematic of the flotation process shown in figure 5.10.

Using the relation,

$$\Delta F^{adh} = \gamma_{PV} - \gamma_{PL} - \gamma_{LV}$$

the values of ΔF^{adh} for the adhesion in flotation can be calculated for the agglomerates per unit area, using results tabulated by Neumann et al. [136]. Figure 5.11 shows these results. It can be seen that at very low oil levels, the energy change due to the formation of the agglomerate-bubble interface is very favourable, but does not increase significantly at higher oil levels for the bituminous and subbituminous samples. The

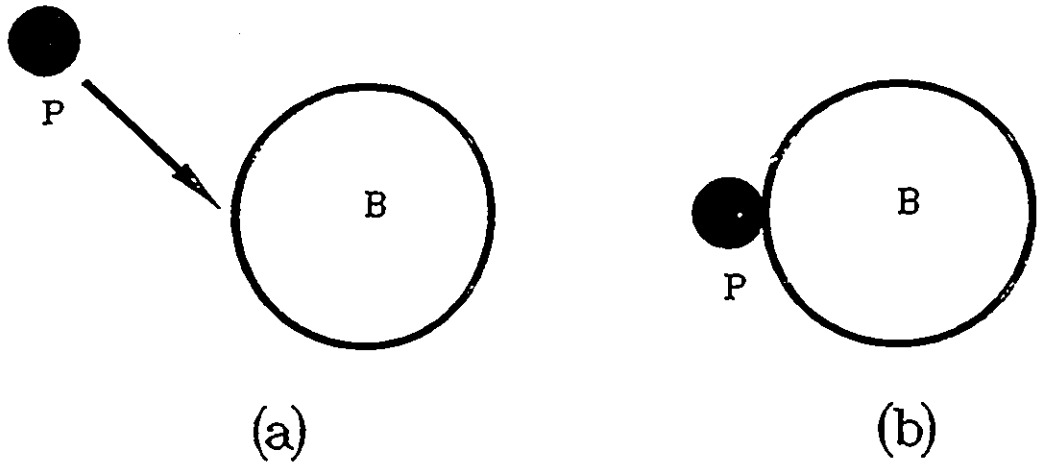

Figure 5.10: Schematic of surface displacements as a particle adheres to a bubble. $\Delta F^{adh} = \gamma_{PV} - \gamma_{PL} - \gamma_{LV}$. (a) particle and bubble interfaces with liquid exist. (b) particle-bubble interface displaces two former interfaces.

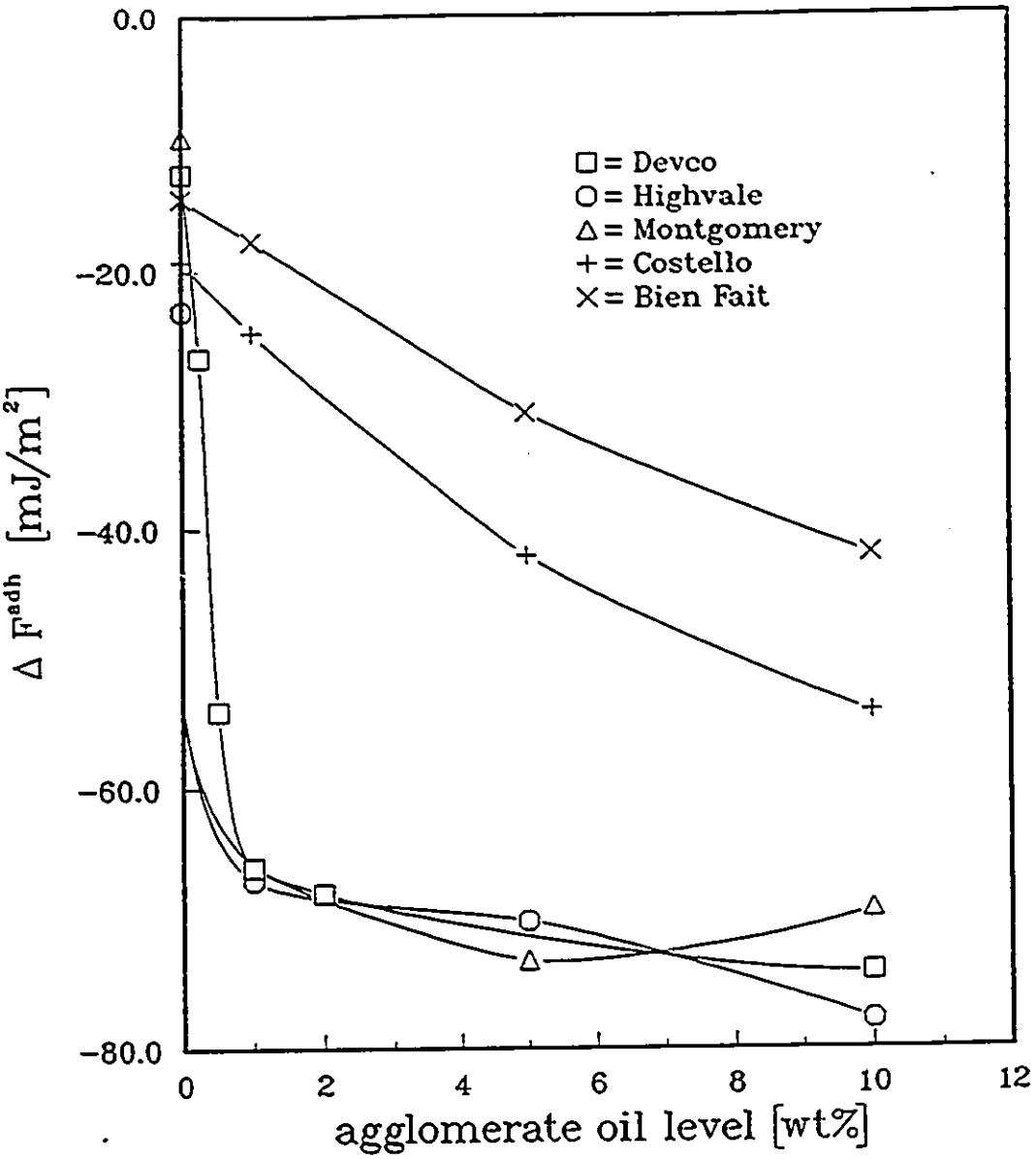

Figure 5.11: ΔF^{adh} vs. oil level.

lignites have a smaller energy advantage for the adhesion process associated with flotation. The favourability of adhesion does not give information about the strength of the bond formed once the adhesion has occurred. In a sense, favourability of adhesion means that an interface will form easily, but the permanence of the interface also requires forms of chemical bonding across the interface and some viscous elasticity to support the structure in a dynamic medium.

5.3.3 General agglomerate surface property model

There are two additional well known factors which exert a significant influence on coal-oil agglomerate flotation recovery. These are the agglomerate diameter and the rank of the coal. These influences were expressed in equation 1.62. The effect of an increased oil level resulting in a large agglomerate is already accounted for by equation 5.21, but this is only in terms of growth from a dispersed diameter. The actual dispersed diameter must be considered, and from equation 1.62, it must be inserted into the model such that when the collision is *already* assumed to have occurred (via the hydrodynamic collision model), a smaller particle will more readily become attached to the bubble. Further, it is known that coals of a higher rank are better recovered. To account for this, we have the hydrophobicity index, h, defined by equation 5.20.

With reference to the Devco sample as a calibration sample, the model of equation 5.21 can be generalized by the empirical factor, $(d_{P_{CAL}}/d_P)^{\beta h}$. By testing this factor with the CFD simulation, a value of $\beta = 0.5$ was determined. So, for a more general model to calculate a value of r_α from the coal-oil agglomerate properties, which can then be input into the CFD simulation to predict flotation recoveries, we have,

$$r_\alpha = \frac{\left(\frac{d_{P_{CAL}}}{d_P}\right)^{\frac{h}{2}}}{\frac{m}{\Delta\gamma} + b} \tag{5.22}$$

Table 5.1 lists the attachment efficiencies associated with each type of agglomerate to be input to the MD-PHASE simulation. These simulations were run, and the

sample	wt% oil	$\Delta\gamma$ [mJ/m^2]	$\frac{d_{P_{CAL}}}{d_P}$	h	r_a
Highvale	1.0	23.02	3.54	2.54	0.07431
Highvale	5.0	24.75	3.54	2.54	0.08191
Highvale	10.0	28.15	3.54	2.54	0.10248
Montgomery	1.0	32.73	1.64	4.18	0.07642
Montgomery	5.0	28.42	1.64	4.18	0.13190
Montgomery	10.0	30.40	1.64	4.18	0.09891

Table 5.1: Parameter inputs for flotation simulation for subbituminous coals for recovery predictions.

calculated recoveries are shown with the dashed lines in figure 5.12, compared to the measured recoveries, given as the discrete data points. The predicted values appear to follow the measured data in figure 5.12 quite well. It should be noticed that the results for the Highvale coal show an increasing recovery as the oil level is increased, while the Montgomery samples passes through a recovery maximum at an intermediate oil level. This is an effect of the absolute size of each sample. The Highvale agglomerates range from 9.4 to 14.1 μm in size. Referring to figure 4.35, this data falls into a size range where the recovery increases monotonically with agglomerate diameter. The Montgomery sample on the other hand, has a size range of 20.3 to 34.5 μm, which passes through the recovery maximum in terms of agglomerate diameter shown in figure 4.35. Thus, the model for attachment efficiency, integrated with CFD simulation, is able to account for these interdependent effects when calculating a recovery.

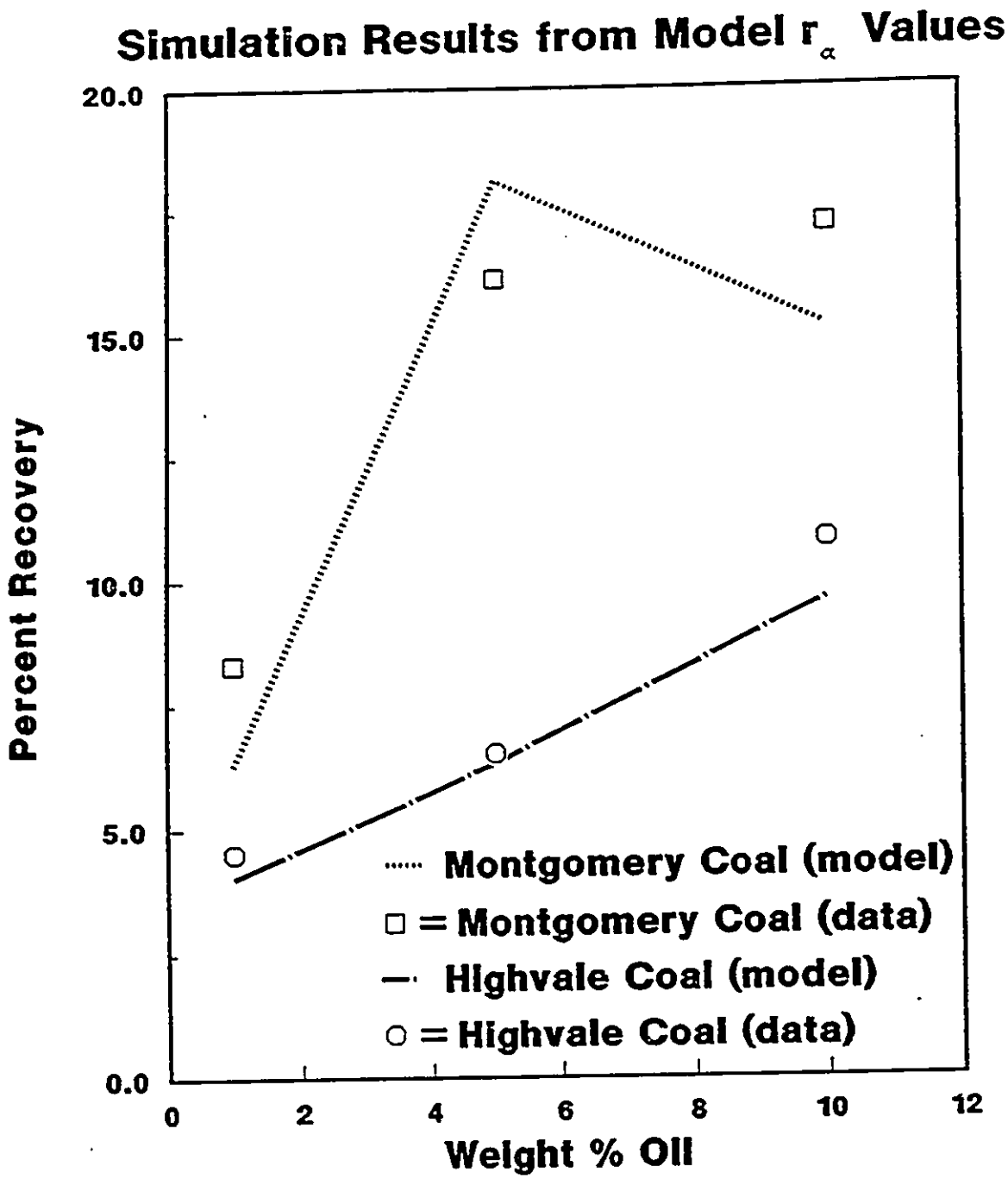

Figure 5.12: Generalized integrated model recovery predictions.

5.4 A discussion of flotation kinetics modeling

There are several known trends and phenomena in flotation and it is the purpose of this section to discuss the results and observations from the present study in view of the overall body of knowledge available in the field.

In general, the influence of an increased bubble size is to reduce the recovery by flotation. This has been observed by Anfruns and Kitchener [14] as well as by Weber [22], and was incorporated into a ratio of d_P/d_B by Reay and Ratcliffe [17]. This is consistent with the findings of this work. This result would be manifested by the reduced residence time in the cell due to buoyancy forces, and by being less subject to the turbulent mixing which determines the collision rate according to equation 1.60.

The effects of the particle size likewise are often put into expressions for the flotation kinetics. Kinetics are typically applied to a batch system, but the rate of flotation given for such a system directly relates to the collection efficiency in a continuous system. Reay and Ratcliffe [17] comment that the flotation rate was found for particles up to 15 μm proportional to,

$$R_f = k\left(\frac{d_P}{d_B}\right)^{2.05}$$

At particle sizes larger than 15 μm, the attachment efficiency was said to become very dependent on d_P, and the exponent was found to become even greater than 2.05. In such a specialized study, the hydrodynamic influence of larger particles could not be accounted for. The present study can easily treat bubble and particle size effects independently. Certain hydrodynamic assumptions were made by Reay and Ratcliffe which they considered valid for $d_P/d_B < 0.25$. The present work makes no such assumptions.

A more updated model, based on some of the original work by Reay and Ratcliffe was presented by Dobby and Finch [134]. Independent effects of bubble and particle size were given be them. However, the model goes only as far as predicting values of E_A, and how this parameter is manifested in a three phase float cell is left unresolved. The work presented here integrates the collision models and flow field effects and can treat ranges of the input parameters as prescribed by the local conditions in the float

cell. That is, variables such as dispersed phase concentrations, velocities and bubble loading are treated in an interdependent and dynamic way, so that these effects need not be generalized or shown one at a time in an illustrative sense.

The influence of the rank of a coal and hence its flotability is often expressed in term of an induction time. This factor reduces to a probability function arising in a cell model for collision frequencies. If a field solution is used to account for the collisions, as done in this work, this probability which is determined as an integral over all possible collision angles, can be replaced in the model with a quantity tied to the surface properties. In the absence of surface free energy data, an induction time which is compared to an averaged, integrated sliding time is used as the attachment efficiency. A value of the agglomerate surface free energy uniquely corresponds to this *integrated* probability.

Work by Ye and Miller [48], estimated the induction times for attachment for various ranks of coal. In general, except for anthracite, the higher the rank, the lower the induction time. In terms of the expression,

$$R_f = k\left(\frac{d_P}{d_B}\right)^n$$

from Reay and Ratcliffe, and which was also employed in other work, the value of n was found to vary from 0 to 2.1 [17, 46]. The density of the particles was varied in these experiments, but the surface properties of the various materials were not considered. The results of Ye and Miller could be interpreted in terms of this exponent n, where a higher rank corresponds to a larger exponent. The anomaly of the reduced flotability of anthracite could be explained by this density effect, in that anthracite is typically denser than other coals which have otherwise similar densities. Density aside, the hydrophobicity index, which is a very simple expression, could be weighted to favour volatiles, since they, more than fixed carbon, contribute to a lower surface free energy. Thus, since anthracites contain a lower volatiles fraction than other high rank coals, their inherent flotability should be less.

In this work, the exponent used was $h/2$ since it was a quantity relating the flotability of the coal to its material composition. Thus, this work has advanced a step beyond simple curve fitting for the model exponent, providing a measured quantity

reflective of the particulate surface, which was used to regulate the determination of r_a values. A paper by Fuerstenau et al. [137] discusses the flotability in terms of surface functional groups in coals. The content of phenolic and carboxylic groups correlated very strongly with the flotation response. Coal wettability was found to depend on the balance of hydrophobic and hydrophilic sites, and this was essentially how the attachment efficiency equation developed here employed the extent of wetting and hydrophobicity index.

An additional influence is the extent of turbulence in the float cell. Although conditions were specified as turbulent in the MD-PHASE model, the turbulence parameters themselves were not investigated as operating variables. These effects would not have a general bearing on elucidating the influence of the surface properties of the coal-oil agglomerates on their flotation recovery in a relative sense, but would come into play for designing a cell geometry where energy inputs, turbulent conditions and the resulting flow scheme affecting the net recovery would have to be balanced [138].

Chapter 6

Conclusions and Recommendations

6.1 Conclusions

The research detailed in this thesis touches on several diverse topics which are all connected to modeling the flotation of coal-oil agglomerates.

The adhesion surface tension method and a laser diffraction particle sizer provided means of measuring respectively the surface free energy and mean particle-sizes of agglomerates formed from various ranks of coal and *n*-hexadecane in an aqueous medium. These data were then used to correlate the enlargement factor obtained at each oil level, with structural features of the agglomerates. The measurement of agglomerate surface free energies was a novel result.

From the work carried out, it can be said that there is a direct correlation between the measured surface free energy of coal-oil agglomerates in aqueous media and the agglomeration/flotation recovery results. Coals of subbituminous and bituminous rank will acquire an oil-like surface at oil levels as low as 1 weight%. Lower rank lignites show a decrease in surface free energy as oil level is increased, but their ability to be agglomerated and floated is limited. For the two subbituminous coals, despite showing similar wetting curves, the agglomeration/flotation recovery

was markedly different, and this difference has been attributed to how their composition contributes to their macroscopic surface behaviour. Coals high in ash are more likely to have restricted wetting on the surface and this in turn depresses the agglomeration/flotation recovery. Further, smaller particles and smaller agglomerates will encounter more hydrodynamic resistance to successful flotation, and even collisions leading to agglomeration and wetting.

Ash rejection among the coals tested was high, no matter what oil level is used. It was found to be most selective at low oil levels where hydrophobic and hydrophilic properties of microscopic regions on the coal surface are more pronounced. In this case, there is not an excessive amount of oil present to wet less thermodynamically favoured regions such as ash, when the fuel bearing portions have already been oil wetted. Provided that the hydrophobicity index h is greater than about 2, small amounts of oil are required to give the agglomerate surface an oil character, which promotes agglomeration and recovery.

Lignites do not show good recovery and agglomeration at low oil levels. The agglomerating oils used in this project were not suitable for obtaining favourable recoveries of lignites.

From this study it can be said that the amount of oil introduced to a coal-water slurry for forming agglomerates determines several properties on the agglomerate surface. The net agglomerate surface free energy was found to approach that of the pure oil at increased oil levels, and as such, the three-phase contact angle between the agglomerate, the oil meniscus and the suspending water decreased. Thus at oil levels below 2 weight%, the bond volumes were great enough to consume the available oil in forming agglomerates no larger than doublets and triplets. With smaller contact angles at higher oil levels, the particle bonding is more economical and larger, more compact agglomerates are seen. A constraining system of linear equations was developed to illustrate this.

A full Navier-Stokes two-dimensional primitive-variable boundary element method scheme for incompressible flow by time difference was formulated and implemented. The results for a driven-cavity flow compared well with results obtained by other numerical methods. This was a novel formulation and implementation. Numerical

difficulties prevented this approach from being carried forward any further.

A two-dimensional turbulent, three-phase finite-volume code was formulated and implemented. A simulation involving mass transfer between dispersed phases was developed. Convergence for a test case in a unidirectional tube, and then in a float cell configuration involving cross-flow of the inlet streams was obtained.

By altering input values of an attachment efficiency and the particle sizes, the behaviour of the float cell was characterized and correlated to the measured surface properties of the Devco bituminous coal.

The collisions were predicted by a model based on turbulent energy dissipation and local populations of the dispersed phases.Modeling of an attachment efficiency parameter from fundamental agglomerate properties produced estimates of this attachment efficiency which when input to the hydrodynamic simulation of the float cell operation, accurately predicted the recoveries of two other subbituminous coal samples, including handling the changing functional nature of the recovery curves that arise over changing agglomerate diameter regimes. Specifically, this attachment efficiency was expressed as $\tau_\alpha = f(\Delta\gamma, d_P, h)$, accounting for agglomerate size, inherent material hydrophobicity and oil wettability.

The integrated nature of this approach, basing recovery predictions on fundamental material properties, and using micro-flotation collision models in a macroscopic hydrodynamic context where all local variables are prescribed, ensures soundness of results and an adaptability to various behaviour regimes. The degree of empiricism in this model was kept to a minimum. The model constants are specific to the experiments of this study, but the general functional form should be applicable elsewhere. The integrated flotation model with resolved field equations accounting for the flotation recovery is a novel method.

6.2 Recommendations

The results obtained and conclusions drawn from this work were done so with the realization that the work could not hope to be all-encompassing, but with the understanding that the assumptions made, and limitations imposed would still allow

sufficient scope to the results to render them interesting, novel, enlightening and useful.

In the course of the project, various further avenues of research arose, as well as various questions which could not be included in the scope of the present work. These items are mentioned below as suggestions or recommendations for further work on the topic.

Computer routines and experience with TURCOM based coding are already in place to extend the model to three dimensions. The flow model itself is in a generalized form, so it would be mostly a computational coding task to convert to three dimensions. In three dimensions, the full effects of cell geometries come into resolution, and as such, the cell configuration and the turbulence parameters would be highly useful for real engineering design work.

The present model mainly discusses the recovery of the coal-oil agglomerates by flotation. Ash particles could be included in the simulation by adding equations for their motion and volume fraction in the cell, as well as their mass transfer properties. This would allow a more complete simulation for the study of deashing and/or product enrichment.

Hexadecane was used as a binding oil since it is a well characterized pure substance. It would be constructive to determine agglomerate surface properties with a more effective binding oil, and to verify the model in a high recovery regime. Further, the model could be tested with the flotation of other types of ores. At the present, the surface free energy measurement techniques for particulates are extremely cumbersome and time consuming. A more efficient experimental method would be most welcome in this area of research.

Finally, if computer size and speed increase, equations detailing agglomerate size distributions, bubble size distributions and bubble coalescence could be implemented to provide a more complete and physically realistic simulation of the processes occurring in a flotation cell.

6.3 Original Research Contributions

Given below are the principal original contributions to research accomplished over the course of the project.

- novel surface tension measurements for liquid-bound agglomerated particles
- novel BEM formulation for unsteady flow with a time step
- novel formulation and solution of field equations for mineral flotation
- novel means for decoupling collision and attachment phenomena in flotation
- novel demonstration of the simultaneous effects of size enlargement and surface improvement for coal-oil agglomerate flotation

References

[1] Deryagin, B.V., Dukhin, S.S. and Rulev, N.N., "Kinetic theory of flotation of small particles", Surf. Colloid Sci. 13, 71-113 (1984).

[2] Sutherland, K.L., "Kinetics of the flotation process", J. Phys. Chem., 52, 394-425 (1948).

[3] Capes, C.E., Coleman, R.D., Croteau, S., Jonasson, K. and Thayer, W.L., "Agglomerate recovery methods and yield-impurity relationships in oil agglomeration", Proc. Coal Liq. and Alternative Fuel Tech. Meeting, Halifax, NS, Sept. 29-Oct. 3 (1986).

[4] Wojcik, W. and Al Taweel, A.M., "Beneficiation of coal fines by aggregative flotation", Powder Tech. 40, 179-185 (1984).

[5] Hirajima, T., Chan, E., Whiteway, S., Stefanski, M. and Stewart, I., "Beneficiation of char, from a pyrolyzed eastern Canadian coal, by aggregative flotation", Coal Prep. 5, 85-108 (1987).

[6] Capes, C.E. , "Oil Agglomeration Process Principles and Commercial Application for Fine Coal Cleaning", in "Coal Preparation", 5th ed., J.W. Leonard and B.C. Hardinge, Eds., SME/AIME, Littleton, CO (1991), pp. 1020-1041.

[7] Froment, A., "Improvements relating to the concentration of ores", U.K. Patent, No. 12,778, June 4 (1902).

[8] Capes, C.E., Coleman, R.D. and Thayer, W.L., "Recovery and utilization of fine coal", paper 6b-301, World Congress III of Chemical Engineering, Tokyo, vol. 1 (1986), pp. 525-528.

[9] Brown, D.J., "Particle trajectories, collision and attachment in froth flotation", in "Aerodynamic Capture of Particles", E.G. Richardson, Ed., Pergamon Press, London (1960), pp. 35-43.

[10] Usenko, V.G., Samsonov, V.V., Popov, K.I., Polonskii, S.B. and Leonov, S.B., "Nonstandardised measurement devices for the investigation of the hydrodynamics of of multiphase flows in flotation machines", Sov. Non-Ferrous Met. Res. 27(4), 262-266 (1985).

[11] Absolom, D.R., Eom, K., Vargha-Butler, E.I., Hamza, H.A. and Neumann, A.W., "Surface properties of coal particles in aqueous media. II. Adhesion of coal particles to polymeric substrates", Colloids Surf. 17(2), 143-157 (1986).

[12] Lamb, H., "Hydrodynamics", 6th Ed., Cambridge Univ. Press (1932).

[13] Herne, H., "The classical computations of the aerodynamic capture of particles by spheres", in "Aerodynamic Capture of Particles", E.G. Richardson, Ed., Pergamon Press, London (1960), pp. 35-43.

[14] Anfruns, J.F. and Kitchener, J.A., "Rate of capture of small particles in flotation", Trans. Inst. Min. Metall. (Sect. C: Mineral Process. Extr. Metall.) 86, 9-15 (1977).

[15] Evans, L.F., "Bubble-mineral attachment in flotation", Ind. Eng. Chem. 46, 11, 2420-2424 (1954).

[16] Flint, L.R. and Howarth, W.J., "The collision efficiency of small particles with spherical air bubbles", Chem. Eng. Sci. 26, 1155-1168 (1971).

[17] Reay, D. and Ratcliff, G.A., "Removal of fine particles from water by dispersed air flotation: effects of bubble size and particle size on collection efficiency", Can. J. Chem. Eng. 51, 178-185 (1973).

[18] Reay, D. and Ratcliff, G.A., "Experimental testing of the hydrodynamic collision model of fine particle flotation", Can. J. Chem. Eng. 53, 481-486 (1973).

[19] Derjaguin, B.V., Dukhin, S.S. and Rulev, N.N., "Importance of hydrodynamic interaction in the flotation of fine particles", Koll. Zh. 38(2), 251-257 (1976).

[20] Brenner, H., "The slow motion of a sphere through a viscous fluid towards a plane surface", Chem. Eng. Sci. 16(3+4), 242-251 (1961).

[21] Schulze, H.J. and Gottschalk, G., "Investigations of the hydrodynamic interaction between a gas bubble and mineral particles in flotation", in "Mineral Processing", 13th Intl. Mineral Processing Congress, Warsaw, June 4-9, 1979, J. Laskowski, Ed., Elsevier, Amsterdam, Part A (1981), pp. 63-85.

[22] Weber, M.E., "Collision efficiencies for small particles with a spherical collector at intermediate Reynolds numbers", J. Separ. Proc. Technol. 2(1), 29-33 (1981).

[23] Dobby, G.S. and Finch, J.A., "A model of particle sliding time for flotation size bubbles", J. Colloid Interface Sci. 109, 2, 493-498 (1986).

[24] Woo, S-W., "Simultaneous free and forced convection around submerged cylinders and spheres", PhD Thesis, McMaster University (1971).

[25] Mileva, E. and Radoev, B., "Effective zones of hydrodynamical interaction of fluid particles at small separations", Coll. & Polym. Sci. 264(9), 823-828 (1986).

[26] Cox, R.G. and Brenner, H., "The slow motion of a sphere through a viscous fluid towards a plane surface – II Small gap widths, including inertial effects", Chem. Eng. Sci. 22, 1753-1777 (1967).

[27] Banerjee, P.K. and Butterfield, R.,"Boundary Element Methods in Engineering Science", McGraw-Hill, New York (1981).

[28] Wu, J.C. and Thompson, J.F., "Numerical solutions of time-dependent incompressible Navier-Stokes equations using an integro-differential formulation", Comp. & Fluids 1(2), 197-215 (1973).

[29] Wu, J.C., "Fundamental solutions and numerical methods for flow problems", Int. J. Numer. Meth. Fluids 4, 185-201 (1984).

[30] Wu, J.C., "Problems of general viscous flow", in "Developments in Boundary Element Methods - 2", P.K. Banerjee and R.P. Shaw, Eds., Applied Sci. Publ., London (1982), ch. 4, pp. 69-109.

[31] Wu, J.C., "Fundamental solutions and boundary element methods", Eng. Analysis 4(1), 2-6 (1987).

[32] Sokolnikoff, I.S. and Redheffer, R.M., "Mathematics of Physics and Modern Engineering", McGraw-Hill, New York (1966).

[33] Wu, J.C., Rizk, Y.M. and Sankar, N.L., "Problems of time-dependent Navier-Stokes flow", in "Developments in Boundary Element Methods - 3", P.K. Banerjee and S. Mukherjee, Eds., Elsevier, London (1984), ch. 6, pp. 137-169.

[34] Tosaka, N. and Onishi, K., "Boundary integral equation formulations for unsteady incompressible viscous fluid flow by time-differencing", Eng. Analysis 3(2), 101-104 (1986).

[35] Tosaka, N. and Kakuda, K., "Numerical Simulations of the Unsteady-state incompressible viscous flows using an integral equation", in "Boundary Elements. Proc. Intl. Conf.", Beijing, China, October 14-17, 1986, D. Qinghua, Ed., Pergamon Press, New York (1986), pp. 163-172.

[36] Schulze, H.J., "Dimensionless number and approximate calculation of the upper particle size of floatability in flotation machines", Int. J. Mineral Process. 9, 321-328 (1982).

[37] Carnahan, B., Luther, H.A. and Wilkes, J.O., "Applied Numerical Methods", Wiley & Sons, New York (1969).

[38] Gosman, A.D. and Ideriah, F.D.K., "Teach-2E: A general computer programme of two-dimensional turbulent recirculating flows", Internal Report, Dept. of Mech. Eng., Imperial College, U. of London (1976).

[39] Lai, K.Y.M. and Salcudean, D.B., "TEMA: A computer program for two-phase, multi-dimensional turbulent recirculating flows", Internal Report, Dept. of Mech. Eng., U. of Ottawa (1985).

[40] Lai, K.M.Y., "TURCOM: A computer code for the calculation of transient, multi-dimensional, turbulent, multi-component chemically reactive fluid flows. Part I: Turbulent, isothermal and incompressible flow", NRC No. 27632, TR-GD-011 (1987).

[41] Inoue, T., Nonaka, M. and Imaizumi, T., "Flotation process modelling", in "Advances in Mineral Processing: A Half-Century of Progress in Application of Theory to Practice", SME, Littleton, CO (1986), ch. 12, pp. 209-228.

[42] Abrahamson, J., "Collision rates of small particles in a vigorously turbulent fluid", Chem. Eng. Sci. 30, 1371-1379 (1975).

[43] Bischofberger, C. and Schubert, H., "Untersuchungen zur hydrodynamischen Optimierung des Flotationsprozesses bei der Kalisalz-flotation", Neue Bergbautechnik **10**, 58-62 (1980).

[44] Yoon, R.H. and Luttrell, G.H., "The effect of bubble size on fine coal flotation", Coal Prep. **2**, 179-192 (1986).

[45] Szatkowski, M. and Freyberger, W.L., "Model describing mechanism of the flotation process", Trans. Inst. Min. Metall. (Sect. C: Mineral Process. Extr. Metall.) **94**, 129-135 (1985).

[46] Jiang, Z.W. and Holtham, P.N., "Theoretical model of collision between particles and bubbles in flotation", Trans. Inst. Min. Metall. (Sect. C: Mineral Process. Extr. Metall.) **95**, 187-194 (1986).

[47] Al Taweel, A.M., Delory, B., Wozniczek, J., Stefanski, M., Andersen, N. and Hamza, H.A., "Influence of the surface characteristics of coal on its floatability", Colloids Surf. **18**, 9-18 (1986).

[48] Ye, Y., Miller, J.D., "Bubble/particle contact time in the analysis of coal flotation", Coal Prep. **5**, 147-166 (1988).

[49] Chibowski, E. and Holysz, L., "Surface free energy and floatability of minerals", Mat. Sci. Forum **25-26**, 521-524 (1988).

[50] Wojick, W., Janczuk, B. and Bialopiotrowicz, T., "Adhesion of air bubbles to the surface of low-rank coals", in "Processing and Ultilization of High-Sulfur Coals III", R. Markuszewski and T.D. Wheelock, Eds., Elsevier, Amsterdam, (1990), pp. 133-143.

[51] Janczuk, B., Bialopiotrowicz, T. and Wojick, W., "Adhesion of air bubbles to low-rank coals surface in the presence of *n*-alkanes and diacetone alcolhol", Acta Chim. Hung. **128**(1), 3-17 (1991).

[52] Janczuk, B., Wojick, W., Staszczuk, P., Bialopiotrowicz, T. and Chibowski, E., "Detachment forces of air bubble from pyrite surface covered with apolar and polar liquids", J. Min. Met. Fuels **9**, 380-384 (1989).

[53] Darcovich, K., Smyth, T.J. and Capes, C.E., "Coal rank and surface properties of oil agglomerates", Adv. Powder Tech. **4**(2), 115-128 (1993).

[54] Holtham, P.N. and Cheng, T-W., "Study of probability of detachment of particles from bubbles in flotation", Trans. Inst. Min. Metall. (Sect. C: Mineral Process. Extr. Metall.) **100**, C147-C153 (1991).

[55] Finch, J.A. and Smith, G.W., "Bubble-solid attachment as a function of bubble surface tension", Can. Metall. Quarterly **14**(1), 47-51 (1975).

[56] Kelebek, S., Smith, G.W., Finch, J.A. and Yoruk, S., "Critical surface tension of wetting and flotation separation of hydrophobic solids", Sep. Sci. Tech. **22**(6), 1527-1546 (1987).

[57] Ennis, B.J., Li, J., Tardos, G.I. and Pfeffer, R., "The influence of viscosity on the strength of an axially strained pendular liquid bridge", Chem. Eng. Sci. **45**(10), 3071-3088 (1990).

[58] Janczuk, B., Wojcik, W. and Bialopiotrowicz, T., "Studies on contact angle and work of adhesion in the system coal/*n*-alkane film-air bubble-water", Powder Tech. **61**, 211-216 (1990).

[59] Ek, C., "Flotation Kinetics", in "Innovations in Flotation Technology", P. Mavros and K.A. Matis, Eds., Kulwer, The Netherlands (1992), pp. 183-210.

[60] Coleman, R.D., Bennett, A., Capes, C.E., Clarkin, G., Croteau, S., Dal-Cin, M., Goring, C., Hazlett, J.D., Jonasson, K., Lick, A., McCracken, T. and Toll, F., "Pilot demonstration of fine Obed coal beneficiation and recovery (1988) at National Research Council, Ottawa, Ontario", NRC Report No. C-1172-89S, April 14 (1989).

[61] Wen, W.W. and Sun, S.C. "An electrokinetic study on the oil flotation of oxidized coal", Sep. Sci. Tech. **16**(10), 1491-1521 (1981).

[62] Briker, Y., Szymocha, K., Pawlak, W., Kramer, J. and Ignasiak, B., "Feasibility of Aglofloat process for deashing and desulfurization of high-sulfur coals", in "Processing and Ultilization of High-Sulfur Coals IV", P.R. Dugan, D.R. Quigley and Y.A. Attia, Eds., Elsevier, Amsterdam (1991), pp. 357-374.

[63] Knight, J.C., "Florence mining OK's oil agglomeration", Coal **5**, 57-60 (1989).

[64] Al Taweel, A.M. and Kasireddy, V.K., "Column flotation of aggregated ultrafine coal", in "Advances in Coal and Mineral Processing Using Flotation", SME-AIME, Littleton, CO, (1989), pp. 356-366.

[65] Seaman, B., "Chasing the American Dream", Time **140**(1), 46-51 (1992).

[66] Drzymala, J., Markuszewski, R. and Wheelock, T.D., "Influence of air on oil agglomeration of carbonaceous solids in aqueous suspension", Int. J. Mineral Process. **18**, 277-286 (1986).

[67] Absolom, D.R., Zingg, W., Thomson, C., Policova, Z., Van Oss C.J. and Neumann, A.W., "Erythrocyte adhesion to polymer surfaces", J. Colloid Interface Sci. **104**(1), 51-59 (1985).

[68] Darcovich, K., Capes. C.E. and Talbot, F.D.F., "Surface properties of coal-oil agglomerates in the floc regime", in, "Preprints 196th ACS Natl. Meeting", Los Angeles, CA, Sept. 25-30, 1988, **33**(4), 765-776 (1988).

[69] Neumann, A.W., Good, R.J., Hope, C.J. and Sejpal, M.A. "An equation-of-state approach to determine surface tensions of low-energy solids", J. Colloid Interface Sci. **49**, 291-304 (1974).

[70] Smith, R.P., Absolom, D.R., Spelt, J.K. and Neumann, A.W. "Approaches to determine the surface tension of small particles: equation-of-state considerations", J. Colloid Interface Sci. **110**, 521-532 (1986).

[71] Stephen, H. and Stephen, T., Eds., in "Solubilities of Inorganic and Organic Compounds. Volume 2: Ternary and Multicomponent Systems", Pergamon Press, New York (1964), Part 2, No. 5160, 1740.

[72] "CRC Handbook of Chemistry and Physics", R.C. Weast, Ed., CRC Press Inc., Boca Raton, FL (1987).

[73] Darcovich, K., Kotlyar, L.S., Tse, W.C., Ripmeester, J.A., Capes, C.E. and Sparks, B.D., "Wettability Study of Organic-Rich Solids Separated from Athabasca Oil Sands", Energy Fuels 3, 386-391 (1989).

[74] Hörmander, L., "Linear partial differential operators", 2nd revised printing, Springer, Berlin (1964).

[75] Tosaka, N., "Integral equation formulations with the primitive variables for imcompressible viscous fluid flow problems", Comp. Mech. 4, 89-103 (1989).

[76] Darcovich, K., Talbot, F.D.F. and Capes, C.E., "Hydrodynamic interactions in mineral flotation: moving boundary aspects", in "ISCFD-Nagoya", Nagoya, Japan, August 28-31 (1989), pp. 1228-1233.

[77] Darcovich, K., "Letter to the Editor on the 'Integral equation formulations with primitive variables for viscous fluid flow' ", Comp. Mech. 6, 465 (1990).

[78] Lebedev, N.N., "Special Functions and Their Applications", Dover, New York (1972).

[79] Launder, B.E. and Spalding, D.B., "The numerical computation of turbulent flows", Comp. Meth. Appl. Mech. Eng. 3, 269-289 (1974).

[80] Bird, R.B., Stewart, W.E. and Lightfoot, E.N., "Transport Phenomena", Wiley, New York (1960).

[81] Bilger, R.W., "A note on Favre averaging in variable density flows", Comb. Sci. Tech. 11, 215-217 (1975).

[82] Jones, W.P., "Models for turbulent flows with variable density and combustion", in "Prediction Methods for Turbulent Flows", Von Karman Institute for Fluid Dynamics, Rhode Saint Genèse, Belgium, January 15-19 (1979).

[83] Boussinesq, M.J., "Theory de l'écoulement tourbillant", Mémoires présentés par divers savants à l'académie des sciences de l'Institut national de France et imprimés par son ordre, Imprimerie Nationale, Paris 23, 46 (1877).

[84] Watkins, A.P., "Flow and heat transfer in piston/cylinder assemblies", Ph.D. Thesis, Imperial College, U. of London (1977).

[85] Reynolds, A.J., "Turbulent Flows in Engineering", John Wiley, New York (1974).

[86] Jones, W.P. and Launder, B.E., "The calculation of low-Reynolds number phenomena with a two-equation model of turbulence", Int. J. Heat Mass Transfer 16, 1119-1130 (1973).

[87] Hinze, J.O., "Turbulence", McGraw-Hill, New York (1959).

[88] Schlicting, H., "Boundary Layer Theory", 4th Ed., McGraw-Hill, New York (1960).

[89] Launder, B.E. and Spalding, D.B., "Mathematical Models of Turbulence", Academic Press, London (1972).

[90] Brebbia, C.A., Telles, J.C.F. and Wrobel, L.C., "Boundary Element Techniques. Theory and Applications in Engineering", Springer-Verlag, Berlin (1984).

[91] Cruse, T.A., "Numerical solutions in three dimensional elastostatics", Intl J. Solids Struct. 5, 1259-1274 (1969).

[92] Darcovich, K., Talbot, F.D.F. and Capes, C.E., "Hydrodynamic Interactions in Mineral Flotation: Moving Boundary Aspects", in "Numerical Methods in Fluid Dynamics II", M. Yasuhara, H. Daiguji and K. Oshima, Eds., Japan Soc. of CFD, Sagemihara, Japan (1990), pp. 1055-1062.

[93] Press, W.H., Flannery, B.P., Teukolsky, S.A. and Vetterling, W.T., "Numerical Recipes", Cambridge Univ. Press (1987).

[94] Spalding, D.B., "A novel finite-difference formulation for differential equations involving both first and second derivatives", Int. J. Num. Meth. Eng. 4, 551-559 (1972).

[95] Patankar, S.V. and Spalding, D.B., "A calculational procedure for heat, mass and momentum transfer in three-dimensional parabolic flows", Int. J. Heat Mass Transfer 15, 1787-1806 (1972).

[96] Householder, A.S., "The Theory of Matrices in Numerical Analysis", Blaisdale, New York (1964).

[97] Lai, K.M.Y. and Salcudean, M., "Computer analysis of multi-dimensional, turbulent, buoyancy-induced, two-phase flows in gas-agitated-liquid reactors", Comp. & Fluids 15(3), 281-295 (1987).

[98] Lyczkowski, R.W. and Wang, C.S., "Hydrodynamic modeling and analysis of two-phase non-Newtonian coal/water slurries", Powder Tech. 69, 285-294 (1992).

[99] Soo, S.L., "Fluid Dynamics of Multiphase Systems", Blaisdale, Waltham, MA (1967).

[100] Ergun, S., "Fluid Flow Through Packed Columns", Chem. Eng. Prog. 48, 89-94 (1952).

[101] Wen, C.Y. and Yu, Y.H., "Mechanics of fluidization", Chem. Eng. Prog. Symp. Ser. 62(62), 100-111 (1966).

[102] Rowe, P.N., "Drag forces in a hydraulic model of a fluidized bed. II", Trans. Inst. Chem. Eng. 39, 175-180 (1961).

[103] Spalding, D.B., "Developments in the IPSA procedure for numerical computation of multi-phase-flow phenomena with inter-phase slip, unequal temperatures, etc.", in "Advances in Computer Methods for Partial Differential Equations - IV", R. Vichnevesky and R.S. Stepleman, Eds., Office of Naval Research, Bethesda, MD (1981), 19 pp.

[104] Lai, K.M.Y., "TURCOM: A computer code for the calculation of transient, multi-dimensional, turbulent, multi-component chemically reactive fluid flows. Part II: Compressible and Combusting Flow", NRC No. 29287, TR-GD-012 (1988).

[105] Pendse, H., Tien, C. and Turian, R.M., "Drag force measurement of single spherical collectors with deposited particles", AIChE J. 27(3), 364-372 (1981).

[106] Happel, J. and Brenner, H., "Low Reynolds Number Hydrodynamics", 2nd Ed., Nordhoff, Leydeon (1973).

[107] Lai, K.M.Y. and Salcudean, M., "Computation of three-dimensional flow associated with heat and mass transfer in gas-agitated-liquid reactors", Num. Heat Transf.", 14, 97-111 (1988).

[108] Borghesani, A.F., "Non-Newtonian flow behavior of coal-fuel oil suspensions", in "Encyclopedia of Fluid Mechanics", N.P. Cheremisinoff, Ed., Gulf Pub. Co., Houston (1988), v. 7, ch. 4, pp. 89-134.

[109] Rumpf, H., "The strength of granules and agglomerates", in "Agglomeration; Intl. Symp.", Philadelphia, PA, Apr. 12-14, 1961, W.A. Knepper, Ed., Interscience Publishers, New York (1962), pp. 379-418.

[110] Vargha-Butler, E.I., Kashi, M., Hamza, H.A. and Neumann, A.W., "Direct Contact angle measurements on polished sections of coal", Coal Prep. 3, 53-75 (1986).

[111] Sablik, J., "Free surface energy of coals of highest hydrophobicity", Pol. J. Chem. 59(4), 433-438 (1985).

[112] Capes, C.E. and R.J. Germain, R.J., "Selective oil agglomeration in fine coal beneficiation", in "Physical Cleaning of Coal", Y.A. Liu, Ed., Marcel Dekker Inc., New York, ch. 6, 293-352 (1982).

[113] Coleman, R.D., Bennett, A., McCracken, T. and Toll, F., "Fine waste coal recovery demonstration at Quintette Coal Limited, Tumbler Ridge, B.C.", NRC Report No. C-1184-89S (Nov., 1989).

[114] Tosaka, N. and Kakuda, K., "Numerical simulations of laminar and turbulent flows by using an integral equation", in "Boundary Elements IX Vol. 3: Fluid Flow and Potential Applications", C.A. Brebbia, W.L. Wendland and G. Kuhn, Eds., Comp. Mech. Publ., Southampton, UK (1987), pp. 489-502.

[115] Standish, N., Yu, A.B. and Igusti-Ngurah, A., "Estimation of bubble-size distribution in flotation columns by dynamic bubble-disengagement technique", Trans. Inst. Min. Metall. (Sect. C: Mineral Process. Extr. Metall.) 100, C31-C41 (1991).

[116] Darcovich, K., Capes, C.E. and Talbot, F.D.F., "Surface Characteristics of Coal-Oil Agglomerates in the Floc Regime", Energy Fuels 3, 64-70 (1989).

[117] Pietsch, W.B., "Tensile strength of granular materials", Nature 217, 736-737 (1968).

[118] Germain, R.J.,"Rejection of suspending liquid from fine particles by agglomeration methods", Masters Thesis, U. of Waterloo (1977).

[119] Newitt, D.M. and Conway-Jones, J.M., "A contribution to the theory and practice of granulation", Trans. Inst. Chem. Engrs. 36, 422-442 (1958).

[120] Cassie, A.B.D., "Contact Angles", Discuss. Faraday Soc. 3, 11-16 (1948).

[121] Crawford, R., Koopal, L.K. and Ralston, J., "Contact angles on particles and plates", Colloids Surf. 27, 57-64 (1987).

[122] Capes, C.E., "Basic research in particle technology and some novel applications", Can. J. Chem. Eng. 54, 3-12 (1976).

[123] Capes, C.E., Coleman, R.D., Hazlett, J.D. and Thayer, W.L., "Application of fine particle technologies in coal processing", in "Proc. 37th Can. Chem. Eng. Conf.", Montreal, May 18-22 (1987), pp. 413-415.

[124] Melrose, J.C., "Model calculations for capillary condensation", AIChE J. 12(5), 986-994 (1966).

[125] Capes, C.E. and Germain, R.J., "Rejection of suspending liquid from fine particles by agglomeration methods", in "Drying '80", A.S. Mujumdar, Ed., Hemisphere Publ. Corp., New York (1980), v. 2, pp. 460-466.

[126] Jin, R., Ye, Y., Miller, J.D. and Hu, J.S., "Characterization of coal hydrophobicity by contact angle, bubble attachment time, and FTIR spectroscopy", preprint no. 87-146, in "116th AIME Annual Meeting", Denver, CO, Feb. 23-27 (1987), 19 pp.

[127] Naka, N. and Nishida, Y., "Water wettabilites of foreign coals", Yukagaku 33(2), 80-87 (1984).

[128] Rosenbaum, M. and Fuerstenau, D.W., "On the variation of contact angles with coal rank", Int. J. Miner. Process. 12, 313-316 (1984).

[129] Wojcik, W., Bialopiotrowicz, T. and Janczuk, B., "The critical surface tension of Polish coals and their surface free energy components", Fuel 67(5), 688-692 (1988).

[130] Good, R.J., Srivasta, N.R., Islam, M., Huang, H.T.L. and Van Oss, C.J., "Theory of the acid-base hydrogen bonding interactions, contact angles, and the hysteresis of wetting: application to coal and graphite surfaces", J. Adhesion Sci. Technol. 4(8), 607-617 (1990).

[131] Tampy, G.K., Prudish, M.E., Savage, R.L. and Williams, R.R., "Free energy changes and hydrogen bonding in the wetting of coal", Energy Fuels 2, 787-793 (1988).

[132] Sekar, S. and Nath, G., "Boundary element solution of the Navier-Stokes equations for the flow in a square cavity", Acta Tech. Ceskoslovenskia akademie vned 36(1), 123-135 (1991).

[133] Gresho, P.M. and Sani, R.L., "On pressure boundary conditions for the incompressible Navier-Stokes equations", Int. J. Num. Meth. Fluids 7, 1111-1145 (1987).

[134] Dobby, G.S. and Finch, J.A., "Particle size dependence in flotation derived from a fundamental model of the capture process", Int. J. Mineral Process. 21, 241-260 (1987).

[135] Himmelblau, D.M.,"Process Analysis by Statistical Methods", Sterling Swift Pub. Co., Manchaca, TX (1970).

[136] Neumann, A.W., Absolom, D.R., Francis, D.W. and Van Oss, C.J., "Conversion tables of contact angles to surface tensions", Sep. Purif. Methods 9(1), 69-163 (1980).

[137] Fuerstenau, D.W., Rosenbaum, J.M. and Laskowski, J., "Effect of surface functional groups on the flotation of coal", Colloids Surf. 8, 153-174 (1983).

[138] Fallenius, K., "Turbulence in flotation cells", Int.. J. Mineral Process. 21, 1-23 (1987).

[139] Aris, R., "Vectors, Tensors, and the Basic Equations of Fluid Mechanics", Dover Publications, New York (1989).

[140] Suh, I.-G.,"Application of the Boundary Element Method to Coupled Problems in Thermoelasticity", PhD. Thesis, Grad. School of Industrial Technology, Nihon U. (1990).

Appendix A

Nomenclature

For the following variables, the units will be given under the M-K-S system.

Section 1.2.1

a particle radius [m]

d particle distance from bubble motion axis [m]

D maximum radial distance from bubble path axis for particle collision [m]

E collision efficiency

E_I collision efficiency at intermediate Reynolds numbers

E_S collision efficiency in Stokes regime

F force of distorted bubble acting on a particle [N]

G dimensionless inertial parameter

h elastic collision penetration depth [m]

h_c film rupture thickness [m]

m particle mass [kg]

n rate of collisions [collisions / s]

n_f rate of fruitful collisions [collisions / s·m^3]

N_0 particle concentration [particles / m^3]

N' bubble concentration [bubbles / m^3]

r polar coordinate relative to bubble [m]

r^* dimensionless flotation radius

R bubble radius [m]

R_f rate of flotation [kg / m^3·s]

S liquid velocity, $v(r,\theta)$, relative to bubble [m / s]

t_c particle sliding time [s]

u^* dimensionless flotation velocity

U_B bubble rise velocity [m / s]

$v_{p\theta}$ particle tangential velocity [m / s]

v_r liquid radial velocity [m / s]

v_T particle terminal settling velocity [m / s]

v_θ liquid tangential velocity [m / s]

V particle-bubble approach velocity [m / s]

W work done to increase bubble surface area [J]

Greek Letters

α fraction fruitful collisions floated

β_1, β_2 model constants from [17, 18]

γ bubble-liquid surface tension [J / m^2]

λ induction period [s]

θ polar coordinate relative to bubble [deg.]

θ_{Cr} maximum interception angle [deg.]

θ_{GR} interception angle for collision/sliding demarcation [deg.]

θ_m limiting angle of particle-bubble contact [deg.]

ρ_L liquid density [kg / m^3]

ρ_p particle density [kg / m^3]

Ψ streamline constant

Ψ_p particle stream function

ω voricity [1 / s]

Section 1.2.2

B boundary of region R

g general Poisson equation function

n_i unit outward normal vector

p pressure [N / m^2]

$P_B = P(\vec{r_B}, \vec{r_0})$

$P(\vec{r}, \vec{r_0})$ BIE fundamental solution for Poisson's equation

$\vec{r}$ BIE position vector [m]

$\vec{r_B}$ boundary point-field point vector [m]

$\vec{r^j}$ source point-field point vector [m]

R region for solution of field equation

u_i transport velocity vector [m / s]

Greek Letters

μ viscosity [N·s / m^2]

ϕ BEM field variable

Section 1.2.3

d problem dimensionality

e_i unit vector

G_i fundamental solution tensor

m time level

$Q(r,t)$ fundamental solution of vorticity transport equation

r source point-field point distance [m]

S surface of solution domain

t time [s]

Δt time step [s]

V solution domain

x_i field point

Greek Letters

β source point coefficient

δ_{ij} Kronecker delta function

$\delta(\xi,x)$ 2D Dirac delta function

ϵ_{ijk} tensor cross-product operator

ξ source point

τ_{ij} shear stress tensor [1 / s]

ω_i vorticity tensor [1 / s]

Section 1.3

i x-direction index

j y-direction index

u x-direction velocity

v y-direction velocity

x abscissa coordinate

y ordinate coordinate

Sections 1.4 to 1.6

d_B bubble diameter [m]

d_P particle diameter [m]

d_{PB} $r_P + r_B$ [m]

E_c collection efficiency

k, n exponents from [17]

n_B number concentration of bubbles [bubbles / m^3]

n_P number concentration of particles [particles / m^3]

P_a probability of attachment

P_c probability of collision

P_d probability of detachment

P_f probability of flotation

r_B bubble radius [m]

r_P particle radius [m]

r_a attachment efficiency

v_i turbulent collision velocity [m / s]

z_{PB} collisions per unit volume per unit time [collsions / m^3·s]

Greek Letters

ν_L kinematic viscosity of the liquid phase [N·s·m / kg]

ϵ turbulence energy dissipation [N·m / kg·s]

$\Delta\rho$ $|\rho_i - \rho_L|$

Section 2.2

Sections on the topic of particulate surface properties use these symbols. These also appear in Section 4.1.

ΔF^{adh} free energy of adhesion per unit area

Greek Letters

γ_{LV} liquid-vapour interfacial tension [J / m^2]

γ_{PL} particle-liquid interfacial tension [J / m^2]

γ_{PS} particle-substrate interfacial tension [J / m^2]

γ_{PV} particle-vapour interfacial tension [J / m^2]

γ_{SL} substrate-liquid interfacial tension [J / m^2]

γ_{SV} substrate-vapour interfacial tension [J / m^2]

θ_c contact angle formed with water in air | deg. |

Section 2.5

Also refer to the list for section 1.2.2.

B_α forcing vector

$c(y)$ source point coefficient

D_i differential operator

i, j, k, l tensor subscripts

$K_n(z)$ modified Bessel function of third kind, order n

$L_{\alpha\beta}$ matrix of differential operators

r distance between source and field point

s_i vector between source and field point

u_i^0 initial boundary velocity

$\tilde{U}_\alpha$ field variable vector at previous time level

U_β field variable vector

$W_{\alpha\gamma}$ fundamental solution tensor

x_i field point

y_i source point

$z = \sqrt{\lambda} r$

Greek Letters

α, β, γ spatial indicies

Γ field boundary

Δ Laplacian operator

$\lambda = \frac{\mathrm{Re}}{\Delta t}$

$\Sigma_{i\gamma}$ boundary velocity fundamental solution tensor

τ_i boundary traction

τ_{ij} dimensionless Cauchy stress

ϕ scalar Green's function

Ω field domain

Section 2.6

Also refer to the list for section 1.3.

a' mean fluctuation

a'' density-weighted ensemble-averaged fluctuation

C_μ $k-\epsilon$ model constant

C_1 $k-\epsilon$ model constant

C_2 $k-\epsilon$ model constant

C_3 $k-\epsilon$ model constant

E turbulence model wall velocity constant

G finite-volume curvature variable

I turbulence intensity

k turbulent energy

ℓ turbulence length scale

n subscript for normal direction to boundary

P pressure [N / m^2]

P_{eff} finite-volume effective pressure

r, z, θ cylindrical coordinates

S_ϕ volumetric source rate

t time [s]

T_0 period of turbulent oscillation [s]

u, v, w r, z, θ velocities

u_i liquid velocity [m / s]

u_τ wall friction velocity

U one-dimensional wall velocity

Y normal distance from wall [m]

Y^+ local wall Reynolds number

Greek Letters

Γ_ϕ effective exchange coefficient

κ turbulence model wall velocity constant

μ laminar viscosity [N·s / m^2]

μ_t turbulent viscosity

ρ density [kg / m^3]

σ_k $k - \epsilon$ model constant

σ_ϵ $k - \epsilon$ model constant

τ_{ij} shear stress tensor [N / m^2]

τ_w wall shear stress

ϕ generalized transport variable

Section 3.1

Also refer to the list for section 2.5.

a_1, a_2 integration limits on τ for singular case

a_i, b_i domain element shape function parameters

A, A_i^0 domain element shape function parameters

$C_{\gamma iq}$ BEM global matrix coefficient

$C_\alpha = (-1)^\alpha$

$\bar{C}_\alpha = 1 - C_\alpha$

$dS(x)$ line differential on a boundary element

$\mathcal{F}_1(x_2), \mathcal{F}_2(x_2)$ domain integration limits

$f_i(\mathrm{X})$ non-linear functions for the Newton-Rhapson method

f_{TOL} Newton-Rhapson total error criterion

$G_{\gamma in}$ BEM global matrix coefficient

$\mathcal{G}(\eta_1, \eta_2, \eta_3)$ general transformed domain integrand

$H_{\gamma in}$ BEM global matrix coefficient

I general integrated result

$I_{\Gamma W}$

$I_{\Gamma\Sigma}$ singular integral over boundary element for fundamental solution tensor $W_{\alpha\gamma}$

$I_{\Gamma\Sigma}$ singular integral over boundary element for fundamental solution tensor $\Sigma_{i\gamma}$

I_Ω singular integral over domain element

J Jacobian for a transformed element

$\vec{\mathrm{n}}$ vector form of n_i

N quadrature order for boundary integrals

Q quadrature order for domain integrals

$\vec{\mathrm{r}}$ vector form of s_i

$R(\varphi)$ maximum value of $r(\varphi)$ for singular integration

$S(z^m K_n(z))$ series result for integrals of the form $\lim_{\epsilon\to 0}\int_{a_1}^{a_2} z^m K_n(z)\,dz$

w_i quadrature weight factors

x_i^m value of x_i at domain's mth corner

x_n node point

$\mathrm{x}_1^J, \mathrm{x}_2^J, \mathrm{x}_1^K, \mathrm{x}_2^K$ domain element shape function parameters

x_{TOL} Newton-Rhapson zero-correction criterion

$Z_{\gamma i q p \alpha}$ BEM global matrix coefficient

Greek Letters

α shape function index for singular domain transform

α_{ij} Newton-Rhapson matrix coefficients

β_i Newton-Rhapson vector coefficients

δx_i Newton-Rhapson field variable corrections

ϵ lower integration limit for singular case

η_1, η_2 normalized transformed domain element coordinates

$\Theta_\alpha(\varphi)$ component of transformed shape function for singular treatment

$\Lambda_{\gamma l}$ BEM global matrix coefficient

ξ boundary element interpolating parameter

ξ_i normalized transformed boundary element coordinates

ς domain element index at singularity

φ polar coordinate for singular domain transform

φ_n boundary element shape function

ψ_n domain element shape function

$\tilde{\psi}_\alpha$ transformed shape function for singular treatment

Section 3.2

Also refer to the list for section 2.6.

a_W area of wall cell face

A_C cell control surface

$A_{[i,j,k]}$ recurrence coefficients for solving difference equations

$B_{[i,j,k]}$ recurrence coefficients for solving difference equations

$C_{[i,j,k]}$ recurrence coefficients for solving difference equations

A_N, A_S combined convective/diffusive transport coefficient of the north and south cell boundary faces

A_E, A_W combined convective/diffusive transport coefficient of the east and west cell boundary faces

A_B, A_F combined convective/diffusive transport coefficient of the back and front cell boundary faces

A_P combined convective/diffusive transport coefficient of the central node

$A_P^P = (\rho V)_P^o/\delta t)$

D_e velocity correction coefficient (eg; east)

f under-relaxation factor

f_e spatial linear interpolation factor (eg; east)

f_v linearized weighting factor for centrifugal force

i, j, k subscripts, -indices for the x, y and z-directions

$[i, j, k]$ subscripts, -indices for the node on the flow domain grid

m_e mass flow rate (eg; east)

n, o superscripts, -new and old time levels

n, s, e, w subscripts, -north, south, east, west, for cell boundaries relative to point P

b, f subscripts, -back, front, for cell boundaries relative to point P

N, S, E, W subscripts, -north, south, east, west, for grid points relative to point P

B, F subscripts, -back, front, for grid points relative to point P

n_i normal unit vector to boundary

P central node for finite-volume equation

P subscript, -for node P, especially for quantities at nodes neighbouring a wall

P' pressure correction

P^* pressure from preliminary velocity field

Pe Peclet Number

Q_Z total transport (eg; z-direction)

R_ϕ local residual for ϕ-equation

$R_{\phi,\mathrm{REF}}$ reference residual for ϕ-equation

S_B source due to a neighbouring boundary

S_P implicit source term

S'_P implicit source term at boundary

S_P^ϕ general implicit source term

S_U explicit source term

S'_U explicit source term at boundary

$S_U^{P'}$ source term for pressure correction

S_U^ϕ general explicit source term

t time [s]

u, v, w x, y and z-direction velocities [m / s]

u^*, v^*, w^* preliminary velocities (do not necessarily satisfy continuity)

U_P velocity resultant at point P

V_C cell volume

V_P element of volume

W subscript, -for wall cells

Y_P normal distance from wall to cell center

Y_P^+ local wall Reynolds number

Greek Letters

γ_e spatail difference function (eg; east)

δt time step [s]

$\delta z, \delta r, \delta \theta$ grid spacing

$\Delta z, \Delta r, \Delta \theta$ cell spacing

λ convergence coefficient for residuals

μ_{eff} effective viscosity, composed of sum of laminar and turbulent contributions

Section 3.3

Also refer to the list for section 3.2.

A area of cell face for flux

B coefficient for liquid-solid drag

C_D drag coefficient

d_{B_0} bubble diameter at start of iteration

$f_{\rho J}$ density fraction of Jth phase

$f'_{\rho J}$ density fraction of Jth phase after mass transfer

$\mathcal{F}_i$ curvature related source terms

F_{GL} gas-liquid interphase drag term

F_{SL} solid-liquid interphase drag term

g_i gravity force

G_i flux of ith phase

G, L, S subscripts, -refer to gas, liquid or solid phase

J_{Ji} diffusion flux vector for Jth phase

m_S mass of one solid particle

$N_{P/B}$ bubble loading, particles per bubble

r_G gas bubble radius

r_S solid particle radius

R_i mass generation or consumption of ith phase

Re_s particle Reynolds number

V_{CELL} volume of local cell

Greek Letters

α_G gas volume fraction

$\tilde{\alpha_G}$ shadow gas volume fraction

α_L liquid volume fraction

α_S solids volume fraction

ϵ normalized liquid volume fraction

ϵ_S normalized solids volume fraction

Section 3.3.8

a bubble radius

b particle radius

$f(M:M)$ interaction for two particles on Mth level

$f(M:M-1)$ interaction for one particle on Mth level and one on $M-1$st level

$\Delta F_{D,M_j}$ increment on drag due to jth particle in Mth level

$\Delta F_D[N:j]$ overall change in drag for a loaded bubble of N levels, with j particles

$\Delta F_{D,0}$ bubble drag increase due to one adhering particle

l center-to-center distance between two attached particles

M the Mth hexagonal level

N number of hexagonal levels

N_n number of particles in each hexagonal patch level

$N'_{P/B_{MAX}}$ maximum bubble loading under mass-flux constraint

$P_{M_{i,j}}$ jth particle in ith level

q number of interactions among $[M : M-1]$ pairs

$r_M = r_P + r_B$

v number of interactions among $[M : M]$ pairs

Greek Letters

$\alpha_{[M:M-1]}$ angle between the flow line of motion and the line of centers of the particles in Mth and $M-1$st levels

$\gamma_{[N:1]}$ sector angle for Nth haxagonal patch level

Section 3.3.9

b_j multivariate regression coefficients

k_μ laminar viscosity coefficient from non-Newtonian model

Greek Letters

μ_{SLURRY} solid-liquid suspension viscosity

μ_{TOTAL} three-phase viscosity

Section 3.3.10.3

p_i positon of fluid particle at ith time level

u_{pi}, v_{pi} velocities at point p_i

x, y coordinates in flow field

0 subscript, -initial time

Greek Letters

δt time step

Section 4.3

L unit cavity length

t time [s]

x, y coordinates in flow field

0 subscript, -initial time

Section 4.4

D tube diameter

i, o subscripts, -inner, outer regions

D axial velocity

Section 5.1

a meniscus profile parameter

a_{1i} mean size of agglomerate

a_{2i} agglomerate number count coefficient

a_{3i} bond volume per agglomerate based on oil level

a_{4i} probability of agglomerate break up

b curvature radius on binder-liquid interface

b_s agglomerate bond strength

c_i fraction of ith component on heterogeneous solid surface

F agglomerate enlargement factor

$\mathcal{F}_1(y)$ particle surface profile

$\mathcal{F}_2(y)$ meniscus surface profile

h hydrophobicity index

n number of agglomerates

n_b number of bonds in an agglomerate

P_b overall probability of agglomerate break up

q_i fraction of singlets, doublets, triplets or quadruples

(u_1, u_2) particle surface direction vector

(v_1, v_2) meniscus surface direction vector

V_B bonding volume fraction

V_{BA} absolute bond volume

V_O volume of oil as a fraction of total solids volume

V_{OB} volume of oil bond relative to volume of two bonded particles

V_R "real" bonding volume

V_{SB} fraction of the total solid volume bonded in doublets

V_T theoretical bonding volume

V_W wetting volume fraction

y_c three-phase contact point y-coordinate

Greek Letters

γ_H macroscopic surface free energy of heterogeneous solid

γ_i surface free energy of ith component in heterogeneous solid

θ_C contact angle

θ_m meridian angle of oil bond

Section 5.3

Also refer to the list for section 3.2.

b, m regression parameters

CAL subscript, -refers to calibration sample

E_K theoretical collection efficiency

t_i induction time

Greek Letters

β model exponent coefficient

$\Delta\gamma$ extent of wetting

Section 5.4

E_A theoretical attachment efficiency

k, n flotation rate model parameters

Appendix B

Tensor Notation

In the Einsteinian indicial notation, or tensor notation, a vector $\vec{v}$, is written as v_i where $i = 1, \rightarrow n$, where n is the number of spatial dimensions.

Thus in three dimensions v_i implies three terms, v_1, v_2 and v_3.

A repeated index implies summation. Thus,

$$a_i b_i = a_1 b_1 + a_2 b_2 + a_3 b_3$$

or,

$$a_{ij} b_j = a_{11} b_1 + a_{12} b_2 + a_{13} b_3 \quad \text{for } i = 1 \text{ etc.}$$

A comma before an index implies differentiation with respect to the spatial dimensions. Hence, $a_{i,j}$ is 9 terms,

$$a_{i,j} = \begin{bmatrix} \frac{\partial a_1}{\partial x_1} & \frac{\partial a_1}{\partial x_2} & \frac{\partial a_1}{\partial x_3} \\ \frac{\partial a_2}{\partial x_1} & \frac{\partial a_2}{\partial x_2} & \frac{\partial a_2}{\partial x_3} \\ \frac{\partial a_3}{\partial x_1} & \frac{\partial a_3}{\partial x_2} & \frac{\partial a_3}{\partial x_3} \end{bmatrix}$$

and,

$$b_{i,i} = \frac{\partial b_1}{\partial x_1} + \frac{\partial b_2}{\partial x_2} + \frac{\partial b_3}{\partial x_3}$$

B.1 Notation Used for MD-PHASE modeling

The generalized tensor indicial notation is employed here to write the equations. The continuity and momentum equations involve differential operators such as gradient, divergence and the Laplacian. As a guide to constructing the equations into explicit forms, the operators mentioned above are expressed below in terms of the metric tensor a_{ij}, which is the tensor used to transform a differential equation into an explicit form with partial derivatives rather than a general form containing absolute derivatives which are independent of the coordinate system chosen. Velocity is known as a contravariant vector [139] and is operated on as:

gradient,

$$\nabla\varphi = \varphi_{,i} = \frac{\partial\varphi}{\partial x_i}$$

divergence,

$$\nabla\cdot\vec{\varphi} = \varphi_{i,i} = \frac{1}{\sqrt{a}}\frac{\partial}{\partial x_i}\left(\sqrt{a}\varphi_i\right)$$

the Laplacian,

$$\nabla^2\varphi = \varphi_{,ii} = \frac{1}{\sqrt{a}}\frac{\partial}{\partial x_i}\left(\sqrt{a}\frac{\partial\varphi_i}{\partial x_i}\right)$$

Above, a is the determinant of the metric tensor a_{ij}. $a = a_{ii}$ for three-dimensional coordinate systems. For cylindrical coordinates, we have,

$$a_{ij} = \begin{bmatrix} 1 & 0 & 0 \\ 0 & r^2 & 0 \\ 0 & 0 & 1 \end{bmatrix}$$

Appendix C

2D Navier-Stokes BEM formulations

Below are given some explicit derivations for some of the functions used in the BEM computational implementation for the reader's benefit.

C.1 2D Navier-Stokes BEM differential operator

The two-dimensional differential operator equivalent to the Dirac function was given by Tosaka and Onishi for the fundamental solution scalar ϕ[34]. It is:

$$(-\lambda + \Delta)\Delta\phi = \delta(x - y)$$

Now, let $\Delta\phi = \Psi$, so that $(-\lambda + \Delta)\Psi = \delta(x - y)$. $(-\lambda + \Delta)$ is the modified Helmholtz operator so that,

$$\Psi = -\frac{1}{2\pi} K_0(\sqrt{\lambda} r)$$

Let,

$$(-\lambda + \Delta)\phi = \Upsilon$$

So by the original equation,

$$\Delta\Upsilon = (-\lambda + \Delta)\Delta\phi = \delta(x - y)$$

Hence the differential operator on Υ is simply the Laplacian, and the corresponding Green's function is,

$$\Upsilon = (-\lambda + \Delta)\phi = \frac{1}{2\pi} \ln r$$

C.2 Analytical Form for a Singular Domain

Given below is a step-by-step illustration of how a singular domain analytical integral is approached.

C.2.1 Sample Calculation

We begin by making a Taylor series expansion of the modified Bessel function [140]. In general,

$$K_n(z) = (-1)^{n+1} \sum_{l=0}^{\infty} \frac{\left(\frac{z}{2}\right)^{2l+n}}{l!\Gamma(n+l+1)} \left(\gamma + \ln\left(\frac{z}{2}\right)\right)$$
$$+ \frac{(-1)^n}{2} \sum_{s=0}^{\infty} \frac{\left(\frac{z}{2}\right)^{n+2s}}{s!(n+s)!} \left[\sum_{m=1}^{s} \frac{1}{m} + \sum_{m=1}^{s+n} \frac{1}{m}\right]$$
$$+ \frac{1}{2} \sum_{q=0}^{n-1} (-1)^q \frac{(n-q-1)!}{q!} \left(\frac{z}{2}\right)^{2q-n}$$

Above, $\gamma = 0.5772156649...$, which is Euler's constant.

So, for example,

$$K_2(z) = -\sum_{l=0}^{\infty} \frac{\left(\frac{z}{2}\right)^{2l+2}}{l!\Gamma(l+3)} \left(\gamma + \ln\left(\frac{z}{2}\right)\right) + \frac{1}{2} \sum_{s=0}^{\infty} \frac{\left(\frac{z}{2}\right)^{2s+2}}{s!(2+s)!} \left[\sum_{m=1}^{s} \frac{1}{m} + \sum_{m=1}^{s+2} \frac{1}{m}\right] + \frac{1}{2} \left(\left(\frac{z}{2}\right)^{-2} - 1\right)$$

Now consider $\lim_{\epsilon \to 0} \int_{a_1}^{a_2} K_2(z)\, dz$. First, let $z/2 = x$, so $dz = 2\, dx$. Also, when $z = a_1 \Longrightarrow x = a_1/2$ and when $z = a_2 \Longrightarrow x = a_2/2$.

$$\lim_{\epsilon \to 0} \int_{a_1}^{a_2} K_2(z)\, dz = 2 \lim_{\epsilon \to 0} \int_{a_1/2}^{a_2/2} K_2(2x)\, dx$$

Inserting the infinite series form of $K_2(z)$ into the above equation gives,

$$\lim_{\epsilon \to 0} \int_{a_1}^{a_2} K_2(z)\, dz = 2 \lim_{\epsilon \to 0} \int_{a_1/2}^{a_2/2} \left\{ -\sum_{l=0}^{\infty} \frac{x^{2l+2}}{l!\Gamma(l+3)} (\gamma + \ln x) \right.$$

$$
\begin{aligned}
&+\frac{1}{2}\sum_{s=0}^{\infty}\frac{x^{2s+2}}{s!(2+s)!}\left[\sum_{m=1}^{s}\frac{1}{m}+\sum_{m=1}^{s+2}\frac{1}{m}\right]-\frac{1}{2}\Bigg\}dx\\
&+2\lim_{\epsilon\to 0}\int_{a_1}^{a_2}\frac{1}{z^2}\,dz\\
&=2\lim_{\epsilon\to 0}\int_{a_1/2}^{a_2/2}\Bigg\{-\sum_{l=0}^{\infty}\frac{x^{2l+2}}{l!\Gamma(l+3)}(\gamma+\ln x)\\
&+\frac{1}{2}\sum_{s=0}^{\infty}\frac{x^{2s+2}}{s!(2+s)!}\left[\sum_{m=1}^{s}\frac{1}{m}+\sum_{m=1}^{s+2}\frac{1}{m}\right]-\frac{1}{2}\Bigg\}dx\\
&+2\lim_{\epsilon\to 0}\int_{a_1}^{a_2}\frac{1}{z^2}\,dz\\
&=2\lim_{\epsilon\to 0}\Bigg\{-\sum_{l=0}^{\infty}\frac{1}{l!\Gamma(l+3)}\Bigg\{\frac{\gamma}{2l+3}x^{2l+3}\Big|_{a_1/2}^{a_2/2}\\
&+\frac{1}{2l+3}(\ln x)x^{2l+3}\Big|_{a_1/2}^{a_2/2}-\frac{1}{(2l+3)^2}x^{2l+3}\Big|_{a_1/2}^{a_2/2}\Bigg\}\\
&+\frac{1}{2}\sum_{s=0}^{\infty}\frac{1}{s!(2+s)!}\frac{1}{2s+3}x^{2s+2}\Big|_{a_1/2}^{a_2/2}\left[\sum_{m=1}^{s}\frac{1}{m}+\sum_{m=1}^{s+2}\frac{1}{m}\right]\\
&-\frac{1}{2}x\Big|_{a_1/2}^{a_2/2}\Bigg\}\\
&+2\lim_{\epsilon\to 0}\int_{a_1}^{a_2}\frac{1}{z^2}\,dz
\end{aligned}
$$

Recall that when $x=(a_1/2)\Longrightarrow z=(\sqrt{\lambda}R\epsilon/2)$, and when $x=(a_2/2)\Longrightarrow z=(\sqrt{\lambda}R/2)$. Thus,

$$\lim_{\epsilon\to 0}\frac{a_1}{2}=0\quad\text{and,}\quad\lim_{\epsilon\to 0}\frac{a_2}{2}=\frac{\sqrt{\lambda}R}{2}$$

Applying and evaluating the limits gives,

$$
\begin{aligned}
&\lim_{\epsilon\to 0}\int_{a_1}^{a_2}K_2(z)\,dz=\\
&2\Bigg\{-\sum_{l=0}^{\infty}\frac{1}{l!\Gamma(l+3)}\Bigg\{\frac{\gamma}{2l+3}\left(\frac{a_2}{2}\right)^{2l+3}\\
&+\frac{1}{2l+3}\ln\left(\frac{a_2}{2}\right)\left(\frac{a_2}{2}\right)^{2l+3}-\frac{1}{(2l+3)^2}\left(\frac{a_2}{2}\right)^{2l+3}\Bigg\}\\
&+\frac{1}{2}\sum_{s=0}^{\infty}\frac{1}{s!(2+s)!}\frac{1}{2s+3}\left(\frac{a_2}{2}\right)^{2s+2}\left[\sum_{m=1}^{s}\frac{1}{m}+\sum_{m=1}^{s+2}\frac{1}{m}\right]
\end{aligned}
$$

$$
\begin{aligned}
&- \frac{1}{2}\left(\frac{a_2}{2}\right)\Bigg\} \\
&+2\lim_{\epsilon\to 0}\int_{a_1}^{a_2}\frac{1}{z^2}\,dz
\end{aligned}
$$

Using the relation for integers that $\Gamma(n+1) = n!$, we can finally write,

$$
\begin{aligned}
&\lim_{\epsilon\to 0}\int_{a_1}^{a_2} K_2(z)\,dz = \\
&\quad -2\Bigg\{\sum_{l=0}^{\infty}\frac{1}{l!(l+2)!}\frac{1}{2l+3}\left(\frac{a_2}{2}\right)^{2l+3} \\
&\quad \left[\gamma + \ln\left(\frac{a_2}{2}\right) - \frac{1}{2l+3} - \frac{1}{2}\left[\sum_{m=1}^{l}\frac{1}{m} + \sum_{m=1}^{l+2}\frac{1}{m}\right]\right]\Bigg\} \\
&\quad -\frac{a_2}{2} + 2\lim_{\epsilon\to 0}\int_{a_1}^{a_2}\frac{1}{z^2}\,dz
\end{aligned}
\tag{C.1}
$$

C.2.2 General Series Description

In general the singular integrals of the modified Bessel functions,

$$\lim_{\epsilon\to 0}\int_{a_1}^{a_2} z^m K_n(z)\,dz$$

have a series solution of the form

$$
\begin{aligned}
S(z^m K_n(z)) = C_1&\Bigg\{\sum_{l=0}^{\infty}\frac{1}{l!(l+C_2)!}\frac{1}{2l+C_3}\left(\frac{a_2}{2}\right)^{2l+C_3} \\
&\left[\gamma + \ln\left(\frac{a_2}{2}\right) - \frac{1}{2l+C_3} - \frac{1}{2}\left[\sum_{m=1}^{l}\frac{1}{m} + \sum_{m=1}^{l+C_2}\frac{1}{m}\right]\right]\Bigg\} \\
&+C_4 + F(z)
\end{aligned}
\tag{C.2}
$$

Table C.1 summarizes the particular coefficients for all nine series required in this paper. Computational testing with the set of series detailed in Table C.1 has shown that using $a_2 = 1.5$ gives satisfactory convergence for all the series, and produces suitable element partitioning.

integral	variable	C_1	C_2	C_3	C_4	$F(z)$
$\lim_{\epsilon\to 0}\int_{a_1}^{a_2} K_2(z)\,dz$	$S(K_2(z))$	-2	2	3	$\frac{-a_2}{2}$	$2\lim_{\epsilon\to 0}\int_{a_1}^{a_2}\frac{1}{z^2}\,dz$
$\lim_{\epsilon\to 0}\int_{a_1}^{a_2} zK_2(z)\,dz$	$S(zK_2(z))$	-4	2	4	$\frac{-a_2^2}{4}$	$2\lim_{\epsilon\to 0}\int_{a_1}^{a_2}\frac{1}{z}\,dz$
$\lim_{\epsilon\to 0}\int_{a_1}^{a_2} z^{-1}K_1(z)\,dz$	$S(z^{-1}K_1(z))$	1	1	1	0	$\lim_{\epsilon\to 0}\int_{a_1}^{a_2}\frac{1}{z^3}\,dz$
$\lim_{\epsilon\to 0}\int_{a_1}^{a_2} K_1(z)\,dz$	$S(K_1(z))$	2	1	2	0	$\lim_{\epsilon\to 0}\int_{a_1}^{a_2}\frac{1}{z}\,dz$
$\lim_{\epsilon\to 0}\int_{a_1}^{a_2} z^2K_2(z)\,dz$	$S(z^2K_2(z))$	-8	2	5	$4(\frac{a_2}{2}-\frac{a_2^3}{24})$	0
$\lim_{\epsilon\to 0}\int_{a_1}^{a_2} zK_1(z)\,dz$	$S(zK_1(z))$	4	1	3	a_2	0
$\lim_{\epsilon\to 0}\int_{a_1}^{a_2} K_3(z)\,dz$	$S(K_3(z))$	8	3	4	$\frac{a_2^2}{48}$	$8\lim_{\epsilon\to 0}\int_{a_1}^{a_2}\frac{1}{z^3}\,dz-\lim_{\epsilon\to 0}\int_{a_1}^{a_2}\frac{1}{z}\,dz$
$\lim_{\epsilon\to 0}\int_{a_1}^{a_2} zK_3(z)\,dz$	$S(zK_3(z))$	2	3	5	$-a_2+\frac{a_2^3}{72}$	$8\lim_{\epsilon\to 0}\int_{a_1}^{a_2}\frac{1}{z^3}\,dz$
$\lim_{\epsilon\to 0}\int_{a_1}^{a_2} z^{-1}K_2(z)\,dz$	$S(z^{-1}K_2(z))$	-1	2	2	0	$2\lim_{\epsilon\to 0}\int_{a_1}^{a_2}\frac{1}{z^3}\,dz-\frac{1}{2}\lim_{\epsilon\to 0}\int_{a_1}^{a_2}\frac{1}{z}\,dz$

Table C.1: Summary of series expansions of modified Bessel function singular integrals.

Appendix D

MD-PHASE data structure

Given below is a data file for an MD-PHASE simulation.

```
c-----problem title (name) .........
 float example
c-----cpu time data (cptime) .......
  3000.
c-----file (dumpr, clinit, qtrace) ..................
                .false.  .true.  .true.
c-----monitoring location (imon, jmon, kmon) ..
                           5     5      2
c-----output control (numpri) ..................
                          5
c-----pressure reference points (ipref, jpref, kpref) .......
 2 2 2
c-----iteration and convergence limits (maxit,sormax) .......
         2000 1.0d-3
c-----equation indices (lu, lv, lw, lp, lte, led, len, lsp, lgas)..
                         1   2   3   4   5    6    7    8    9
c-----more equation indices (lcoal, lucl, lvcl, lshdw)
                         10    11    12  13
c-----dependent variables selection (incal) ...........
.true.  .true.  .false.  .true.  .true.  .true.  .false.  .true.  .true.
c-----more dependent variables selection (incal) ...........
  .true.  .true.  .true.  .true.
c-----wall condition (tfixf, tfixb, tfixe, tfixw, tfixn, tfixs)
                     .true. .true. .true. .true. .true. .true.
c-----wall temperature (kelven) modify the program to compute enthalphy
      300.0
```

```
c-----relaxation factors (urf,urfvis,urfden) ..........
0.15  0.15  0.15  0.35   0.35  0.35  0.35  0.15  0.15 0.15 0.15 0.15  0.15
0.5 0.5
c-----sweeps numbers (nswp) ............................
2    2    2    2    2    2    2    2    2    2    2
2    2    2
c-----control the scan (ixsw,jysw,kzsw)
   2  2 0
c-----number of species (nsp) ..........................
           1
c-----control for chemistry involved (incomb) .........
 0
c----- initial dispersed phase concs. (vo0, vono0, voc0, vocno0)
       0.10  0.50 0.075 0.1
c----- starting values for dispersed phase field velocities (ugst,vgst,uclst,vclst)
0.05  0.0   0.01   0.01
c------collision-adhesion fraction (ralpha)
    0.2
c-----total number of inlet groups (nnoz) ..............
                                    2
c-----inlet boundary conditions (si units) .............
c----1st inlet (gas)
0.025           119910.0  300.0         xmass(m3/s), pnoz, tnoz
0.0      0.0                          angn (u,v),  angn1 [ (u,w), (v,w)]
   0.005       0.01                          turbin, alamda
c----2nd inlet (water and coal)
0.005335           113326.0  300.0         xmass(m3/s), pnoz, tnoz
0.0      0.0                          angn (u,v),  angn1 [ (u,w), (v,w)]
   0.005       0.002665                      turbin, alamda
```

Logical flags are used to control which variables are to be solved, if the initial fields are to be set up with a data dump from a previous run and if a particle or gas trace is desired in the post-processing.

A block data section of the main fortran control file is also used for some of the physical properties of the materials in the simulation. For example,

```
      block data
c
c-------------------------data block routine-----------------------
c
chapter  0  0  0  0  0  0  0  0  preliminaries  0  0  0  0  0  0  0  0
c
      include 'float.copy'
```

```
c
chapter  1  1  1  1  1  parameters and control indices  1  1  1  1  1  1
c
chapter  1.0  1.0  1.0  constants  and problem data  1.0  1.0  1.0  1.0
c
c-----inital data
      data great,small/1.0d30,1.0d-30/
c-----transient data
      data steady/.true./
c
chapter  1.1  1.1  1.1  program control parameters  1.1  1.1  1.1  1.1
c
c-----file and tape
      data nwrite,ntape/0,1/
      data dumpw,mtape0,mtape/.true.,.false.,.false./
c-----output control
      data indpri,numpri/1,5/
c-----fluid and flow properties
      data lamin/.false./
      data incomp/.true./
chapter  1.2  1.2  thermodynamic data and fluid properties  1.2  1.2
c
c-----turbulence constants
      data   cmu ,  cd ,  c1  ,  c2  ,  c3 ,  cappa
     +    /0.09d0,1.0d0,1.44d0,1.92d0,1.0d0,0.4187d0/
c-----constant for smooth wall and constant shear stress
      data elog/9.793d0/
c-----prandtl and schmidt number
      data prht,prhl,scnum,prte,pred/0.9d0,0.7d0,0.7d0,1.0d0,1.3d0/
c-----thermodynamic constant for gas
      data rgas/8.3143d3/
      data airmu1,airmu2/1.42d-6,1.0d2/
c-----aggregate radius of bubble
      data arad,aradcl/2.5d-4,2.0d-5/
c-----thermodynamic data for water
      data densit/997.1/
      data dncoal/1200.1/
      data viscos/8.94d-4/
      data visgas/1.42d-6/
c-----flow properties of gas
      data dengas/1.200/
c-----set directional body force effects
```

```
data gaccx/-9.81/
data gaccy/0.0/
data gaccz/0.0/
```

Appendix E

Convergence Tolerance Comparison

Table E.1 is the output for the field values of particles per bubble, $N_{P/B}$ with a convergence tolerance of 10^{-1}. In this case, $d_P = 43.6\mu$m, $d_B = 2.5$ mm, $\tau_\alpha = 0.20$. In the table, the indices i and j refer respectively to nodes along the x and y axes. The x axis was used as the vertical direction in this simulation. The data under the column $i = 16$ are the exit bubble loading values which are integrated to determine the flotation recovery.

Table E.2 shows $N_{P/B}$ for the same conditions as above, but with a convergence tolerance of 10^{-3}. The differences can be seen to be very slight, especially for the overall flotation recovery.

Note that for the two extra orders of magnitude of convergence tolerance, the computational time went from 973 seconds to 4182 seconds, a factor of about 4.3, for an essentially negligible difference in the calculated recovery.

---------- particle load per bubble ----------

i =	1	2	3	4	5	6	7	8	y =
j									
16	1.96E-05	1.96E-05	1.40E+01	1.40E+01	1.40E+01	1.40E+01	1.23E+01	1.08E+01	1.37
15	5.80E-05	5.80E-05	1.40E+01	1.40E+01	1.22E+01	1.27E+01	1.20E+01	1.11E+01	1.31
14	1.85E-04	1.85E-04	1.40E+01	1.40E+01	7.66E+00	1.05E+01	1.09E+01	1.06E+01	1.25
13	8.71E-04	8.71E-04	1.40E+01	6.06E+00	4.68E+00	7.86E+00	8.69E+00	8.67E+00	1.14
12	8.82E-03	8.82E-03	1.40E+01	3.49E+00	3.73E+00	6.15E+00	7.41E+00	8.02E+00	1.01
11	0.00E+00	3.08E-05	1.18E-01	9.16E-01	2.47E+00	4.74E+00	6.29E+00	7.14E+00	0.919
10	0.00E+00	1.51E-05	8.94E-02	7.06E-01	2.33E+00	3.87E+00	5.40E+00	6.31E+00	0.831
9	0.00E+00	7.48E-06	7.51E-02	7.73E-01	1.80E+00	3.36E+00	4.58E+00	5.48E+00	0.744
8	0.00E+00	1.16E-01	2.48E-01	9.12E-01	1.56E+00	2.76E+00	3.83E+00	4.81E+00	0.656
7	0.00E+00	1.99E-01	5.76E-01	1.06E+00	2.25E+00	2.61E+00	3.35E+00	4.30E+00	0.569
6	0.00E+00	4.00E-01	4.91E-01	1.76E+00	4.03E+00	3.01E+00	3.21E+00	3.94E+00	0.481
5	2.39E+00	2.39E+00	3.52E+00	4.47E+00	7.20E+00	3.91E+00	3.50E+00	3.77E+00	0.394
4	1.65E-01	1.65E-01	3.09E-01	1.24E+01	1.19E+01	6.16E+00	5.17E+00	4.59E+00	0.262
3	2.16E-02	2.16E-02	4.45E-01	1.23E+01	1.18E+01	7.87E+00	6.42E+00	5.41E+00	0.131
2	1.50E-01	1.50E-01	2.08E+00	1.15E+01	1.15E+01	8.84E+00	7.89E+00	7.11E+00	4.375E-02
1	0.00E+00	1.50E-01	2.08E+00	0.00E+00	0.00E+00	8.84E+00	7.89E+00	7.11E+00	0.000E+00

x = 0.000E+00 6.250E-02 0.188 0.275 0.325 0.475 0.700 0.900

i =	9	10	11	12	13	14	15	16	y =
j									
16	1.04E+01	1.40E+01	1.40E+01	1.40E+01	1.26E+01	1.24E+01	7.51E+00	7.42E+00	1.37
15	1.07E+01	1.04E+01	1.36E+01	7.86E+00	7.10E+00	7.17E+00	6.45E+00	6.38E+00	1.31
14	1.05E+01	1.03E+01	1.08E+01	7.64E+00	6.92E+00	6.57E+00	6.25E+00	6.18E+00	1.25
13	9.03E+00	8.76E+00	8.07E+00	7.32E+00	6.71E+00	6.37E+00	5.98E+00	5.92E+00	1.14
12	8.47E+00	8.36E+00	8.20E+00	6.88E+00	6.16E+00	6.12E+00	5.61E+00	5.59E+00	1.01
11	7.87E+00	7.61E+00	7.29E+00	6.35E+00	5.72E+00	5.34E+00	5.00E+00	4.96E+00	0.919
10	7.25E+00	6.87E+00	6.55E+00	5.75E+00	5.21E+00	4.91E+00	4.65E+00	4.61E+00	0.831
9	6.64E+00	6.03E+00	5.72E+00	5.14E+00	4.78E+00	4.58E+00	4.42E+00	4.38E+00	0.744
8	6.01E+00	5.22E+00	4.85E+00	4.66E+00	4.51E+00	4.41E+00	4.36E+00	4.32E+00	0.656
7	5.40E+00	5.08E+00	4.74E+00	4.57E+00	4.46E+00	4.38E+00	4.42E+00	4.38E+00	0.569
6	4.87E+00	4.77E+00	4.59E+00	4.48E+00	4.44E+00	4.39E+00	4.56E+00	4.53E+00	0.481
5	4.50E+00	4.48E+00	4.43E+00	4.44E+00	4.49E+00	4.47E+00	4.79E+00	4.77E+00	0.394
4	4.54E+00	4.52E+00	4.48E+00	4.59E+00	4.75E+00	4.64E+00	5.27E+00	5.25E+00	0.262
3	4.85E+00	4.83E+00	4.71E+00	5.32E+00	5.60E+00	5.47E+00	5.90E+00	5.90E+00	0.131
2	6.45E+00	6.38E+00	6.13E+00	6.13E+00	6.13E+00	6.00E+00	6.00E+00	6.00E+00	4.375E-02
1	6.45E+00	6.38E+00	6.13E+00	6.13E+00	6.13E+00	6.00E+00	6.00E+00	6.00E+00	0.000E+00

x = 1.10 1.25 1.35 1.42 1.48 1.54 1.59 1.60

Flotation recovery = 0.3724

time used for total iterations = 9.727E+02 seconds

Table E.1: $N_{P/B}$ values for convergence tolerance of 10^{-1}

---------- particle load per bubble ----------

i =	1	2	3	4	5	6	7	8	y =
j									
16	8.95E-06	8.95E-06	1.31E+01	1.38E+01	1.40E+01	1.39E+01	1.26E+01	1.11E+01	1.37
15	3.44E-05	3.44E-05	1.29E+01	1.38E+01	1.30E+01	1.29E+01	1.21E+01	1.10E+01	1.31
14	1.31E-04	1.31E-04	1.39E+01	1.37E+01	7.65E+00	1.03E+01	1.08E+01	1.06E+01	1.25
13	7.86E-04	7.88E-04	1.40E+01	6.05E+00	4.69E+00	7.86E+00	8.70E+00	8.88E+00	1.14
12	8.46E-03	8.46E-03	1.39E+01	3.49E+00	3.74E+00	6.14E+00	7.42E+00	8.03E+00	1.01
11	0.00E+00	3.09E-05	1.19E-01	9.18E-01	2.48E+00	4.75E+00	6.29E+00	7.14E+00	0.919
10	0.00E+00	1.51E-05	8.92E-02	7.06E-01	2.34E+00	3.87E+00	5.40E+00	6.30E+00	0.831
9	0.00E+00	7.45E-06	7.51E-02	7.72E-01	1.80E+00	3.35E+00	4.57E+00	5.47E+00	0.744
8	0.00E+00	1.14E-01	2.46E-01	9.10E-01	1.54E+00	2.75E+00	3.82E+00	4.80E+00	0.656
7	0.00E+00	1.97E-01	5.74E-01	1.05E+00	2.24E+00	2.60E+00	3.35E+00	4.29E+00	0.569
6	0.00E+00	3.98E-01	4.89E-01	1.75E+00	4.02E+00	3.00E+00	3.20E+00	3.94E+00	0.481
5	2.37E+00	2.37E+00	3.51E+00	4.46E+00	7.20E+00	3.90E+00	3.49E+00	3.76E+00	0.394
4	1.63E-01	1.63E-01	3.07E-01	1.23E+01	1.16E+01	6.14E+00	5.15E+00	4.58E+00	0.262
3	2.13E-02	2.13E-02	4.43E-01	1.22E+01	1.17E+01	7.86E+00	6.41E+00	5.40E+00	0.131
2	1.48E-01	1.48E-01	2.06E+00	1.13E+01	1.13E+01	8.82E+00	7.87E+00	7.09E+00	4.375E-02
1	0.00E+00	1.48E-01	2.06E+00	0.00E+00	0.00E+00	8.82E+00	7.87E+00	7.09E+00	0.000E+00
x =	0.000E+00	6.250E-02	0.188	0.275	0.325	0.475	0.700	0.900	

i =	9	10	11	12	13	14	15	16	y =
j									
16	1.05E+01	1.41E+01	1.40E+01	1.40E+01	1.26E+01	1.24E+01	7.50E+00	7.41E+00	1.37
15	1.08E+01	1.05E+01	1.36E+01	7.86E+00	7.10E+00	7.17E+00	6.44E+00	6.37E+00	1.31
14	1.05E+01	1.03E+01	1.07E+01	7.64E+00	6.92E+00	6.56E+00	6.24E+00	6.17E+00	1.25
13	9.02E+00	8.76E+00	8.06E+00	7.31E+00	6.71E+00	6.36E+00	5.97E+00	5.92E+00	1.14
12	8.47E+00	8.34E+00	8.20E+00	6.88E+00	6.15E+00	6.12E+00	5.60E+00	5.58E+00	1.01
11	7.87E+00	7.61E+00	7.28E+00	6.34E+00	5.71E+00	5.34E+00	4.99E+00	4.95E+00	0.919
10	7.25E+00	6.86E+00	6.55E+00	5.74E+00	5.20E+00	4.90E+00	4.65E+00	4.61E+00	0.831
9	6.62E+00	6.01E+00	5.71E+00	5.13E+00	4.77E+00	4.56E+00	4.42E+00	4.38E+00	0.744
8	6.00E+00	5.20E+00	4.83E+00	4.65E+00	4.50E+00	4.40E+00	4.36E+00	4.32E+00	0.656
7	5.39E+00	5.07E+00	4.72E+00	4.56E+00	4.45E+00	4.37E+00	4.42E+00	4.38E+00	0.569
6	4.86E+00	4.76E+00	4.58E+00	4.47E+00	4.43E+00	4.40E+00	4.57E+00	4.54E+00	0.481
5	4.51E+00	4.47E+00	4.42E+00	4.43E+00	4.49E+00	4.48E+00	4.79E+00	4.78E+00	0.394
4	4.53E+00	4.51E+00	4.48E+00	4.58E+00	4.74E+00	4.65E+00	5.28E+00	5.25E+00	0.262
3	4.85E+00	4.82E+00	4.70E+00	5.30E+00	5.59E+00	5.46E+00	5.89E+00	5.89E+00	0.131
2	6.44E+00	6.38E+00	6.13E+00	6.13E+00	6.12E+00	5.99E+00	6.00E+00	6.00E+00	4.375E-02
1	6.44E+00	6.38E+00	6.13E+00	6.13E+00	6.12E+00	5.99E+00	6.00E+00	6.00E+00	0.000E+00
x =	1.10	1.25	1.35	1.42	1.48	1.54	1.59	1.60	

Flotation recovery = 0.3722

time used for total iterations = 4.182E+03 seconds

Table E.2: $N_{P/B}$ values for convergence tolerance of 10^{-3}

Appendix F

Raw Experimental Data

Given below in tabular form is the raw data from experiments conducted over the course of the research. This data includes the percent area adhesion results from the agglomerate surface tension work (Figures 4.1 to 4.4 on pages 121 to 124), the flotation results (Figure 4.7 on page 127 for recovery data, and Figure 4.8 on page 128 for deashing data) the data from the agglomerate particle sizing measurements (Figure 4.6 on page 126).

Raw Data from Adhesion Surface Tension Experiments

Devco Coal-Hexadecane Agglomerates (0% n-$C_{16}H_{34}$)

sample	substrate	% CH_3OH	% area adhesion
1	SPS	24.0	0.46
2	SPS	51.0	1.94
3	SPS	95.0	1.62
4	SPS	9.0	0.65
5	PET	51.0	4.85
6	PET	95.0	10.88
7	PE	95.0	4.90
8	PE	24.0	7.49
9	PS	95.0	6.82
10	PS	9.0	0.21
11	PS	0.0	2.13
12	PS	95.0	22.93
13	PET	24.0	1.92
14	PET	51.0	2.49
15	PET	95.0	10.54
16	PET	9.0	0.92
17	PE	9.0	0.87
18	PE	95.0	6.08
19	PE	51.0	3.71
20	PE	0.0	1.13
21	SPS	95.0	2.69
22	SPS	0.0	1.10
23	PS	9.0	0.20
24	PS	24.0	0.29
25	PS	51.0	0.16
26	PS	24.0	1.07
27	PS	51.0	0.61
28	PS	0.0	4.32
29	SPS	9.0	0.70
30	SPS	0.0	0.41
31	SPS	24.0	5.21
32	SPS	51.0	13.54
33	PET	0.0	3.18
34	PET	9.0	1.23
35	PET	0.0	1.23
36	PET	24.0	0.50
37	PE	0.0	1.97
38	PE	51.0	2.67
39	PE	24.0	5.27
40	PE	0.0	6.31

Devco Coal-Hexadecane Agglomerates (0.25% n-$C_{16}H_{34}$)

sample	substrate	% CH_3OH	% area adhesion
1	SPS	51.0	0.30
2	SPS	9.0	4.32
3	SPS	24.0	1.17
4	SPS	0.0	6.93
5	PS	24.0	0.95
6	PS	51.0	5.98
7	PS	9.0	0.25
8	PS	95.0	60.69
9	PET	95.0	5.79
10	PET	9.0	1.25
11	PET	95.0	4.04
12	PET	51.0	5.11
13	PE	0.0	0.57
14	PE	51.0	2.63
15	PE	9.0	6.28
16	PE	95.0	13.34
17	PET	24.0	2.21
18	PET	9.0	1.69
19	SPS	24.0	1.26
20	SPS	95.0	13.70
21	PE	24.0	1.06
22	PE	51.0	3.34
23	PS	0.0	1.13
24	PS	51.0	3.83
25	PE	0.0	0.98
26	PE	24.0	0.58
27	PE	9.0	3.32
28	PE	95.0	12.00
29	PET	0.0	0.94
30	PET	24.0	0.83
31	PET	0.0	15.52
32	PET	51.0	1.30
33	PS	24.0	0.05
34	PS	0.0	0.99
35	PS	95.0	0.62
36	PS	9.0	1.18
37	SPS	95.0	19.78
38	SPS	51.0	1.86
39	SPS	0.0	6.45
40	SPS	9.0	6.37

Devco Coal-Hexadecane Agglomerates (0.5% n-$C_{16}H_{34}$)

sample	substrate	% CH_3OH	% area adhesion
1	PET	9.0	4.70
2	PET	95.0	23.40
3	PET	51.0	4.18
4	PET	24.0	2.18
5	SPS	24.0	2.52
6	SPS	9.0	0.08
7	SPS	0.0	4.90
8	SPS	51.0	22.89
9	PS	95.0	18.79
10	PS	0.0	3.00
11	PS	9.0	0.23
12	PS	95.0	4.67
13	PE	9.0	1.48
14	PE	51.0	18.14
15	PE	95.0	25.13
16	PE	9.0	1.90
17	SPS	24.0	6.83
18	SPS	51.0	31.30
19	SPS	9.0	0.48
20	SPS	95.0	29.80
21	PET	24.0	3.19
22	PET	0.0	1.31
23	PET	9.0	1.37
24	PET	0.0	2.62
25	PE	24.0	2.83
26	PE	95.0	50.27
27	SPS	0.0	3.76
28	SPS	95.0	33.32
29	PE	0.0	7.34
30	PE	24.0	0.41
31	PE	51.0	8.52
32	PE	0.0	7.29
33	PS	24.0	1.66
34	PS	9.0	2.28
35	PET	95.0	3.61
36	PET	51.0	4.24
37	PS	51.0	0.29
38	PS	0.0	2.39
39	PS	24.0	3.88
40	PS	51.0	0.11

Devco Coal-Hexadecane Agglomerates (1% n-$C_{16}H_{34}$)

sample	substrate	% CH_3OH	% area adhesion
1	PE	9.0	3.14
2	PE	24.0	1.00
3	PE	0.0	2.21
4	PE	24.0	1.33
5	SPS	0.0	0.72
6	SPS	51.0	0.58
7	SPS	95.0	0.77
8	SPS	24.0	0.82
9	PET	24.0	1.57
10	PET	9.0	5.23
11	PET	95.0	0.71
12	PET	95.0	1.10
13	PS	95.0	1.06
14	PS	0.0	5.34
15	PS	24.0	0.91
16	PS	51.0	1.29
17	PS	9.0	3.64
18	PS	95.0	1.10
19	PET	0.0	2.55
20	PET	9.0	5.16
21	SPS	24.0	0.59
22	SPS	9.0	3.30
23	PE	51.0	1.96
24	PE	0.0	4.15
25	PE	95.0	1.70
26	PE	9.0	2.41
27	PE	51.0	1.55
28	PE	95.0	1.01
29	PS	0.0	1.81
30	PS	24.0	1.05
31	PS	9.0	3.78
32	PS	51.0	0.76
33	SPS	95.0	0.70
34	SPS	51.0	0.96
35	SPS	0.0	2.11
36	SPS	9.0	1.73
37	PET	24.0	1.15
38	PET	51.0	0.92
39	PET	0.0	1.73
40	PET	51.0	1.39

Devco Coal-Hexadecane Agglomerates (2% n-$C_{16}H_{34}$)

sample	substrate	% CH_3OH	% area adhesion
1	PS	24.0	1.51
2	PS	9.0	2.25
3	PS	9.0	2.72
4	PS	51.0	4.56
5	PS	0.0	1.46
6	PS	95.0	1.50
7	PS	0.0	5.20
8	PS	51.0	3.31
9	PE	95.0	47.75
10	PE	51.0	6.33
11	PE	9.0	8.50
12	PE	0.0	7.85
13	SPS	9.0	1.81
14	SPS	0.0	0.67
15	PE	9.0	0.70
16	PE	24.0	1.39
17	PE	24.0	3.73
18	PE	95.0	10.65
19	PE	0.0	2.69
20	PE	51.0	4.05
21	SPS	24.0	1.47
22	SPS	95.0	36.55
23	SPS	9.0	0.71
24	SPS	95.0	8.86
25	SPS	24.0	1.48
26	SPS	51.0	4.00
27	SPS	0.0	1.11
28	SPS	51.0	3.89
29	PET	24.0	6.78
30	PET	51.0	2.06
31	PS	24.0	6.40
32	PS	95.0	0.63
33	PET	24.0	4.58
34	PET	9.0	1.73
35	PET	0.0	3.38
36	PET	95.0	1.77
37	PET	9.0	2.28
38	PET	0.0	1.77
39	PET	51.0	2.28
40	PET	95.0	1.77

Devco Coal-Hexadecane Agglomerates (10% n-$C_{16}H_{34}$)

sample	substrate	% CH_3OH	% area adhesion
1	PET	95.0	3.43
2	PET	24.0	15.02
3	PET	9.0	5.29
4	PET	0.0	6.85
5	SPS	51.0	0.30
6	SPS	51.0	1.77
7	SPS	24.0	6.93
8	SPS	9.0	2.34
9	SPS	0.0	16.14
10	SPS	0.0	1.24
11	SPS	95.0	36.80
12	SPS	9.0	2.26
13	PS	0.0	0.59
14	PS	0.0	2.51
15	PS	51.0	5.95
16	PS	95.0	1.36
17	PET	24.0	5.27
18	PET	51.0	10.10
19	PET	95.0	8.45
20	PET	9.0	4.43
21	PS	24.0	1.67
22	PS	24.0	1.48
23	PS	9.0	0.75
24	PS	51.0	10.55
25	SPS	24.0	2.55
26	SPS	95.0	43.07
27	PS	9.0	0.16
28	PS	95.0	8.31
29	PET	0.0	13.64
30	PET	51.0	12.24
31	PE	0.0	5.70
32	PE	95.0	24.29
33	PE	95.0	18.87
34	PE	51.0	5.85
35	PE	51.0	5.98
36	PE	0.0	10.40
37	PE	9.0	5.17
38	PE	9.0	1.40
39	PE	24.0	1.61
40	PE	24.0	7.71

Highvale Coal-Hexadecane Agglomerates

% CH_3OH	substrate	% area adhesion			
		0% $C_{16}H_{34}$	1% $C_{16}H_{34}$	5% $C_{16}H_{34}$	10% $C_{16}H_{34}$
0.0	PS	0.40	2.99	1.56	0.56
0.0	PS	0.85	1.49		0.89
0.0	PE	2.51	1.86	1.51	1.12
0.0	PE	1.20	2.20		0.80
0.0	PET	1.37	1.24	1.62	0.25
0.0	PET	0.76	1.59	1.55	0.13
0.0	SPS	0.39	0.61	1.26	0.13
0.0	SPS	0.23	3.20	1.09	
9.0	PS	0.25	6.71	0.86	0.21
9.0	PS	0.66		0.91	0.14
9.0	PE	1.17	4.08	0.81	0.08
9.0	PE	1.10	3.20	1.06	0.09
9.0	PET	0.65	9.82	1.14	0.07
9.0	PET	1.32	9.35	1.04	
9.0	SPS	0.21	2.61	0.66	0.07
9.0	SPS	0.31	5.96	0.84	0.07
24.0	PS	0.72	1.07	0.78	0.14
24.0	PS	0.37	1.46	0.69	
24.0	PE	0.72	1.26	1.01	0.32
24.0	PE	0.85	2.02	0.99	0.26
24.0	PET	0.74	2.21	0.88	0.21
24.0	PET	1.09	1.37	1.22	0.10
24.0	SPS	0.39	0.50	0.85	0.14
24.0	SPS	0.25	0.95	0.45	
51.0	PS	0.64	1.92	1.66	0.89
51.0	PS	0.16	0.80	0.91	
51.0	PE	1.27	2.11	0.83	0.83
51.0	PE	0.65	2.95	1.79	0.78
51.0	PET	0.96	1.79	0.69	0.88
51.0	PET	0.81	1.00	0.67	0.51
51.0	SPS	0.61	1.00	0.61	
51.0	SPS	0.61	0.52	0.76	
95.0	PS	1.60	1.49	0.85	1.18
95.0	PS	2.05	1.45	0.91	0.89
95.0	PE	1.08	1.34	0.97	0.80
95.0	PE	2.57	2.73	0.65	1.43
95.0	PET	2.50	1.29	1.14	1.02
95.0	PET	2.09	0.70	1.35	0.89
95.0	SPS	0.50	0.68	3.04	1.79
95.0	SPS	0.62	10.50	0.95	0.74

Bien Fait Coal-Hexadecane Agglomerates

% CH_3OH	substrate	% area adhesion			
		0% $C_{16}H_{34}$	1% $C_{16}H_{34}$	5% $C_{16}H_{34}$	10% $C_{16}H_{34}$
0.0	PS	0.40	0.23	0.82	0.35
0.0	PS	0.57	1.05	0.64	0.27
0.0	PE	1.46	1.68	4.19	1.86
0.0	PE	9.25	1.07	1.65	1.39
0.0	PET	1.21	0.84	1.07	0.12
0.0	PET	0.29	0.44	3.02	0.12
0.0	SPS	0.08	0.45	1.39	0.22
0.0	SPS	0.32	0.55	1.39	0.02
9.0	PS	0.40	0.74	1.09	0.05
9.0	PS	0.43		0.81	1.53
9.0	PE	0.91	0.99	1.30	0.08
9.0	PE	1.55		1.13	0.18
9.0	PET	0.20	0.87	1.02	0.08
9.0	PET	0.28		2.80	0.59
9.0	SPS	0.90	0.88	0.97	0.07
9.0	SPS			1.83	0.20
24.0	PS	1.19	0.84	0.80	0.48
24.0	PS	1.35	1.05	1.50	0.23
24.0	PE	0.16	0.67	0.94	0.23
24.0	PE	0.75	0.94	0.82	0.39
24.0	PET	0.54	0.49	0.70	0.05
24.0	PET	0.17	0.44	0.71	0.11
24.0	SPS	2.32	0.38	1.03	0.21
24.0	SPS	2.16	0.54	0.81	0.03
51.0	PS	0.32	0.40	0.95	0.10
51.0	PS	1.58	0.64	1.00	0.27
51.0	PE	0.64	0.65	0.75	0.32
51.0	PE	0.37	0.82	0.85	0.80
51.0	PET	0.32	0.83	0.74	0.20
51.0	PET	1.44	0.84	0.74	0.35
51.0	SPS	0.04	1.11	0.53	1.06
51.0	SPS	0.09	0.75	0.70	0.88
95.0	PS	0.09	0.62	0.87	0.13
95.0	PS	0.38	0.73	0.88	0.13
95.0	PE	1.42	0.85	0.44	0.19
95.0	PE	0.93	1.45	0.69	0.48
95.0	PET	0.11	0.80	0.65	0.40
95.0	PET	0.17	1.07	0.82	0.19
95.0	SPS	0.20	0.85	0.82	0.54
95.0	SPS	0.01	0.86	0.62	0.21

Costello Coal-Hexadecane Agglomerates

% CH_3OH	substrate	% area adhesion			
		0% $C_{16}H_{34}$	1% $C_{16}H_{34}$	5% $C_{16}H_{34}$	10% $C_{16}H_{34}$
0.0	PS	0.36	1.19	0.78	0.22
0.0	PS		1.03	0.75	0.20
0.0	PE	0.36	0.81	0.62	0.15
0.0	PE		0.72	0.71	0.16
0.0	PET		0.69	0.59	0.08
0.0	PET	0.12	1.32		1.40
0.0	SPS		0.69	0.91	0.55
0.0	SPS	0.09	1.43		0.13
9.0	PS	0.05	1.43	1.99	0.25
9.0	PS		1.05	0.97	0.59
9.0	PE	0.27	0.89	0.68	0.43
9.0	PE	0.20	0.58	0.70	1.18
9.0	PET	0.04	0.52	0.77	0.04
9.0	PET	0.05	0.88	0.69	1.05
9.0	SPS	0.23	0.49	0.77	0.25
9.0	SPS	0.30	0.47	0.80	0.13
24.0	PS	0.48	0.67	0.88	0.95
24.0	PS	0.99	0.93	0.86	0.35
24.0	PE	0.84	0.68	0.65	0.48
24.0	PE		0.99	0.68	0.09
24.0	PET	0.16	1.03	0.66	0.08
24.0	PET	0.13	0.98		0.13
24.0	SPS	0.12		0.74	0.40
24.0	SPS	0.14			0.11
51.0	PS	1.27	0.58	0.63	0.05
51.0	PS				0.37
51.0	PE	0.87	0.80	0.94	0.10
51.0	PE			0.92	0.04
51.0	PET	0.47	0.67	1.56	0.39
51.0	PET				0.07
51.0	SPS	1.01	0.87	0.91	0.08
51.0	SPS				0.51
95.0	PS	0.78	0.63	0.60	0.06
95.0	PS	2.66	0.63	0.62	0.06
95.0	PE	0.76	0.63	0.89	0.05
95.0	PE	0.55	0.73	1.06	0.04
95.0	PET	0.43	0.69	0.74	0.02
95.0	PET		0.85	1.67	0.95
95.0	SPS	0.76	0.79	1.63	0.65
95.0	SPS		6.53	0.62	1.29

Montgomery Coal-Hexadecane Agglomerates

% CH_3OH	substrate	% area adhesion			
		0% $C_{16}H_{34}$	1% $C_{16}H_{34}$	5% $C_{16}H_{34}$	10% $C_{16}H_{34}$
0.0	PS	10.30	7.68	1.09	14.11
0.0	PS	22.77	2.13	2.36	1.42
0.0	PE	18.55	2.56	4.69	6.23
0.0	PE	3.28	6.09	5.53	9.86
0.0	PET	25.49	2.22	0.84	0.61
0.0	PET	5.48	3.50	0.70	0.10
0.0	SPS	17.39	0.84	0.52	0.02
0.0	SPS	4.25	0.99	0.76	0.09
9.0	PS	0.98	0.84	0.91	0.06
9.0	PS	0.70	0.80	0.83	
9.0	PE	1.35	2.20	0.82	0.04
9.0	PE	0.93	1.61	0.77	0.07
9.0	PET	1.08	0.64	0.64	0.08
9.0	PET	0.99	0.97	0.79	
9.0	SPS	2.49	0.84	0.80	0.22
9.0	SPS	1.49	0.63	0.85	
24.0	PS	0.69	0.75	0.74	0.04
24.0	PS		0.63	1.07	0.14
24.0	PE	1.19	0.74	0.72	0.19
24.0	PE		0.91	0.83	0.26
24.0	PET	0.85	0.93	0.76	0.02
24.0	PET	0.52		0.67	
24.0	SPS		0.68	2.16	0.48
24.0	SPS	1.02		1.63	
51.0	PS	0.84	0.65	0.96	0.77
51.0	PS	0.64	0.73	0.77	
51.0	PE	0.84	0.98	0.85	0.40
51.0	PE	0.68	0.96	0.79	0.05
51.0	PET	1.24	0.98	0.68	0.08
51.0	PET	2.21	0.84	0.78	0.15
51.0	SPS	0.84	0.92		0.24
51.0	SPS	0.84	0.63		
95.0	PS	0.90	0.63	0.63	0.01
95.0	PS	0.95	0.75	0.75	0.02
95.0	PE	0.76	0.67	0.78	0.70
95.0	PE	0.75	0.67	0.84	0.78
95.0	PET	1.11	0.91	0.84	1.37
95.0	PET	0.86	0.72	0.64	0.02
95.0	SPS	0.82	0.85	1.75	0.87
95.0	SPS		0.66	0.86	

Flotation Recovery Data

Wt % oil	dry weight product [g]	dry weight ash [g]	coal and oil
1.0	38.40	11.60	Montgomery, no. 4 fuel
5.0	39.90	10.10	
10.0	38.65	11.35	
1.0	26.05	23.95	Devco, no. 4 fuel
5.0	32.25	17.75	
10.0	34.10	15.90	
1.0	10.0	40.00	Highvale, no. 4 fuel
5.0	24.65	25.35	
10.0	30.05	19.95	
1.0	3.60	46.40	Bien Fait, no. 4 fuel
5.0	9.15	40.85	
10.0	10.75	39.25	
1.0	2.50	47.50	Costello, no. 4 fuel
5.0	7.50	42.50	
10.0	10.0	40.00	
1.0	4.15	45.85	Montgomery, n-$C_{16}H_{34}$
5.0	8.05	41.95	
10.0	8.60	41.40	
1.0	3.25	46.75	Devco, n-$C_{16}H_{34}$
5.0	6.55	43.45	
10.0	7.20	42.80	
1.0	2.30	47.70	Highvale, n-$C_{16}H_{34}$
5.0	3.25	46.75	
10.0	5.40	44.60	

Flotation Ash Rejection Data

Wt % oil	Wt % ash in product	coal and oil
1.0	3.96	Montgomery, no. 4 fuel
5.0	2.94	
10.0	3.15	
1.0	18.59	Highvale, no. 4 fuel
5.0	15.02	
10.0	13.16	
1.0	13.85	Bien Fait, no. 4 fuel
5.0	13.28	
10.0	12.89	
1.0	8.71	Costello, no. 4 fuel
5.0	7.89	
10.0	7.76	
1.0	18.14	Highvale, n-$C_{16}H_{34}$
5.0	18.11	
10.0	18.06	
1.0	8.12	Montgomery, n-$C_{16}H_{34}$
5.0	8.09	
10.0	8.07	

Volume-Mean Agglomerate Diameter Data

Wt % n-$C_{16}H_{34}$	diameter [μm]	coal
0.0	33.30	Devco
0.5	34.30	
1.0	40.29	
2.0	43.62	
5.0	48.28	
10.0	53.28	
0.0	9.40	Highvale
0.5	9.59	
1.0	11.09	
2.0	11.94	
5.0	13.07	
10.0	14.10	
0.0	20.30	Montgomery
0.5	21.31	
1.0	25.38	
2.0	27.40	
5.0	29.64	
10.0	34.51	
0.0	6.00	Bien Fait
1.0	6.12	
5.0	6.54	
10.0	6.96	
0.0	7.40	Costello
1.0	7.77	
5.0	8.36	
10.0	8.88	